

Portland State University

PDXScholar

Dissertations and Theses

Dissertations and Theses

1-1-2011

Numerical and Experimental Analysis of Composite Sandwich Links for the LCF System

Max Taylor Stephens
Portland State University

Follow this and additional works at: https://pdxscholar.library.pdx.edu/open_access_etds

Let us know how access to this document benefits you.

Recommended Citation

Stephens, Max Taylor, "Numerical and Experimental Analysis of Composite Sandwich Links for the LCF System" (2011). *Dissertations and Theses*. Paper 579.
<https://doi.org/10.15760/etd.579>

This Thesis is brought to you for free and open access. It has been accepted for inclusion in Dissertations and Theses by an authorized administrator of PDXScholar. Please contact us if we can make this document more accessible: pdxscholar@pdx.edu.

Numerical and Experimental Analysis of Composite Sandwich Links for the
LCF System

by
Max Taylor Stephens

A thesis submitted in partial fulfillment of the
requirements for the degree of

Master of Science
in
Civil and Environmental Engineering

Thesis Committee:
Peter Dusicka, Chair
Manouchehr Gorji
Hormoz Zareh

Portland State University
©2011

Abstract

Shear links are used as fuse elements in lateral load resisting systems to provide ductility and dissipate seismic energy. These links have traditionally been employed in eccentrically braced frames, but have more recently been suggested for use in the innovative linked column frame system (LCF). Current design specifications for shear links require intermediate web stiffeners to provide out-of-plane web stability so ductility requirements can be achieved. This research focused on moving from discrete transverse web stiffening to continuously stiffened webs in built up shear links. Built up links were designed to yield in shear when subjected to severe cyclic loading, however the webs of the links were designed using two metal sheets joined by an elastic core. These composite “sandwich” webs allowed for an increase in web thickness (and inherent flexural rigidity) without increasing the shear strength of the links. Numerical and experimental investigations were conducted to assess the performance of composite sandwich links subjected to severe loading. Numerical results showed improved web behavior in sandwich links in which the core material was assigned an elastic modulus greater than 5000psi. Due to fabrication limitations, experimental specimens were fabricated with a core material elastic modulus of 1000psi. These specimens did not perform as well as unstiffened base case links in terms global hysteretic behavior or ductility.

Dedication

To my love Angelique...for your love and support throughout this process. Also to my parents...thank you for supporting me throughout my academic career. I wouldn't have made it this far without you.

Acknowledgements

I would like to thank Dr. Peter Dusicka for taking me on as a grad student and mentoring me throughout my academic career. Your unorthodox approach to seismic engineering has helped me grow as an engineering student. The experimental and analytical experience I have gained working in the iSTAR lab will prove invaluable in my future endeavors.

I would additionally like to acknowledge Dr. Gorji and Dr. Zareh. Thank you both for taking the time to sit on my thesis committee. You are two of the most challenging and inspiring professors I have faced during my time at PSU. Dr. Gorji, the structural engineering fundamentals you have imparted on me have guided me through my research. Without your passion and dedication for teaching, I would not be where I am today. Dr. Zareh, your enthusiasm for finite element analysis sparked my interest in numerical modeling. I will never forget that there is more to FEA than pretty colors.

Greg Lewis, thank you for all of your help on this project. Without your guidance, I would have spent an eternity on both the numerical and experimental sections of this research.

Funding support for this research was provided by the American Institute of Steel Construction and the National Science Foundation under Grant Award 0830414.

Any opinions, findings, conclusions and recommendations presented in this paper are those of the writer and do not reflect the views of the sponsors.

Table of Contents

Abstract	i
Dedication	ii
Acknowledgements	iii
List of Tables	vi
List of Figures	vii
List of Abbreviations/Symbols	x
Preface	xiii
1.0 Introduction	1
1.1 Shear Link Hysteretic Energy Dissipaters	4
1.1.1 A992 Steel in Shear Links	5
1.1.2 Link Overstrength	6
1.1.4 Link to Column Connection	7
1.1.5 Built Up Shear Links	10
1.1.6 Qualification of EBF Through Testing	11
1.2 Web Stability	11
1.2.1 Intermediate Stiffeners	13
1.2.2 Issues with Intermediate Web Stiffeners	15
1.2.3 Required Web Stiffness	17
1.2.4 Plate Girders and Steel Plate Shear Walls	19
1.3 Sandwich Plates	23
1.3.2 Sandwich Webs in HPS Plate Girders	25
1.3.3 Sandwich Webs in Shear Links	27
2.0 Numerical Modeling	28
2.1 Model Description	28
2.2 Material Modeling	29
2.2.1 Hyperelastic Materials	29
2.2.2 Steel	32
2.2.3 Bonding	34
2.3 Element Selection	34
2.4 Link Selection	37
2.5 Web End Stiffeners and Web Stability	38
2.6 Model Validation through Flexural Bending Tests	43
2.7 Results and Observations	44
2.7.1 Base Link Behavior	45
2.7.2 Effects of Core Elastic Modulus	46
2.7.3 Effects of Core Thickness	49
2.7.4 Numerical and Predicted Buckling Behavior	51
2.7.5 Web Panel Aspect Ratio Analysis	53
2.7.6 Effects of Rubber to Steel Bond Strength	55
2.8 Conclusions and Implementation Decisions	56
3.0 Experimental Test Setup	58
3.1 Test Specimens	59
3.1.1 Link to Column Connection	60
3.2 Test Setup and Instrumentation Procedure	61

4.0 Experimental Results and Discussion.....	63
4.1 Link 14DBase.....	64
4.2 Link 25DBase.....	65
4.3 Link 14DN3_1000.....	66
4.4 Link 25DN1_1000.....	67
4.5 25DN3_1000	68
4.6 Effects of Core Thickness on Web Stability and Web Strain	69
4.7 Large Initial Imperfection and Core Fracture	72
4.8 End Stiffener Effects on Strain.....	73
4.9 Numerical Model Validation.....	74
4.9.1 14in Deep Link Numerical Comparison.....	75
4.9.2 25in Deep Link Numerical Comparison.....	76
5.0 Summary and Conclusions	80
5.1 Numerical Conclusions	82
5.2 Experimental Conclusions	83
6.0 Recommendations for Future Work.....	85
Tables.....	87
Figures.....	91
References	150
Appendix.....	155
A. Link and End Plate Design.....	155
A.1 14in Deep Link Design.....	155
A.2 25in Deep Link Design.....	161
A.3 Link End Plate Connection Design – 14in Deep Link	166
A.4 Link End Plate Connection Design – 25in Deep Link	172
B. Shop Drawings of Links	179
C. Finite Element Analysis Web Strain Distributions	182
C.1 14in Deep Links.....	182
C.2 25in Deep Links.....	185
D. Experimental Data Sets	189
D.1 Data Set Instrumentation Schematic.....	189
D.2 Link 14DBase	190
D.3 Link 14DN3_1000	201
D.4 Link 25DBase	212
D.5 Link 25DN1_1000.....	223
D.6 Link 25DN3_1000	234

List of Tables

Table 1: Qualification Testing Loading Protocol for Links in EBF	87
Table 2: Summary of Base Link Properties	87
Table 3: Summary of Analytical Specimens	88
Table 4: Predicted Link Performance	89
Table 5: Numerical Link Performance	89
Table 6: Experimental Link Performance	90

List of Figures

Figure 1: Steel Lateral Load Resisting Systems (Lewis, 2010).....	91
Figure 2: Link Column Frame Overview.....	91
Figure 3: Link Rotation Angle Due to Lateral Frame Displacement (Lewis, 2010)	92
Figure 4: Final Stable Hysteretic Loops of Shear Links Subjected to (a) Symmetric and (b) Unsymmetric Cyclic Loading from Kasai and Popov (1986).....	92
Figure 5: Failure of Web at Stiffener Weld Termination from Lewis (2010)	93
Figure 6: Optimum Stiffener Rigidity vs. Load Relationship.....	93
Figure 7: Basler's Tension Field Action Equilibrium Model.....	93
Figure 8: Strip Model.....	94
Figure 9: Sandwich Plate Overview	94
Figure 10: Typical Failure Modes of Sandwich Plates	95
Figure 11: Proposed Sandwich Web Systems in HPS Girders	95
Figure 12: Model Overview.....	96
Figure 13: Convergence Curves.....	97
Figure 14: Rubber Material Properties Used to Calibrate Hyperelastic Material Formulation.....	98
Figure 15: Half Cycles Used to Calibrate Cyclic Hardening Properties of Steel and Modified Half Cycle Material Properties put into ABAQUS for Material Calibration ...	99
Figure 16: Material Calibration Verification Curve.	100
Figure 17: Shell and Full 3-Dimensional Element Monotonic Response Comparison .	101
Figure 18: Shell and Full 3-Dimensional Element Hysteretic Response Comparison ..	102
Figure 19: Shell and Full 3-Dimensional Model Verification Links at 3% and 5% Inelastic Rotation	103
Figure 20: Weld Heat Dissipation Analysis.....	104
Figure 21: Summary of Final Link Designs	105
Figure 22: 14in Deep Sandwich Web Core Stiffness/Thickness Relationship to Provide Equivalent Flexural Rigidity.....	106
Figure 23: 25in Deep Sandwich Web Core Stiffness/Thickness Relationship to Provide Equivalent Flexural Rigidity.....	106
Figure 24: Web Buckling Deformation Angle/Core Material Thickness Relationships for 14in and 25in Deep Composite Links.....	107
Figure 25: (a) Flexural Bending Test Setup and (b) Flexural Bending Model Overview	108
Figure 26: Flexural Bending Behavior of Sandwich Plate from Link 14DN3_1000	109
Figure 27: Flexural Bending Behavior of Sandwich Plate from Link 25DN1_1000	110
Figure 28: Flexural Bending Behavior of Sandwich Plate from Link 25DN3_1000	111
Figure 29: Analytic (a) Monotonic and (b) Cyclic Behaviors of Link 14DBase.....	112
Figure 30: Analytic (a) Monotonic and (b) Hysteretic Behaviors of Link 25DBase.....	113
Figure 31: Web Strain Distribution in Link 14DBase	114

Figure 32: Web Strain Distribution in Link 25DBase	115
Figure 33: Analytic (a) Monotonic and (b) Hysteretic Behaviors of Link 14DN1_385	116
Figure 34: Analytic (a) Monotonic and (b) Hysteretic Behaviors of Link 14DN1_1000	117
Figure 35: Analytic (a) Monotonic and (b) Hysteretic Behaviors of Link 14DN1_5000	118
Figure 36: Analytic (a) Monotonic and (b) Hysteretic Behaviors of Link 14DN1_10000	119
Figure 37: Analytic (a) Monotonic and (b) Hysteretic Behaviors of Link 25DN1_385	120
Figure 38: Analytic (a) Monotonic and (b) Hysteretic Behaviors of Link 25DN1_1000	121
Figure 39: Analytic (a) Monotonic and (b) Hysteretic Behaviors of Link 25DN1_5000	122
Figure 40: Analytic (a) Monotonic and (b) Hysteretic Behaviors of Link 25DN1_10000	123
Figure 41: Core Stiffness Parameter Back Bone Analysis for 14in Deep Links	124
Figure 42: Core Stiffness Parameter Back Bone Analysis for 25in Deep Links	124
Figure 43: Core Stiffness Parameter Web Strain Analysis for 14in Deep Links.....	125
Figure 44: Core Stiffness Parameter Web Strain Analysis for 25in Deep Links.....	125
Figure 45: Analytic (a) Monotonic and (b) Hysteretic Behaviors of Link 14DN2_1000	126
Figure 46: Analytic (a) Monotonic and (b) Hysteretic Behaviors of Link 14DN3_1000	127
Figure 47: Analytic (a) Monotonic and (b) Hysteretic Behaviors of Link 25DN2_1000	128
Figure 48: Analytic (a) Monotonic and (b) Hysteretic Behaviors of Link 25DN3_1000	129
Figure 49: Core Thickness Parameter Back Bone Analysis for 14in Deep Links.....	130
Figure 50: Core Thickness Parameter Back Bone Analysis for 25in Deep Links.....	130
Figure 51: Core Thickness Parameter Web Strain Analysis for 14in Deep Links	131
Figure 52: Core Thickness Parameter Web Strain Analysis for 25in Deep Links	131
Figure 53: Debonding Propagation in Link 14DN1_1000	132
Figure 54: Debonding Propagation in Link 25DN1_1000	132
Figure 55: Debonding Parameter Web Strain Analysis for Link 14DN1_1000.....	133
Figure 56: Debonding Parameter Web Strain Analysis for Link 25DN1_1000.....	133
Figure 57: Experimental Apparatus (Lewis, 2010).....	134
Figure 58: Traditional and Modified Bolted End Plate Connections	134
Figure 59: Instrumentation Schematic	135
Figure 60: Experimental Hysteresis of Link 14DBase	135
Figure 61: Experimental Hysteresis of Link 25DBase	136

Figure 62: Experimental Hysteresis of Link 14DN3_1000	136
Figure 63: Experimental Hysteresis of Link 25DN1_1000	137
Figure 64: Experimental Hysteresis of Link 25DN3_1000	137
Figure 65: Experimental Back Bone Comparisons for 14in Deep Links	138
Figure 66: Experimental Back Bone Comparisons for 25in Deep Links	138
Figure 67: White Wash Strain Distribution in Link 14DBase.....	139
Figure 68: White Wash Strain Distribution in Link 25DBase.....	139
Figure 69: White Wash Strain Distribution in Link 14DN3_1000.....	140
Figure 70: White Wash Strain Distribution in Link 25DN1_1000.....	140
Figure 71: White Wash Strain Distribution in Link 25DN3_1000.....	141
Figure 72: Discrete Experimental Strain Distribution in Link 14DBase.....	142
Figure 73: Discrete Experimental Strain Distribution in Link 25DBase.....	143
Figure 74: Discrete Experimental Strain Distribution in Link 14DN3_1000.....	144
Figure 75: Discrete Experimental Strain Distribution in Link 25DN1_1000.....	145
Figure 76: Discrete Experimental Strain Distribution in Link 25DN3_1000.....	146
Figure 77: Link 14DBase Numerical and Experimental Hysteretic Comparison.....	147
Figure 78: Link 25 DBase Numerical and Experimental Hysteretic Comparison.....	147
Figure 79: Link 14DN3_1000 Numerical and Experimental Hysteretic Comparison ..	148
Figure 80: Link 25DN1_1000 Numerical and Experimental Hysteretic Comparison ..	148
Figure 81: Link 25DN3_1000 Numerical and Experimental Hysteretic Comparison ..	149

List of Abbreviations/Symbols

A36	Steel with a 36ksi yield point
A992 Gr. 50	Steel with a 50ksi yield point
BRBF	Buckling Restrained Braced Frame
B32	ABAQUS 3-node quadratic beam element
CBF	Concentrically Braced Frame
CJP	Complete Joint Penetration
C3D8	ABAQUS linear 8-node brick element
EBF	Eccentrically Braced Frame
FEA	Finite Element Analysis
HPS	High Performance Steel
IMF	Ordinary Moment Frame
LCF	Linked Column Frame
LVDT	Linear Variable Displacement Transducer
LYP	Low Yield Point steels
MPC	Multiple Point Constrain in ABAQUS
MRF	Moment Resisting Frame
OCBF	Ordinary Concentrically Braced Frame
OMF	Ordinary Moment Frame
SCBF	Special Concentrically Braced Frame
SMF	Special Moment Frame
SPSW	Steel Plate Shear Wall
S4	ABAQUS linear shell element
S4R	ABAQUS linear shell element with reduced integration
S8R	ABAQUS quadratic shell element with reduced integration
A_w	Area of web
a	Spacing of transverse web stiffeners
b	Web height
b_{ABA}	Rate at which the size of the yield surface of steel changes as plastic strain develops in ABAQUS
b_f	Flange width
b_s	AISC minimum allowable width of transverse web stiffeners
C	The kinematic hardening modulus of steel in ABAQUS
C_B	Constant used to calculate required transverse stiffener spacing based on design link rotation angle
C_v	Ratio of critical web shear stress to shear yield stress
c	Sandwich web core thickness
D	Flexural rigidity of a unit width of web
d	Beam/link depth
e	Link length

e_{eff}	Effective link length
E_c	Modulus of elasticity of the core in a generic sandwich plate
E_F	Modulus of elasticity of the face plates in a generic sandwich plate
E_S	Modulus of elasticity of steel
E_R	Modulus of elasticity of rubber
F_{TS}	Axial force in transverse stiffener in Basler's theory
F_y	Yield strength of steel
G	Plate shear modulus = $E/(2(1+\nu))$
G_c	Shear modulus of core material generic sandwich plates
G_s	Plate secant modulus at buckling
G_{xz}	Core shear modulus associated with the plane perpendicular to the face plates in a sandwich plate
G_{yz}	Core shear modulus associated with the plane parallel to the face plates in a sandwich plate
h	Story height
I_s	Moment of inertia of a discrete transverse stiffener
K	Cyclic strain coefficient for steel
K_s	Plate buckling coefficient
L	Bay width (column center to column center)
L_1	Displacement measured by a diagonally oriented LVDT for the purpose of measuring rotation angles. This displacement is coupled with a displacement L_2 measured by another diagonally oriented LVDT for the purpose of calculating rotation.
L_2	Displacement measured by a diagonally oriented LVDT for the purpose of measure rotation angles. This displacement is coupled with a displacement L_1 measured by another diagonally oriented LVDT for the purpose of calculating rotation.
M_p	Shear link plastic moment capacity
n	Cyclic hardening coefficient for steel
P_{cr}	Bifurcation or critical buckling load
P_{crmax}	Maximum critical load achieved with discrete transverse web stiffeners
Q	Sandwich plate constant which is a function of core elastic modulus, core thickness, and buckle wave length
Q_∞	Maximum change in size of the yield surface of steel in ABAQUS
R_y	Ratio of expected yield strength to minimum specified yield strength
t	Distance from centroid of composite sandwich plate to centroid of a face plate
t_c	Sandwich plate core thickness
t_f	Flange thickness
t_{fp}	Sandwich plate face thickness

t_s	AISC minimum allowable thickness for transverse web stiffeners
t_w	Traditional web thickness
t_{ws}	Sandwich web steel plate thickness
V_p	Shear link plastic shear capacity
V_t	Shear strength due to tension field action predicted by Basler
V_{tw}	Actual shear strength carried by web in Basler's theory
α	Web panel aspect ratio
β	Web panel depth to thickness ratio
Δ	Frame displacement
ΔF_f	Tensile flange forces in Basler's theory
ε	Strain
γ	Link rotation angle
γ_{ABA}	The rate at which the kinematic hardening modulus decreases with strain in ABAQUS
γ_B	Panel web buckling deformation angle
γ_s	Relative flexural rigidity of a discrete transverse web stiffener
γ_s^*	Optimum stiffener rigidity
γ_I^*	Optimum stiffener rigidity of the first kind
γ_{II}^*	Optimum stiffener rigidity of the second kind
γ_{III}^*	Optimum stiffener rigidity of the third kind
γ_u	Design web buckling rotation angle
ν	Poisson's Ratio
η	Plastic reduction factor
ϕ	AISC specified resistance factor
ρ	Link length ratio
σ_o	Equivalent stress defining the size of the yield surface of steel in ABAQUS
σ_r	Flange residual stress from welding
σ_t	Diagonal stress due to tension field action
σ_{wr}	Sandwich plate face wrinkling stress
θ_p	Frame rotation angle
τ_E	Elastic shear buckling stress of an un-stiffened plate
τ_{scr}	Elastic shear buckling stress of sandwich web
τ_{scrimp}	Elastic shear face crimping buckling stress of sandwich web

Preface

Shear links are used in lateral load resisting systems to provide ductility and dissipate seismic energy. These links have typically been used in eccentrically braced frames; however they have more recently been suggested for use in the innovative linked column frame system (LCF). This system incorporates components from traditional lateral load resisting systems, but combines them to achieve performance objectives including rapid return to occupancy. The LCF utilizes shear links placed between closely spaced columns independent of the gravity system to dissipate seismic energy and control drift. Thus for the LCF to satisfy performance goals, the link component must provide sufficient ductility to achieve displacement requirements.

Web stability in shear links plays a pivotal role in load carrying capacity and energy dissipation performance. It has been shown that elastic and early plastic web buckling causes a significant drop in load carrying capacity and energy dissipation during subsequent link deformation (Kasai and Popov, 1986). Thus current specifications for energy dissipating links require the use of intermediate web stiffeners to increase ductility and provide web stability (AISCa, 2005). Stiffener requirements provided in the seismic provisions are based on experimental studies which investigated the criteria for web stiffener spacing as a function of inelastic cyclic shear link deformation (Kasai and Popov, 1986).

Although current code provisions require intermediate web stiffeners to restrain out-of-plane web deformation in shear links, there have been issues with crack initiation and propagation at the root of stiffener welds. Experimental studies conducted by Okazaki, Arce, and Ryu (2005) showed web fracture at the root of intermediate stiffener

welds prior to the onset of web buckling. Further numerical investigations conducted by Chao, Khandelwal, and Tawil (2006) concluded that low k-area yield strengths reduce to potential for ductile fracture at the termination of stiffener welds.

To eliminate ductility issues associated with intermediate stiffeners, this research is aimed at the development of shear link in which out-of-plane web rigidity is provided continuously throughout the web area instead of at discrete stiffener locations. The web design consists of two steel face plates attached using a hyperelastic core material to form a composite “sandwich” plate. The composite web design allows for an increase in web thickness (and inherent flexural rigidity) without increasing the shear strength of the link. The spacing of the two web plates and stiffness of the core material influence the out-of-plane rigidity of the web, allowing for flexibility in design. Numerical parameter studies were conducted to assess the performance of shear dominated links with continually stiffened “sandwich” webs with varying core thickness and core material elastic modulus. Results from the numerical analyses were used to develop full scale experimental specimens to validate numerical results, and performance analyses are provided.

1.0 Introduction

Code provisions governing the design of lateral load resisting systems in the United States rely on ductile inelastic behavior to limit internal forces and prevent structural collapse. This ductility is achieved by isolating damage due to lateral loading to deformation controlled fuse elements designed into the gravity and lateral load resisting systems of structures. These elements are designed to deform plastically and dissipate energy during seismic events, while the remainder of the structure continues to act in the elastic range.

Five lateral load resisting systems are used in steel construction in the United States: moment resisting frames (MRF), concentrically braced frames (CBF), buckling restrained braced frames (BRBF), eccentrically braced frames (EBF), and steel plate shear walls (SPSW). The layout of these systems can be seen in Figure 1. MRF consist of an open bay design in which beams and columns are attached using moment resisting connections. These frames are designed such that plastic hinges develop toward the ends of the beams under lateral loading to dissipate energy and ensure the remainder of the structure remains elastic. There are three common classifications of MRF based on the inelastic performance of the specified moment connection: ordinary moment frames (OMF), intermediate moment frames (IMF), and special moment frames (SMF). OMF are detailed for gravity and light seismic loading, while SMF are detailed to withstand severe reversed cyclic loading and large amounts of inelastic deformation (AISC 2005a). CBF are designed using steel cross bracing to dissipate energy through yielding and buckling during seismic events. There are two common classifications of CBF, the

ordinary concentrically braced frame (OCBF), and the special concentrically braced frame (SCBF), which are designed to withstand limited and significant amounts of inelastic deformation, respectively (AISC 2005a). Similar to CBF, BRBF are designed with steel cross bracing to dissipate energy. The braces in these systems are, however, restrained from buckling, allowing them to achieve full yield strength in both tension and compression. EBF are designed such that the damage from lateral loading is confined to a link in the system which undergoes plastic deformation to dissipate energy. Many EBF design layouts are currently employed, but the most common is created through isolation of a small section or “link” in the beam using diagonal bracing, and detailing this link to withstand severe cyclic loading (AISC 2005a). Finally, SPSW are shear walls designed to increase structure stiffness, resist horizontal story shear, and dissipate energy through development of tension and compression field action similar to that seen in built up plate girders (Astaneh, 2000).

While the aforementioned lateral systems are designed to a life safety performance criteria by preventing structural collapse, there is an interest in moving toward use of an improved performance criteria in design, such that structures can be easily repaired to allow for quick occupation following seismic events. In MRF and EBF in particular, damage is concentrated on the load carrying beams, making it difficult to achieve rapid post earthquake repair and occupancy. Thus this research focuses on the linked column frame (LCF) lateral load resisting system which incorporates components from traditional systems, but combines them to achieve various performance directives including rapid return to occupancy. The LCF consists of two closely spaced columns linked independent of the gravity system placed throughout a moment frame structure.

The links between the columns are designed to dissipate energy, control drift, and limit forces to surrounding members when subjected to lateral loading, while the moment frame provides gravity load carrying capacity and secondary lateral stiffness. The links are bolted to the columns to allow for rapid replacement following seismic events, and the stiffness of the moment frame serves as a self centering mechanism to restore the structures geometry following the removal of plastically deformed links. The overall layout of the LCF can be seen in Figure 2.

Testing was conducted by Lewis (2010) to investigate the link component of the LCF system. Specifically, the effectiveness of using shear and flexure dominated rolled w-sections with bolted endplate connections was examined. End stiffeners were provided to shift plastic strain away from the bolted end plates, and recommendations for intermediate link stiffeners were taken from the 2005 *AISC Seismic Provisions* for links in EBF. It was determined that end stiffeners were effective in moving plastic strain towards the center of the links, and bolted end plates allowed for rapid and relative ease of link replacement; however residual stresses from intermediate stiffener welds resulted in web fracture failure in all shear dominated links tested.

This research is specifically focused on the further development of the link component of the LCF. Built up shear links were designed to yield in shear using recommendations from the 2005 *AISC Seismic Provisions* for EBF links, and end stiffener placement and design was implemented following recommendations provided by Lewis (2010). Rather than incorporating intermediate stiffeners to provide discrete web stability, however, a composite steel-rubber-steel sandwich plate was used for the web in the built up links. This design allows for an increase in web thickness (and

inherent flexural rigidity) without increasing the shear strength of the link, resulting in a web which is continually stiffened. The spacing of the two web plates and stiffness of the core material influence the out-of-plane rigidity of the web, allowing flexibility in design. This innovative stiffening technique eliminates the need for transverse web stiffeners which have been shown to introduce ductility related performance issues. Intermediate web stiffener welds have been shown to change the characteristics of the base metal in the link web, resulting in the initiation of web fracture (see Section 1.2.2). The basic concept of the composite link can be seen in Figure 2. The following sections provide a literature review on EBF links and sandwich webs and discuss in detail the numeric modeling and experimental testing conducted on composite link specimens.

1.1 Shear Link Hysteretic Energy Dissipaters

To reduce lateral load demands during seismic events, shear links have been used as energy dissipaters in EBF for buildings and major bridges. The links in these frames are designed to deform inelastically at performance levels below that of the frame so as to concentrate damage at the location of the link (Okazaki, Arce, Ryu, & Engelhardt, 2005). Provisions for link design are given in the *2005 AISC Seismic Provisions for Structural Steel Buildings*, and the maximum design link rotation is specified according to the length ratio of the link. From the *2005 AISC Seismic Provisions*, the length ratio is given as:

$$\rho = \frac{e}{M_P/V_P} \quad [1]$$

Links with length ratios less than 1.6 and greater than 2.6 are known as short (shear dominated) and long (flexure dominated) links respectively. Links with length ratios between 1.6 and 2.6 are known as intermediate links, and experience a combination of

flexural and shear yielding. The 2005 *AISC Seismic Provisions* require that short and long links be designed to rotation angles of 0.08 and 0.02 radians respectively. Links in eccentrically braced frames generally consist of rolled wide flange sections, however built up shear links are sometimes preferred as they allow for increased geometric and strength design freedom. Many studies have been conducted regarding various EBF link parameters including overstrength, intermediate stiffener configurations, and link-to-column connection details.

1.1.1 A992 Steel in Shear Links

Current building code standards for shear links in EBF are based almost exclusively on experimental studies conducted on rolled wide flange sections composed of A36 steel; however A992 Grade 50 steel has become the standard for fabricating common structural steel shapes in the United States (Okazaki T. E., 2006). With higher yield and tensile strengths, many studies have been conducted to evaluate A992 link behavior and relevant code specifications including the limiting width to thickness ratio and the adopted load history protocol. The limiting width-to-thickness ratio developed from experimental results using A36 steel was $0.30(E_s/F_y)^{1/2}$ for EBF links, corresponding to 8.5 for A36 steel and 7.2 for A992 steel. Many rolled wide flange sections meet the slenderness limit of 8.5 but not the limit of 7.2, excluding them from use in EBF (Okazaki T. E., 2006). Testing by Okazaki and Engelhardt (2006) determined that the limiting thickness ratio could be relaxed to $0.38(E_s/F_y)^{1/2}$ for shear dominated EBF links composed of A992 steel, increasing the limiting slenderness ratio to 9.15. Further analytical studies conducted by Richards and Uang justified the relaxation of the limiting width-to-thickness ratio proposed by Okazaki and Engelhardt. Studies by Okazaki et al (2004)

investigated the effects of load history on A992 EBF link behavior. This testing was motivated by premature failure in many specimens due to a fracture of the web when subjected to the loading protocol specified in the 2002 *AISC Seismic Provisions*. It was determined that link performance was directly related to the applied loading protocol, and thus a protocol was adopted in the 2005 *AISC Seismic Provisions* which realistically reflects the demands caused by earthquake loading on EBF links.

1.1.2 Link Overstrength

When subjected to post yield cyclic loading, links develop increased strength due to a combination of strain hardening and the development of shear resistance in the flanges. Known as overstrength, this strength increase is defined as the maximum shear force developed by the link divided by the plastic shear of the link (Okazaki, Arce, Ryu, & Engelhardt, 2005). To account for overstrength during the design phase, and to ensure the strength of the link does not surpass that of the connection or surrounding components, two link overstrength factors are specified in the seismic provisions. An overstrength factor of 1.25 is specified to account for general material overstrength, and a factor R_y is specified to account for uncertainties regarding the material yield point. For A36 and Grade 50 A992 steels, the R_y factors are 1.5 and 1.1 respectively (AISCa, 2005). The total overstrength factor is calculated by combining the overall material overstrength factor, the yield point overstrength factor, and the design phi (ϕ) factor (total overstrength factor = $1.25R_y/\phi$). Thus to ensure link connections are designed to adequate capacities, overstrength factors of 2.1 and 1.5 must be used for A36 and Grade 50 A992 steels respectively (AISCa, 2005).

Recent studies have suggested that the AISC specified overstrength factor of 1.5 for Grade 50 A992 steel is reasonable for rolled wide flange sections, but inadequate for built up members. Okazaki et al. (2005) investigated overstrength in shear and flexure dominated rolled wide flange links subjected to cyclic loading. Average overstrength values of 1.41 and 1.22 were recorded for the shear and flexure dominated links respectively, suggesting that code specifications are conservative in accounting for link overstrength when using A992 steel in rolled sections. Dusicka, Itani, and Buckle (2004) conducted studies evaluating the cyclic behavior of built up shear links composed of conventional and specialty steels. Experimental studies were conducted on four types of shear dominated links composed of United States conventional and high performance steels (HPS) and two types of Japanese low yield point (LYP) steels. All specimens displayed overstrength values greater than the specified design factor of 1.5. The built up link composed of conventional A992 steel showed overstrength in excess of 2, while even larger overstrengths were observed in links composed of the LYP steels. Corte and Mazzolani (2006) conducted testing on a full scale two story concrete frame retrofitted using eccentric bracing. Link connection failures were observed for all link configurations tested, and an overstrength factor of up to 3 was suggested in place of the code specified 1.5. Finally, overstrengths of up to 1.93 were recorded for shear dominated links in the San Francisco Bay Bridge in work by McDaniel, Uang, and Seible (2003).

1.1.4 Link to Column Connection

Complete joint penetration (CJP) welds have traditionally been required at link to column joints to increase stiffness and account for inelastic deformation caused by cyclic loading.

A recent study suggested, however, that bolted end plate connections offer a promising and economic alternative to fully welded link-to-column connections. Testing conducted by Ramadan and Ghobarah (1995) showed that links with adequately designed bolted connections sustained the same displacement demands and dissipated nearly the same amount of energy as links with shop welded end plate connections.

Link end plate behavior is influenced by various parameters including bolt slip, end plate thickness, and link-to-end plate weld design. Bolt slip causes connections to dissipate a lower amount of energy, and in shear links the effects of bolt slip are magnified due to the large shear loads imposed on the bolts. To eliminate the effects of bolt slip, it is recommended that bolted end plate connections be designed to slip critical standards (Ramadan & Ghobarah, 1995). Testing has shown that preloading bolts to yield capacity results in higher initial connection stiffness, a more stable hysteretic response, and a larger deformation capacity (Stratan & Dubina, 2004) (Broderick & Thomson, 2000).

End plate thickness has a large effect on the behavior of bolted end plate connections. Studies conducted by Broderick and Thomson (2000) investigated the failure mechanisms of end plates with different thicknesses. Three different end plate thicknesses (thin plates, intermediate plates, and thick plates) were chosen to investigate the three bolted end plate failure modes defined in Eurocode 3. Mode 1 failure occurs when plastic hinges are formed at the bolt line and at the beam flange, mode 2 failure occurs due to a combination of yielding in the plate and bolts, and mode 3 failure occurs purely as a result of bolt yielding. The failures observed in the end plates in the experimental studies were consistent with the modes described in Eurocode 3. The thin

plate displayed a highly ductile behavior, as a complete yielding of the end plate was eventually observed consistent with mode 1 failure. The intermediate plate showed yielding in the end plate followed by bolt yield and rupture consistent with mode 2 failure. The thick plate specimen showed purely elastic endplate behavior and bolt failure consistent with mode 3, however, the bolt failure was brittle in nature and, it was suggested that this configuration not be used for seismic design (Broderick & Thomson, 2000). Despite the recommendations of Broderick and Thomson, studies conducted by Stratan and Dubina (2004) and McDaniel, Uang, and Seible (2003) have shown that thicker end plates help with ease of link replaceability due to the purely elastic behavior of the endplate.

Link to end plate weld design has a large impact on the overall cyclic performance of shear links. Studies by Stratan and Dubina (2004) and Fortney, Shahrooz, and Rassati (2007) showed that fillet welds do not perform well when subjected to cyclic loading due to crack initiation at weld roots. It has been suggested that providing end returns at the ends of links could delay the formation and propagation of weld fractures at large rotation angles, and that providing partial or full penetration groove welds minimizes the potential for weld fracture ((Fortney, Bahram, & Rassati, 2007). In testing conducted by Okazaki and Englehardt (2007), fractures were observed at the throat of fillet welds and at the weld to base metal interface in link flanges at link to end plate connections. In an attempt to alleviate these failures in remaining specimens, the leg sizes of the fillet welds were increased to 1.5 times the link flange or web thicknesses, and weld tabs were used at the edges of the flanges to avoid introducing undercuts or weld defects. The modified connections performed well under cyclic

loading, however due to the required end plate thicknesses needed to achieve this performance (3 to 5 times the link flange thickness) further research needs to be conducted to develop practical link-to-column fillet weld connection details.

1.1.5 Built Up Shear Links

Utilizing built up shear links as hysteretic energy dissipaters allows designers to overcome the geometric constrictions of rolled wide flange sections. Testing has been conducted to evaluate the hysteretic behavior, overstrength characteristics, and replaceability of built up links. McDaniel, Uang, & Seible (2003) investigated two prototype built up shear links for the main tower of the San Francisco-Oakland Bay bridge. The links were shear dominated, intermediate stiffeners were placed along the web in accordance with the requirements in the 2005 *AISC Seismic Provisions*, and bolted endplate connections were used to allow for link replacement. The main objective of the research was to evaluate the link force and deformation capacities including an assessment of link overstrength and replacability after experiencing large plastic deformation. The built up links in the test were unable to achieve the code specified plastic deformation angle of 0.08 radians due to brittle fracture in the link web resulting from stress concentrations at the root of intermediate stiffener welds. It was shown that alleviating the stress concentration caused by these welds is necessary to prevent brittle fracture in the web. Results from an FEA investigation of the links additionally showed that vertical fillet welds in intermediate stiffeners should be terminated at a minimum distance of three times the web thickness from the toe of the web to flange weld to avoid introducing stress concentrations in this highly restrained area.

Dusicka, Itani, and Buckle (2004) investigated the viability of designing shear links without intermediate web stiffeners through use of LYP steels. These steels allow for an increase in web thickness (and inherent web rigidity) to delay web buckling without significantly increasing V_p or M_p of the link. The LYP links displayed a significantly improved deformation capacity over conventional steel and HPS links due to the combination of the reduced plastic strain demand, the reduction of weldments in the effective length of the link, and the ductile characteristics of the link itself.

1.1.6 Qualification of EBF Through Testing

The required loading protocol for qualification testing of links in EBF can be found in Appendix S of the *2005 AISC Seismic Provisions*. The protocol was developed specifically for A992 steel based on experimental studies conducted by Okazaki et al. (2005) and Richards and Uang (2006). The AISC specified loading requirements are based on link rotation angle, γ (See Table 1). This rotation angle is a function of the bay width, L , link length, e , and frame rotation, θ_p . Frame rotation, θ_p , and link rotation, γ , are defined in Equations 2 and 3 respectively, and the relationship between link and frame rotation is described in Figure 3.

$$\theta_p = \frac{\Delta}{h} \quad [2]$$

$$\gamma = \frac{L}{e} \theta_p \quad [3]$$

1.2 Web Stability

Web stability in shear links plays a pivotal role in load carrying capacity and energy dissipation performance. It has been shown that elastic and early plastic web shear buckling causes a significant drop in load carrying capacity and energy dissipation during

subsequent link deformation (Kasai and Popov, 1986). The elastic buckling strength of an un-stiffened plate subjected to pure shear has been presented by Timoshenko (1936) as:

$$\tau_E = K_s \frac{\pi^2 D}{b^2 t_w} \quad [4]$$

As the elastic buckling stress approaches or supersedes plate yield stress, inelastic plate buckling may occur due to the effects of strain hardening under cyclic loading (Lee and Yoo, 1998). The plastic buckling strength of un-stiffened plates has been related to the elastic critical stress through use of a plastic reduction factor, η , which is a function of plate strain hardening. An empirical study conducted by Kasai and Popov (1986) was used to derive an expression for the plastic reduction factor for webs in shear links. The relationship between the plastic buckling strength and elastic critical stress and the expression derived for the plastic reduction factor are respectively presented in Equations 5 and 6.

$$\tau_B = \eta \tau_E \quad [5]$$

$$\eta = 3.7 \frac{G_s}{G} \quad [6]$$

Intermediate web stiffeners have traditionally been used to resist elastic and plastic web buckling in members subjected to reversed cyclic loading; however innovative stiffening techniques have been introduced including the use of composite sandwich webs. Additionally, the post buckling strength contribution from tension field action in stiffened webs and steel plate shear wall (SPSW) has been investigated. Design criteria for transverse stiffener spacing and geometry to prevent web buckling are given in the 2005 *AISC Seismic Provisions*, and many experimental and theoretical studies

discuss the required effective web and stiffener rigidity to prevent out-of-plane displacement. Criteria regarding the design of SPSW are additionally provided in the 2005 *AISC Seismic Provisions* including analysis techniques and the post buckling shear capacity from tension field action.

1.2.1 Intermediate Stiffeners

The 2005 *AISC Seismic Provisions* provide guidelines as to the required spacing and geometry of intermediate stiffeners to inhibit web buckling in shear links. The required maximum spacing, a , and minimum width, b_s , of transverse stiffeners in shear links have been respectively defined in the seismic provisions as:

$$a \leq 30t_w - d/5 \quad [7]$$

$$b_s \geq \frac{b_f}{2} - t_w \quad [8]$$

Additionally, a minimum stiffener thickness, t_s , of the greater of t_w or 3/8in is specified, and intermediate stiffeners are only required on a single side of the web for links with a depth less than 25in.

The stiffener spacing requirement in the 2005 *AISC Seismic Provisions* are based on experimental studies conducted by Kasai and Popov (1986), which investigated the criteria for web stiffener spacing as a function of inelastic cyclic shear link deformation. Thirty shear links subjected to a variety of loading histories were analyzed to develop a relationship between the link web deformation angle, the web panel aspect ratio, and the beam depth-to-web-thickness ratio. The web panel aspect ratio, α , and the web panel depth-to-thickness ratio, β , are respectively defined in Equations 9 and 10 as:

$$\alpha = \frac{a}{b} \quad [9]$$

$$\beta = \frac{b}{t_w} = \frac{(d-2t_f)}{t_w} \quad [10]$$

The panel web buckling deformation angle, γ_B , can be expressed in terms of the web panel aspect ratio and the web panel depth to thickness ratio as defined in Equation 11:

$$\gamma_B = 8.7K_s(\alpha)\left(\frac{1}{\beta^2}\right)^2 \quad [11]$$

where the plate buckling coefficient, K_s , is a function of the web panel aspect ratio and the assumed boundary conditions of the web panel. γ_B in Equation 11 is defined from the rotation angle at zero load to the rotation angle at which buckling occurs. It should be noted that Equation 11 was derived assuming a Poisson's ratio of 0.3 for structural steel. Due to the short length and lateral end bracing of shear links, Kasai and Popov assumed the link flange provided significant restraint along the longitudinal edges of the web. Thus a clamped edge condition was assumed when calculating the panel web buckling deformation angle, and $K_s(\alpha)$ became

$$K_s(\alpha) = \begin{cases} 8.98 + \frac{5.60}{\alpha^2} & (\alpha \geq 1) \\ 5.60 + \frac{8.98}{\alpha^2} & (\alpha \leq 1) \end{cases} \quad [12]$$

The panel web buckling deformation angle, γ_B , described in Equation 11 can be more conveniently written in terms of the target link deformation angle which results in web buckling. Through analysis of experimental data, Kasai and Popov concluded that the total link rotation angle from extreme tension to extreme compression in the final cycle prior to buckling was only 5-10% larger than the rotation angle measured from zero load

to the point of extreme compression. The relative magnitude of these rotation angles can be seen in Figure 4, which displays the final stable hysteretic loops of a shear link subjected to symmetric and unsymmetric cyclic loading. Additionally, it was determined that the beam-depth-to-web-thickness ratio, d/t_w could be used in place of β , and that a maximum permissible spacing of a/d equal to one could be assumed due to the lowered potential for lateral torsional buckling as a result of the presence of transverse stiffeners. Taking into account the above parameters, Equation 13 represents a conservative approximation for the panel web buckling deformation of a shear link (Kasai and Popov, 1986).

$$\frac{a}{t_w} + \frac{1}{5} \frac{d}{t_w} = C_B \quad (a \leq d) \quad [13]$$

The constant C_B is equal to 56, 38, and 29 for web buckling rotation angles (γ_u) of 0.03, 0.06, and 0.09 radians respectively. C_B can be calculated using linear interpolation for other values of γ_u , and the required stiffener spacing, a , can be determined. (Kasai and Popov, 1986).

1.2.2 Issues with Intermediate Web Stiffeners

Although current code provisions require intermediate web stiffeners to restrain out-of-plane web deformation in shear links, there have been issues with crack initiation and propagation at the root of stiffener welds. Testing conducted by Okazaki, Arce, and Ryu (2005) on A992 links showed fractures in the web at the root of stiffener welds prior to the occurrence of web buckling. It was suggested that the material properties in the k-area of the link were responsible for the cracking, as the proximity of the ends of the stiffener welds to the k-line had an impact on link performance. The k-line areas describe

the web toe areas of rolled w-sections. Coupon testing conducted by Okazaki and Engelhardt (2007) showed that the material in the area of the k-line had a higher tensile strength and lower ductility than the surrounding steel. Finite Element Analyses were conducted by Chao, Khandelwal, and Tawil (2006) to investigate the ductile fracture of shear links. FEA results showed that large local strains develop around stiffener welds due to warping of the stiffener cross sections. The numerical analyses additionally showed that higher k-area yield strengths permit yielding to penetrate farther into the k-area, increasing the size of the yielded zone in the web, reducing the potential for ductile fracture at the termination of stiffener welds. Further examination of the FEA results produced by Chao, Kahndelwal, and Tawil, and an investigation into industry straightening standards revealed potential reasons for the web fracture that was not observed in older testing. Traditional straightening methods resulted in k area yield strengths close to that of the base metal, while current methods result in higher strengths and lower ductility in the k-line area of rolled sections. It has been hypothesized that the increased stress concentration due to current straightening methods coupled with the introduction of welding stresses is responsible for crack initiation at the root of intermediate stiffener welds.

Due to the pre-buckle initiation of cracking at the termination of stiffener welds, various modified web stiffener configurations and design considerations have been suggested. These include limiting the minimum distance from the k-line to the web stiffener weld, utilizing horizontal web stiffeners, and welding the intermediate stiffeners only at the link flanges. Testing conducted by Lewis (2010) evaluated the cyclic behavior of flexure and shear dominated links with intermediate web stiffeners.

Recommendations were taken from Okazaki and Engelhardt (2007) regarding the required distance from the termination of intermediate stiffener welds to the k-line zone of the links to inhibit crack initiation. Despite the fact that the recommended distance of $5t_w$ was substantially larger than the code specified requirement, all shear dominated specimens with intermediate stiffeners failed as a result of crack initiation at the root of intermediate stiffener welds. Figure 5 shows a representative failure of a shear dominated link with intermediate stiffeners tested by Lewis (2010).

1.2.3 Required Web Stiffness

While the 2005 *AISC Seismic Provisions* provide geometric requirements for transverse stiffeners, linear plate buckling theory may additionally be used to determine the required flexural rigidity of discrete transverse stiffeners to restrain web buckling. The relative flexural rigidity of a discrete transverse stiffener, γ_s , the moment of inertia of a discrete stiffener, I_s , and flexural rigidity of a unit width of web, D , are respectively defined by Equations 14, 15, and 16 (Narayanan, 1983).

$$\gamma_s = \frac{EI_s}{Db} \quad [14]$$

$$I_s = \frac{b_s^3 t_s}{3} \quad [15]$$

$$D = \frac{Et_w^3}{12(1-\nu^2)} \quad [16]$$

The minimum value of the relative flexural rigidity, γ_s , to ensure discrete stiffeners behave rigidly is known as the optimum stiffener rigidity, γ_s^* . When defining the optimum stiffener rigidity using linear buckling theory, two assumptions are made regarding web and stiffener behavior. The first assumption describes the initial

conditions of both the web and stiffener as perfectly plane prior to loading without consideration of material or geometrical imperfection. The second assumption describes web deflections as small compared to web thickness to ensure that the linear theory accurately describes web buckling.

When using linear buckling theory, the limit state of the web is defined by the bifurcation or critical buckling load, P_{cr} . It is assumed the web remains perfectly plane for any loads under P_{cr} , and that buckling occurs as soon as this load is reached. As P_{cr} governs the design of webs, stiffeners must be designed at least to γ_s^* so as to act fully rigid at this load. Three common definitions exist to quantify the requirement that discrete transverse stiffeners act fully rigid at P_{cr} . The first states that if the stiffener is in a possible nodal line of the corresponding unstiffened web, there exists a finite stiffener flexural rigidity at which a maximum critical load, P_{crmax} , may be reached. The optimum rigidity defined for this condition is known as optimum rigidity of the first kind, γ_I^* , and ensures that the stiffener remains perfectly rigid as adjacent web panels buckle. A further increase in the flexural rigidity of the stiffener in this condition does not bring about an increase in critical load. The second definition states that if the stiffener is not in a nodal line of the corresponding unstiffened web, the maximum critical load, P_{crmax} , may not be reached for a finite stiffener flexural rigidity. The optimum rigidity defined for this condition is known as optimum rigidity of the second kind, γ_{II}^* , and allows small stiffener deflection as the adjacent web panels buckle. A further increase in the flexural rigidity of the stiffener in this condition results in a slight increase in P_{cr} , and the maximum critical buckling load may only be obtained for γ_{II}^* equal to infinity. While definitions 1 and 2 provide a suitable basis for stiffener design, neither γ_I^* nor γ_{II}^* exist

for most practical cases. Thus the third condition introduces the optimum rigidity of the third kind, γ_{III}^* , for which the critical load of the entire stiffened web is equal to the critical stress of the most unfavorably loaded and slender web panel. The third definition of the optimum stiffener flexural rigidity is applicable for all types of stiffening and loading of webs. Despite the fact that there is no guarantee that a nodal line will form at the stiffener axis and that the critical load attains the highest possible value for γ_{III}^* , γ_{III}^* is always equal to γ_I^* if γ_I^* exists. The load vs. stiffener rigidity relationship for optimum flexural rigidities of the first and second kind can be seen in Figure 6. Using the third definition of the optimum flexural rigidity greatly simplifies the design of stiffened webs, as the analysis is reduced to the design of individual web panels. For this reason, the basis for the design of stiffened webs and flanges are formed using the third definition, and γ_{III}^* is generally denoted simply as γ_s^* . Through experimental research, general solutions have been developed for the optimum flexural rigidity of discrete stiffeners for varying loading and stiffener configurations. For the purpose of this investigation, the optimum flexural rigidity of transverse stiffeners in a web subjected to pure shear is of interest and is defined in Equation 17 (Narayanan, 1983).

$$\gamma_s^* = \frac{28}{\alpha^2} - 20 \quad 0.2 \leq \alpha \leq 1.0 \quad [17]$$

1.2.4 Plate Girders and Steel Plate Shear Walls

As plates are subjected to shearing forces, equal tensile and compressive principle stresses are developed to the point of plate shear buckling, at which time the compressive stress capacity of the plate is greatly reduced (Marsh, Ajam, Ha, 1988). Depending on plate boundary conditions, post buckling shear capacity is provided by the remaining forces in the plate's tension field. AISC design criteria for plate girders and SPSW allow

for a post buckling strength contribution due to the development of tension field action (AISC, 2005a; AISC, 2005b). Equation 18 defines the AISC specified plate girder shear capacity according to the limit state of tension field yielding, Equation 19 defines the ultimate shear capacity of SPSW with a limit state of shear yielding, and Equation 20 defines the tension field angle in SPSW. It should be noted that the second term in Equation 18 describes the shear strength contribution from tension field action.

$$V_n = 0.6F_y A_w \left(C_v + \frac{1-C_v}{1.15 \sqrt{1+(\frac{a}{b})^2}} \right) \quad [18]$$

$$V_n = 0.42F_y t_w L_{cf} \sin 2\alpha \quad [19]$$

$$\tan^4 \alpha = \frac{1 + \frac{t_w L}{2A_c}}{1 + t_w h \left(\frac{1}{A_b} + \frac{b^3}{360 I_c L} \right)} \quad [20]$$

Many theoretical and experimental studies have been conducted to evaluate the tension field behavior of plate girders. Studies conducted by Nishino and Hasegawa (1977) investigated Basler's plate girder shear strength theory which influenced the AISC allowable shear strength contribution due to tension field action. Basler developed an ultimate shear strength formula for plate girders considering both the shear field and tension field action in the web while ignoring the existence of bending rigidity in the flanges. The shear strength contribution due to tension field action was determined by Basler using the equilibrium model shown in Figure 7. In this model, the post buckling shear stress is carried entirely by the web while the vertical stiffener resists only axial compression, and the three unknown forces, V_t , F_{TS} , and ΔF_f can be determined using equilibrium conditions and are defined in Equations 21, 22, and 23 respectively.

$$V_t = \sigma_t h_w t_w \frac{1}{2\sqrt{1+\alpha^2}} \quad [21]$$

$$F_{TS} = \sigma_t h_w t_w \left(\frac{\alpha}{2} - \frac{\alpha^2}{2\sqrt{1+\alpha^2}} \right) \quad [22]$$

$$\Delta F_f = -\sigma_t h_w t_w \frac{\alpha}{2\sqrt{1+\alpha^2}} \quad [23]$$

It has been noted by many researchers that equilibrium conditions are not satisfied in Basler's shear strength theory. By ignoring the shear carrying capacity of the flanges and stiffeners and assuming the shear force is carried entirely by the web, the variable, V_t , in Equation 21 becomes

$$V_{tw} = \frac{1}{2} \sigma_t h_w t_w (\sqrt{1+\alpha^2} - \alpha) \quad [24]$$

leaving only F_{TS} , and ΔF_f to satisfy three equilibrium conditions. Modifications have been made to the theory to satisfy equilibrium conditions by taking into account shear forces in the stiffeners and/or flanges, and it has been empirically shown that Basler's original model conservatively predicts the ultimate post buckle shear capacity of plate girders (Nishino & Hasegawa, 1977). Marsh et al. (1988) conducted an analytic investigation to determine the influence of flange strength on the post buckled shear capacity of steel panels. Finite element analyses were run on single square panels with flanges along the four sides subjected to diagonal tension corner displacements. The flanges were assigned varying cross sectional areas to account for the effects of axial stiffness, but were not given independent flexural strength. It was determined that oversized flanges contributed to the shear capacity of the panels via their torsional and bending rigidities which respectively increased the buckling stress of the panel and allowed for the development of diagonal tension field action. It was further stated that the flanges in girders used in many civil engineering applications are generally proportioned such that web buckling occurs before the maximum plastic shear capacity

can be obtained. Analytic studies were additionally conducted by Lee and Yoo (1998) to evaluate the ultimate strength behavior of web panels subjected to pure shear. Studies were conducted on a typical plate girder web panel, and varying parameters were investigated including the effects of flange rigidity and initial web deformation on the shear carrying capacity. It was determined that flange rigidity directly affected the elastic shear buckling strength of the web panels but had little effect on the post buckling strength. Large initial web deformations were shown to result in a significant reduction in ultimate shear capacity for web panels with low slenderness ratios and in cases where the elastic shear buckling strength was greater than the shear yield strength of the web. Additionally, it was noted that, although through bending stresses are neglected when analyzing existing failure mechanisms of web panels, considerable bending stresses developed in the web panels, resulting in a substantial reduction in the ultimate strength (Lee & Yoo, 1998).

SPSW are typically compared to plate girders when describing ultimate behavior as they exhibit large post buckling load carrying capacities due to the development of tension field action (Astaneh, 2000). The strip model currently outlined in the 2005 AISC Seismic provisions was developed by Thorburn et al. (1983) to describe the ultimate post buckling strength capacity of SPSW. The model describes the post buckling tension field behavior of steel panels by breaking the panels into tension only strips oriented at an angle α from vertical (α has been described in Equation 20). The ultimate capacity of the panels was controlled by the material tensile yield point, and the pre buckling shear resistance was neglected. Figure 8 shows a SPSW panel analyzed using the strip model. Many analytic and experimental investigations have been

conducted to assess the post buckling capacity of SPSW. Shishkin et al. (2009) utilized a modified strip model to investigate the effect panel geometry on the elastic ultimate strength predications of SPSW. In the modified model, a “compression field” was introduced to account for the pre buckling compressive capacity of the panel, and was modeled using a single pin-pin compression strut. To eliminate the compression field strength contribution at the onset of web buckling, a rigid-plastic axial hinge was placed at a discrete point on the strut to simulate buckling. Equation 25 defines the area of the compression strut assuming the entire panel contributes to the compressive resistance.

$$A_{CS} = \frac{Ltsin^2(\alpha)}{2sin\phi sin2\phi} \quad [25]$$

Analytic studies were conducted by Lashgari (2009) to investigate the use of LYP steels in SPSW, and to assess the post buckling performance of panels with differing width-to-thickness ratios. LYP panels were shown to yield at low loads and dissipate energy via plastic deformation, and panels with smaller width to thickness ratios were shown to have an increased capacity for energy dissipation. Studies were conducted by Berman and Bruneau (2004) to compare the post buckling behavior of SPSW and plate girders. The theoretical shear strengths of both SPSW and vertical cantilevering plate girders were determined, and compared to experimental results to demonstrate the differences in the tension field behavior of the two systems. It was shown that the tension field inclination angles for SPSW and plate girders differed due to the contrasting stiffness in the panel boundary conditions, resulting in differing tension field behavior.

1.3 Sandwich Plates

Sandwich plates are composite structures in which two thin face sheets with high stiffness are bonded to a relatively thick low stiffness core for the purpose of increasing

structural stability (see Figure 9). The face plates and core are bonded to facilitate load transfer between the layers, and flexural stiffness is provided by the face sheets while shear is transmitted by the core material (NASA, 1971). Sandwich plate design is generally controlled by two modes of instability failure; global panel buckling in which the face plates and core material act uniformly out-of-plane, and local buckling as a result of face sheet dimpling or wrinkling, shear buckling of the core, or bond failure between the core and face materials (see Figure 10) (NASA, 1971). The critical stresses which result in global shear buckling, axial face sheet wrinkling, and core shear buckling are defined in Equations 25, 26, and 27 respectively for sandwich webs with continuous foam cores (Sullens et al., 1969). It should be noted that the critical stress expression for face sheet dimpling has not been included because this failure mode occurs only in sandwich plates with discontinuous webs, and is thus not relevant to this research.

$$\tau_{scr} = \left(\frac{\pi^2}{b_s^2} \right) (K_S)(D) \quad [26]$$

$$\sigma_{wr} = Q \left[\frac{\eta E_f E_c G_c}{(1-\nu^2)} \right]^{\frac{1}{3}} \quad [27]$$

$$\tau_{scrimp} = \frac{h^2}{(t_1+t_w)t_c} \sqrt{G_{xz}G_{yz}} \quad [28]$$

Many studies have been conducted to evaluate the buckling behavior of sandwich webs. Analytic studies conducted by Briscoe et al. (2010) investigated the shear buckling behavior of web core panels subjected to distributed shearing stresses using a Pasternak elastic foundation model. The face plates in the sandwich web were assumed to be perfectly bonded to the elastic foundation, and parameter studies were conducted to determine the effects of core and face plate material constants and plate aspect ratio on the buckling behavior. Studies conducted by Lopatin and Morozov (2008) and Fagerberg

and Zenkert (2005) evaluated the face wrinkling instability failure mode of sandwich plates. Both studies utilized the Winkler elastic foundation model to investigate the effects of initial geometric face plate deformation and core to facing thickness ratios on the wrinkling behavior of sandwich plates. Additional studies have been conducted to analytically assess the local and global buckling behaviors of sandwich plates with varying core and face plate parameters by Meyer Piening (2010) and Vinson (1999).

1.3.2 Sandwich Webs in HPS Plate Girders

The strength benefits of high performance steel (HPS) in plate girders have not fully been realized due to web stability issues associated with the reduction of required material based on strength requirements alone. To overcome these stability issues, the use of a sandwich web plate system with the web plates tied together using a core material or internal stiffeners has been suggested (see Figure 11). Czaplicki (1996) introduced three modes of web instability which must be overcome in composite sandwich webs: bend buckling, shear buckling, and vertical buckling. Bend buckling occurs when the web buckles due to compression stresses as a result of flexure in the girder. This results in out-of-plane deformations of the web which decreases the overall strength. It is suggested that to prevent bend buckling of a composite web, Equation 29 be used (Czaplicki, 1996).

$$\frac{b}{c+t_{ws}} \leq 1.65 \sqrt{\frac{K_s E_s}{F_y}} \quad [29]$$

where F_y is the web yield strength. Shear buckling occurs due to shear stresses in the web. The use of Equation 30 has been suggested to prevent shear buckling the web in a composite girder (Czaplicki, 1996).

$$\frac{b}{c+t_{ws}} \leq 1.93 \sqrt{\frac{K_s E_s}{F_y}} \quad [30]$$

where F_y is the web yield strength. Vertical buckling occurs due to the vertical stress imposed on the web as a result of the curvature of the compression flange. To prevent vertical buckling of a composite web, use of Equation 31 has been suggested (Czaplicki, 1996).

$$\frac{b}{c+t_{ws}} \leq 1.16 E_s \sqrt{K_s \frac{2t_{ws}b}{A_f} \left(\frac{1}{F_y(F_y + \sigma_r)} \right)} \quad [31]$$

where F_y is the yield strength of the flange.

Experimental studies were conducted by Driver et al. (2002) to investigate the web buckling behavior of HPS I-girders with internally stiffened webs. Tests on five panels were conducted which simulated the bend buckling case. Both the buckling performance of the web and the required properties of the core material to improve web performance were analyzed. It was determined that the three modes of web buckling described by Czaplicki occurred as a result of either overall web buckling or local plate buckling. The geometry of the girder and the overall stiffness of the internal stiffeners were shown to determine whether local or global buckling controlled in the specimens. If the bond between the web plates and the internal stiffeners was not broken, localized buckling of the face plates was prevented. It was also found that the web could be proportioned to prevent overall buckling, in which case the face plates yielded prior to the occurrence of web instability. The effects of the core material properties on overall web behavior were additionally investigated. It was determined that the most important properties of the core material were the ability of the material to transfer stresses between

the two plates, its yield stress, durability under cyclic loading, and the bond strength between the core layer and the face plates.

1.3.3 Sandwich Webs in Shear Links

Analytic studies were conducted by Dusicka and Lewis (2007) to investigate the hysteretic behavior of steel shear links with composite sandwich webs. The purpose of this research was to illustrate the feasibility of a continuous web stiffening technique to eliminate the need for intermediate web stiffeners and the inherent problems they potentially cause (see 1.2.2). Parameter studies were conducted using ABAQUS to investigate the effects of the core material elastic modulus and core thickness on the global behavior of the links. The core material in the model was assumed perfectly elastic and perfectly bonded to the steel face plates. The steel components in the links were modeled using shell elements, while the elastic core material was modeled using full 3-dimensional continuum elements to accurately capture the shear behavior of the links. It was shown that the hysteretic behavior of the composite links improved as the core thickness and/or elastic modulus increased, and the plastic shear strength of the composite web was eventually achieved. The study ultimately illustrated the viability of utilizing an elastic core sandwich web for continuous web constraint in shear links, and it was recommended that further analytic and experimental studies be conducted.

2.0 Numerical Modeling

2.1 Model Description

The commercially available finite element computer program ABAQUS v6.9 was used to numerically investigate the cyclic behavior of shear dominated sandwich links. Three dimensional modeling was used, and material and geometric non-linear behaviors were incorporated. Section 2.2 describes the non-linear material formulations used to model rubber and steel in the composite link. Model geometry included the effective length of the link, the stiffened end zones, the end plate connection, and the columns. The remainder of the test setup was excluded. Material failure criterion was not incorporated into the model, however many link performance parameters were investigated including a) the required web thickness and core material elastic modulus to provide adequate web stability b) the effects of web aspect ratio on overall behavior, and c) the importance of rubber to steel bond strength. Full 3-dimensional 8 node elements were used to model the composite link, while beam elements were used to model columns in the test setup. Element selection is described in more detail in Section 2.3. Rigid elements were used to connect the composite link to the columns. The rigid elements were “tied” to the end plates of the composite link using ABAQUS multiple point constraints (MPC), which fixed the degrees of freedom of the nodes on the end plate to a node on the end of the rigid element. The other end of the rigid element was fixed to the columns. Section 2.3 describes the link to column assembly in further detail. Loading was applied to the composite link by assigning linear displacements to the top of the columns which corresponded to target link rotation angles specified in the 2005 *AISC Seismic Provisions*. A model overview can be seen in Figure 12.

A Convergence study was run on the model by analyzing the global cyclic behavior of the composite link. Global hysteretic behavior was chosen as the convergence metric because the objective of the FEM was to investigate overall link behavior as opposed to local material conditions. A cyclic, as opposed to monotonic, protocol was used to perform the convergence study due to discrepancies between the cyclic and monotonic element and material behaviors. The columns were excluded from the modeling process during the convergence study for computational efficiency. The final mesh refinement of the composite links consisted of two elements across the thickness of the flanges, one element across the thicknesses of the two steel sections in the web, and 5 elements across the thickness of the neoprene. Cyclic convergence curves can be seen in Figure 13.

The steel components of the composite link including the flanges, webs, end stiffeners, and end plates were assembled using ABAQUS tie constraints. These constraints restrain relative displacements and rotations and allow for rapid mesh transition between varying components of the composite link. A cohesive interaction property with calibrated damage initiation and evolution parameters was used to define the bond between steel and rubber in the composite web. Section 2.2.3 describes the interaction property used to model the interaction between rubber and steel.

2.2 Material Modeling

2.2.1 Hyperelastic Materials

To effectively model the shear dominated sandwich link in ABAQUS, a material formulation had to be developed to capture the hyperelastic behavior of rubber. Fenz and Constantinou (2005) discuss three major issues in the FEA of materials which exhibit

hyperelastic behavior. 1) Hyperelastic materials have a non linear stress strain relationship and are virtually incompressible, which lead to numeric instabilities, 2) Hyperelastic materials are highly extensible, which means that small deformation and rotation assumptions are not valid, and 3) Hyperelastic materials exhibit stick-slip friction at the contact interface which requires a robust contact algorithm to account for the change in boundary configuration. These issues can be generalized as material, geometric, and boundary nonlinearities. For hyperelastic materials, ABAQUS uses strain energy potentials to relate stress to strain. Fitted material coefficients are required to develop the stress strain relationships, thus the ability of a model to predict material behavior is strongly dependent on these coefficients.

Duncan, Maxwell, and Hunt (1999) compared the experimentally determined material coefficients to the coefficients calculated by three hyperelastic material formulations in ABAQUS; the Mooney-Rivlin, Ogden, and hyperfoam formulation. Both the Mooney-Rivlin and Ogden models assume that the material is incompressible ($\nu=0.5$) unless volumetric data is included. The Ogden formulation is a special form of the Valanis-Landel function which is capable of capturing the shear behavior of materials with only the input of uniaxial test data (Bradley, Chang, & McKenna, 2001). The hyperelastic foam formulation is distinct from the Mooney-Rivlin and Ogden models in that it is highly compressible (Simulia, 2010). It was shown that the material coefficients calculated by ABAQUS compared well with the experimentally determined coefficients; however the resulting stress strain predictions were more linear than the measured data.

Fenz and Constantinou utilized FEA to investigate the behavior of the rubber restoring force element in seismic base isolation pads. The hyperelastic constitutive neo-

Hookean model was used to capture the behavior of the rubber. The shortcoming of this model is that it uses a single valued shear modulus for all ranges of strain when in actuality at large strains the shear modulus decreases significantly. Due to this limitation, the model gives good results to only 40% strain in uniaxial tension and 90% strain in simple shear (Fenz Daniel, 2005). Bradly, Chang, and McKenna (2001) investigated the use of a multi term version of the Ogden strain-energy density function in ABAQUS to model vulcanized rubber bearing pads using only uniaxial test data. The results of the Ogden formulation were compared to the results obtained using polynomial strain-energy density function and experimental data, and it was shown that the model accurately captured the hyperelastic behavior of the bearing rubber.

Due to the positive results presented by Duncan, Maxwell, and Hunt (1999) and Bradly, Chang and McKenna (2001) regarding the effectiveness of the Ogden formulation in capturing the hyperelastic behavior of rubber with only the input of uniaxial test data, the Ogden formulation was used to model the rubber in the composite links. Uniaxial data from Bradly, Chang, and McKenna (2001) was used to model the hyperelastic material in all links. This data was scaled accordingly to achieve the desired elastic modules of the core material for the numerical parametric core elastic modulus study. The original uniaxial data and the scaled data are shown in Figure 14. Additionally, as of the writing of this thesis, uniaxial test data has not been obtained for the hyperelastic material in the experimental specimens. The elastic modulus of the core material was estimated using the Shore Durometer Hardness and an empirical relationship provided by Gent (1958). The hyperelastic core material used in the experimental specimens was 70 Durometer A, which corresponded to an elastic modulus of approximately 1000psi.

2.2.2 Steel

To accurately model the non-linear cyclic behavior of the steel in the composite link, the combined Isotropic/Kinematic hardening formulation was used. In this formulation, the nonlinear Kinematic and Isotropic hardening components respectively describe the translation of the yield surface in stress space, and the change in the equivalent stress defining the size of the yield surface as a function of plastic deformation. The Kinematic hardening formulation captures the Bauschinger effect on materials during reversed cyclic loading by accounting for the translation of the yield surface at equivalent plastic strains, while the Isotropic formulation describes the change in the size of the yield surface of the material (Simulia, 2010). The Kinematic and Isotropic hardening behaviors of materials in ABAQUS are defined using material parameters calibrated with experimental data. The Kinematic hardening parameters consist of σ_o , C , and γ_{ABA} which respectively describe the equivalent stress defining the size of the yield surface at zero plastic strain, the kinematic hardening modulus, and the rate at which the kinematic hardening modulus decreases with plastic strain. The Isotropic hardening parameters consist of σ_o , Q_∞ , and b_{ABA} , where Q_∞ and b_{ABA} respectively describe the maximum change in size of the yield surface and the rate at which the size of the yield surface changes as plastic strain develops (Simulia, 2010).

Experimental data was used to verify the accuracy with which the combined Isotropic/Kinematic hardening parameters predicted the cyclic behavior of steel.

Dusicka, Itani, and Buckle (2006) conducted studies to investigate the cyclic response of plate steels under large inelastic strains. Specifically, the cyclic behavior of Grade 50 structural steel was analyzed, and a power law relationship was developed to define the

cyclic backbone curve of the steel (Dusicka et al., 2006). This relationship is defined by equation 32:

$$\varepsilon = \frac{\sigma}{E} + \left(\frac{\sigma}{K}\right)^{1/n} \quad [32]$$

Using the last half cycle of the cyclic response of the Grade 50 steel from the study by Dusicka, Itani, and Buckle, combined Isotropic/Kinematic material constants were developed in ABAQUS. The last half cycle used to develop the material constants is shown in Figure 15. These constants were used to define the material in a simple coupon model, and the coupon was subjected to the experimental reversed cyclic loading protocol. The power law defined in Equation 32 was used to assess the accuracy of the parameters in predicting the plastic cyclic behavior of the Grade 50 steel. From Figure 16, it can be seen that the cyclic backbone behavior of the steel compares well with the backbone predicted by the power curve developed by Dusicka, Itani, and Buckle.

After it was verified that material constants could accurately be derived to define the combined Isotropic/Kinematic hardening parameters of steel using experimental data, the hardening formulation used to model the composite links was calibrated. As of the writing of this thesis, coupon testing has not been conducted on steel from the webs and flanges of the experimental specimens for model calibration. The cyclic data from the last half cycle provided by Dusicka, Itani, and Buckle (2006) was scaled according the nominal yield strengths of the specimen steel from the mill certification testing sheets to calibrate the material properties. Data from the scaled cycle was used in a single element model to generate the material constants necessary to describe the combined

isotropic/kinematic hardening behavior of the steel. Figure 15 shows the process used to scale the steel properties.

2.2.3 Bonding

To effectively define the interaction between the rubber core and steel in the web of the composite link, the rubber to steel bond strength was incorporated in the numeric model. An implicit cohesive contact surface was defined between the rubber and steel in the web such that bond strength parameters such as failure shear and tensile stresses and damage evolution could be specified. Damage initiation was assigned to the cohesive surface based on ultimate allowable shear and tensile stresses, while damage evolution was defined based on the subsequent strain required for the stress in the cohesive surface to reduce to zero. Shear and tension strengths of the bond in the bond failure parameter study were calibrated by analyzing the bond strength demands in a model with a perfect face plate to core bond. Additionally, as of the writing of this thesis, information has not been obtained regarding the bond characteristics of the webs in the experimental specimens. Bond failure was not observed in any of the specimens, however, so this parameter was not essential for model validation.

2.3 Element Selection

Prior to modeling the composite link, verification tests were run using experimental data and finite element results generated by Lewis (2010). Specifically, the effectiveness of modeling shear links subjected to severe reverse cyclic loading using shell elements was analyzed. Lewis (2010) conducted numeric analyses and experimental testing on a W12X22 flexure dominated link with intermediate and end stiffeners. ABAQUS v.6.9 was used to perform the numeric analyses, and all components of the link were modeled

using the 8 node linear brick element C3D8. The link in the model was subjected to the same reverse cyclic loading protocol applied to the experimental specimen, and the experimental and numeric hysteretic results compared well, thus validating the use of 3-dimensional elements. To validate the modeling of shear links subjected to cyclic loading using shell elements, a shell model was created of a W12X22 link with end and intermediate stiffeners. The geometry, material properties, and loading protocol in the model were consistent with the full 3-dimensional model created by Lewis. The monotonic and hysteretic results of the shell and full 3-dimensional models were compared to assess the accuracy of the shell model. Figure 17 shows the monotonic responses of the models, while the hysteretic responses can be seen in Figure 18. From Figure 17, it can be seen that although the shell model shows less post yield hardening than the full 3-dimensional model, the monotonic responses compare reasonably well. From Figure 18, conversely, it can be seen that large differences exist in the cyclic force deformation behavior of the two models. The cyclic responses compared well at small rotation angles; however, a large amount of strength degradation was seen in the shell model at large rotations due to the onset of flange and web buckling. This buckling can be seen in Figure 19, which shows the deformed link shapes for both models at 3% and 5% inelastic rotation.

Many approaches were taken to overcome the strength degradation in the shell model including the use of varying element formulations, integration parameters, and constraint conditions. To investigate the effects of the shell element formulation on post buckling behavior, link models were created using the ABAQUS shell elements S4, S4R, and S8R. These formulations respectively correspond to a linear element formulation, a

linear element formulation with reduced integration, and a quadratic element formulation with reduced integration. The effects of the number of integration points taken across the shell thicknesses were also investigated, as models were run using both Simpson and Gauss integration with 3, 7, 9, and 12 integration points across shell thicknesses. Finally, the reverse cyclic behavior of ABAQUS tie constraints was investigated by creating two independent shell models in which tie constraints were only incorporated into one.

Large amounts of strength degradation were seen at the onset of flange and web buckling in the shell models for all of the parameters discussed above. The reasons for the poor post buckle shell performance are subject to an ongoing investigation, which is outside the scope of this research. Thus, to capture the behavior of the composite link, the ABAQUS 8 node linear brick element C3D8 was used to model all link components including the end plates, end stiffeners, steel web sections, flanges, and neoprene.

To model the behavior of the composite link in the experimental setup, beam elements were used to incorporate the effects of frame elasticity. Specifically, the ABAQUS 3 node quadratic beam element B32 with 6 degrees of freedom per node was used to model the columns in the test setup. The beam elements were assigned a cross section consistent with the W14X145 columns used in the experimental assembly. The steel in these columns was assigned a perfectly elastic material formulation as the columns used in the experiment were designed to behave elastically throughout testing. The columns were incorporated into the model to investigate the effects of the axial load placed on the link as deformation is applied to the frame. The axial load occurs due to the fact that the link is not attached directly at the center of the columns, which results in relative displacements between the centerline of the link end connections as the frame

undergoes translation. To model this behavior, rigid elements with a length of half the depth of the W14X145 columns were used to connect the composite link to the columns.

2.4 Link Selection

Built up shear links were designed in accordance with the 2005 *AISC Seismic Provisions* for the purpose of the finite element investigation (See section 3.1 for a detailed design description). The nominal shear capacity of a link in an EBF is defined as the smaller of $2M_p/E$ or V_p depending on whether yielding is controlled by moment or shear respectively. The composite specimens were designed as shear controlled “short” links with similar nominal shear capacities but different web aspect ratios to conduct parameter studies and assess the hysteretic behavior of composite sandwich webs. With the exception of the web to flange and web to endplate weld designs, the strength design of the webs in the composite links was completed assuming a uniform steel cross section. That is, the potential strength contribution of the neoprene web core to overall strength was ignored during the design phase. The final composite link designs consisted of 14in deep and 25in deep shear dominated links with 0.25in and 0.125in steel web plates respectively. It should be noted that base case links were additionally designed for the 14in and 25in deep links with 0.50in and 0.25in steel webs respectively. While intermediate web stiffeners are required by the 2005 AISC Seismic Provisions for links in EBF, unstiffened shear links were analyzed in the base performance investigation due to impractical stiffening requirements for the 25in deep link. Additionally, the links were checked for seismic compactness using Table I-8-1 in the seismic provisions. The flanges of both links and web of the 14in deep links met requirements for seismic compactness; however the web of the 25in deep link was not seismically compact. End

stiffeners were provided in accordance with recommendations provided by Lewis (2010) to shift plastic strains away from the end plate connection. Tests were conducted using heat sensitive crayons to determine the required distance between the edges of the face plates in the web and core material to allow for adequate weld heat dissipation. These tests were conducted by fabricating a sandwich link with no core material and assessing the heat distribution on the inside of the face plates (see Figure 20). It was determined that a 2in gap between the core material and weld surfaces was adequate to allow for heat dissipation. A summary of the final link designs can be found in Table 2 and are shown in Figure 21. The links investigated in the analytic parametric study will hereafter be referred to using the following metric: 14DBase – 14in deep base link, 25DBase – 25in deep base link, 14D N_y_x , and 25D N_y_x – 14in and 25in deep links where y and x are the thickness and elastic modulus of the core material in inches and psi respectively. It should additionally be noted that all parameter studies concerning core thickness and core to steel bond strength were performed using a core with an elastic modulus of 1000psi because this was anticipated elastic modulus of the hyperelastic core material in the experimental specimens.

2.5 Web End Stiffeners and Web Stability

End stiffeners were used in the composite links to limit plastic strain at the link to endplate connection. Analytical and experimental studies by Lewis (2010) investigated the effects of end stiffener configuration on the behavior of the connection zone of shear links. Various stiffener configurations were analyzed, including full depth stiffeners parallel to the web at varying locations including directly on the web, half way between the flange edge and the web, and at the flange edge. It was shown that the connection

zone behavior of the link stiffened directly on the web was most effective in moving plastic strains away from the link to column connection. Thus the end stiffener design utilized for the composite links consisted of full depth end stiffeners placed directly on the web in the connection zones. The end stiffeners were designed with a thickness consistent with requirements for intermediate stiffeners given in the 2005 *AISC Seismic Provisions* for EBF links.

As discussed in Section 1.2.1, Intermediate stiffeners have traditionally been used to restrict out-of-plane motion of the web in shear links. The stability of the web in the composite links was, however, primarily based on the thickness and modulus of elasticity of the core neoprene layer. Discreet transverse stiffeners increase the flexural rigidity of the web in shear links, thus increasing stability. Equation 33 defines the effective flexural rigidity per unit length of a web with transverse stiffeners:

$$D = \frac{E_w t_w^3}{12(1-\nu^2)} + \frac{E_s I_s}{a} \quad [33]$$

This equation was used to determine the flexural rigidity per unit length of a traditional web stiffened according to two independent guidelines relative to the required geometry and spacing of transverse stiffeners. For the purpose of this analysis, the thickness of steel in the traditional web was taken to be equivalent to the total thickness of steel in the composite web. The guidelines used to evaluate the flexural rigidity of the traditionally stiffened webs included the code based requirements for stiffener geometry presented in the 2005 *AISC Seismic Provisions* for transverse stiffeners in EBF, and the optimum stiffener rigidity presented by Narayanan (1983) defined in Equation 17 in Section 1.2.1. Required stiffener spacing for the 14in and 25in deep links were respectively determined

to be 12in and 2.5in, while the code specified stiffener thicknesses and widths were respectively 0.5in and 4.75in for the 14in deep link and 0.375in and 3in for the 25in deep link. Using these stiffener geometries, out-of-plane stiffener rigidities of $3.30 \times 10^5 \text{ kip-in}^2$ and $8.61 \times 10^4 \text{ kip-in}^2$ were calculated for the 14in and 25in deep links. On the other hand, the optimum flexural rigidities of intermediate stiffeners in the 14in and 25in deep links based on the recommendations provided by Narayanan were calculated to be $2.12 \times 10^4 \text{ kip-in}^2$ and $2.63 \times 10^5 \text{ kip-in}^2$ respectively.

The required code and non code based stiffener flexural rigidities presented above were used in Equation 33 to determine the flexural rigidity per unit length of traditional 1/2in and 1/4in steel webs with intermediate stiffeners. These flexural rigidities were calculated for the code and non code based recommendations to be respectively $2.74 \times 10^4 \text{ kip-in}^2/\text{in}$ and $2.12 \times 10^4 \text{ kip-in}^2/\text{in}$ for the 14in link and $3.45 \times 10^4 \text{ kip-in}^2/\text{in}$ and $9.56 \times 10^4 \text{ kip-in}^2/\text{in}$ for the 25 in link. To determine the required moment of inertia and inherent thickness of a composite sandwich web to provide equivalent rigidity taking into account the out-of-plane bending strength of the core material, Equation 16 was modified as follows:

$$D = \frac{2(\frac{1}{12}t_{fp}^3 + t_{fp}t^2)}{(1-\nu_{fp}^2)} E_{fp} + \frac{\frac{1}{12}(2t-t_{fp})^3}{(1-\nu_c^2)} E_c \quad [34]$$

where the first and second terms respectively account for the flexural rigidities of the face plates and core layer. Rearranging Equation 34, it was possible to develop a relationship between required core elastic modulus and thickness of a sandwich web plate to provide equivalent out-of-plane rigidity as traditionally stiffened webs. Core elastic modulus to thickness relationships have been plotted in Figure 22 and Figure 23 for a varying

number of out-of-plane rigidities for sandwich plates with fixed face plate thickness.

Using these relationships, approximate core thickness requirements can be determined for fixed core material elastic modulus and the elastic modulus requirements of the core can be determined for fixed core thickness. From the relationships in Figure 22 and Figure 23, it can be seen that the required core thicknesses for the 25in links were impractically large for a core material with an elastic modulus of 1000psi, so only the required thicknesses for the 14in link were taken into consideration in development of the analytical specimen test matrix. It should additionally be noted that the relationships shown in Figure 22 and Figure 23 were developed for a sandwich web with steel face plates and a nearly incompressible core material. That is, the Poisson's ratio of the face plates and core material were respectively taken to be 0.3 and 0.49. Relationships can be developed for different face plate and core materials using Equation 34.

The performance of 14in and 25in deep composite sandwich links could additionally be assessed in terms of the predicted buckling deformation angle γ_B . Using the geometric requirements for intermediate stiffeners in the seismic provisions and the approximation for the panel web buckling deformation angle of shear links provided by Popov and Kasai (1986) (see Equation 13), the buckling deformation angle of the composite links was estimated as a function of the core thickness. Equation 34 was used to calculate the flexural rigidity of composite links with varying core thicknesses. These rigidities were used in Equation 33 to calculate the corresponding stiffener spacing of traditionally stiffened 14in and 25in deep links with intermediate stiffeners whose geometric properties were consistent with the specifications provided in the seismic provisions (AISCa, 2005). Thus, substituting Equation 34 into Equation 33, and

Equation 33 into Equation 13, the buckling deformation of composite sandwich links was estimated as the following:

$$C = \frac{E_s I_s}{t_w \left(\frac{2(\frac{1}{12} t_{fp}^3 + t_{fp} t^2)}{(1-\nu_s^2)} E_{fp} + \frac{\frac{1}{12} (2t - t_{fp})^3}{(1-\nu_c^2)} E_c - \frac{t_w^3}{12(1-\nu^2)} E_{fp} \right)} + \frac{1}{5} \frac{d}{t_w} \quad [35]$$

where C is used to determine the buckling deformation angle as described in Section 1.2.1. Equation 35 was used to develop the core thickness/buckling deformation angle relationships shown in Figure 24 for the 14in and 25in deep sandwich links. The relationships shown in Figure 24 are for a sandwich link with a core elastic modulus of 1000psi, however the elastic modulus of the core did not have a large impact on the web buckling deformation angle/core material thickness relationship. It should be noted that similar to the previous section, the relationships shown in Figure 24 were developed assuming Poisson's ratios of 0.3 and 0.49 for the face plate and core material respectively.

The relationships regarding equivalent flexural rigidity and predicted web buckling deformation angle for the composite links shown in Figure 22, Figure 23, and Figure 24 were used to develop the analytical specimen test matrix. The final matrix consisted of 14in and 25in deep links with 1in, 2in, and 3in hyperelastic core layers. The required core thicknesses for the 25in deep composite links based on the aforementioned relationships were impractically large, so only the thicknesses required for the 14in deep links were considered when developing the test matrix. The out of plane web plate flexural rigidities, elastic buckling loads, predicted buckling deformation angles, and calculated post buckling shear capacities of all composite analytical specimens are shown in Tables 3 and 4. The web plate out of plane flexural rigidities, elastic buckling loads,

and predicted buckling deformation angles were calculated using Equation 34, Equation 4, and Equation 35 respectively. The predicted buckling loads of the base links have not been shown because they violated the web panel aspect ratio limits established by Kasai and Popov (1986). The post buckling shear capacities have been calculated assuming tension field action develops in the links. Due to the geometric properties and inherent post buckling behaviors of the links, the post buckling capacity of the 14in and 25in deep links were calculated assuming tension field characteristics similar to those in plate girders and steel plate shear walls respectively (see Equation 18 and Equation 19).

2.6 Model Validation through Flexural Bending Tests

Prior to fabrication of the experimental sandwich links, flexural bending tests were run on composite sandwich web plates from links 14DN3_1000, 25DN1_1000, and 25DN3_1000 to assess model validity. The plates were loaded along the longitudinal weak axis, and deformations were recorded at two locations on the top and bottom of the plates. The plates were simply supported, load was applied using an Enerpac 18 ton ram, and force was monitored using an Omegadyne 20kip capacity Z - load cell.

Deformations were recorded at the same locations on the top and bottom of the plates to determine if the plate sections remained plane as load was applied. Each plate was loaded using two different edge constraint conditions. The first condition (unclamped condition) allowed the steel face plates to deform independently along the plate edges as load was applied, while the face plates were clamped together along the edges in the second condition (clamped condition) to simulate the boundary condition if flanges were welded to the sandwich plates. The basic test setup used in the flexural bending tests can be seen in Figure 25. Analytic models were additionally created to assess the flexural

bending behavior of the sandwich webs in links 14DN3_1000, 25DN1_1000, and 25DN3_1000. These models consisted of the sandwich plates taken directly from the full link models, including mesh distributions, element formulations, material parameters, and contact conditions. The sandwich plate models were modified only to incorporate the boundary and loading conditions of the flexural bending tests. Loading was applied by assigning deformation to the “top” face plate, and the boundary conditions were adjusted for the clamped and unclamped conditions. An overview of the flexural bending model created for the three sandwich plates can be seen in Figure 25.

The numerical and experimental sandwich plates displayed similar load deformation behaviors. Figure 26 through Figure 28 show the experimental and analytic load deformation behaviors of a single LVDT in each sandwich plate. From these figures, it can be seen that the experimental flexural stiffnesses compare well to the flexural stiffnesses predicted by the models for the clamped and unclamped edge conditions. Results from only a single LVDT on each plate have been presented because the load deformation behavior recorded on the top and bottom of each plate was identical, suggesting that the plate sections remained plane under these loading conditions.

2.7 Results and Observations

Each model was subjected to the cyclic loading protocol specified in the 2005 *AISC Seismic Provisions* for links in EBF. As the material models did not incorporate fracture behavior, all models were run to a common elastic rotation angle of 13%. Various parameter studies were conducted regarding the effects of core elastic modulus, core thickness, web aspect ratio, and rubber to steel bond strength on web stability and overall link hysteretic behavior. The hysteretic behaviors of the numerical specimens including

buckling load, inelastic buckling deformation angle, and post buckling shear capacities are summarized in Table 5.

2.7.1 Base Link Behavior

The monotonic and hysteretic behaviors of links 14DBase and 25DBase can be found in Figure 29 and Figure 30 respectively, while the web strain distribution analyses are shown for the two links in Figure 31 and Figure 32 respectively. 14DBase achieved a capacity of 150% the plastic shear capacity before strength degradation occurred due to out-of-plane web buckling at $\gamma_p = 0.04\text{rad}$. A consistent strength degradation rate was observed in each subsequent post buckling cycles through $\gamma_p = 0.125\text{rad}$, at which point a total strength degradation of 23% was shown. From Figure 31 it can be seen that link 14DBase displayed uniform web strain distributions at pre-buckling rotation angles, while global tension field strains developed at the onset of web buckling due to the development of tension field action. Localized strain pockets developed as the cyclic tension fields continued to reverse direction in the post buckling cycles, suggesting the likelihood that link fracture would occur at these points.

25DBase achieved 100% the plastic shear capacity in the first target rotation angle, $\gamma_p = 0.0015\text{rad}$, before out-of-plane web buckling and subsequent strength degradation occurred at $\gamma_p = 0.003\text{rad}$. Despite experiencing initial strength degradation due to the onset of web buckling, the link maintained a constant shear capacity through $\gamma_p = 0.125\text{rad}$ due to the development of tension field action. From $\gamma_p = 0.003\text{rad}$ to $\gamma_p = 0.06\text{rad}$, a constant strength degradation of 27% was observed, while the total degradation at $\gamma_p = 0.125\text{rad}$ was 40%. From Figure 32, it can be seen that link 25DBase exhibited a global tension field strain pattern throughout the entire loading protocol due

to the early onset of web buckling. As with link 14DBase, this pattern did not result in localized strain concentrations in early cycles. As the tension fields continued to reverse direction, however, localized strain pockets developed at the tension field intersection points suggesting that web fracture would also occur in 25DBase.

2.7.2 Effects of Core Elastic Modulus

The elastic modulus of the core material played a large role in stabilizing the hysteretic behavior of both the 14in and 25in deep shear links. Approximate core material elastic modules of 385psi, 1000psi, 5000psi, and 10000psi were examined for both link depths with 1in core thickness, and the hysteretic behaviors and accumulative web strains were analyzed. The hysteretic behaviors of the 14in and 25in deep links can be seen in Figure 33 through 40, while the back bone and web strain analyses can be seen in Figure 41 through Figure 44. The web strain distributions developed in ABAQUS for each sandwich link analyzed in the core elastic modulus parameter study can be found in Appendix C for select rotation angles. Links 14DN1_385 and 14DN1_1000 displayed similar hysteretic behaviors, and performed worse than 14DBase in terms of cyclic performance and web strain distribution. Both links achieved a capacity of 140% the plastic shear capacity before experiencing strength degradation due to out-of-plane web buckling at $\gamma_P = 0.02\text{rad}$. Although this degradation occurred at lower rotation angles than in link 14DBase, links 14DN1_385 and 14DN1_1000 maintained constant post buckling shear capacities of 111% the plastic shear capacity through $\gamma_P = 0.125\text{rad}$, at which point a total strength degradation of 25% was observed. Links 14DN1_385 and 14DN1_1000 additionally performed worse than the base case link in terms of web strain distribution. Localized strain pockets developed in the webs of these links at lower

rotation angles than in the base link, and Figure 43 shows that the maximum web strains grew at a faster rate than in the base link for rotation angles greater than 0.03rad. Link 14DN1_5000 performed better than links 14DN1_385 and 14DN1_1000, however performed worse than the base case link in terms of strength degradation and cumulative plastic web strain. 14DN1_5000 achieved 156% the plastic shear capacity before strength degradation occurred as a result of out-of-plane web buckling at $\gamma_P = 0.026\text{rad}$. Similar to links 14DN1_385 and 14DN1_1000, 14DN1_5000 maintained a constant post buckling shear capacity of 130% the plastic shear capacity through $\gamma_P = 0.125\text{rad}$, and a total strength degradation of 19% was observed. Additionally, strain concentrations in link 14DN1_5000 developed in the tension field reversal zones at lower rotation angles than in 14DBase, and Figure 43 shows that maximum web strains grew at a faster rate than in the base case for rotation angles greater than 0.04rad. Link 14DN1_10000 performed better than the base link in terms of strength degradation while displaying similar web strain characteristics. 14DN1_10000 achieved a shear strength of 156% the plastic shear capacity before experiencing out-of-plane web deformation and strength degradation at $\gamma_P = 0.03\text{rad}$. While out-of-plane buckling and strength degradation did occur, only a 17% loss of capacity was seen through $\gamma_P = 0.125\text{rad}$. This is less than the overall degradation observed in the base link of 23%. The web strain growth and distribution in 14DN1_10000 were additionally similar to that in the base link. Regions of concentrated strain developed on the web in zones where the tension fields reversed direction, and Figure 43 shows that the web strain growth rate was comparable to that in the base link.

The 25in deep sandwich links showed improved hysteretic behaviors to the base link, but generally displayed higher web strain growth rates. Link 25DN1_385 achieved 93% of the plastic shear capacity prior to experiencing strength degradation due to out of plan web deformation at $\gamma_P = 0.0005\text{rad}$. Although out-of-plane deformation occurred within the first target deformation, the link maintained a constant shear buckling capacity of 72% plastic yield through $\gamma_P = 0.07\text{rad}$ (a strength degradation of 22%), and a total strength degradation of 36% through $\gamma_P = 0.125\text{rad}$. Although 14DN1_385 displayed a higher web buckling capacity and less over strength degradation than the base link, a decreased web strain performance was shown. Strain concentrations developed in tension field reversal zones at lower deformations than the base link, and the web strain growth rate was drastically higher than in the base link for $\gamma_E > 0.01\text{rad}$ (see Figure 44). Link 25DN1_1000 achieved 95% of the plastic shear prior to experiencing out-of-plane web deformation and corresponding strength degradation at $\gamma_P = 0.0005\text{rad}$. The link maintained a constant post buckling shear capacity of 78% plastic shear through $\gamma_P = 0.09\text{rad}$ (a strength degradation of 18%), while experiencing an overall degradation of 74% through $\gamma_P = 0.125\text{rad}$. 14DN1_1000psi also performed worse than the base link in terms of web strain distribution and growth rate. Strain concentrations begin developing in tension field reversal zones at lower rotation angles, and from Figure 44 it can be seen that the web strain growth rate was higher than in the base link for $\gamma_E > 0.03\text{rad}$. Link 25DN1_5000 achieved 101% of the plastic shear capacity before experiencing out-of-plane web deformation at $\gamma_P = 0.012\text{rad}$. This link did not experience any initial degradation due to the onset of web buckling, maintaining the maximum pre-buckling load of 138kips through $\gamma_P = 0.06\text{rad}$. At $\gamma_P = 0.06\text{rad}$, a uniform strength degradation

was observed for each subsequent cycle, and an overall strength degradation of 14% was seen at $\gamma_P = 0.125\text{rad}$. Although showing an improved hysteretic performance to the base link, 25DN1_5000 also performed worse in terms of web strain growth rate and distribution. As was seen in the other composite links, strain concentrations developed at lower deformations than in the base link, and the web strain growth rate was higher than in the base link for $\gamma_E > 0.05\text{rad}$. Link 25DN1_10000 performed better than all composite links and the base link in terms of both hysteretic behavior and web strain growth rate and concentration. The link achieved 132% of the plastic shear capacity before experiencing strength degradation due to out-of-plane web buckling at $\gamma_P = 0.03\text{rad}$. Uniform strength degradation was observed during each post buckling cycle, and an overall strength degradation of 23% was observed at $\gamma_P = 0.125\text{rad}$. In terms of strain performance, 25DN1_10000 developed strain concentrations in tension field reversal zones at higher deformation angles than were observed in the base link, and the web strain growth rate was lower for all cycles (see Figure 44).

2.7.3 Effects of Core Thickness

The composite web core thickness additionally played a role in stabilizing the hysteretic behavior of the links; however the composite links did not perform as well as the base links in terms of web strain distributions or web strain growth rates for all thicknesses analyzed. It should be noted that all thickness parameter studies were conducted using a core material with an elastic modulus of 1000psi due to the availability of core materials to fabricate experimental specimens. Core thicknesses of 1in, 2in, and 3in were analyzed for both the 14in and 25in deep links. The hystereses of all links analyzed in the core thickness parameter study can be seen in Figure 45 through Figure 48, while the back

bone and web strain analyses can be seen in Figure 49 through Figure 52. The web strain distributions developed in ABAQUS for all links analyzed in the core thickness parameter study can be found in Appendix C for select rotation angles. The performance of links 14DN1_1000 and 25DN1_1000 have been described in the previous section. Link 14DN2_1000 achieved 139% plastic yield before experiencing strength degradation due to out-of-plane web deformation at $\gamma_P = 0.01\text{rad}$. After the onset of web buckling and initial degradation, a constant capacity of 113% the plastic shear capacity was observed through $\gamma_P = 0.125\text{rad}$, corresponding to a total overall degradation of 19%. The web strain performance of 14DN2_1000 was worse than that of the base link, as strain concentrations developed in tension field reversal zones at lower deformation angles, and the web strain growth rate was higher for $\gamma_E > 0.03\text{rad}$ (see Figure 51). Link 14DN3_1000 achieved 141% of the plastic shear capacity before the onset of out-of-plane web buckling at $\gamma_P = 0.04\text{rad}$. Strength degradation did not occur as a result of web buckling, and the link maintained the maximum achieved load of 171% of the plastic shear capacity through $\gamma_P = 0.125\text{rad}$ due to the development of tension field action. Although 14DN3_1000 performed better than the composite links with 1in and 2in core thicknesses, the web strain distribution and rate of growth were still worse than that of the base link. Strain concentrations developed in the web due to tension field reversals at lower deformation angles than in the base link, and the web strain growth rate was higher for $\gamma_E > 0.03\text{rad}$.

As stated above, the 25in deep composite links showed improved hysteretic behavior to that of the base link, but did not perform as well in terms of web strain distributions or growth rates. Link 25DN2_1000 achieved 91% of the plastic shear

capacity before experiencing strength degradation due to out-of-plane web deformation at $\gamma_P = 0.001\text{rad}$. 8% strength degradation was observed immediately following the onset of web buckling, however the link began to gain strength due to cyclic hardening at $\gamma_P = 0.02\text{rad}$. The strength continued to increase through $\gamma_P = 0.06\text{rad}$, at which point a strength degradation of only 2% was observed. The capacity decreased for $\gamma_P > 0.06\text{rad}$, and a total strength degradation of 14% was seen at $\gamma_P = 0.13\text{rad}$. 25DN2_1000 behaved worse than the base link in terms of web strain characteristics, as web strain concentrations developed in tension field reversal zones at lower deformation angles, and the web strain growth rate was higher for $\gamma_P > 0.03\text{rad}$. Link 25DN3_1000 achieved 97% of the plastic shear capacity before strength degradation due to the onset of web buckling at $\gamma_P = 0.002\text{rad}$. Immediately following the out-of-plane web deformation, a strength degradation of 4% was observed, however the link gained strength from $\gamma_P = 0.01\text{rad}$ to $\gamma_P = 0.06\text{rad}$, at which point a capacity of 100% the plastic shear capacity was observed. The shear capacity of the link decreased for $\gamma_P > 0.06\text{rad}$, and a total strength degradation of 8% was observed at $\gamma_P = 0.13\text{rad}$. Link 14DN3_1000 additionally performed worse than the base link in terms of web strain. Concentrated web strains developed in tension field reversal zones at lower deformation angles, and the web strain growth rate was higher for $\gamma_P > 0.02\text{rad}$.

2.7.4 Numerical and Predicted Buckling Behavior

Discrepancies were observed between the numerical and predicted buckling behaviors of both the base and composite links. The predicted elastic buckling loads of the 14in and 25in deep base case links were larger than the elastic buckling loads predicted in the numerical models, while the predicted elastic buckling loads of all composite links were

substantially higher than the numerical elastic buckling loads (see Table 4 and Table 5). Additionally, based on the calculated elastic buckling loads, it was expected that the 14in deep base and composite links and the 25in deep composite links would yield prior to the onset of web buckling in the non-linear finite element analyses. While material non-linearity was observed in all 14in deep links prior to the onset of web buckling in the numerical analyses, only the 25in deep links 25DN1_5000 and 25DN1_10000 yielded prior to the onset of web buckling.

Discrepancies additionally existed between the numerical buckling deformation angles and the predicted buckling deformation angles represented by the relationships shown in Figure 24. With the exception of the links with theoretical buckling deformation angles of $\gamma_B = 0\text{rad}$ (25DN1_385, 25DN1_1000, 25DN1_5000, 25DN1_10000), the relationships in Figure 24 over predicted the performance of the composite links, especially for core thicknesses greater than 1in. Buckling deformation angles of $\gamma_B = 0.03\text{rad}$ were predicted for all 14in deep composite links with 1in core thickness. Numerical buckling angles of $\gamma_B = 0.02\text{rad}$, $\gamma_B = 0.02\text{rad}$, $\gamma_B = 0.026\text{rad}$, and $\gamma_B = 0.03\text{rad}$ were observed, however, for links 14DN1_385, 14DN1_1000, 14DN1_5000, and 14DN1_10000 respectively. Buckling deformation angles of $\gamma_B = 0.118\text{rad}$ and $\gamma_B = 0.135\text{rad}$ were predicted for links 14DN2_1000 and 14DN3_1000, on the other hand, while the numerical buckling deformation angles were respectively observed to be $\gamma_B = 0.01\text{rad}$ and $\gamma_B = 0.04\text{rad}$ respectively.

Buckling angles of $\gamma_B = 0\text{rad}$ were predicted for all 25in deep composite links with 1in core thickness. However, numerical buckling angles of $\gamma_B = 0.0005\text{rad}$, $\gamma_B = 0.0005\text{rad}$, $\gamma_B = 0.012\text{rad}$, and $\gamma_B = 0.03\text{rad}$ were observed for links 25DN1_385,

25DN1_1000, 25DN1_5000, and 25DN1_10000 respectively. Conversely, buckling angles of $\gamma_B = 0.04\text{rad}$ and $\gamma_B = 0.05\text{rad}$ were predicted for links 25DN2_1000 and 25DN3_1000, while numerical buckling deformation angles were observed to be $\gamma_B = 0.001\text{rad}$ and $\gamma_B = 0.002\text{rad}$ respectively.

Discrepancies between the predicted and numerical buckling behaviors of the composite links were a result of local material instabilities. The theoretical buckling behaviors were assessed assuming the sandwich web sections remained plane throughout loading. Based on this assumption, the predicted buckling behaviors were affected more by the core thickness than core elastic modulus. The numerical results of the composite sandwich webs, however, suggest that the sandwich plate sections with core material elastic modules less than 5000psi did not remain plane throughout loading. Both 14in and 25in deep composite links with core elastic modules of 385psi and 1000psi showed lower buckling loads and buckling deformation angles than were theoretically predicted. Additionally, all links with core elastic modules of 5000psi and 10000psi yielded prior to the onset of web buckling, and experienced web buckling at deformations consistent with the theoretical predictions.

2.7.5 Web Panel Aspect Ratio Analysis

Through analyses of the results from the core elastic modulus and core thickness parameter studies for the 14in and 25in deep links, it was possible to assess the performance of composite links with similar shear capacities but varying web panel aspect ratios, α . Equation 8 in Section 1.2.1 defines the web panel aspect ratio in shear links, and aspect ratios of approximately 4 and 2 were calculated for the 14in and 25in deep links respectively. From Sections 2.5.2 and 2.5.3, it can be seen that composite

links with lower aspect ratios performed better relative to base link performance in terms of hysteretic behavior and web strain distribution and growth rate. From Section 2.5.2, all 14in deep composite links ($\alpha \approx 4$) experienced out-of-plane web buckling at lower deformation angles than in the base case, and only 14DN1_10000 showed a large improvement in terms of overall strength degradation. Additionally, all 14in deep composite links with the exception of 14DN1_10000 developed web strain concentrations at lower deformation angles than the base link, and showed higher rates of web strain growth. From the results of Section 2.5.2 for the 25in deep links ($\alpha \approx 2$), on the other hand, all composite links showed improvement over the base link in terms of hysteretic behavior and overall strength degradation. In terms of web strain distribution and growth rate, only 25DN1_10000 showed improvement over the base link, as all other composite links developed web strain concentrations at lower deformation angles and showed larger web strain growth rates. From Section 2.5.2, all 14in deep composite links with a 1000psi core elastic modulus performed drastically worse than the base case in terms of hysteretic behavior and web strain distribution and growth rate. All of the composite links experienced out-of-plane web buckling at lower deformation angles than the base case, while none of the sandwich links achieved the maximum shear capacity achieved by the base link. In terms of web strain distribution and growth rates, all 14in deep composite links developed strain concentrations at lower deformation angles than the base case, and showed larger web strain growth rates. From the results of Section 2.5.2 for 25in deep links conversely, it can be seen that all composite links with a 1000psi core elastic modulus showed improvement over the base link in terms of hysteretic behavior and overall strength degradation. In terms of web strain distribution and growth

rate, however, all 25in deep composite links similarly developed strain concentrations at lower deformations than the base link, and showed larger rates of web strain growth.

2.7.6 Effects of Rubber to Steel Bond Strength

The bond strength between the hyperelastic core material and steel face plates in the sandwich web did not affect the global hysteretic behavior of the 14in or 25in deep links, however increased web strain magnitudes were observed when debonding occurred. The hysteretic behaviors and web strain distributions of both links were investigated for bond failure initiation at varying rotation angles. Bond failure propagation and web strain growth rates are shown in Figure 53 through Figure 56 for both links. Broken bond propagation in the web of the two links developed independent of the bond failure initiation deformation, so generic bond failure propagation plots are shown in Figure 53 and Figure 54. The behavior of link 14DN1_1000 was observed when debonding initiated at rotation angles $\gamma_E = 0.02\text{rad}$, $\gamma_P = 0.05\text{rad}$, and 0.09rad . Bond failure initiated at the top and bottom of the neoprene layer at the termination of the tension field lines of action. The bond failure propagated along the primary tension field lines of action, and eventually spread to the secondary tension field lines of action toward the end of the link. Total bond failure was not observed in any of the links through an inelastic rotation $\gamma_P = 0.125\text{rad}$, however when bond failure initiated at $\gamma_E = 0.02\text{rad}$ the entire effective length of the neoprene debonded with exception of small regions adjacent to the end stiffeners (see Figure 53). Web strain in the 14in deep links was largely unaffected by bond failure. The link with a perfect bond showed slightly lower web strains for inelastic rotation angles $\gamma_P > 0.08\text{rad}$, however the web strain growth rate behaviors were the same regardless of the rotation angle in which bond failure initiated (see Figure 55).

The behavior of link 25DN1_1000 was observed for bond failure initiation at rotation angles $\gamma_E = 0.015\text{rad}$ and $\gamma_E = 0.07\text{rad}$. Similar to the 14in deep link, bond failure initiated at the top and bottom of the neoprene layer at the termination of the tension field lines of action. The bond failure propagated along the primary tension field lines of action, and eventually spread to the secondary tension field lines of action towards the ends of the effective web length. Complete bond failure was not observed in any of the 25in deep links analyzed. Even when bond failure initiated at $\gamma_E = 0.015\text{rad}$, only nodes along the primary and secondary tension field lines of action debonded. Thus, the maximum debonding pattern developed as an “X” across the length of the neoprene (see Figure 54). Bond failure had an effect on the web strain growth rates and magnitudes in the 25in deep links. Noticeable increases in web strain growth rate were observed at the bond failure initiation rotation angles $\gamma_E = 0.015\text{rad}$ and $\gamma_E = 0.07\text{rad}$ when compared to the strain growth rates in the link with a perfect bond (see Figure 56).

2.8 Conclusions and Implementation Decisions

Parameter studies were conducted to assess the performance of composite sandwich links with varying core material elastic modules, composite web thickness, and overall web panel aspect ratio. The performance of the links was assessed through evaluation of the hysteretic behavior, overall strength degradation, and web strain distributions and growth rates. It was shown that the elastic modulus of the core material played a large role in stabilizing the hysteretic behavior and strain distributions and growth rates in shear links. Composite links with sandwich web core elastic modules greater than 5000psi showed improved hysteretic behaviors and strain distributions over the base cases for all links analyzed. For the purpose of fabricating experimental specimens, however, only core

materials with an elastic modulus in the range of 1000psi were available. Thus the composite web thickness parameter study was conducted using core a core material with an elastic modulus of approximately 1000psi. The 3in thick 1000psi core material was shown to stabilize the hysteretic behaviors of both the 14in and 25in deep links in terms of overall strength degradation, however performed worse than the base links in terms of web strain distributions and growth rates. The web panel aspect ratio additionally played a role in the performance of the composite links when compared relatively to the performance of the base links. The 25in deep links ($\alpha \approx 2$) performed much better in terms of hysteretic behavior and web strain distributions and growth rates when compared relatively to the base link than the 14in deep composite links ($\alpha \approx 2$).

Specimens were chosen for the experimental phase of the test based on the results of the finite element analyses. Links 14DBase and 25DBase were selected to assess the base link behavior and help demonstrate model validity. Link 14DN3_1000 was chosen because it displayed a more stable hysteretic behavior and lower overall strength degradation than the base link. Links 25DN1_1000 and 25DN3_1000 were chosen because they additionally displayed improved hysteretic behaviors and overall strength degradations. Due to fabrication limitations, only sandwich webs with a core elastic modulus of 1000psi could be selected for experimental analysis despite the fact these links did not show improved strain distributions or growth rates.

3.0 Experimental Test Setup

The experimental apparatus used to test the composite links is consistent with the apparatus described by Lewis (2010) and can be seen in Figure 57. The experimental setup consisted of a reaction frame and a linked column frame (LCF). A 220kip Shore Western 91 series linear actuator with a 20in stroke and ball joints at each end was mounted on the reaction frame, while the LCF transferred displacement and subsequent shear load to the composite links. The reaction frame consisted of two W14X86 columns braced using HSS 6X8X3/8. The columns and bracing were fixed to W14X86 base supports, and the assembly was secured to the strong floor using 32 – 105ksi rods. The actuator was attached to the reaction frame at a height of 13ft above the strong floor. The LCF consisted of two W14X145 columns and two C12X30 channels. The channels were welded together and pinned to the top of the columns to act as a load transfer beam. Bolt holes and stiffeners were added to the columns at mid height to accommodate the bolted end plate connections and to increase the ease of specimen replaceability. The columns were pinned to a steel plate constrained vertically and horizontally by two 14X3X3ft concrete blocks. The concrete blocks were secured to the strong floor using 34 105ksi rods capable of resisting a total of 440kips of uplift during testing. Ten 105ksi rods were inserted horizontally through the blocks and column footings to restrict motion in the lateral direction of the actuator. To resist out-of-plane displacement, the LCF was stabilized using four threaded rods from the top of the columns to the concrete blocks and two lateral supports from either end of the transfer beam to a concrete reaction wall. The dimensions of the assembled LCF frame were 139.25in high by 70.88in wide which

produces a height to width ratio of 1.96. Thus the shear applied to the link was 1.96 the load applied to the LCF by the actuator.

3.1 Test Specimens

The built up composite links were designed according to criteria provided in the 2005 *AISC Seismic Provisions* for links in EBF. The process used to design the links has been provided in Sections 2.4 and 2.5. Flange to web weld designs were conducted according to the built up plate girder design procedure. The 14in and 25in links were welded to 20X15X1.5in and 30X15X1.5in end plates respectively and 4 - 8X0.25in full depth end stiffeners were placed directly on the web of each specimen to shift plastic strains away from the end plate connections. As stated above, a 2in gap was left between the neoprene and all edges of the composite web to allow for weld heat dissipation. All welds in the specimens, including the flange to web, flange to endplate, and web to endplate consisted of fillet welds. The final specimens were designed and selected based on code requirements, web stability considerations, and FEA results. The final experimental specimen matrix was as follows: 2 traditional base links with unstiffened webs – 1-14in link with a single 1/2in steel web, and 1-25in link with a single 1/4in steel web. 2 links with a 3in core neoprene layer – 1-14in link with 2-1/4in steel webs and 1-25in link with 2-1/8in steel webs, and 1-25in link with a 1in core neoprene layer and 2-1/4in webs. Neoprene with a 70 Durometer rating, shear modulus of 330psi, and an approximated modulus of elasticity of 1000psi were used in all specimens. Detailed link and end plate design calculations and drawings can be found in Appendix A, specimen shop drawings can be found in Appendix B, and a summary of the final specimen matrix can be found in Table 2.

3.1.1 Link to Column Connection

To facilitate link replaceability, the link to column connection was designed using the procedures for a bolted end plate connection specified in *AISC Design Guide 4* (Murray and Sumner, 2003). Testing by Stratan and Dubina demonstrated that elastic behavior in bolted connections allows for easier link replacement (2004). Thus the connection was designed as a four bolt unstiffened end plate connection to ensure the plate behaved elastically at the maximum design loads of the composite links. *Design Guide 4* recommends that complete joint penetration (CJP) welds be used for the link to endplate attachment for links subjected to reversed cyclic loading to prevent failure along the link to endplate connection. Experimental studies by Lewis (2010) showed, however, that fillet welds can successfully be used to attach links to bolted end plates in conjunction with end stiffeners to shift plastic strain away from the welded connection zones. Fillet welds were thus used in all link to end plate connections. It should be noted that the fillet welds from the link web to end plate were larger than allowed per section J2b of the *AISC Steel Construction Manual* due to strength requirements. The strength of all link to end plate fillet welds was calculated assuming a degree of base and weld metal overstrength. One and one quarter inch A490 bolts were used to attach the link end plates to the columns to limit bolt thread stripping and ductile response (Broderick & Thomson, 2000). To obtain the required bolt strength to resist the maximum shear and tensile loads from the composite links, the 4 bolt end plate connection described in *Design Guide 4* was modified to 12 bolt and 16 bolt connections for the 14in and 25in deep links respectively. The traditional 4 bolt and modified bolted end plate connections can be seen in Figure 58.

3.2 Test Setup and Instrumentation Procedure

Prior to testing, the composite links were installed in the LCF frame and instrumented. To install the links into the frame, hydraulic rams were used to push the columns apart, and a crane was used to set the link in position. The A490 structural bolts were installed to hold the link in the frame, and the hydraulic rams were removed. To adequately secure the link in the frame for testing, the bolts were tensioned using the turn of the nut method. This method equates nut rotation to equivalent bolt pretension through use of a Skidmore-Wilhelm calibrator tension device. Testing conducted by Lewis (2010) performed a turn of the nut calibration on 1.25in diameter A490 bolts, and it was determined that a half turn past snug resulted in a bolt pretension of approximately 50kips. Thus the bolts were pretensioned to half turn of the nut prior to each experiment to ensure bolt yielding did not occur during installation, and to maintain a consistent bolt pretension across all tests.

After securing the link in the LCF frame, instrumentation was applied to measure rotation angles, displacements, and strain. Threaded rods were welded to the flanges and end plates of the links to secure linear variable displacement transducers (LVDT's) used to measure link rotation angles and displacements. Rotation angles were monitored in three different places along the length of the composite link; the 8in stiffened end zone, the effective link length between the end stiffeners, and over the full length of the link. Consistent with the loading protocol for EBF links given in the 2005 *AISC Seismic Provisions*, the rotation angle across the length of the link was used for control during testing. The four rotation angles were measured using two LVDT's placed diagonally

across the zones of interest, and Equation 35 was used to translate the displacements of the LVDT's into elastic rotation angles:

$$\gamma = \frac{\sqrt{a^2+b^2}(L_1-L_2)}{2ab} \quad [35]$$

Two LVDT's were additionally used to monitor slip between the end plates and LCF columns at both ends of the link. The full LVDT schematic for each test is shown in Figure 59.

Strain in the composite web and in the top flange was monitored by strain gauges placed at selected locations. Prior to applying the strain gauges, rust and material imperfections were removed from the steel surface using a grinder to ensure the gauges achieved a solid bond with the base metal. Rosette strain gauge groups were placed at various locations in the web of each specimen, including at the center of the web, halfway between the center of the web and the termination of the rubber layer in the vertical and horizontal directions, and at the termination of the rubber layer in the vertical and horizontal directions from the center of the web. Unidirectional strain gauges were placed the top flange in the stiffened connection zone to monitor the end stiffener effects on flange strain. The Full strain gage layout for each test can be seen in Figure 59.

Tokyo Sokki Kenkyujo brand post yield strain gauges were used for all testing; models YFLA-5-1L and YEFRA-5-1L were used for strain gauge and rosette groups respectively. To provide an additional method to visually monitor strain progression during testing, the links were whitewashed after application of the strain gauges.

All displacement, strain, and load data was recorded using a 24 channel National Instruments Data Acquisition device collecting data at 10HZ. A virtual instrument was

written using National Instruments Lab View v9.0 to visually display and record data during testing.

4.0 Experimental Results and Discussion

All links were tested to failure using the loading protocol specified in the 2005 AISC Seismic Provisions for links in EBF. The predefined failure criteria for the purpose of this testing was an overall strength degradation of 20%, however the specimens were loaded beyond this point if it was judged safe to do so. Inelastic hysteretic behavior and web strain distributions were used to judge the performance of the links. The inelastic rotation angle was calculated by subtracting the elastic deformation from the total deformation, and is defined in Equation 34.

$$\gamma_P = \gamma_E - \frac{V}{k_{link}} \quad [34]$$

The inelastic link rotation was used to determine whether the links met the displacement requirement of $\gamma_P = 0.08\text{rad}$ specified in the 2005 AISC Seismic Provisions. The performance of all links including; maximum shear capacity, rotation at the onset of web buckling, rotation at web fracture, maximum rotation achieved, and overall strength degradation at the maximum deformation angle can be found in Table 6 . Detailed description of link behavior during testing, web and flange strain distributions, and link failure modes are provided in the following sections for all specimens tested. It should be noted that strain gage failures occurred in many of the test specimens as a result of improper wiring. Specific locations of failure will be noted in the specimen sections below. Additionally, the results from secondary instrumentation including: end panel hystereses, effective length hystereses, strain hystereses, slip displacements, and time history plots from all instrumentation can be found in Appendix D.

4.1 Link 14DBase

From the experimental hysteresis shown in Figure 60, it can be seen that link 14DBase exceeded the plastic shear capacity and the deformation requirements specified in the seismic provisions. A maximum shear capacity of 149% the plastic shear capacity was achieved at an inelastic rotation angle $\gamma_P = 0.08\text{rad}$ before strength degradation occurred due to out-of-plane web deformation. A maximum inelastic rotation of $\gamma_P = 0.105\text{rad}$ was achieved before the initiation of web fracture during the first half cycle at $\gamma_P = 0.12\text{rad}$ (see Figure 67). The test was stopped during the first half cycle at $\gamma_E = 0.15\text{rad}$ due to crack propagation in the web and subsequent losses of load. A total strength degradation of 13% was observed on the last half cycle prior to web fracture, and a strength degradation of only 4% was observed at the AISC required inelastic deformation angle of $\gamma_P = 0.08\text{rad}$.

Strains in 14DBase occurred primarily in the effective length of the web between the stiffeners. The link yielded during the first half cycle at an elastic deformation angle $\gamma_E = 0.0075\text{rad}$. The post yield web strain propagation in the link is illustrated in Figure 67 by the white wash distribution following cycles at rotation angles $\gamma_E = 0.02\text{rad}$, $\gamma_E = 0.05\text{rad}$, $\gamma_E = 0.09\text{rad}$, and $\gamma_E = 0.13\text{rad}$. From Figure 67, it can be seen that strain was concentrated in the web along the effective length of the link. All strain gages on the web of the link failed to record useful data with exception of the rosette gage located half way between the end stiffener and center of the link in the horizontal direction. The maximum principle strains recorded from this gage at elastic rotation angles of $\gamma_E = 0.02\text{rad}$, $\gamma_E = 0.04\text{rad}$, and $\gamma_E = 0.07\text{rad}$ can be seen in Figure 72.

4.2 Link 25DBase

Link 25DBase exceeded the plastic shear capacity, but failed to meet the link rotation requirements specified in the *2005 AISC Seismic Provisions*. From the experimental hysteresis in Figure 61, a maximum shear capacity of 105% the plastic shear capacity was achieved at an inelastic rotation angle $\gamma_P = 0.0042\text{rad}$ before strength degradation occurred due to the onset of web buckling. A maximum inelastic rotation angle of $\gamma_P = 0.008\text{rad}$ was achieved before web fracture initiated in a tension field reversal zone during the first half cycle at $\gamma_P = 0.012\text{rad}$ (see Figure 68). The test was stopped during the first half cycle at $\gamma_E = 0.07\text{rad}$ due to web crack propagation and a subsequent strength degradation of 37%. Although link 25DBase experienced an initial strength degradation of 20% due to the onset of web buckling at $\gamma_P = 0.0042\text{rad}$, a constant post buckling shear capacity was maintained through $\gamma_P = 0.045\text{rad}$. It should be noted that the hysteretic behavior and early onset of web buckling in link 25DBase was possibly affected by control issues experienced during testing. During the 4th cycle at $\gamma_E = 0.00375\text{rad}$, the link was pushed to an elastic rotation angle $\gamma_E = 0.0075\text{rad}$ due to instability in the actuator control loop. The test was stopped and the control issues were resolved, however out-of-plane web deformation developed due to the premature jump to $\gamma_E = 0.0075\text{rad}$.

Strains in 25DBase occurred primarily in the web in the effective length between the stiffeners along the primary tension field zones. Although a maximum shear capacity of 105% the plastic shear capacity was achieved, the web of the link never fully yielded, and tension field action developed with the onset of web buckling at $\gamma_E = 0.005\text{rad}$. The post buckling strain propagation is shown in Figure 68 at rotation angles $\gamma_E = 0.01\text{rad}$, γ_E

$= 0.015\text{rad}$, $\gamma_E = 0.03\text{rad}$, and $\gamma_E = 0.05\text{rad}$. The white wash distributions in Figure 68 show large strains along the tension field zones for all post buckling deformation angles. The maximum principle web strain distribution recorded using rosette strain gages at discrete points on the web can be seen in Figure 73 for rotation angles of $\gamma_E = 0.02\text{rad}$, $\gamma_E = 0.04\text{rad}$, and $\gamma_E = 0.07\text{rad}$. The largest principle web strains were recorded half way between the end stiffener and center of the link and close to the web-to-flange weld in the horizontal and vertical directions respectively. The rosette gage located in the center of the web failed before the test was terminated after the first half cycle at $\gamma_E = 0.07\text{rad}$.

4.3 Link 14DN3_1000

Link 14DN3_1000 exceeded the plastic shear capacity, but did not meet the deformation requirements specified in the *2005 AISC Seismic Provisions*, and did not perform as well as the base link in terms of hysteretic behavior or web strain distribution (AISCa, 2005). The experimental hysteresis for link 14DN3_1000 is shown in Figure 62. A maximum shear capacity of 123% the plastic shear capacity was achieved at an inelastic rotation angle $\gamma_P = 0.025\text{rad}$ before strength degradation was observed due to the development of out-of-plane web deformation. A maximum inelastic rotation angle $\gamma_P = 0.068\text{rad}$ was achieved before web fracture initiated on the first half cycle at $\gamma_P = 0.09\text{rad}$ (see Figure 69). The test was stopped during the first half cycle at $\gamma_E = 0.11\text{rad}$ due to web crack propagation and a subsequent strength degradation of 53%. Although an initial strength degradation of 9.2% was observed at the onset of web buckling, the link maintained a constant post buckling shear capacity through the inelastic rotation angle $\gamma_P = 0.075\text{rad}$. The rate of strength degradation increased for all inelastic rotation angles $\gamma_P > 0.075\text{rad}$.

due to the onset of web fracture, and a degradation of 34% was observed at the AISC specified rotation angle of $\gamma_P = 0.08\text{rad}$.

Strains in 14DN3_1000 occurred primarily in the web in the effective length of the link between the end stiffeners. The link yielded during the first half cycle at an elastic rotation $\gamma_E = 0.01\text{rad}$. The post yield web strain propagation is shown in Figure 69 by the white wash distributions following cycles at $\gamma_E = 0.02\text{rad}$, $\gamma_E = 0.05\text{rad}$, $\gamma_E = 0.07\text{rad}$, and $\gamma_E = 0.09\text{rad}$. From Figure 69, it can be seen that strain in the link was concentrated in the effective web length between the end stiffeners. The maximum principle web strain distribution recorded using rosette strain gages at discrete points in the web is shown in Figure 74 for rotation angles $\gamma_E = 0.02\text{rad}$, $\gamma_E = 0.04\text{rad}$, and $\gamma_E = 0.07\text{rad}$. The largest principle web strains were recorded in the center of the link in both the horizontal and vertical directions. It should be noted that the rosette strain gage located at the termination of the end stiffener in the horizontal direction failed to produce any useful data.

4.4 Link 25DN1_1000

Link 25DN1_1000 did not achieve the plastic shear capacity and failed to meet the rotation requirements specified in the seismic provisions (AISCa, 2005). From the experimental hysteresis in Figure 63, a maximum shear capacity of 64% the plastic shear capacity was achieved at an inelastic rotation angle $\gamma_P = 0.0049\text{rad}$ before strength degradation occurred due to out-of-plane web deformation. A maximum inelastic rotation angle $\gamma_P = 0.0148\text{rad}$ was achieved before fracture initiated in tension field reversal zones (see Figure 70) during the first half cycle at $\gamma_P = 0.018\text{rad}$, and a strength degradation of 25% was observed at the AISC specified rotation angle $\gamma_P = 0.08\text{rad}$. The

test was stopped during the first half cycle at $\gamma_E = 0.11\text{rad}$ due to web fracture propagation, and a subsequent strength degradation of 48%. Although link 25DN1_1000 experienced an initial strength degradation of 20% due to the onset of web buckling, a constant post buckling shear capacity was observed through an inelastic rotation angle $\gamma_P = 0.051\text{rad}$ due to the development of tension field action.

Strains in link 25DN1_1000 occurred in the effective length of the web between the end stiffeners along the primary tension field zones. The web of the link never fully yielded, and tension field action developed at the onset of web buckling at an inelastic rotation $\gamma_P = 0.0049\text{rad}$. The post buckling strain propagation is shown in Figure 70 for rotation angles $\gamma_E = 0.01\text{rad}$, $\gamma_E = 0.02\text{rad}$, and $\gamma_E = 0.03\text{rad}$, and $\gamma_E = 0.05\text{rad}$. The largest strain levels were observed in the tension field reversal zones for all post buckling deformations. The maximum principle web strain distribution determined using rosette strain gages at discrete points on the web is shown in Figure 75 for rotation angles of $\gamma_E = 0.02\text{rad}$, $\gamma_E = 0.04\text{rad}$, and $\gamma_E = 0.07\text{rad}$. The largest principle web strain was recorded at the termination of the end stiffener in the horizontal direction, while strains in the vertical direction remained relatively constant throughout testing.

4.5 25DN3_1000

Link 25DN3_1000 additionally failed to achieve the plastic shear capacity and did not satisfy the rotation requirements specified in the seismic provisions (AISCa, 2005). The experimental hysteresis for link 25DN3_1000 is shown in Figure 64. A maximum shear capacity of 80% the plastic shear capacity was achieved before strength degradation occurred due to the onset of web buckling at an inelastic rotation $\gamma_P = 0.0036\text{rad}$. An inelastic rotation angle $\gamma_P = 0.0073\text{rad}$ was achieved before fracture initiated in tension

field reversal zones (see Figure 71) during the first half cycle at $\gamma_E = 0.01\text{rad}$. The test was stopped during the first half cycle at $\gamma_p = 0.08\text{rad}$ due to web fracture propagation and a subsequent strength degradation of 52%. Although link 25DN3_1000 experienced a 36% strength degradation due to the onset of web buckling, a constant post buckling shear capacity of 50% the plastic shear capacity was observed through $\gamma_p = 0.048\text{rad}$ due to the development of tension field action.

Strains in link 25DN3_1000 developed in the effective length of the web between end stiffeners along the primary tension field zones. The web of the link never fully yielded, and tension field action developed at the onset of web buckling at an inelastic rotation $\gamma_p = 0.0036\text{rad}$. The post buckling strain propagation is shown in Figure 71 at rotation angles of $\gamma_E = 0.01\text{rad}$, $\gamma_E = 0.02\text{rad}$, $\gamma_E = 0.03\text{rad}$, and $\gamma_E = 0.05\text{rad}$. The largest strain concentrations were observed in the tension field reversal zones along the primary tension field lines of action. All rosette strain gages in the web of the link failed to record useful data with the exception of the gage located half way between the termination of the end stiffener and center of the link in the horizontal direction. The maximum principle strains recorded from this gage are shown in Figure 76 at rotation angles of $\gamma_E = 0.02\text{rad}$, $\gamma_E = 0.04\text{rad}$, and $\gamma_E = 0.07\text{rad}$.

4.6 Effects of Core Thickness on Web Stability and Web Strain

The performance of the composite links was assessed based on the hysteretic behavior, web strain distribution, and web strain magnitude. The 14in deep composite link (14DN3_1000) did not perform as well the base case (14DBase) in terms of hysteretic behavior or web strain characteristics. Both 14DN3_1000 and 14DBase exceeded the plastic shear capacity due to cyclic hardening effects; however the composite and base

links experienced web buckling and immediate strength degradations of 13% and 8% at inelastic rotation angles of $\gamma_p = 0.025\text{rad}$ and $\gamma_p = 0.08\text{rad}$ respectively. Additionally, a total strength degradation of 37% was observed in the composite link at the AISC required inelastic rotation angle $\gamma_p = 0.08\text{rad}$. As both links exceeded the plastic shear capacity before the onset of web buckling, the white wash web strain distributions appeared the same (see Figure 67 and Figure 69). It is apparent, however that web strain concentrations developed at the tension field reversal zones in the composite link, as fracture initiated during the first half cycle at $\gamma_E = 0.09\text{rad}$, while fracture was not observed in the base case until the first half cycle at $\gamma_E = 0.13\text{rad}$. It is difficult to compare the maximum principle web strain values at discrete points on the webs of the two links due to strain gage failures. As stated above, all rosette strain gages on the web of 14DBase failed to record useful strain data with the exception of the gage located half way between the termination of the end stiffener and the center of the link in the horizontal direction. At this location, the maximum principle web strains in 14DN3_1000 and 14DBase were recorded to be between 1% and 2% for $0.02\text{rad} < \gamma_E < 0.07\text{rad}$, additionally suggesting that the composite web did not improve web strain magnitudes.

The 25in deep composite links (25DN1_1000 and 25DN3_1000) performed better than the base link (25DBase) in terms of hysteretic behavior, tension field, and web strain characteristics. Although only link 25DBase exceeded the plastic shear capacity before the onset of web buckling, 25DN1_1000 and 25DN3_1000 achieved higher rotation angles. Links 25DBase, 25DN1_1000, and 25DN3_1000 achieved inelastic rotation angles of $\gamma_p = 0.07\text{rad}$, $\gamma_p = 0.09\text{rad}$, and $\gamma_p = 0.09\text{rad}$ respectively before the tests had to

be stopped due to web fracture propagation and subsequent strength degradation. Additionally, strength degradations of 25% and 52% were observed in links 25DN1_1000 and 25DN3_1000 at the AISC specified inelastic rotation angle $\gamma_p = 0.08\text{rad}$. Based on the white wash distributions, the tension field behavior and web strain distributions varied in the base and composite links (see Figure 68, Figure 70, and Figure 71). Tension field action developed in 25DBase across the unstiffened effective length of the web, and the tension field lines of action terminated into the flanges 3in from the end stiffener. The base link showed strain concentrations distributed along the tension field lines of action, with the highest concentrations located in the tension field reversal zones for all rotation angles analyzed. Link 25DN1_1000 developed tension field across the unstiffened effective length of the web, however in contrast to the behavior of the base link, the tension field lines of action terminated at the intersection of the end stiffeners and flange. 25DN1_1000 showed concentrated web strains only in tension field reversal zones for rotation angles $\gamma_E < 0.05\text{rad}$. The web strains spread to the tension field lines of action after large out-of-plane web displacements developed at higher deformation angles. Tension field action additionally developed in the effective unstiffened web length in Link 25DN3_1000, and the tension field lines of action terminated at the intersection of the end stiffeners and flanges. Link 25DN3_1000 showed web strain concentrations along the tension field lines of action for all rotation angles analyzed, and the highest strain concentrations developed in the tension field reversal zones. Additionally, different horizontal web strain profiles and decreased maximum principle strain magnitudes were observed in the composite links. Link 25DBase developed maximum web strains half way between the termination of the end stiffeners and the

center of the link in the horizontal direction. Conversely, maximum web strains were observed at the termination of the end stiffeners in link 25DN1_1000. As stated above, information regarding the horizontal web strain distribution in link 25DN3_1000 is not available due to strain gage failures. Gages located half way between the termination of the end stiffener and center of the link in the horizontal direction recorded maximum principle strain values that were 56% and 61% lower than the base link for links 25DN1_1000 and 25DN3_1000 respectively; suggesting the composite web helped to decrease web strain.

4.7 Large Initial Imperfection and Core Fracture

The experimental behavior of the composite specimens was affected by initial geometric web imperfections and unexpected core material behavior. Global mode one (or bowing) buckling imperfections were observed in the webs of links 25DN1_1000 and 25DN3_1000. These imperfections were a result of dimensional errors in the sandwich face plates introduced during fabrication. The steel face plates were sheared as opposed to cut, resulting in jagged edges which had to be clamped during application of the flanges. This required the sandwich plates to be clamped during application of the flanges. The large initial imperfections resulted in lower buckling loads and deformation angles in links 25DN1_1000 and 25DN3_1000 then would have potentially been observed had the sandwich webs been fabricated in plane.

The experimental behavior of the composite specimens was additionally affected by an unexpected core fracture failure mode. This failure mode was observed in links 14DN3_1000 and 25DN3_1000. Core failure in these links occurred directly in the center of the core layer, suggesting the neoprene was applied in two layers during the

fabrication of the sandwich webs. As the purpose of the core material was to tie the face plates of the sandwich web together to increase flexural rigidity and provide stability, this failure mode was extremely detrimental to link behavior.

4.8 End Stiffener Effects on Strain

Consistent with the results produced by Lewis (2010) the end stiffeners effectively shifted strain away from the connection zone of the link in all specimens. White wash distributions in the connection regions of the links suggested low web and flange strain values throughout testing (see Figure 72 through Figure 76). Additionally, no out-of-plane web deformation was observed in the stiffened connection zone of any of the specimens during post buckling cycles. Flange strain distributions recorded at discrete points along the flanges of all specimens are shown in Figure 72 through Figure 76. Low flange strains were recorded in the stiffened end zone of each link, and link failures occurred in the effective unstiffened web length. The largest flange strain values were recorded at the termination of the end stiffener in all specimens with the exception of link 25DBase in which the largest flange strains were recorded in the effective unstiffened length. Low strain values were additionally observed in the fillet welds used in the end plate connections of all specimens. White wash on the fillet welds of all links remained largely intact throughout testing, and fillet weld fracture did not contribute to the failure of any of the specimens. Base metal weld cracking developed in the top flange-to-endplate weld of link 14DBase during the first half cycle at a rotation angle $\gamma_E = 0.04\text{rad}$. This crack initiation did not, however, result in any strength degradation, and crack growth was not observed for the remainder of the test.

4.9 Numerical Model Validation

The numerical models used to develop the experimental test matrix were valuable in selecting appropriate test specimens and shedding light on link design considerations. The validity of the models had to be confirmed using experimental data, however, so they could be used to conduct further parameter studies on link behavior. Initial models conducted for this study utilized modeling parameters discussed in Lewis (2010). These models had to be refined to account for composite structure behavior, advanced material behavior, and large element deformation. In modeling the sandwich links, assumptions were made regarding steel and hyperelastic material formulations, composite material interface behaviors, and magnitudes of initial geometric imperfection. These assumptions were adjusted throughout testing to reflect experimental behavior, and results from the updated models have been compared to experimental results.

Detailed material formulations used in the updated models are described in Chapter 2. As of the writing of this thesis, coupon testing has not been conducted on plate steel samples from the experimental links. Steel formulations were updated using nominal yield and ultimate strength values from mill certification testing. Additionally, testing data has not been obtained for the hyperelastic core material in the experimental specimens, so the material properties have been scaled accordingly using uniaxial hyperelastic test data from Bradley et al. (2001).

Detailed geometric imperfection procedures for the updated models are given in Chapter 2. Large discrepancies existed between the initial numerical assumptions and the experimental actualities regarding initial geometric web imperfections in the links. The webs of the experimental base case links (14DBase and 25DBase) showed little visual

imperfection prior to testing. Thus initial imperfection magnitudes were decreased in the final models. The webs of the experimental sandwich links, however, showed large global initial imperfections. The buckling mode shape and magnitude of imposed initial displacements were thus adjusted to reflect the experimental specimens.

The numerical models accurately captured the experimental link behaviors to the point of web fracture initiation with the exception of 25DN3_1000. All models accurately predicted the initial link stiffnesses, yield strengths (where applicable), out-of-plane web behaviors, and web strain characteristics. The following sections will discuss similarities and differences between the numerical and experimental results from the 14in and 25in deep links. The updated model hystereses have been plotted over the experimental hystereses in Figure 77 through Figure 81 for the purpose of comparison.

4.9.1 14in Deep Link Numerical Comparison

The 14in deep models accurately captured the experimental behaviors of the shear links. A difference of 6% was observed in the numerical and experimental yield point of link 14DBase. The magnitude of initial imperfection was decreased in the 14in base model to more accurately capture experimental behavior. With 2% buckling mode imperfections applied, the original model showed strength degradation due to out-of-plane web buckling at an inelastic rotation angle $\gamma_P = 0.035\text{rad}$ (see Figure 31). The magnitude of initial imperfection was decreased to 1% the buckling mode deformation profile, and out-of-plane web deformations were not observed until a rotation angle $\gamma_P = 0.06\text{rad}$, which is consistent with the experimental results. Additionally, larger amounts of cyclic hardening were observed in the experimental hysteretic behavior of link 14DBase. This is because the cyclic hardening properties of A36 steel in the model were calibrated using

scaled experimental hardening properties of grade 50 steel. The steel property hardening formulations will be further calibrated after tension and cyclic testing is conducted on the link steel. Similar web strain characteristics were additionally shown in the numerical and experimental results. Global plastic web strain was observed through an inelastic deformation angle $\gamma_P = 0.06\text{rad}$, and strain concentrations developed in the center of the link at higher levels of deformation.

The numerical and experimental results of link 14DN3_1000 additionally showed similar hysteretic behaviors. A difference of 2% was observed in the numerical and experimental yield point of the link. Both the numerical and experimental hysteretic behaviors showed strength degradation due to the onset of web buckling at an inelastic rotation angle $\gamma_P = 0.025\text{rad}$. Additionally, the same post buckling shear capacity was observed through an inelastic rotation angle $\gamma_P = 0.07\text{rad}$, at which point fracture propagation in the web of the experimental specimen resulted in a large strength degradation not captured in the model. The numerical and experimental results also showed similar web strain characteristics for link 14DN3_1000. Global web yielding was observed for inelastic rotation angles $\gamma_P = 0.07\text{rad} < 0.02\text{rad}$, and strain concentrations developed in tension field reversal zones at higher inelastic displacements.

4.9.2 25in Deep Link Numerical Comparison

The 25in deep link models captured the general experimental hysteretic behavior of the links; however discrepancies were observed in the post buckling shear capacities. A difference of 17% was observed in the maximum numerical and experimental pre-buckling loads of link 25DBase. Additionally, a 4% discrepancy was observed between the post buckling loads prior to web fracture in the experimental specimen. Similar to

link 14DBase, these load discrepancies exist because the cyclic behavior of A36 has been approximated using experimental data from Grade 50 steel. Despite these differences, the model accurately captured the post buckling web behavior in the link. Both the numerical and experimental link experienced strength degradation due to the onset of web buckling at an inelastic rotation angle $\gamma_P = 0.0042\text{rad}$, and both maintained constant post buckling shear capacities. Similar to the experimental specimen, global tension field action developed in the link model, and the tension field lines of action terminated into the flanges 2.85in away from the end stiffener. Strain concentrations additionally developed in tension field reversal zones in the model at the same locations fracture occurred in the web of the experimental specimen.

Similar buckling loads and post buckling web behavior were observed in the numerical and experimental results for links 25DN1_1000 and 25DN3_1000, however larger post buckling shear capacities were observed in the composite link models. 20% and 17% discrepancies were observed in the maximum pre-buckling loads in the 25DN1_1000 and 25N3_1000 models respectively. Consistent with experimental results, the numerical hysteretic behaviors of link 25DN1_1000 and 25DN3_1000 both showed strength degradation due to out-of-plane web buckling at an inelastic rotation angle $\gamma_P = 0.005\text{rad}$. The experimental post buckling web behaviors and web strain distributions of links 25DN1_1000 and 25DN3_1000 were additionally captured accurately in the numerical models. Consistent with experimental results, global tension field action developed in the effective length of the web of each model, and the tension field lines of action terminated at the end stiffener to flange joint. Furthermore, web strain

concentrations developed in the numerical models in the same locations experimental strain concentrations and fracture occurred in the tension field reversal zones.

The numerical models of links 25DN1_1000 and 25DN3_1000 exhibited larger post buckling shear capacities than were observed experimentally. Post buckling shear capacity discrepancies of 22% and 61% were observed in the 25DN1_1000 and 25DN3_1000 models respectively. These discrepancies were a result of inconsistencies in the flexural web rigidities in the numerical models and experimental specimens. Larger numerical web rigidities resulted in a compression field contribution in the post buckling shear capacities of the links. These inconsistencies were not observed in the model of link 14DN3_1000 due to the relatively small contribution of the core material to the out-of-plane rigidity of the web. That is, the relatively thick face plates in the 14in deep composite link provided enough rigidity to define the post buckling behavior of the link independent of the elastic modulus of the core material. The discrepancies in flexural web rigidities in the numerical models and experimental specimens of the 25in deep links are a result of the rubber fracture failure mode observed in the experimental specimens and two assumptions used in development of the hyperelastic material formulations in the numerical analyses. These assumptions were as follows: (1) The test data provided by Bradley et al. (2001) was scaled equally in tension and compression to increase the elastic modulus to desired levels. As hyperelastic materials exhibit extremely non-linear stress strain behavior, it is very difficult to scale accurately in tension and compression. Thus it is possible the 1000psi hyperelastic material used to model the experimental specimens exhibited behavior of a much stiffer material. (2) The modulus of elasticity of the hyperelastic material in the experimental specimens was not

provided, so the Durometer rating was used to approximate the elastic modulus. It has been shown, however, that due to testing inconsistencies Durometer rating cannot accurately be correlated to material properties (Hertz, 1998). It is thus possible the hyperelastic material in the experimental specimens was less stiff than the 1000psi approximated for Durometer 50 rubber.

5.0 Summary and Conclusions

Ductility in lateral load resisting systems is achieved by isolating damage due to lateral loading to deformation controlled fuse elements designed into the gravity and lateral load resisting systems of structures. These elements are designed to deform plastically and dissipate energy during seismic events, while the remainder of the structure continues to act in the elastic range. Many lateral load resisting systems currently in use utilize elements of the gravity system to dissipate seismic energy. In MRF and EBF in particular, damage is concentrated to the load carrying beams, making it difficult to achieve rapid post earthquake repair and occupancy.

There is an interest in moving toward use of an improved performance criteria in design, such that structures can be easily repaired to allow for quick occupation following seismic events. This research is focused on the link component of the LCF system. For the LCF system to meet specified performance objectives the energy dissipating link component must provide sufficient ductility to achieve displacement requirements.

Current specifications for energy dissipating links require the use of intermediate web stiffeners to increase ductility and provide web stability (AISCa, 2005). Residual stresses at the roots of intermediate stiffener welds have, however, been shown to decrease ductility by causing premature crack initiation. Thus this investigation is focused on development of a continually stiffened steel-rubber-steel composite web in which intermediate web stiffeners are not required to provide web stability. The composite web design allows for an increase in web thickness (and inherent flexural rigidity) without increasing the shear strength of the link, resulting in a web which is

continually stiffened. Theoretical, numerical, and experimental studies were conducted to assess the performance of the composite sandwich web links.

Theoretical investigations were initially conducted to assess the required geometries and buckling deformation angles of the composite links. This investigation was completed independently using transverse stiffening requirements from the *2005 AISC Seismic Provisions* and stiffener spacing requirements from Popov and Kasai (1986) in conjunction with required stiffener rigidities from Narayanan (1983).

A numerical specimen matrix was developed using the results from the theoretical investigation. Parameter studies were conducted on the 14in and 25in deep shear links to determine the effects of the elastic modulus of the core material, core thickness, and core debonding on link performance. For the core elastic modulus parameter study, links with 1in core thickness and elastic modules of 385psi, 1000psi, 5000psi, and 10000psi were analyzed. For the core thickness parameter study, the behavior of links with 1000psi core modulus and thicknesses of 1in, 2in, and 3in were assessed. Finally, the debonding parameter study was conducted by assigning various bond failure initiation rotation angles, and assessing link performance based on the bond failure rotation angle.

An experimental specimen matrix was developed using results from the numerical analysis. Although the numerical analysis suggested only links with core elastic modules greater than 5000psi show improved results to the base links in terms of hysteretic behavior and web strain distribution, 1000psi core material was used for all specimens due to fabrication restrictions. The final specimen matrix consisted of 1-14in deep base link, 1-14in deep sandwich link with a 1in core, 1-25in deep base link, 1-25in deep sandwich link with a 1in core, and 1-25in deep sandwich link with a 3in core.

5.1 Numerical Conclusions

1. Composite sandwich webs in shear links improve hysteretic behavior and web strain distribution when the elastic modulus of the core material is greater than 5000psi. All composite links with core elastic modules greater than 5000psi achieved the plastic shear capacity before the onset of web buckling. These links additionally showed improved web strain distributions and growth rates when compared relatively to the webs in the base links.
2. Composite sandwich webs with core elastic modules less than 5000psi do not remain plane when loaded in shear. The relationship developed to predict the buckling deformation angle γ_B shown in Equation 32 was derived under the assumption plane sections remain plane throughout loading. The predicted buckling load deformation angles for all specimens with core elastic modules less than 5000psi were over predicted when compared to the numerical results. The discrepancies between the predicted and numerical buckling loads were especially large for core thicknesses greater than 1in. For sandwich webs with core elastic modules greater than 5000psi, on the other hand, the predicted and numerical buckling deformation angles were very similar, suggesting that the sandwich plates remained plane in these links.
3. The continuously stiffened sandwich web concept is more effective in links with smaller web aspect ratios. The hysteretic behaviors and web strain distributions of 14in deep links with $\alpha \approx 4$ and 25in deep links with $\alpha \approx 2$ were analyzed in this investigation. Composite sandwich links with lower aspect ratios but similar shear capacities were shown to perform better relative to base link behavior in terms of hysteretic performance and web strain distribution.

4. Debonding of the core material from the face plates did not impact the overall hysteretic behavior of composite sandwich links, however, effects were observed on web strain growth rates. Debonding was shown to increase the web strain growth rates in both the 14in deep and 25in deep links; however the change was much larger in the 25in deep links. Larger web strain growth rates resulted in higher web strain magnitudes when compared to the base links.

5. Material property tests must be conducted to calibrate numerical material formulations to accurately reproduce experimental results. This is especially important when modeling extremely non-linear hyperelastic materials.

5.2 Experimental Conclusions

1. Consistent with the numerical results, composite sandwich links with a core elastic modulus of approximately 1000psi did not perform well when compared relative to base link behavior in terms of hysteretic behavior. The buckling loads and deformations observed in the composite links were lower than those observed in the base links. The post buckling shear capacities were additionally lower in the composite links.

2. The web of the 14in base link was adequately stiffened. Fracture did not initiate in 14in deep base specimen until an inelastic rotation angle $\gamma_p = 0.11\text{rad}$ which was greater than the AISC specified inelastic rotation angle $\gamma_p = 0.08\text{rad}$. Additionally, the link did not experience any out-of-plane web deformation for rotation angles $\gamma_p < 0.08\text{rad}$.

3. The webs of all composite links and the 25in deep base link were under stiffened. Strain concentrations and fracture developed in the tension field reversal zones of all the composite links and the 25in deep base link at rotation angles lower than the AISC specified inelastic rotation angle $\gamma_p = 0.08\text{rad}$.

4. Large initial web imperfections resulted in early web buckling and subsequent unstable hysteretic behavior in the 25in deep composite links. Early web buckling resulted in the development of strain concentrations and fracture in the tension field reversal zones.
5. Leaving a 2in buffer zone between the core material and the edges of the web plate for weld heat dissipation did not have any effect on the global hysteretic behavior of the shear links.

6.0 Recommendations for Future Work

To further assess the out-of-plane stiffness requirements of webs in shear links and more completely develop the concept of utilizing continuously stiffened sandwich webs in place of traditionally stiffened links, continued research in the following areas is suggested.

1. Experimental results from previous investigations (Dusicka et al., 2004) and results from this research have suggested that traditional shear links without transverse stiffeners provide adequate ductility to satisfy the deformation requirements specified in the seismic provisions. Utilizing un-stiffened links eliminates the possibilities of web fracture due to residual stresses at the root of stiffener welds. It is thus suggested that further numerical and experimental research be conducted to assess the hysteretic performance of un-stiffened shear links with homogenous steel webs.

2. The numerical results from this investigation suggested that composite sandwich links with core material elastic modules greater than 5000psi improved the hysteretic behavior and web strain distribution of compared relatively to un-stiffened shear links.

Unfortunately, at the time of this study, only a core material with an elastic modulus of 1000psi was available due to fabrication restrictions. It is recommended that further experimental research be conducted on composite sandwich links which utilize core materials with elastic modules greater than 5000psi.

3. Due to experimental test setup limitations, only links with two aspect ratios were investigated. It is recommended that further numerical research be conducted to assess the performance of composite sandwich links with a number of differing aspect ratios.

The results from the numerical analysis should be used to develop experimental specimen matrices for future testing.

4. Un-stiffened shear links were used to develop the base line hysteretic performance and web strain distributions in this research. It is recommended that the performance of composite sandwich links additionally be assessed relative to comparable shear links stiffened according the requirements specified in the *2005 AISC Seismic Provisions*.

Tables

Table 1: Qualification Testing Loading Protocol for Links in EBF

Step	Number of Cycles	Link Rotation, γ (rad)
1	6	0.00375
2	6	0.005
3	6	0.0075
4	6	0.01
5	4	0.015
6	4	0.02
7	2	0.03
8	1	0.04
9	1	0.05
10	1	0.07
11	1	0.09
12	1	0.11
13	1	0.13

Table 2: Summary of Base Link Properties

Link	Length	Web		Flanges		Nominal Strengths		
	e (in)	h_w (in)	t_w (in)	b (in)	t_f (in)	V_p (kip)	M_p (kip in)	$\frac{1.6M_p}{V_p}$
14in Deep	53	12.5	0.5	10	0.75	135	5284	63
25in Deep	53	24	0.25	6.25	0.5	130	11190	140

Table 3: Summary of Analytical Specimens

Link	Web			
	t_{fp} (in)	t_c (in)	E_c (psi)	D (kip-in ²)
14DBase	NA	NA	NA	330
14DN1_385	0.25	1	385	6267
14DN1_1000	0.25	1	1000	6267
14DN1_5000	0.25	1	5000	6268
14DN1_10000	0.25	1	10000	6268
14DN2_1000	0.25	2	1000	20120
14DN3_1000	0.25	3	1000	41890
25DBase	NA	NA	NA	5
25DN1_385	0.125	1	385	2515
25DN1_1000	0.125	1	1000	2515
25DN1_5000	0.125	1	5000	2515
25DN1_10000	0.125	1	10000	2516
25DN2_1000	0.125	2	1000	8947
25DN3_1000	0.125	3	1000	19339

*Lengths, flange sizes, nominal strengths, and web heights consistent with values in Table 2.

Table 4: Predicted Link Performance

Link	Elastic Buckling Shear (kips)	Buckling Deformation, γ_B (rad)	Plate Girder Post Buckling Capacity* (kips)	SPSW Post Buckling Capacity* (kips)
14DBase	260	NA	0	101
14DN1_385	4950	0.03	0	101
14DN1_1000	4950	0.03	0	101
14DN1_5000	4950	0.03	0	101
14DN1_10000	4950	0.03	0	101
14DN2_1000	15886	0.118	0	101
14DN3_1000	33075	0.135	0	101
25DBase	2	NA	98	97
25DN1_385	1034	0	98	97
25DN1_1000	1034	0	98	97
25DN1_5000	1034	0	98	97
25DN1_10000	1035	0	98	97
25DN2_1000	3680	0.04	98	97
25DN3_1000	7952	0.05	98	97

*Plate girder buckling capacity calculated in accordance with specifications in chapter G of the steel construction manual. SPSW post buckling capacity calculated in accordance with the strip method. According to chapter G in the steel construction manual, tension field action does not develop in the 14in deep link.

Table 5: Numerical Link Performance

Link	Elastic Buckling Load (kips)	Non Linear Buckling Load (kips)	Buckling Deformation, γ_p (rad)	Post Buckling Capacity (kips)
14DBase	2300	203	0.04	160
14DN1_385	1005	190	0.02	148
14DN1_1000	1005	195	0.02	150
14DN1_5000	1005	207	0.03	187
14DN1_10000	1005	220	0.03	200
14DN2_1000	1007	194	0.01	150
14DN3_1000	1007	172	0.04	165
25DBase	137.4	126	0.0015	100
25DN1_385	13.24	123	0.0005	100
25DN1_1000	13.24	123	0.0005	108
25DN1_5000	13.24	147	0.012	147
25DN1_10000	13.24	178	0.03	162
25DN2_1000	13.26	121	0.001	122
25DN3_1000	218.59	128	0.002	133

Table 6: Experimental Link Performance

Link	Buckling Load (kips)	Buckling Deformation, γ_p (rad)	Post Buckling Capacity (kips)	Web Fracture Initiation Deformation, γ_p (rad)
14DBase	250	0.08	225	0.13
14DN3_1000	190	0.03	158	0.09
25DBase	147	0.004	125	0.02
25DN1_1000	99	0.005	70	0.02
25DN3_1000	125	0.004	72	0.01

Figures

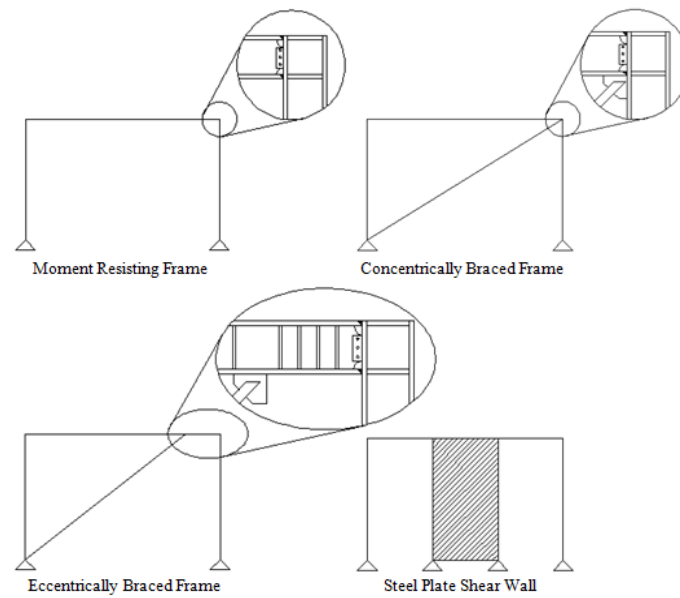


Figure 1: Steel Lateral Load Resisting Systems (Lewis, 2010)

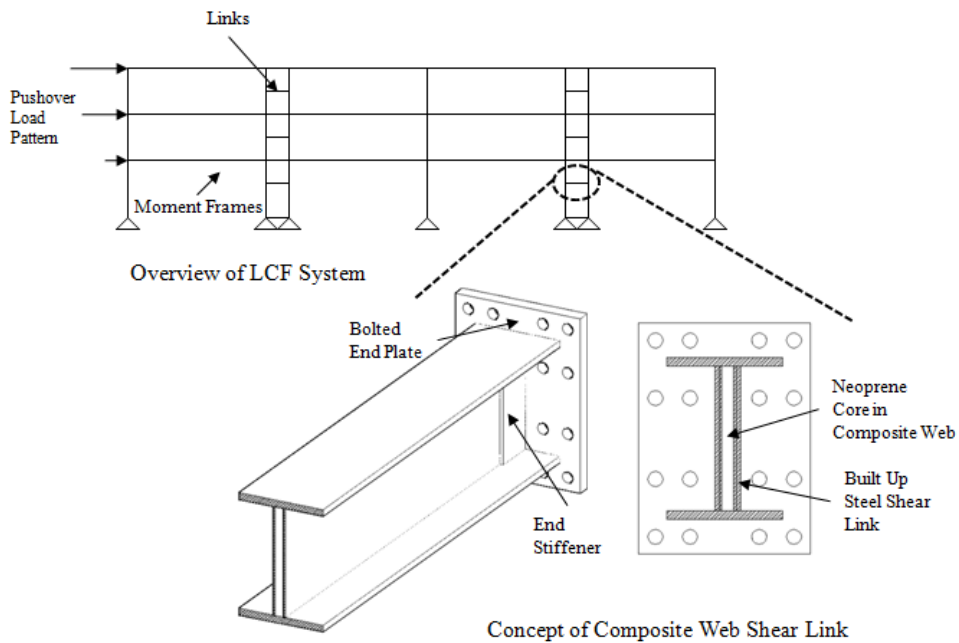


Figure 2: Link Column Frame Overview

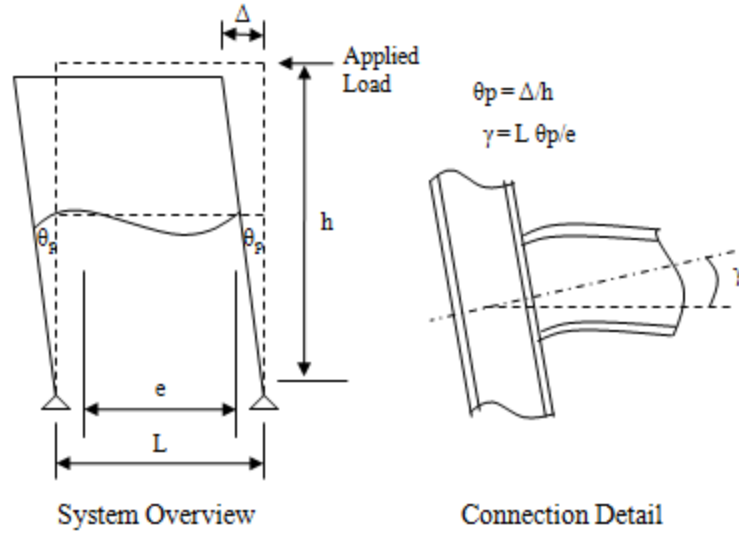


Figure 3: Link Rotation Angle Due to Lateral Frame Displacement (Lewis, 2010)

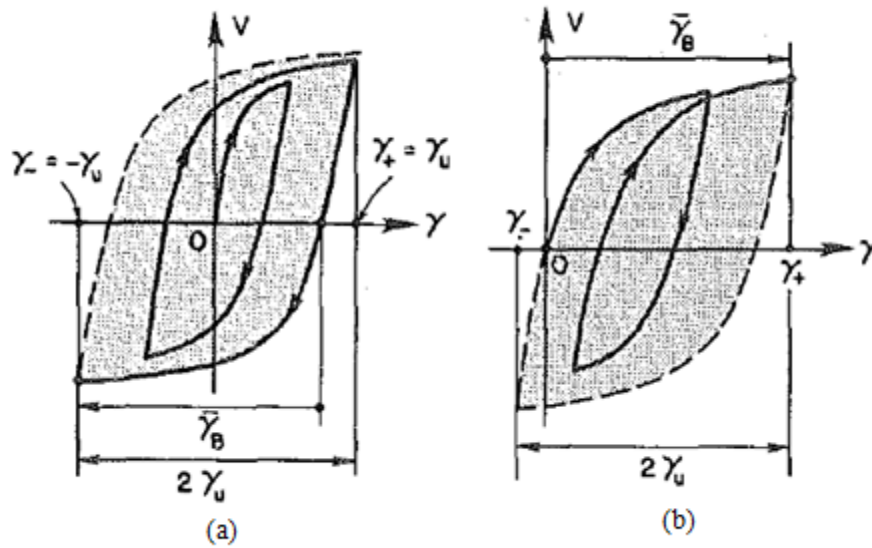
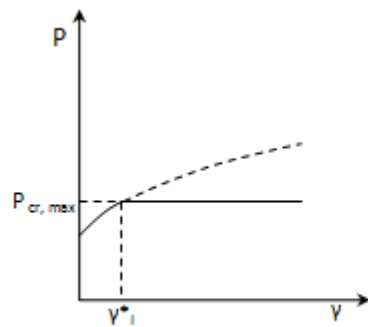


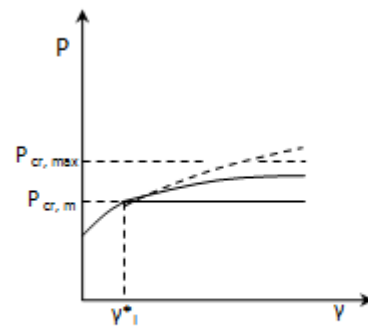
Figure 4: Final Stable Hysteretic Loops of Shear Links Subjected to (a) Symmetric and (b) Unsymmetric Cyclic Loading from Kasai and Popov (1986)



Figure 5: Failure of Web at Stiffener Weld Termination from Lewis (2010)

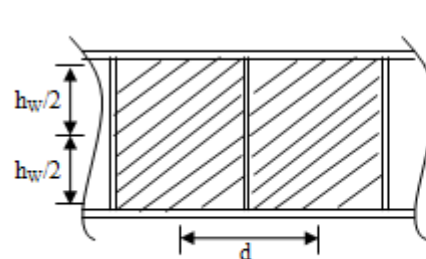


Optimum Rigidity of the First Kind

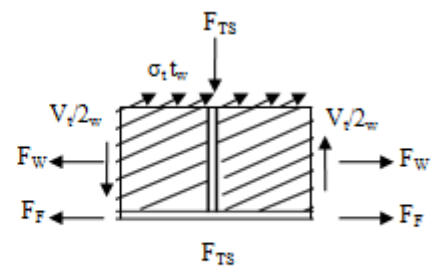


Optimum Rigidity of the Second Kind

Figure 6: Optimum Stiffener Rigidity vs. Load Relationship



Section From Built Up Plate Girder



Equilibrium Model Used in Basler's Theory

Figure 7: Basler's Tension Field Action Equilibrium Model

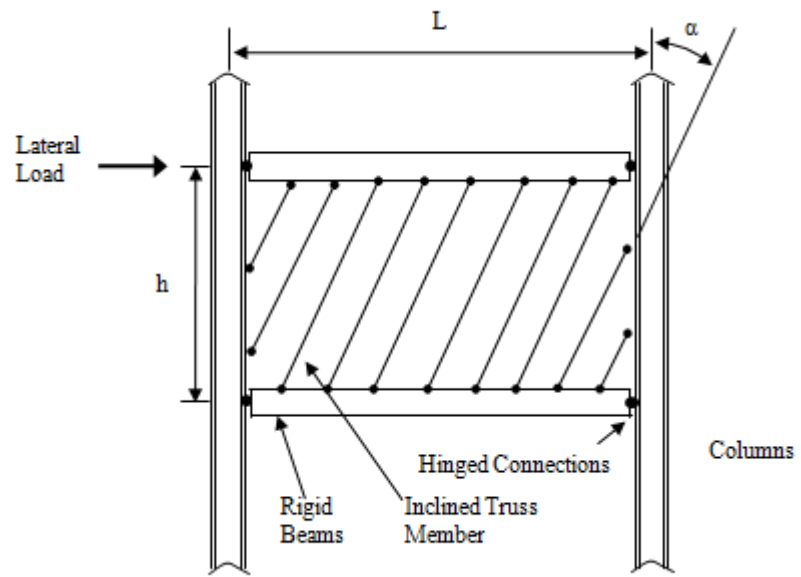


Figure 8: Strip Model

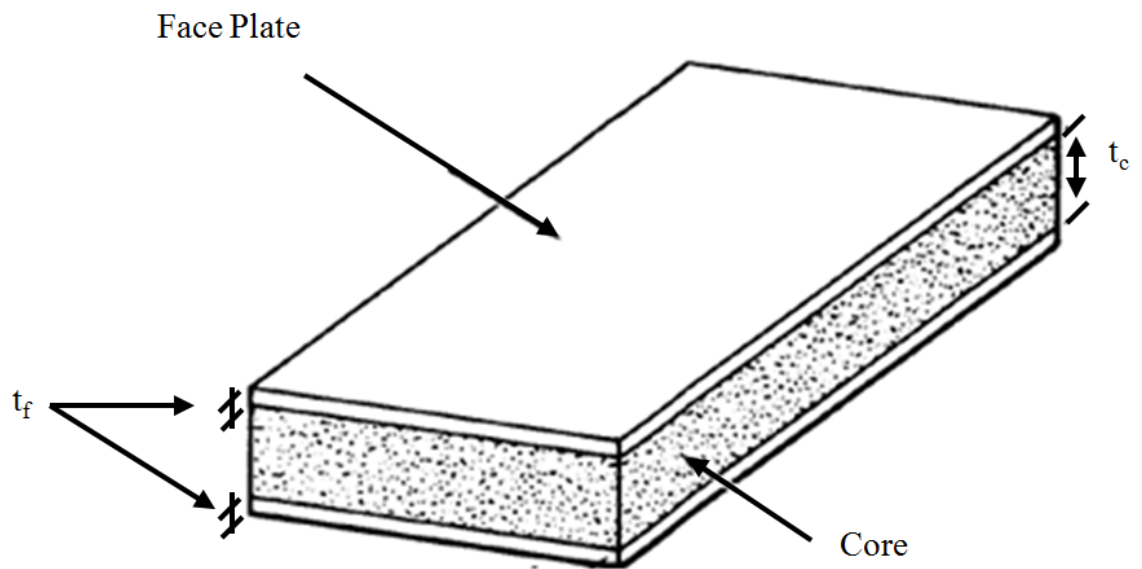


Figure 9: Sandwich Plate Overview

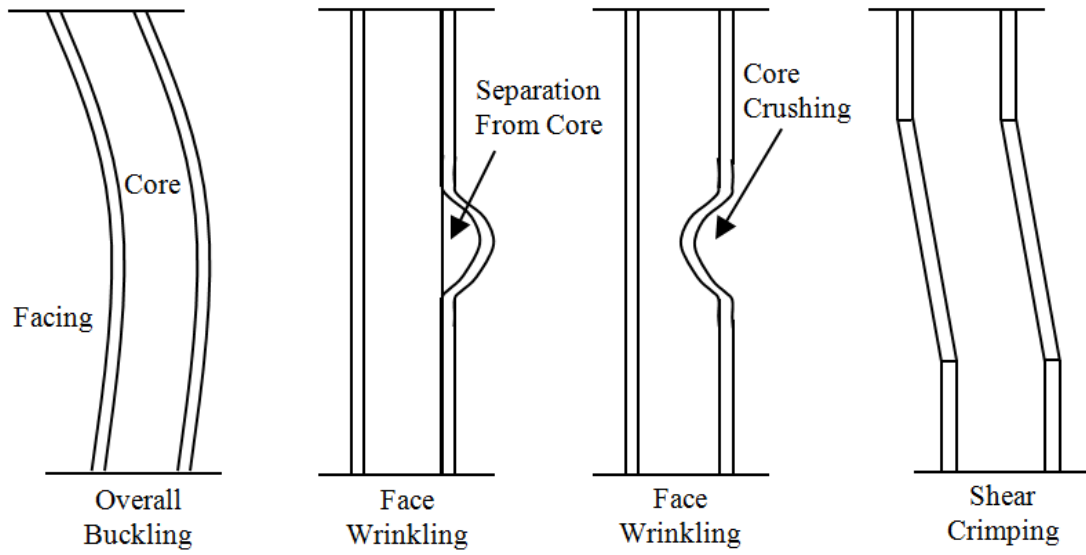


Figure 10: Typical Failure Modes of Sandwich Plates

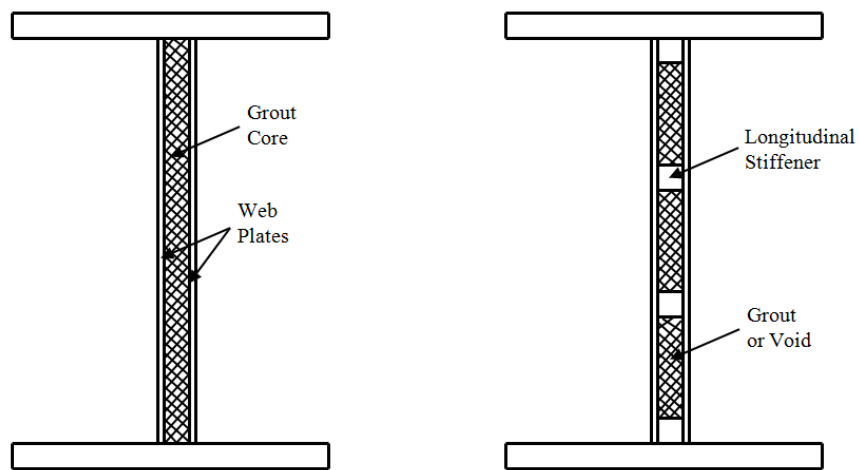


Figure 11: Proposed Sandwich Web Systems in HPS Girders

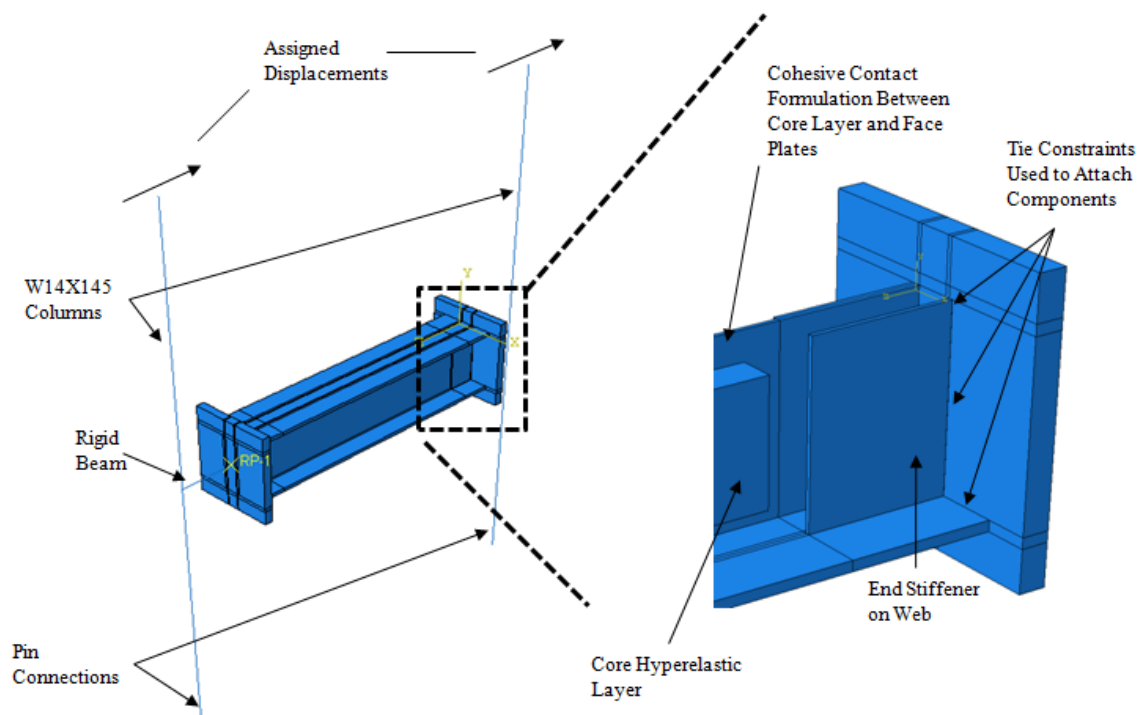


Figure 12: Model Overview

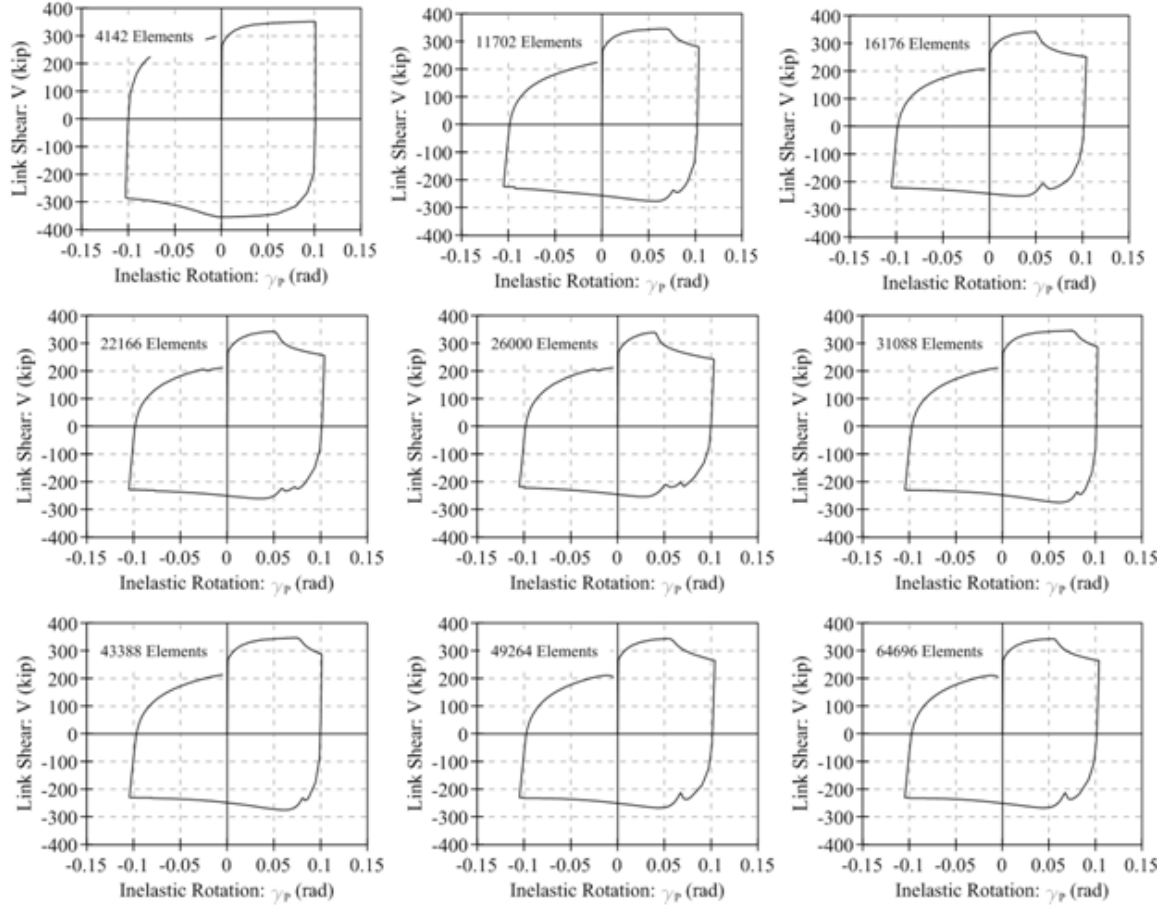


Figure 13: Convergence Curves

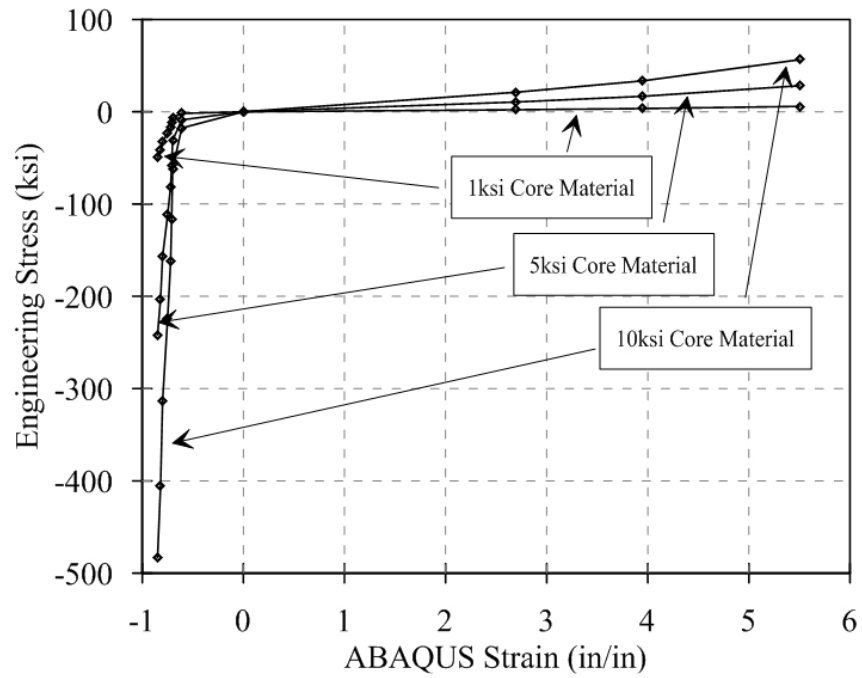
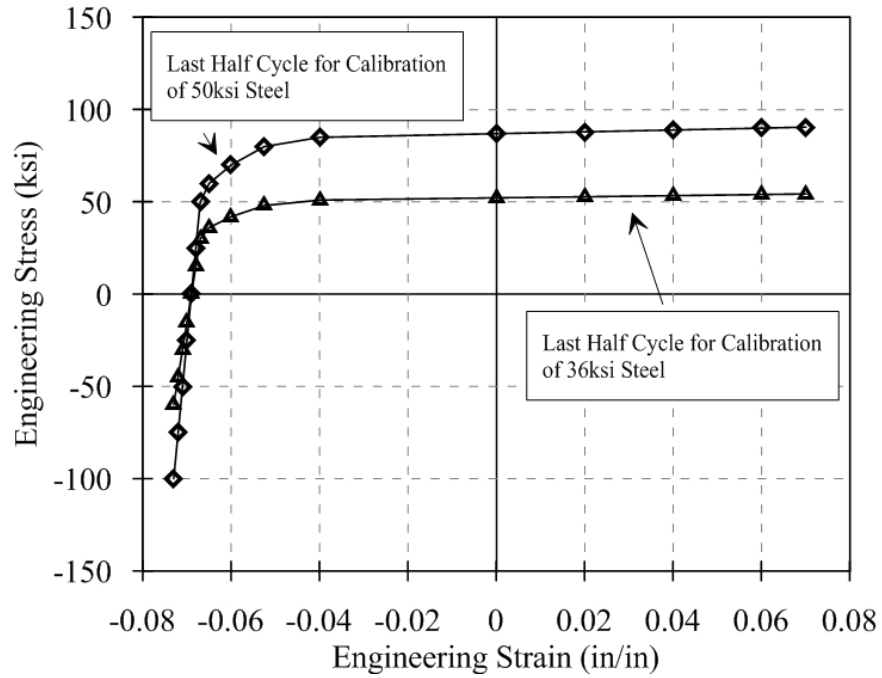
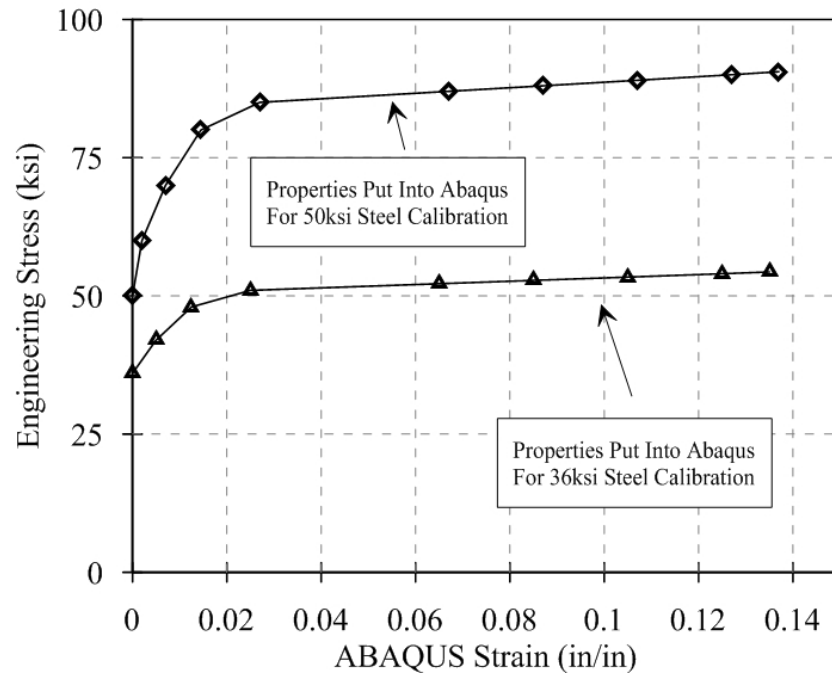


Figure 14: Rubber Material Properties Used to Calibrate Hyperelastic Material Formulation.



Last Half Cycles Used for Material Calibration



Modified Half Cycles Put into ABAQUS for Material Calibration

Figure 15: Half Cycles Used to Calibrate Cyclic Hardening Properties of Steel and Modified Half Cycle Material Properties put into ABAQUS for Material Calibration

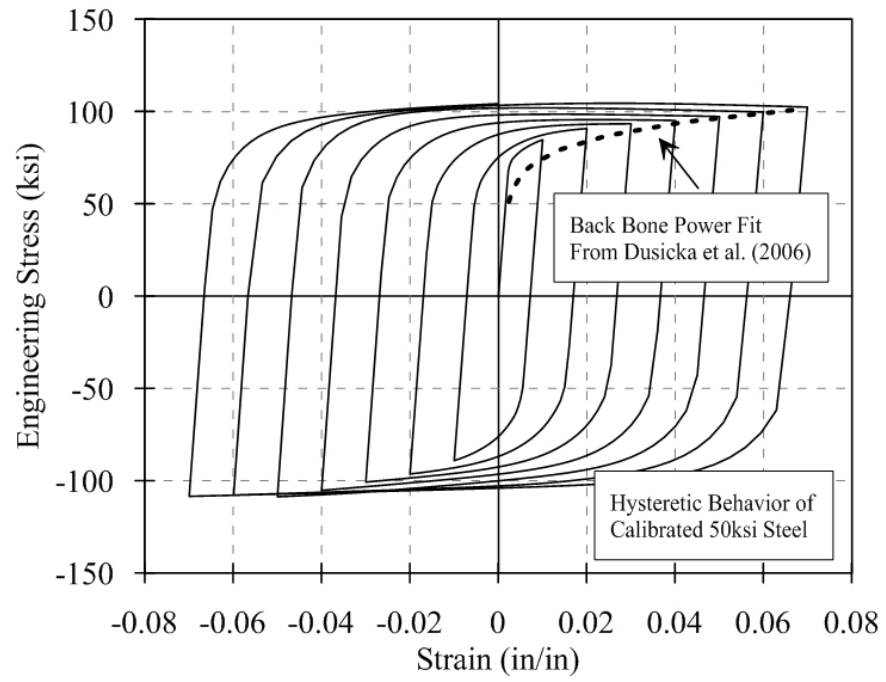


Figure 16: Material Calibration Verification Curve.

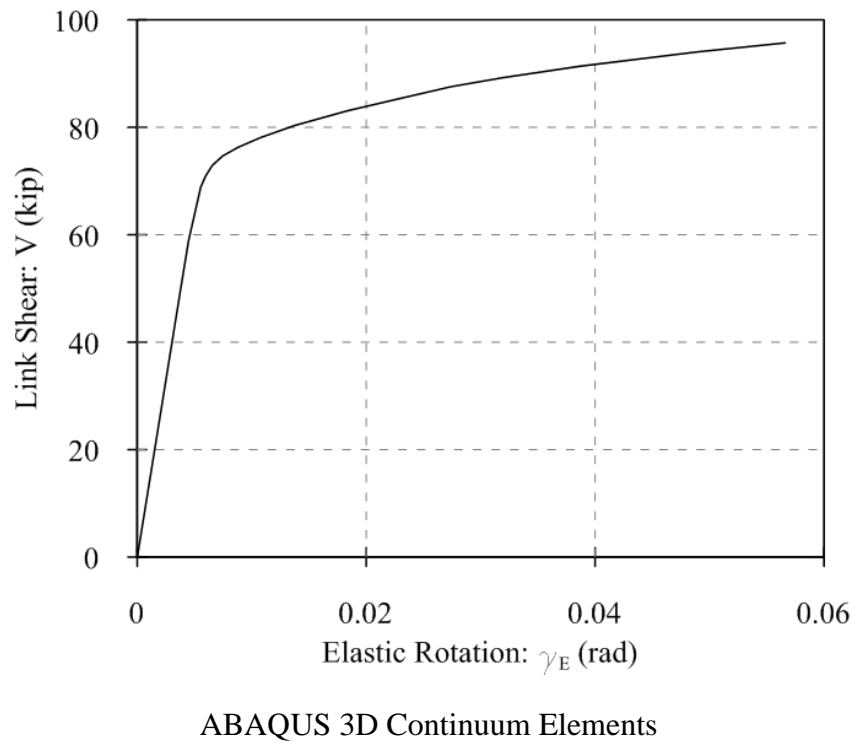
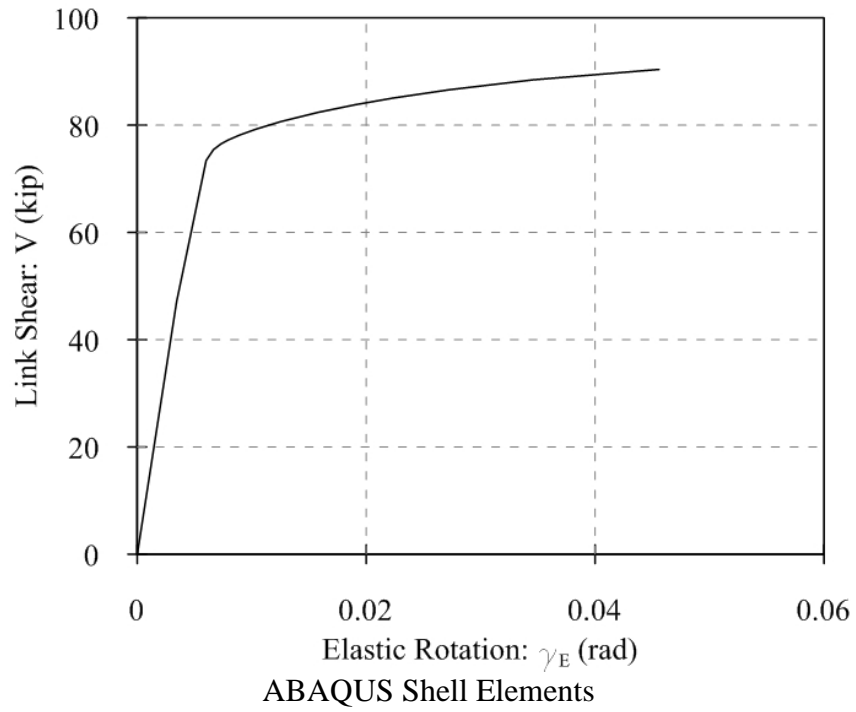


Figure 17: Shell and Full 3-Dimensional Element Monotonic Response Comparison

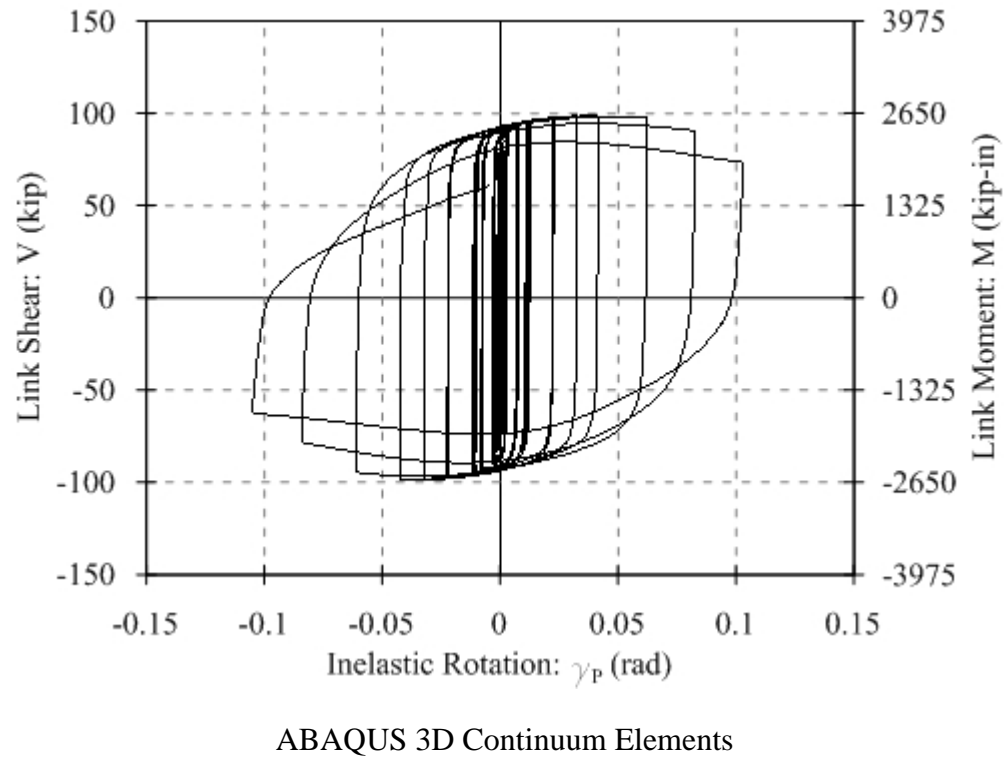
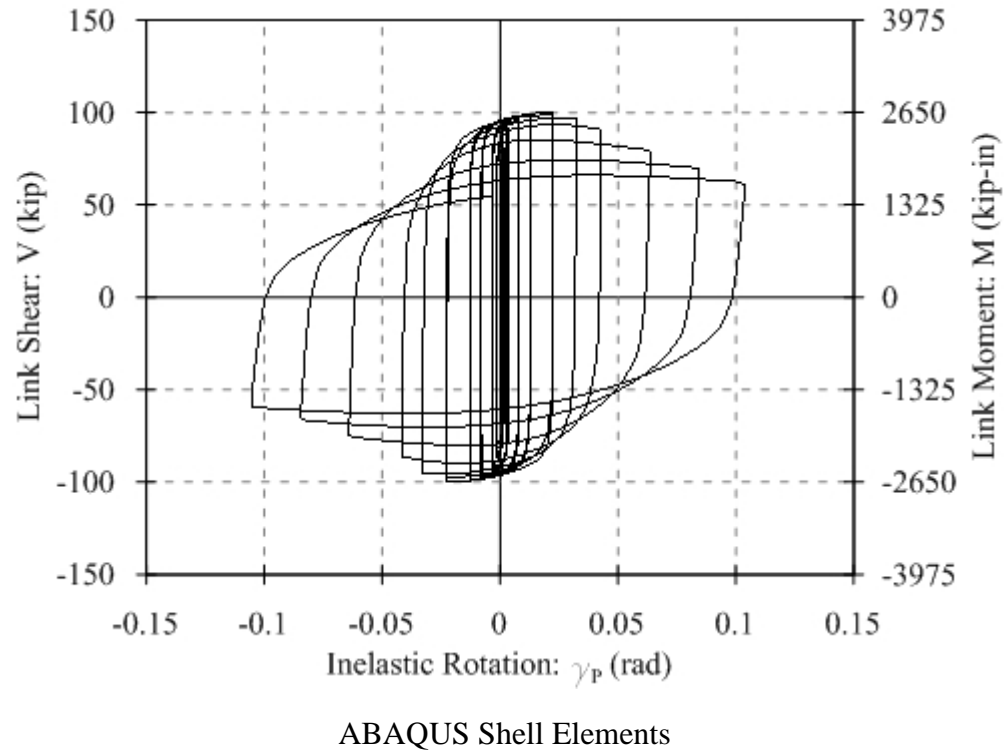
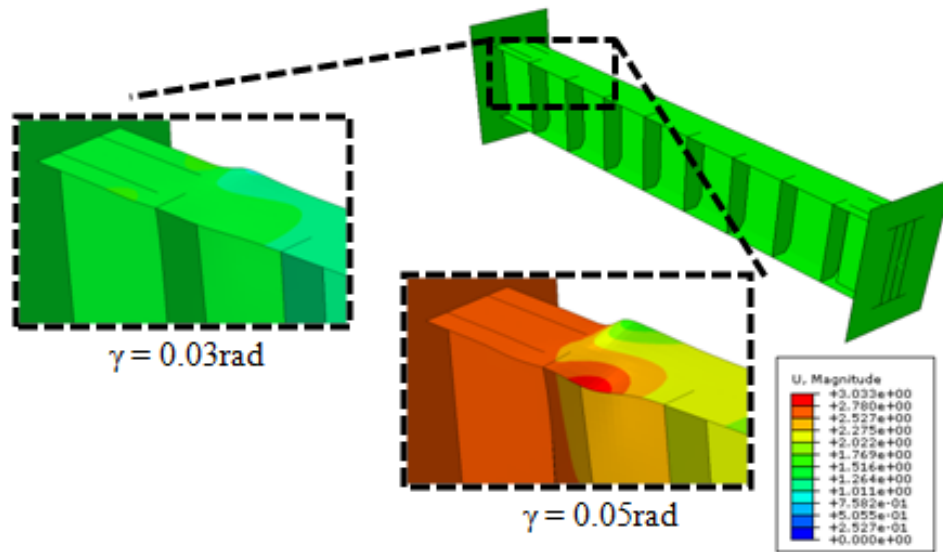
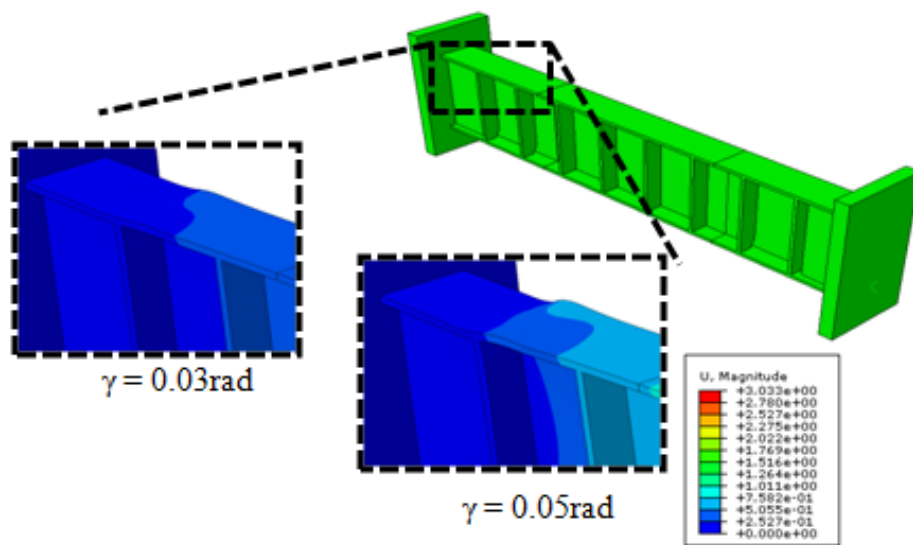


Figure 18: Shell and Full 3-Dimensional Element Hysteretic Response Comparison



ABAQUS Shell Elements



ABAQUS 3D Continuum Elements

Figure 19: Shell and Full 3-Dimensional Model Verification Links at 3% and 5% Inelastic Rotation

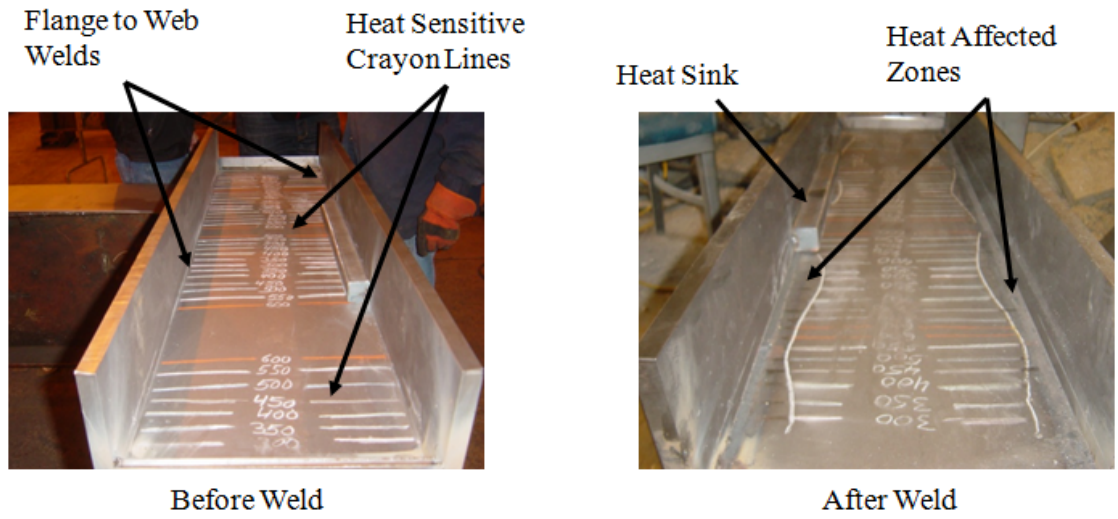
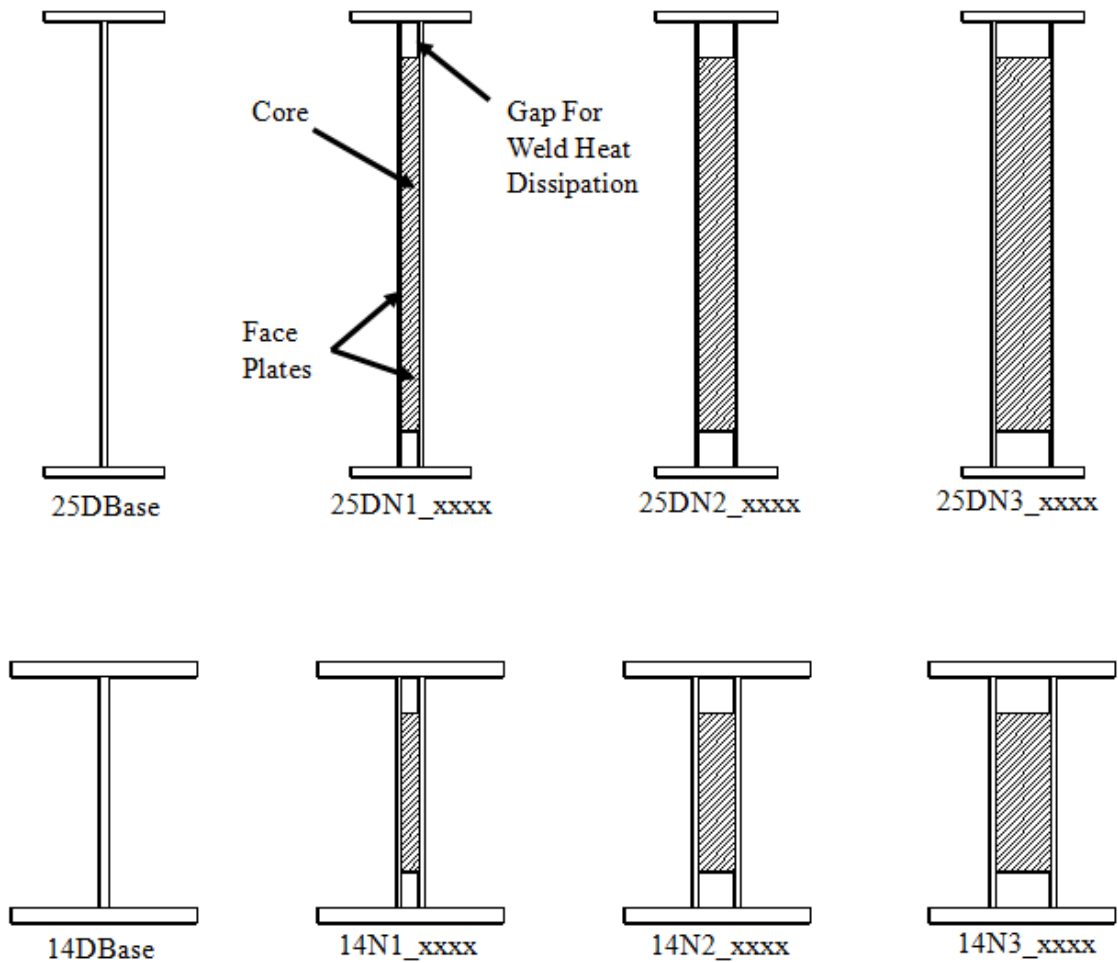


Figure 20: Weld Heat Dissipation Analysis



*Dimensions can be found in Table 2

Figure 21: Summary of Final Link Designs

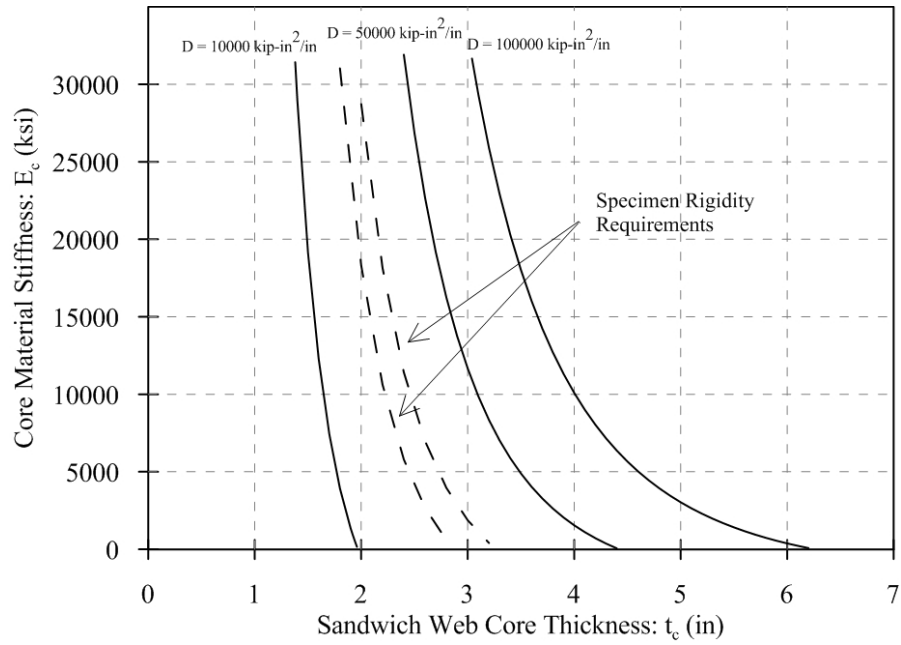


Figure 22: 14in Deep Sandwich Web Core Stiffness/Thickness Relationship to Provide Equivalent Flexural Rigidity

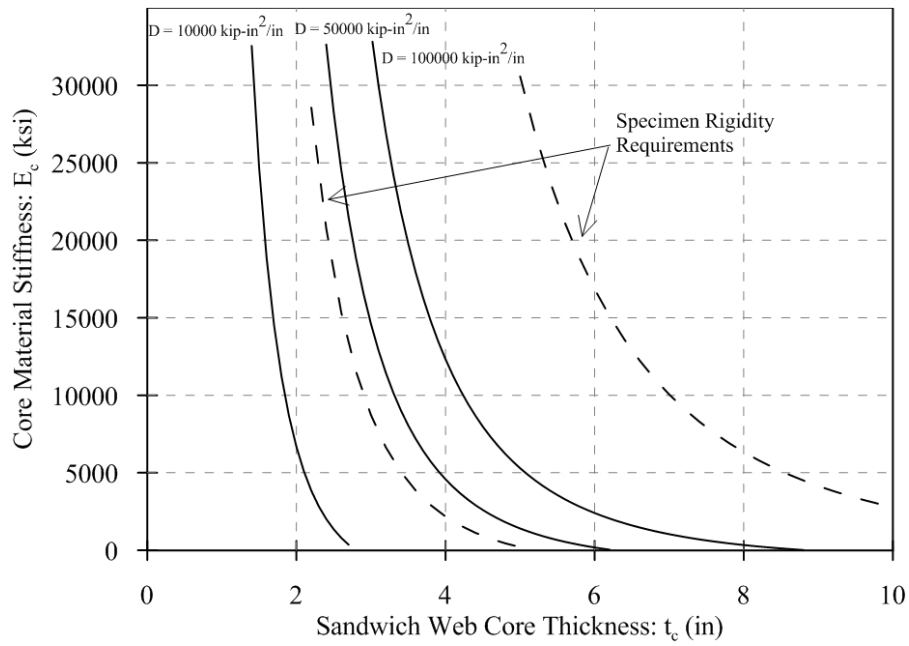


Figure 23: 25in Deep Sandwich Web Core Stiffness/Thickness Relationship to Provide Equivalent Flexural Rigidity

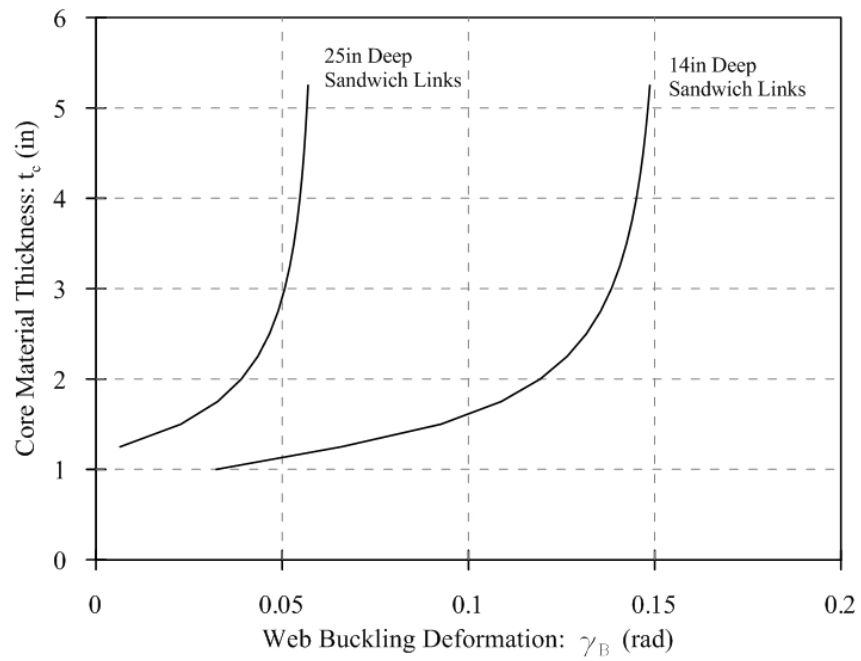
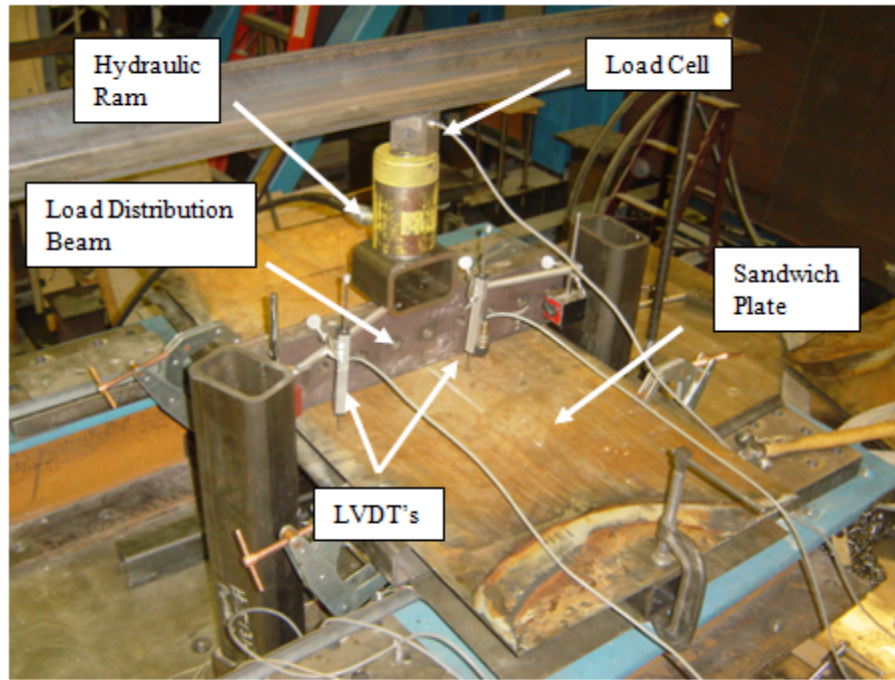
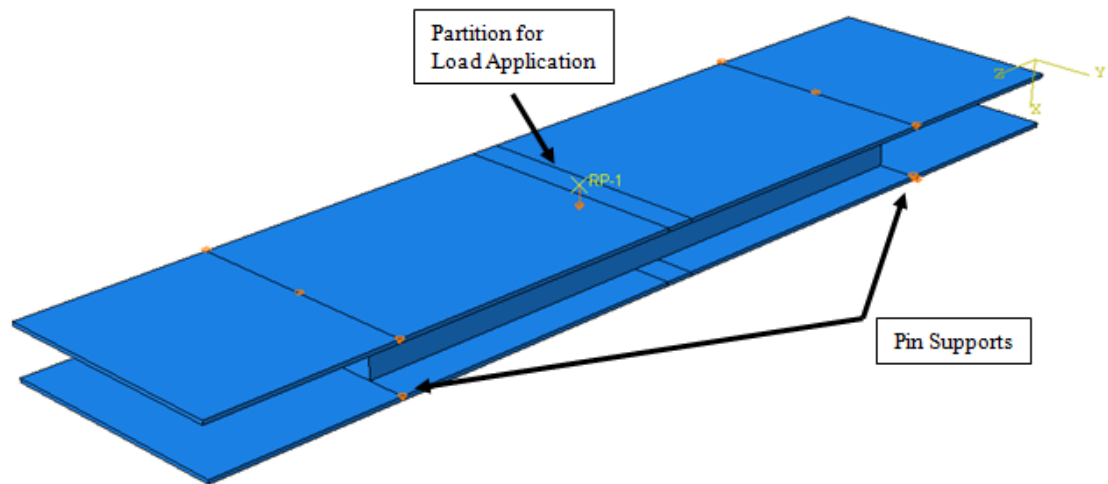


Figure 24: Web Buckling Deformation Angle/Core Material Thickness Relationships for 14in and 25in Deep Composite Links



(a)



(b)

Figure 25: (a) Flexural Bending Test Setup and (b) Flexural Bending Model Overview

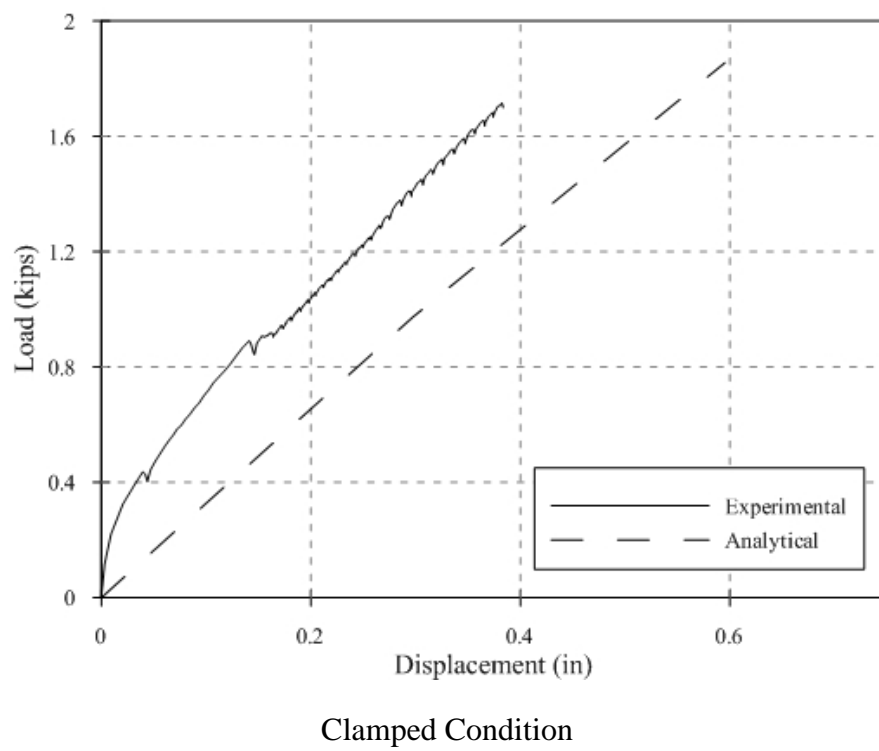
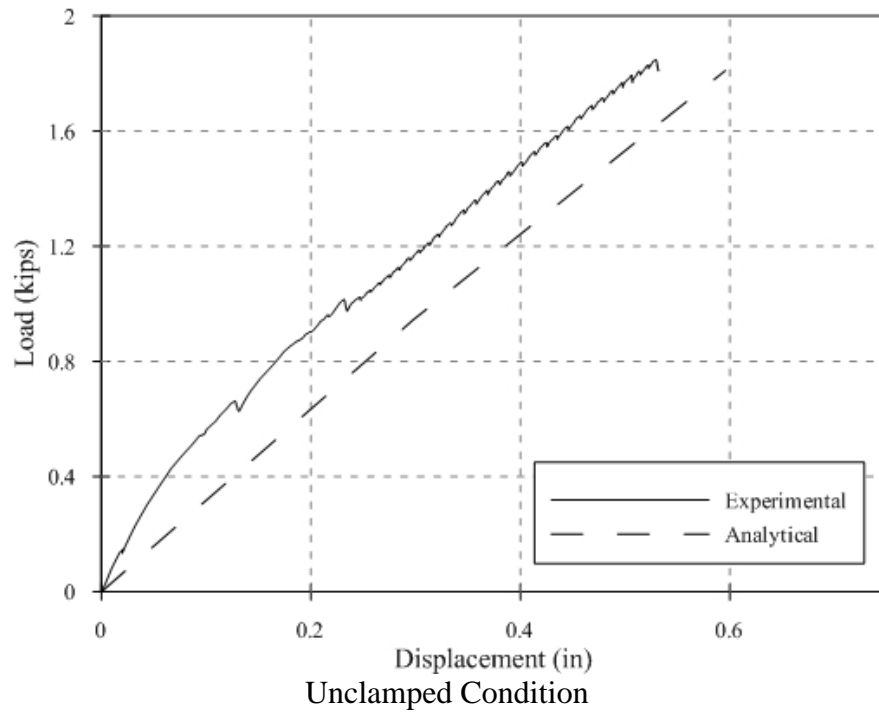
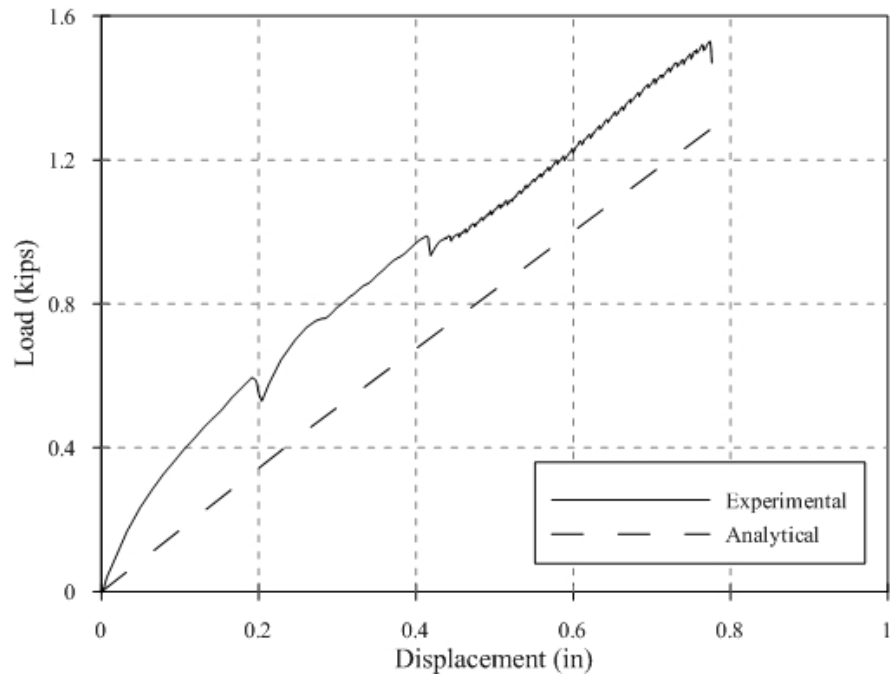
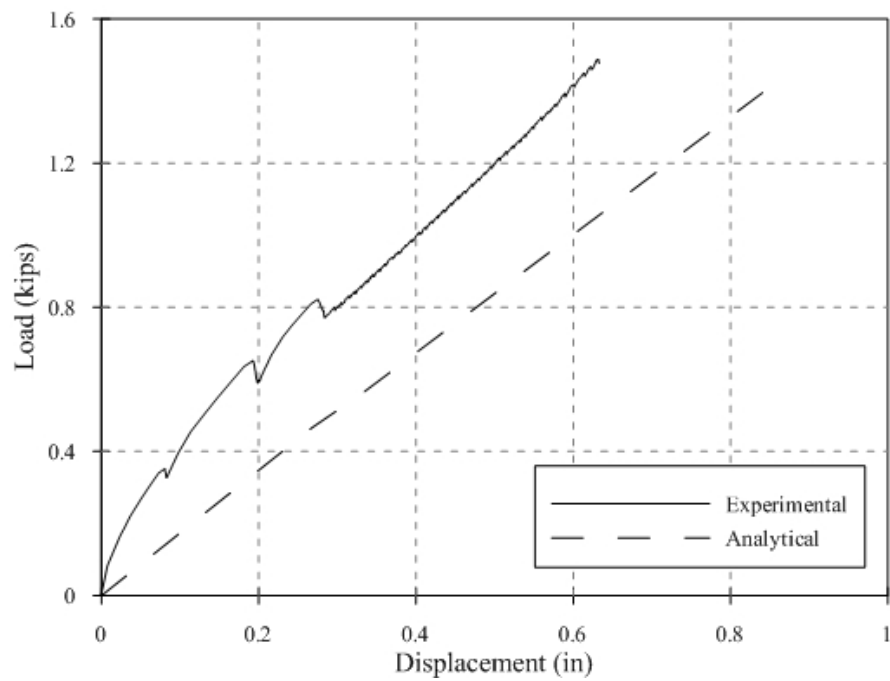


Figure 26: Flexural Bending Behavior of Sandwich Plate from Link 14DN3_1000

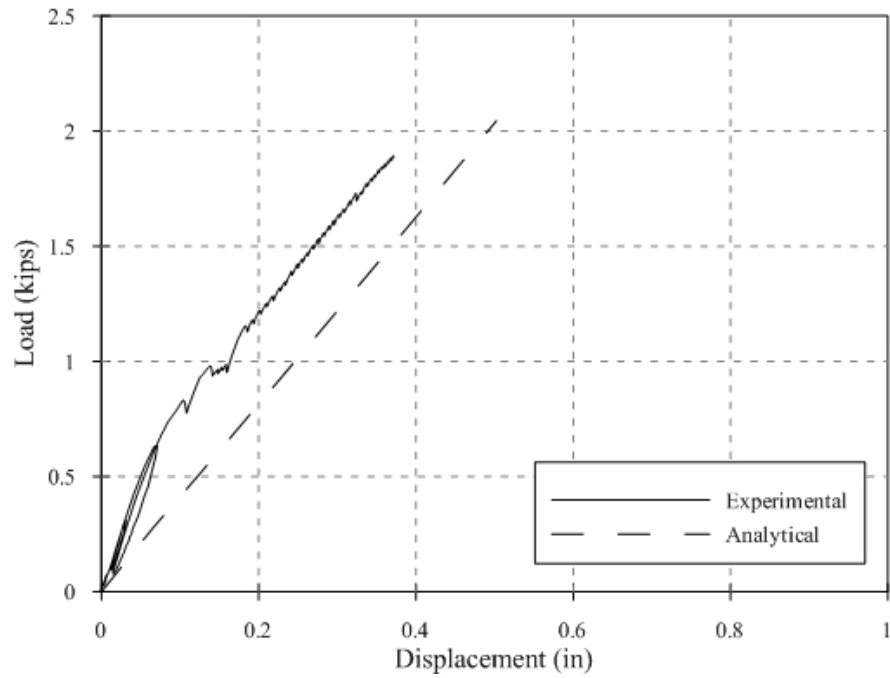


Unclamped Condition

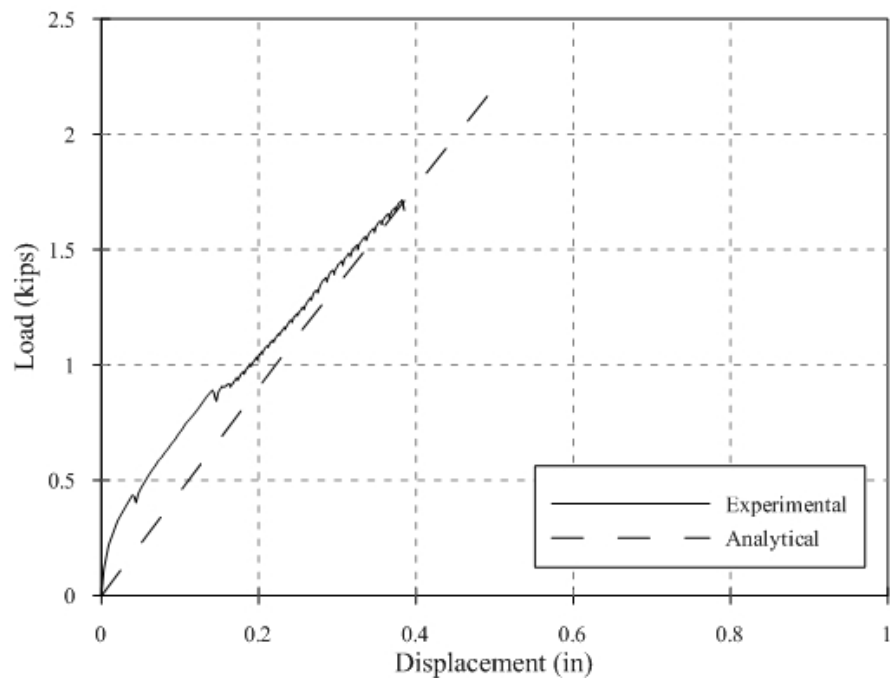


Clamped Condition

Figure 27: Flexural Bending Behavior of Sandwich Plate from Link 25DN1_1000

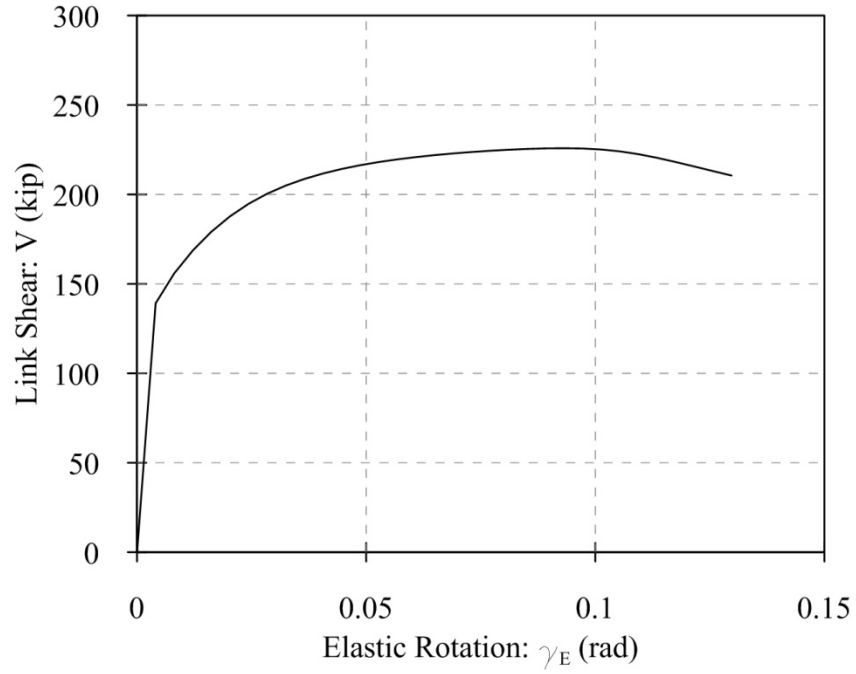


Unclamped Condition

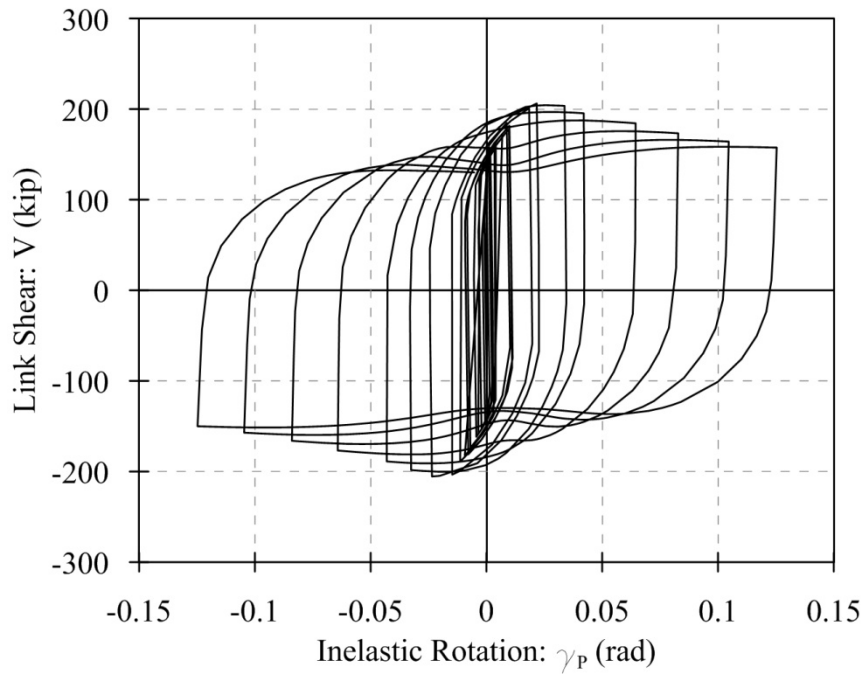


Clamped Condition

Figure 28: Flexural Bending Behavior of Sandwich Plate from Link 25DN3_1000

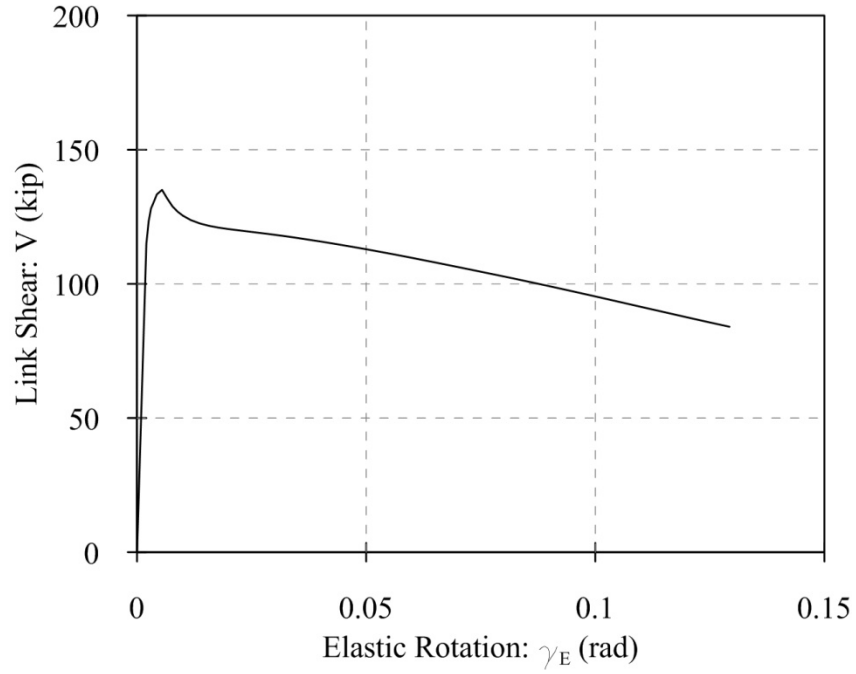


(a)

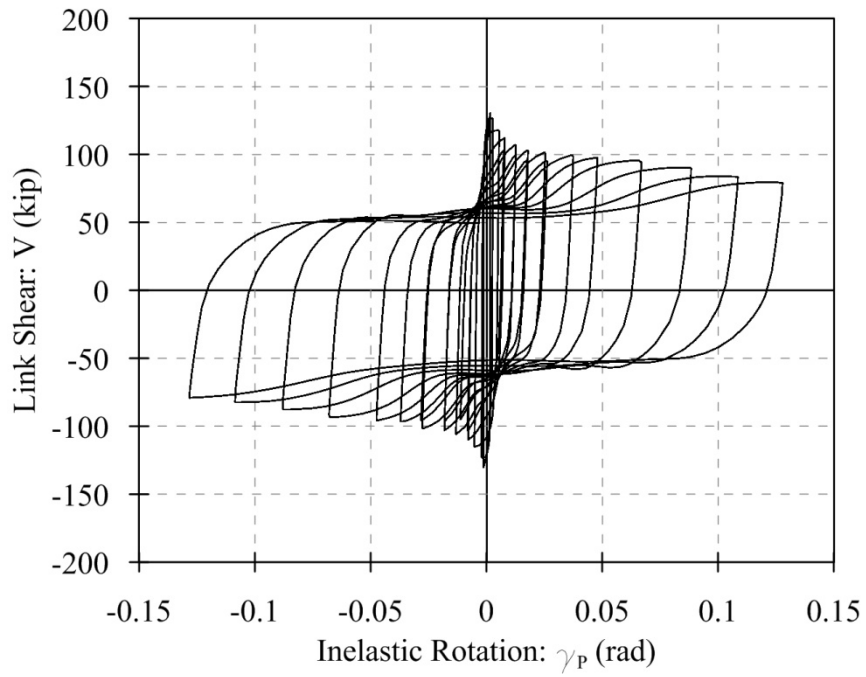


(b)

Figure 29: Analytic (a) Monotonic and (b) Cyclic Behaviors of Link 14DBase



(a)



(b)

Figure 30: Analytic (a) Monotonic and (b) Hysteretic Behaviors of Link 25DBase

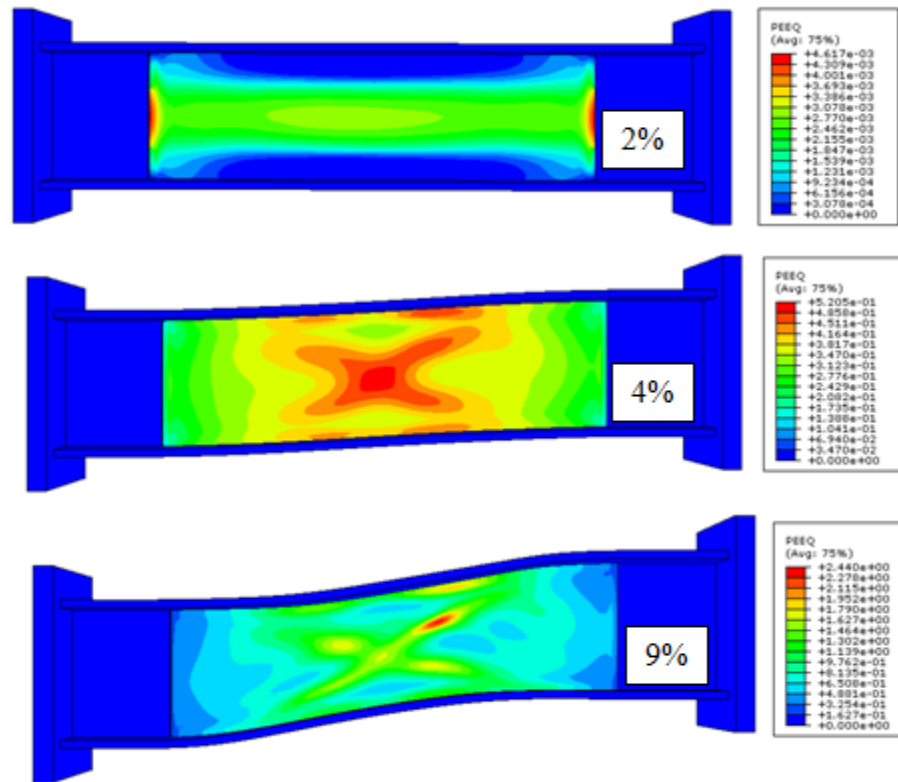


Figure 31: Web Strain Distribution in Link 14DBase

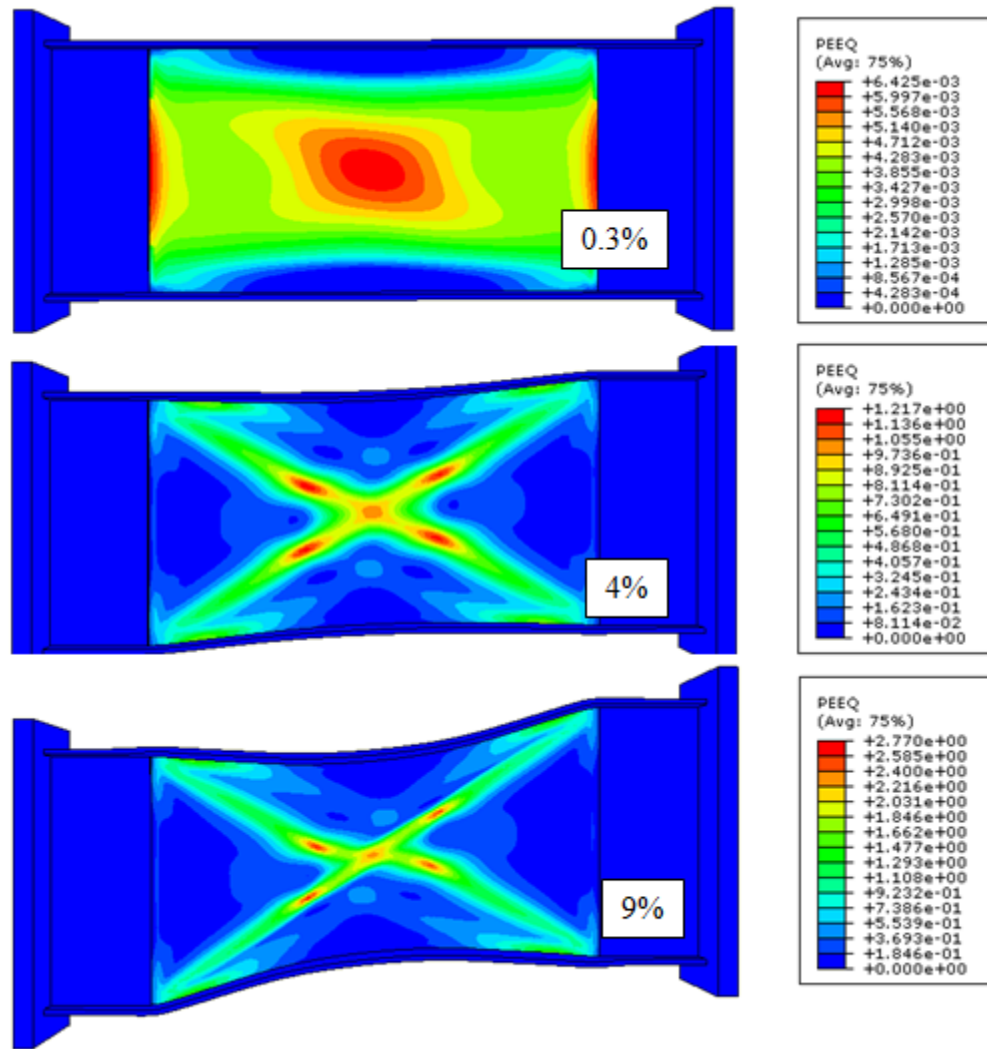
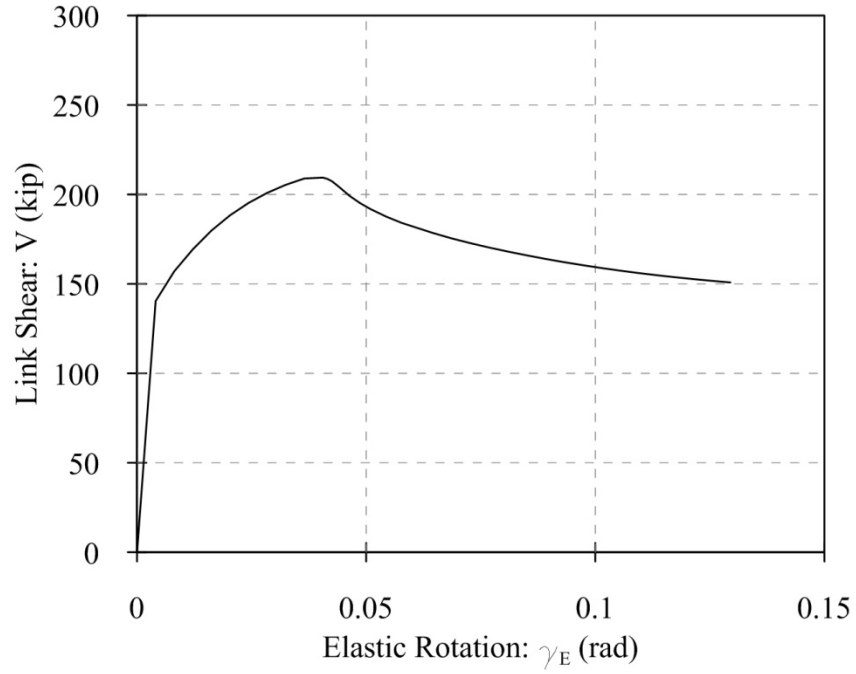
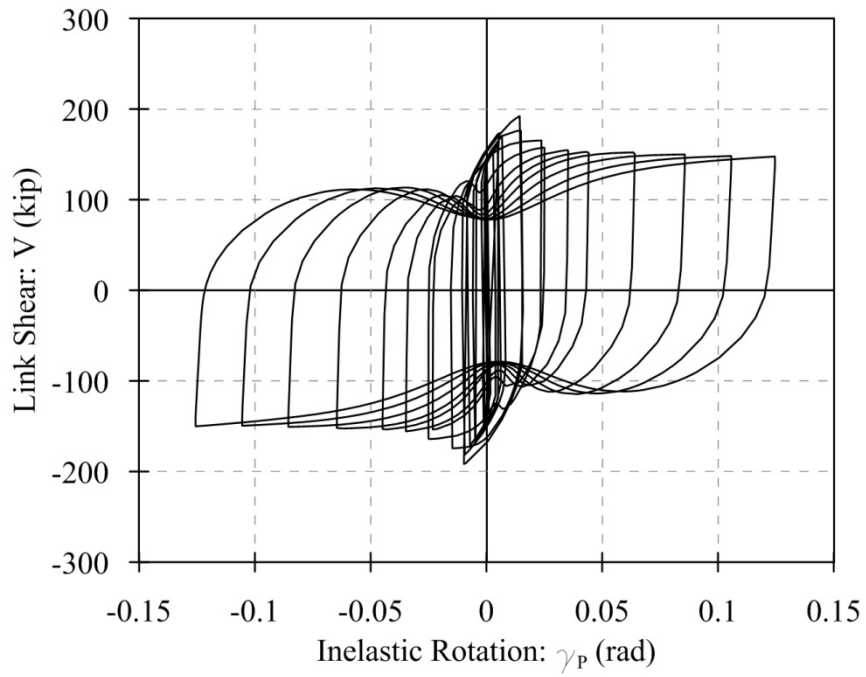


Figure 32: Web Strain Distribution in Link 25DBase

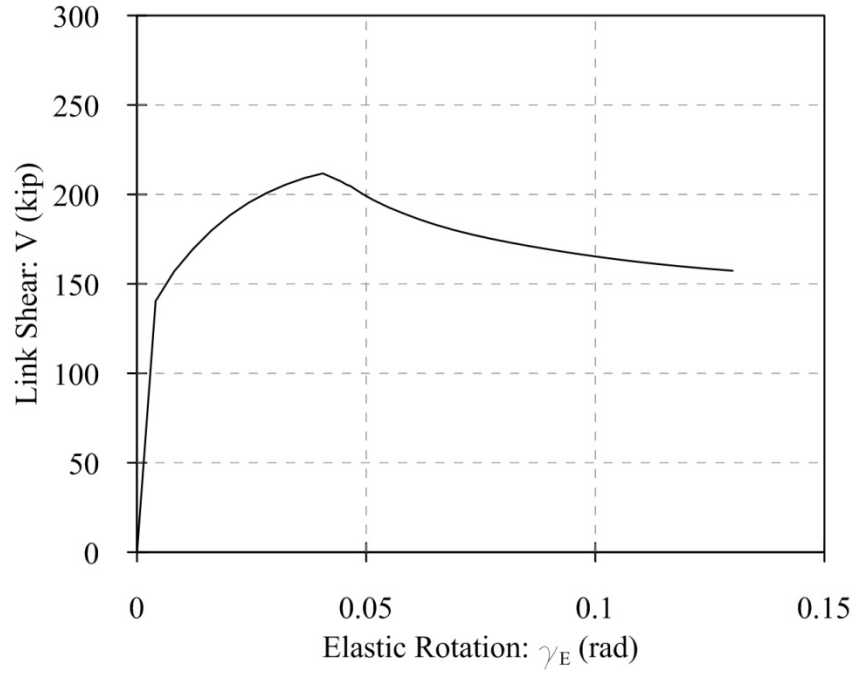


(a)

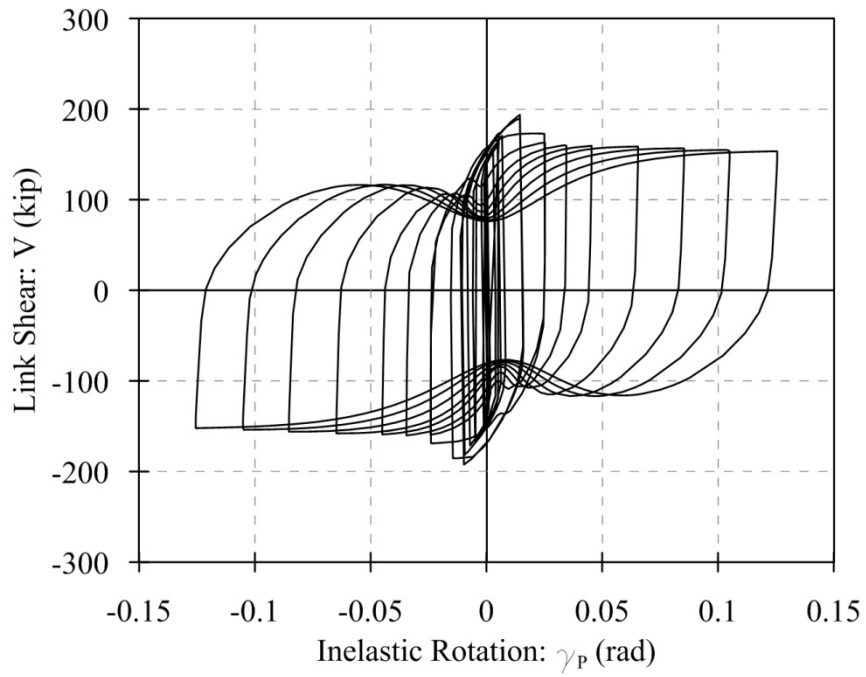


(b)

Figure 33: Analytic (a) Monotonic and (b) Hysteretic Behaviors of Link 14DN1_385

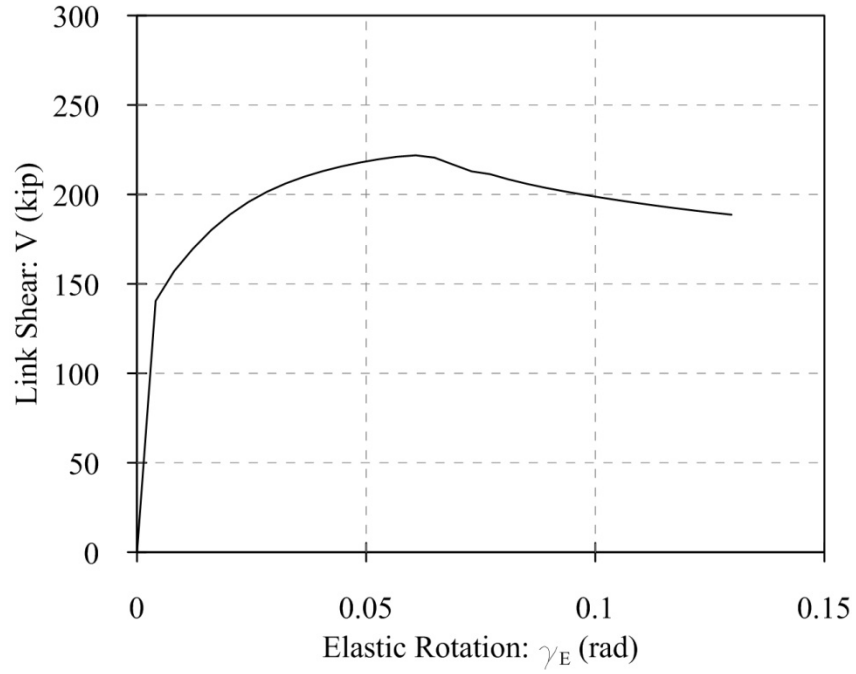


(a)

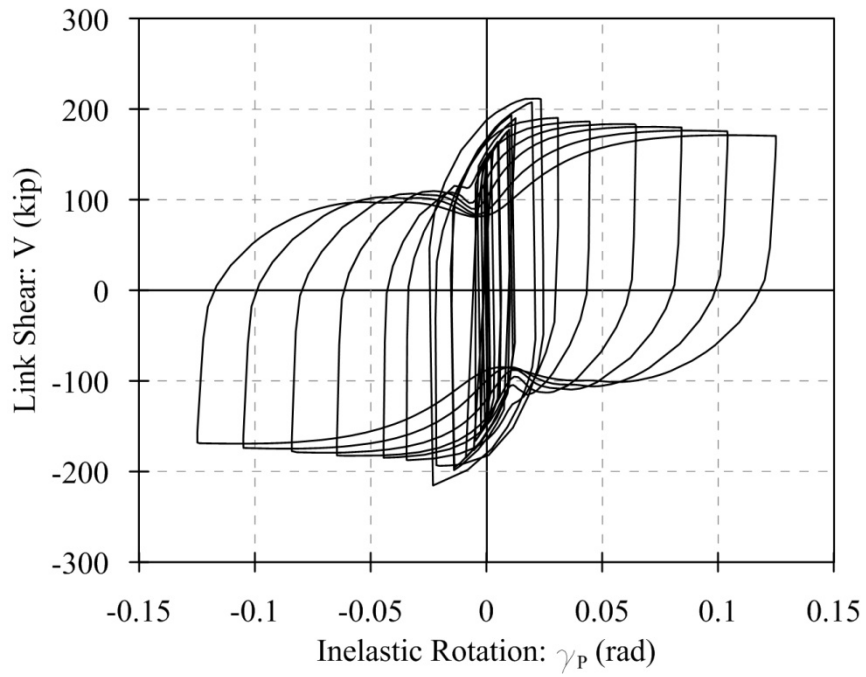


(b)

Figure 34: Analytic (a) Monotonic and (b) Hysteretic Behaviors of Link 14DN1_1000

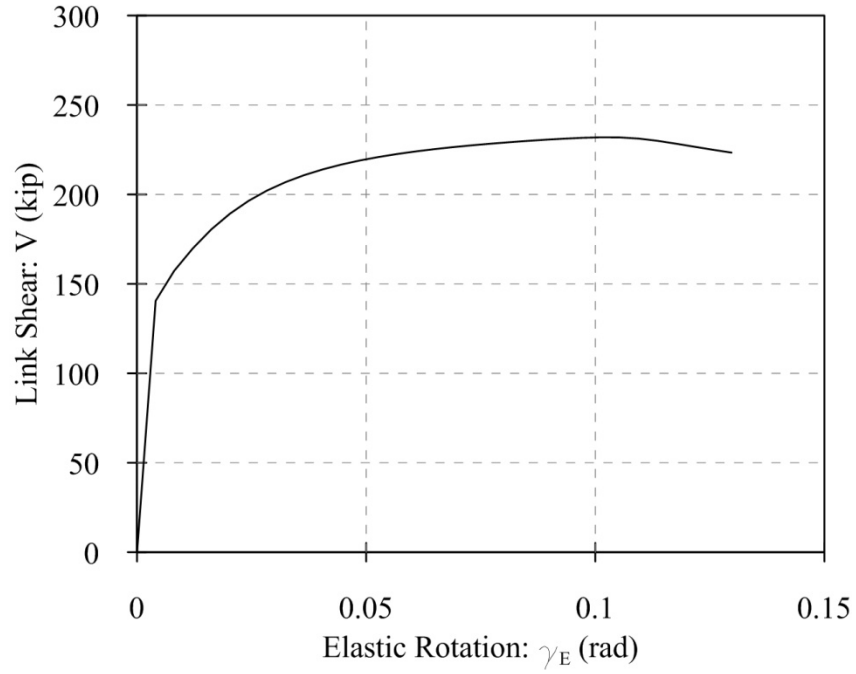


(a)

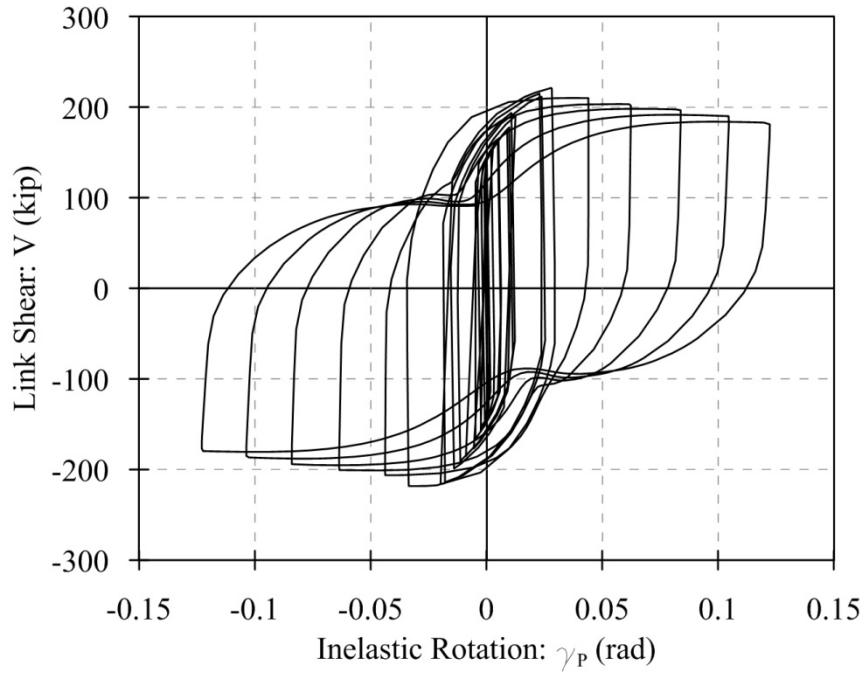


(b)

Figure 35: Analytic (a) Monotonic and (b) Hysteretic Behaviors of Link 14DN1_5000

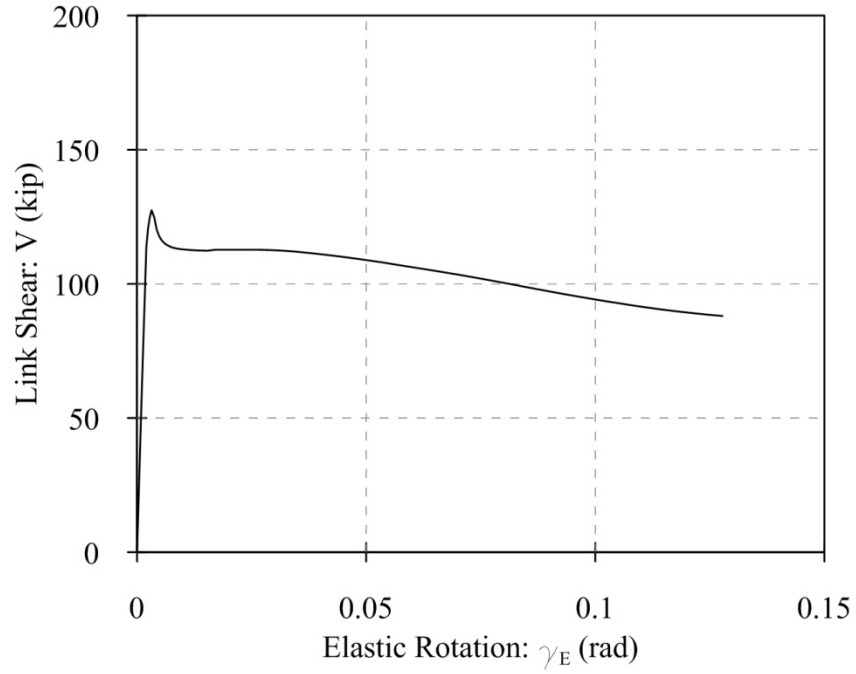


(a)

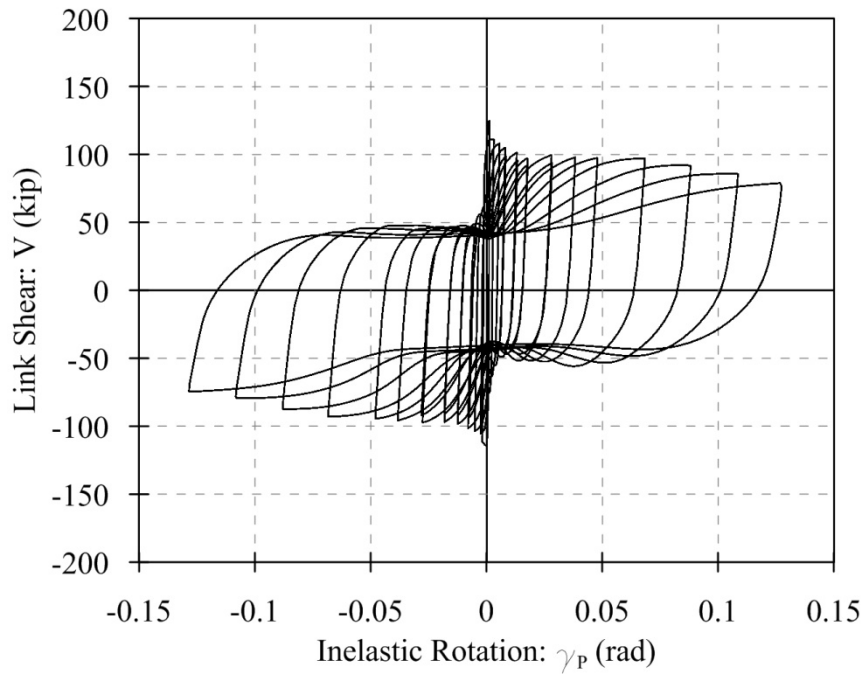


(b)

Figure 36: Analytic (a) Monotonic and (b) Hysteretic Behaviors of Link 14DN1_10000

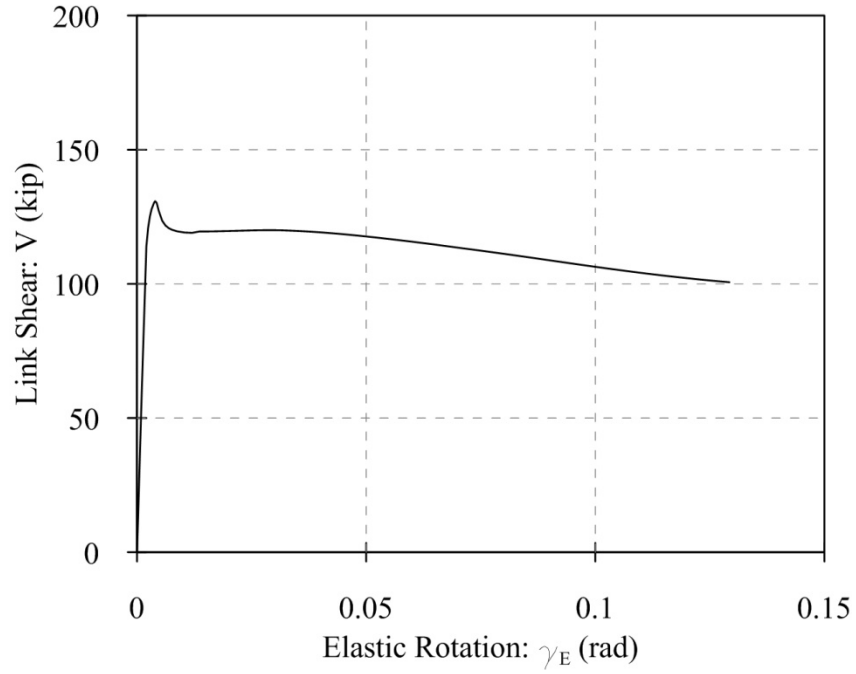


(a)

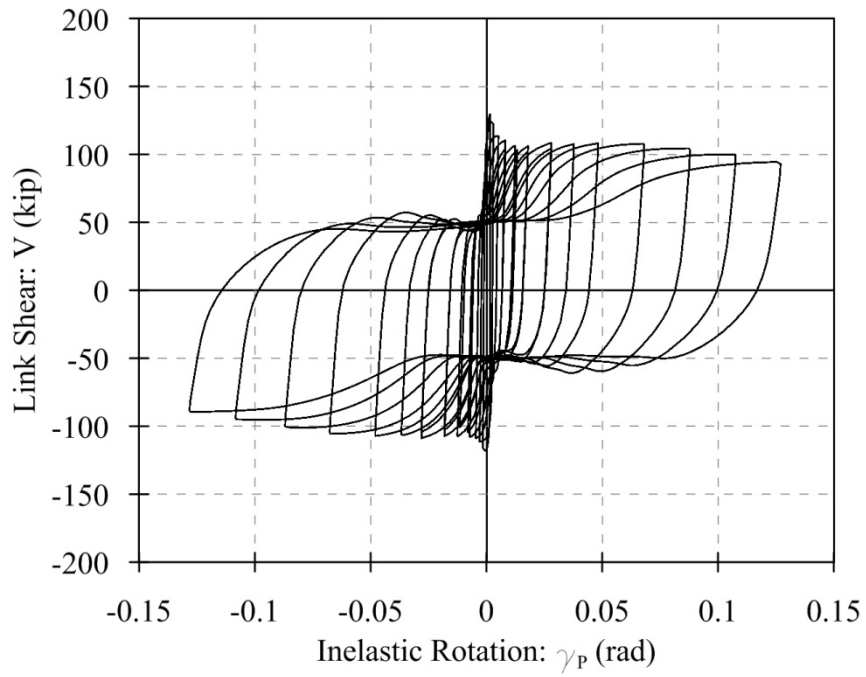


(b)

Figure 37: Analytic (a) Monotonic and (b) Hysteretic Behaviors of Link 25DN1_385

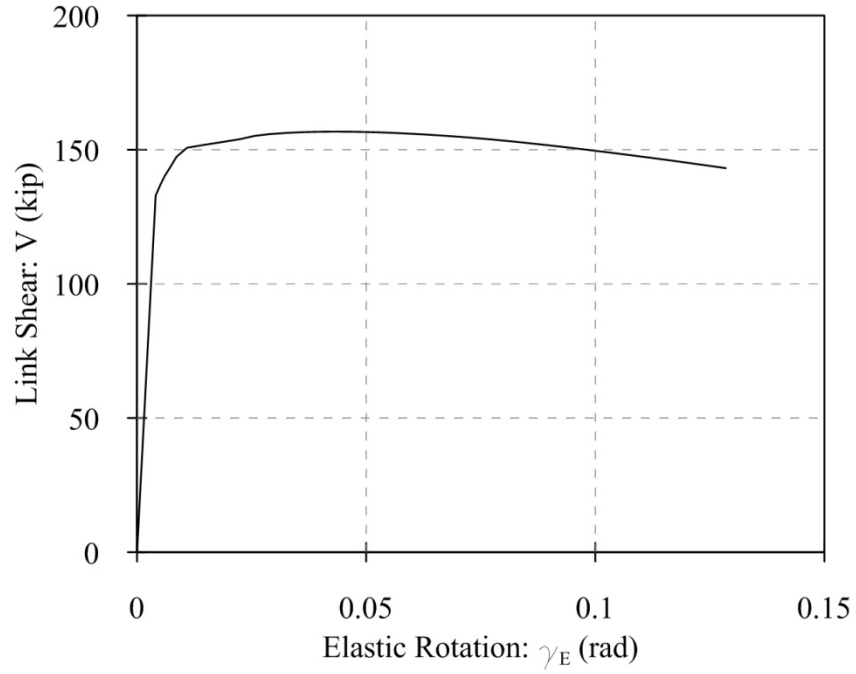


(a)

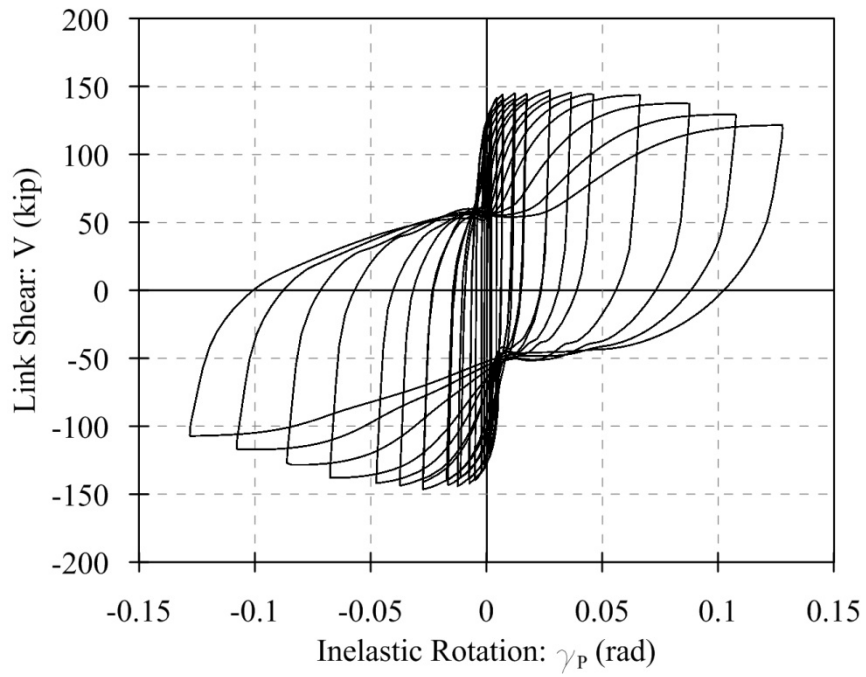


(b)

Figure 38: Analytic (a) Monotonic and (b) Hysteretic Behaviors of Link 25DN1_1000

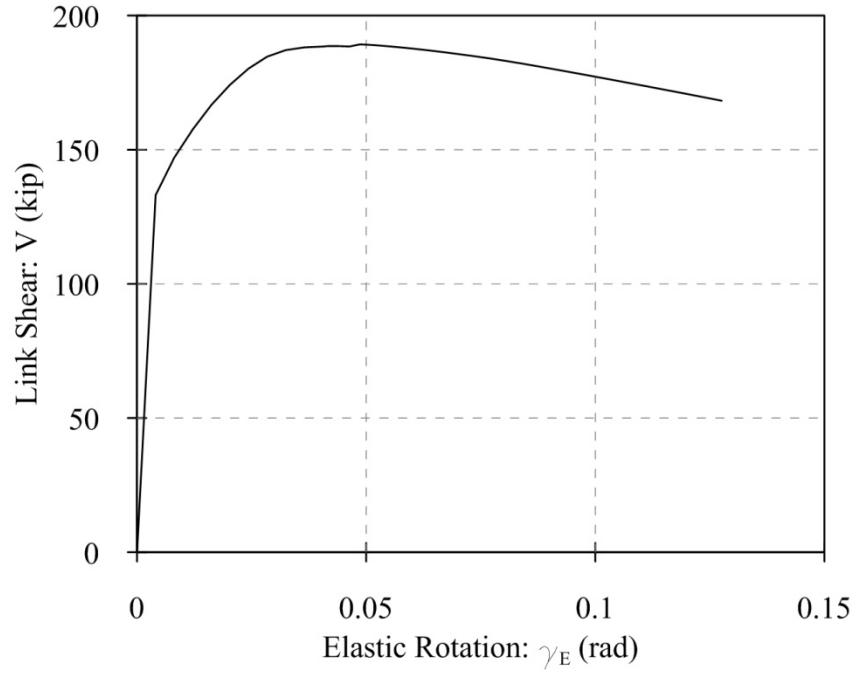


(a)

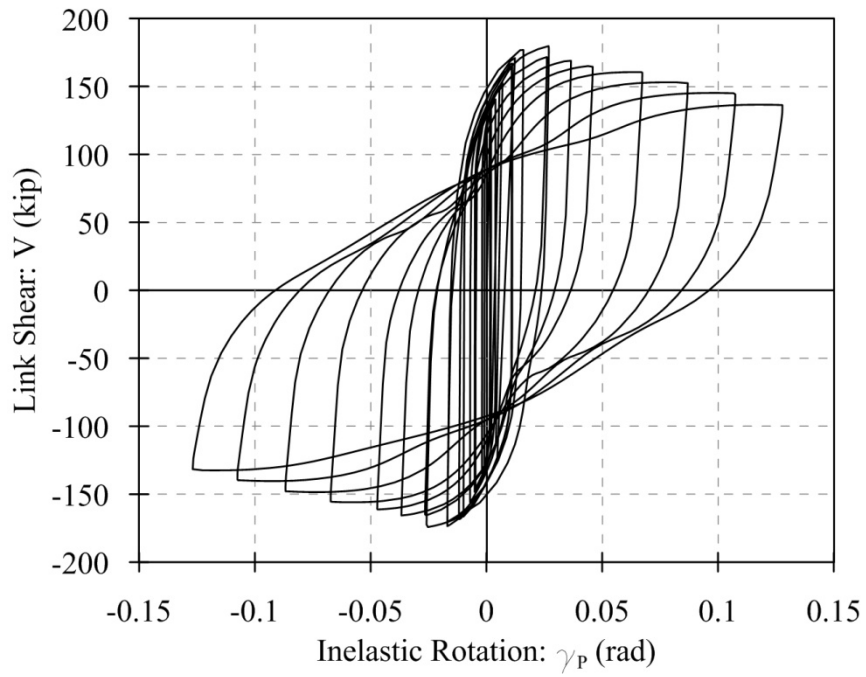


(b)

Figure 39: Analytic (a) Monotonic and (b) Hysteretic Behaviors of Link 25DN1_5000



(a)



(b)

Figure 40: Analytic (a) Monotonic and (b) Hysteretic Behaviors of Link 25DN1_10000

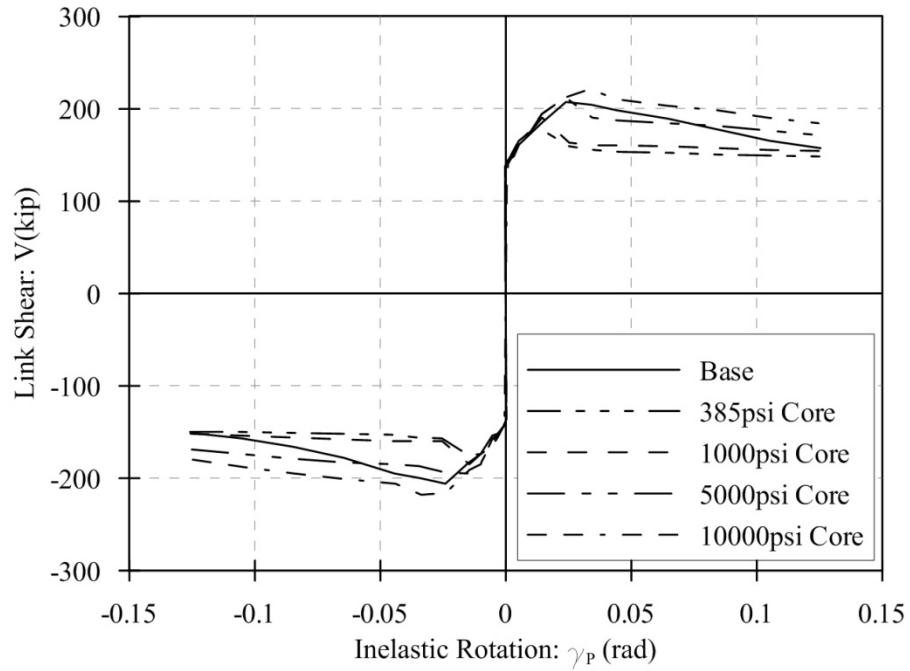


Figure 41: Core Stiffness Parameter Back Bone Analysis for 14in Deep Links

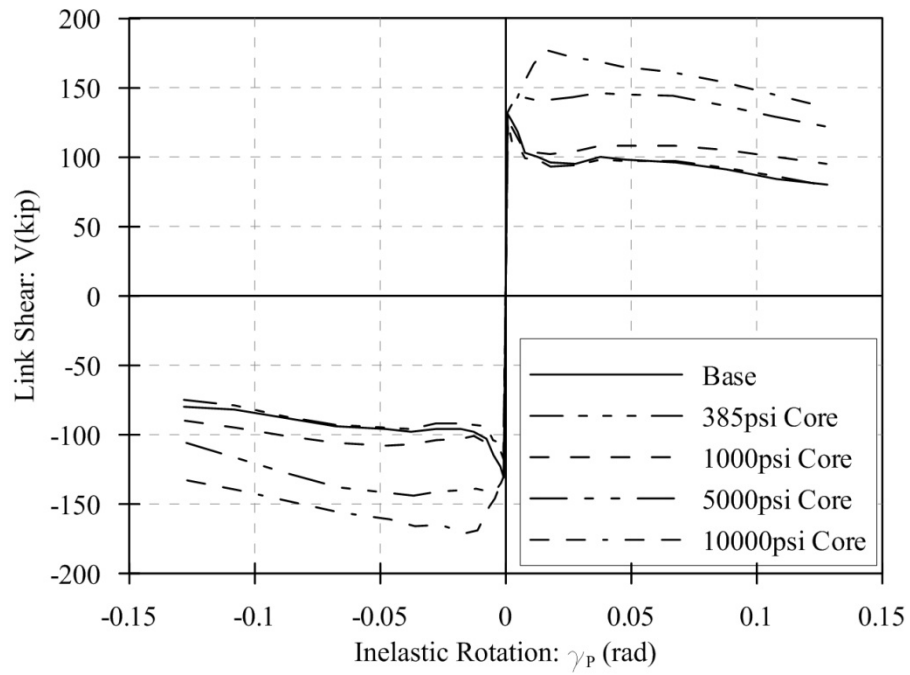


Figure 42: Core Stiffness Parameter Back Bone Analysis for 25in Deep Links

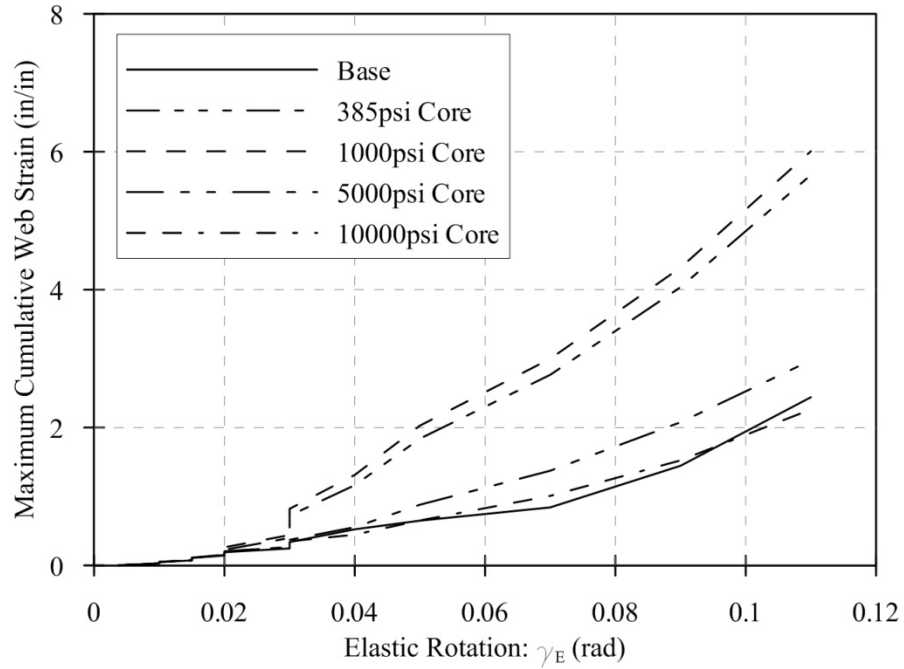


Figure 43: Core Stiffness Parameter Web Strain Analysis for 14in Deep Links

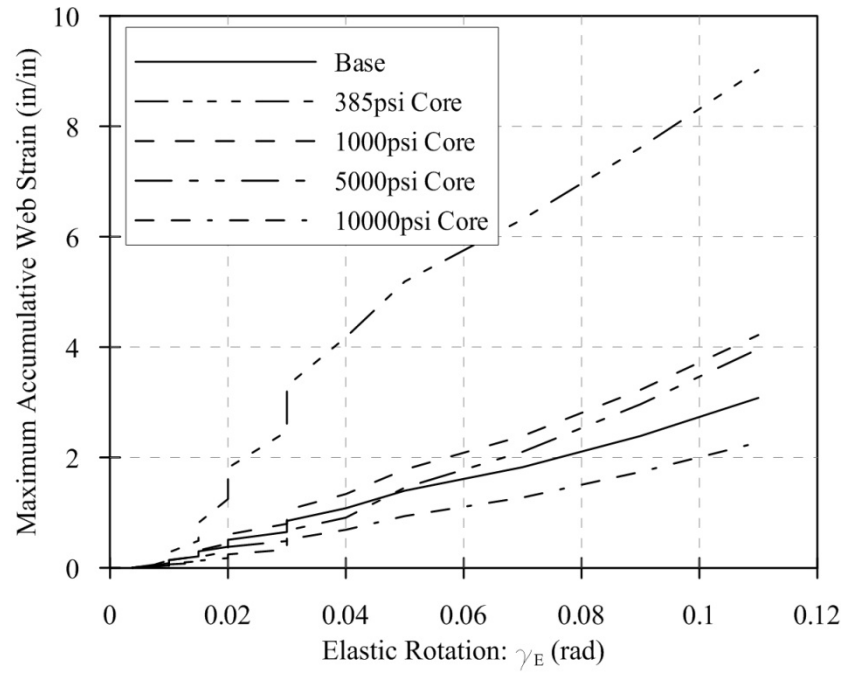
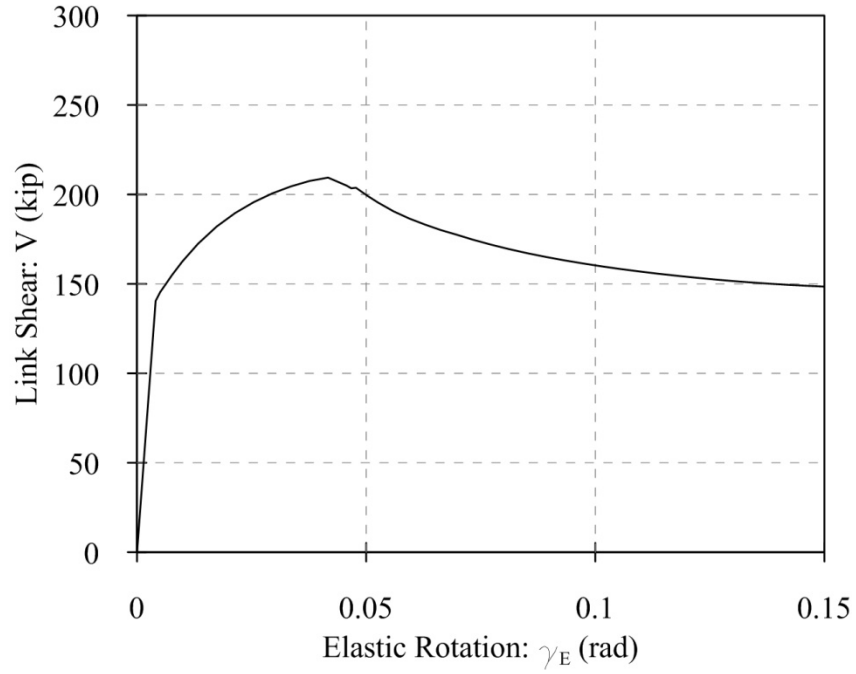
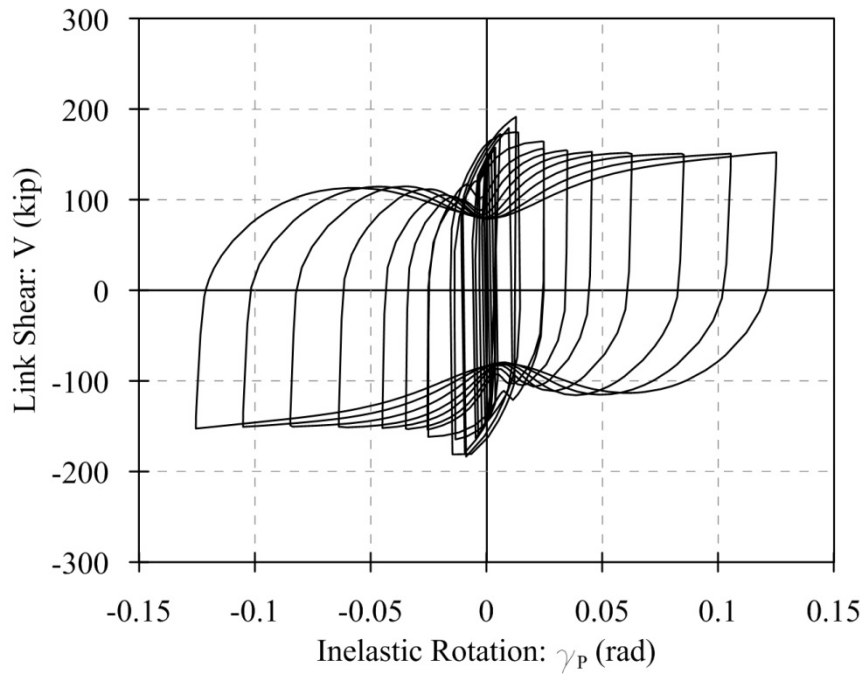


Figure 44: Core Stiffness Parameter Web Strain Analysis for 25in Deep Links

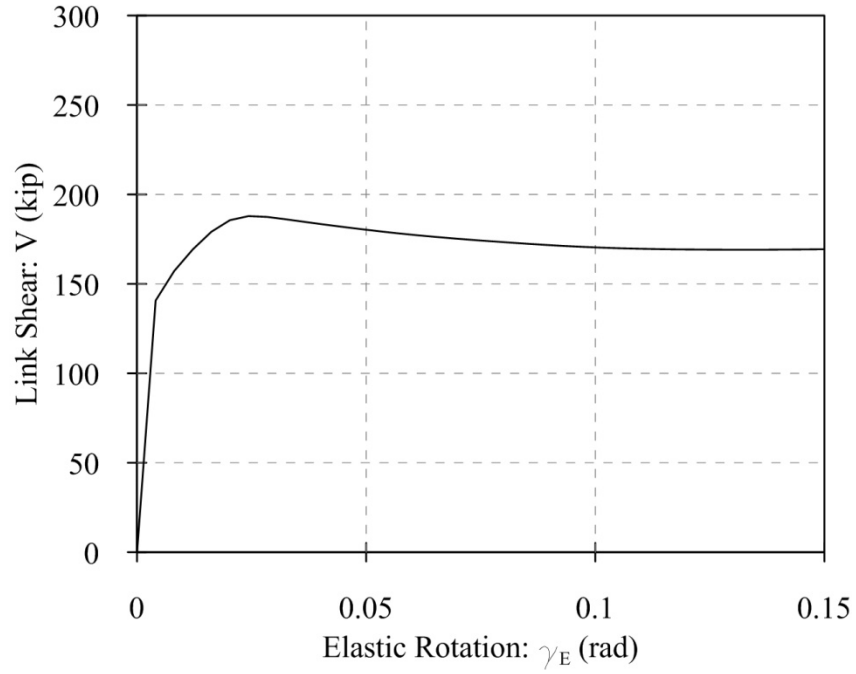


(a)

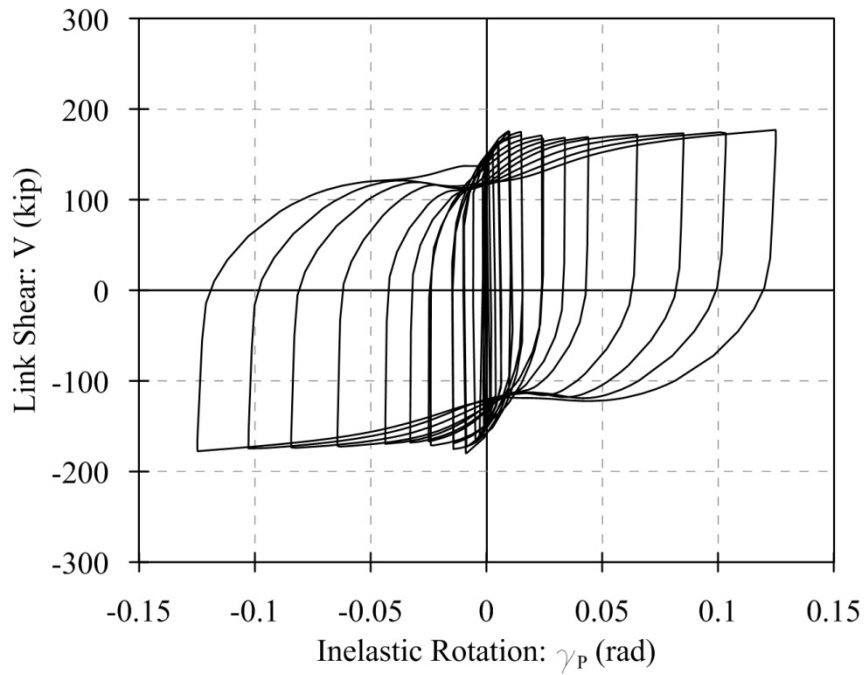


(b)

Figure 45: Analytic (a) Monotonic and (b) Hysteretic Behaviors of Link 14DN2_1000

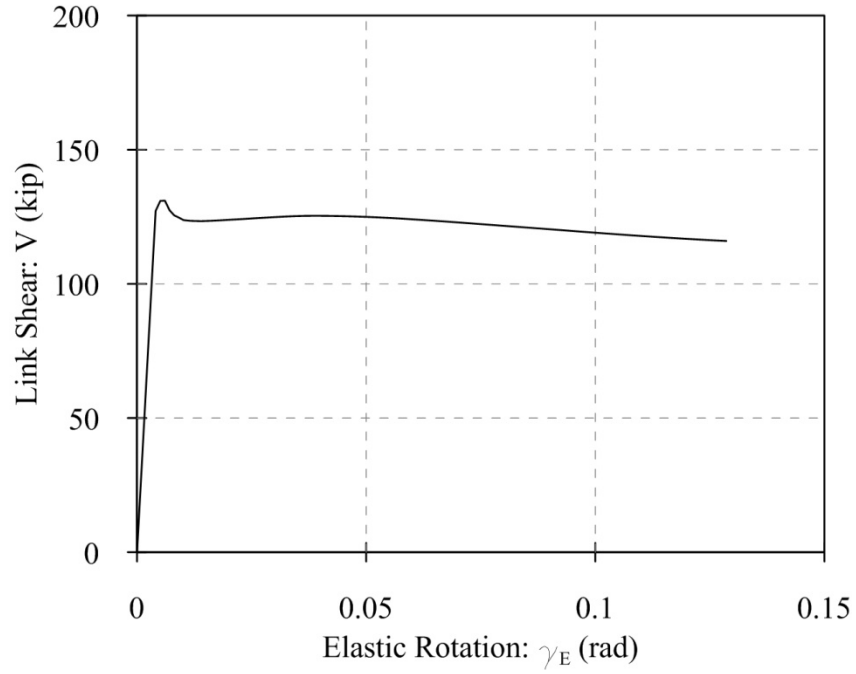


(a)

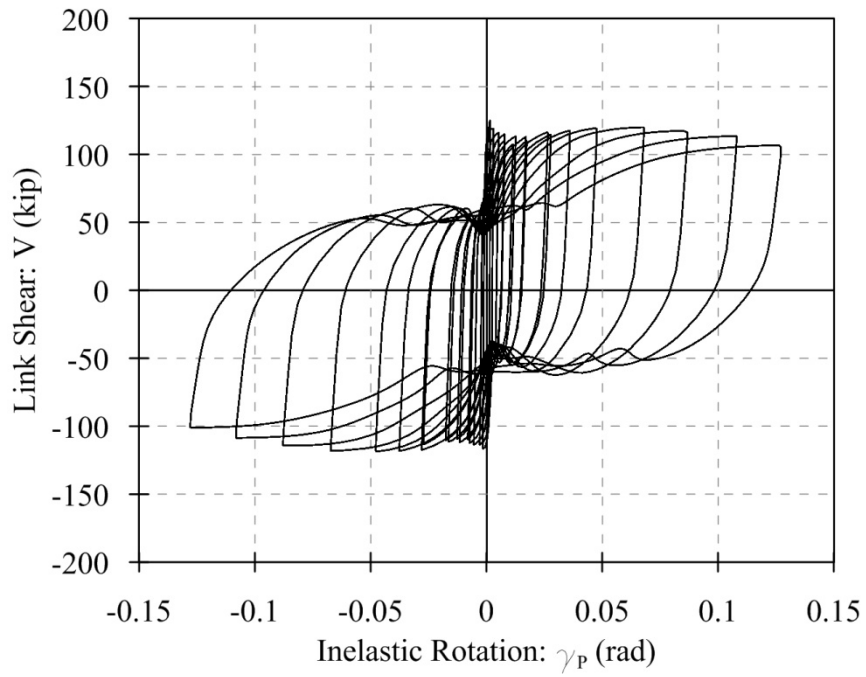


(b)

Figure 46: Analytic (a) Monotonic and (b) Hysteretic Behaviors of Link 14DN3_1000

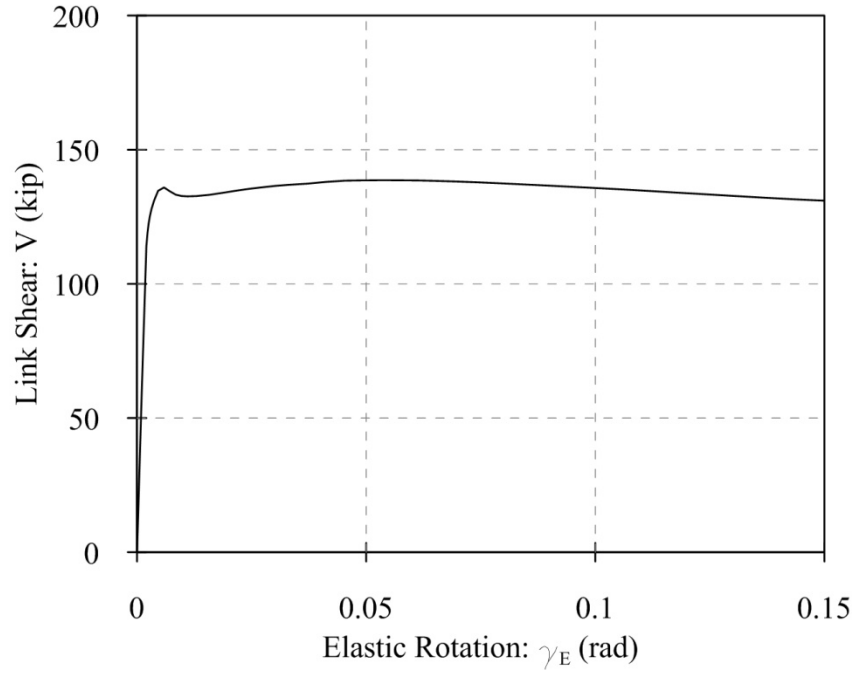


(a)

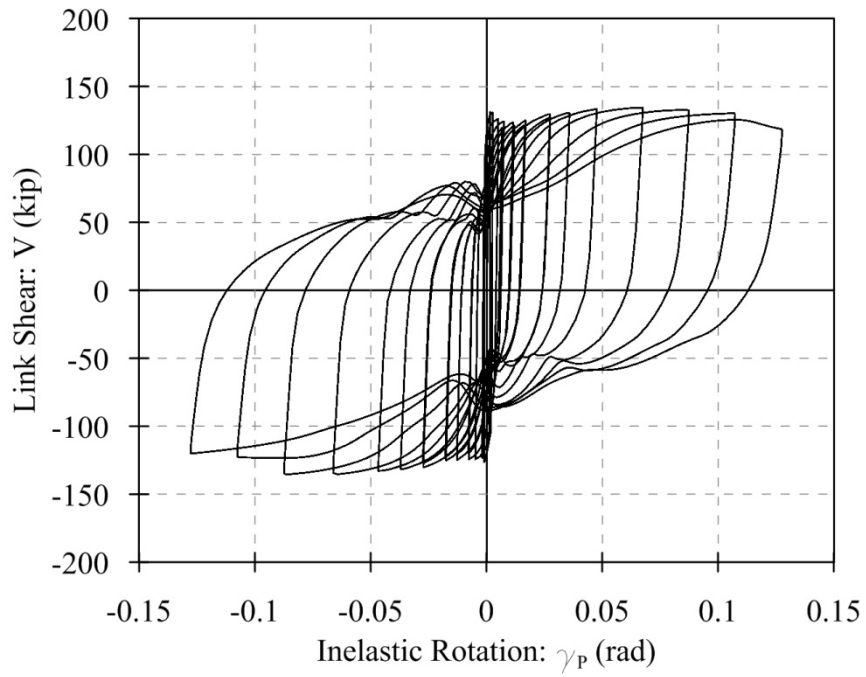


(b)

Figure 47: Analytic (a) Monotonic and (b) Hysteretic Behaviors of Link 25DN2_1000



(a)



(b)

Figure 48: Analytic (a) Monotonic and (b) Hysteretic Behaviors of Link 25DN3_1000

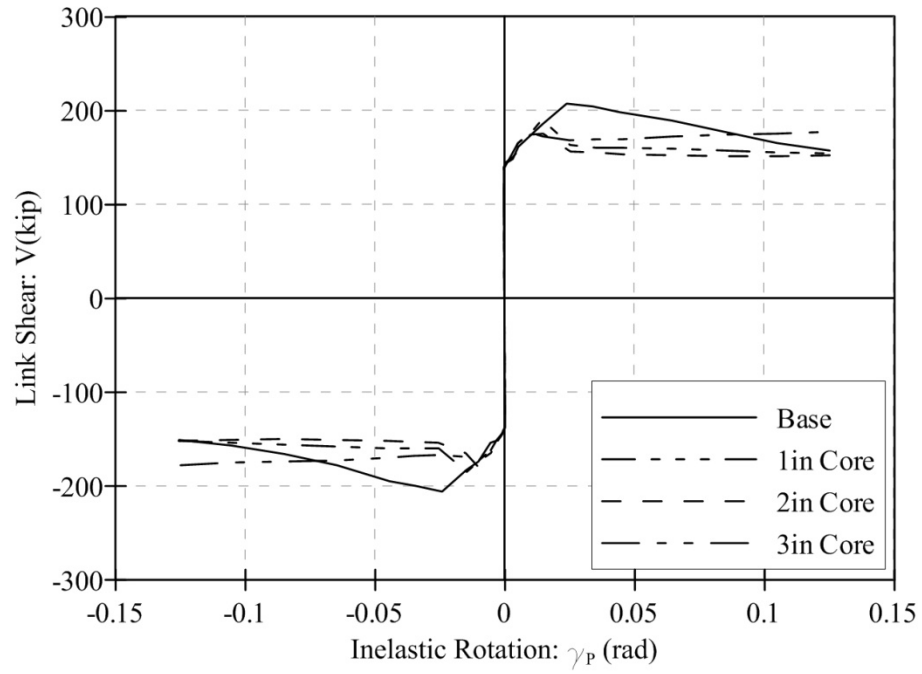


Figure 49: Core Thickness Parameter Back Bone Analysis for 14in Deep Links

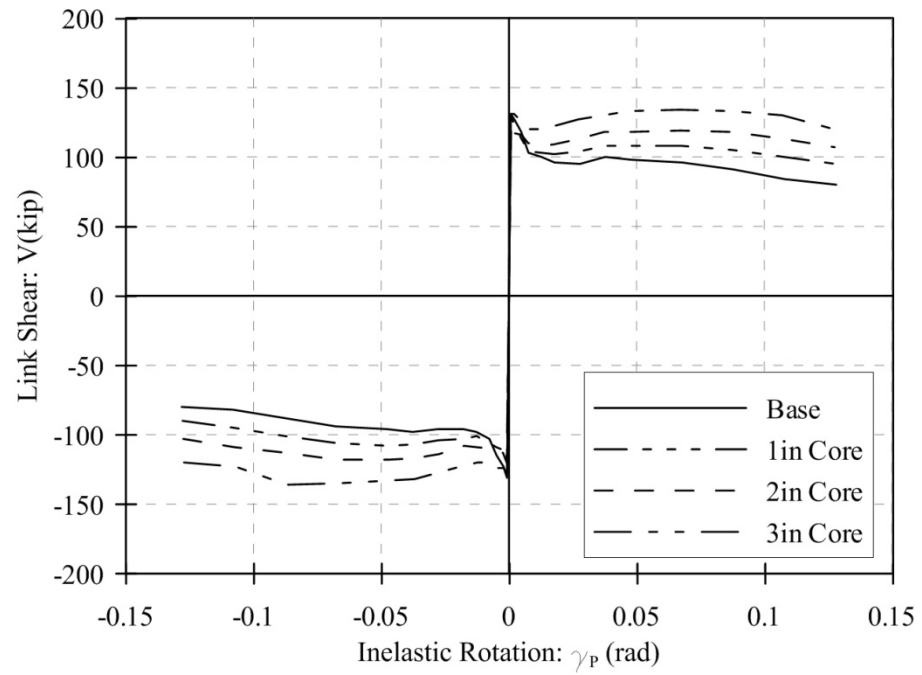


Figure 50: Core Thickness Parameter Back Bone Analysis for 25in Deep Links

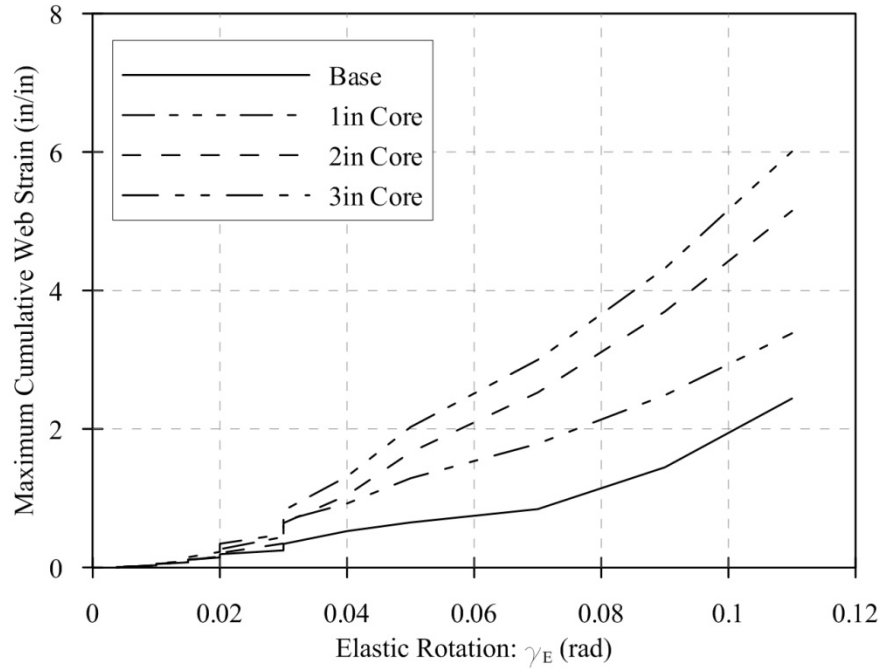


Figure 51: Core Thickness Parameter Web Strain Analysis for 14in Deep Links

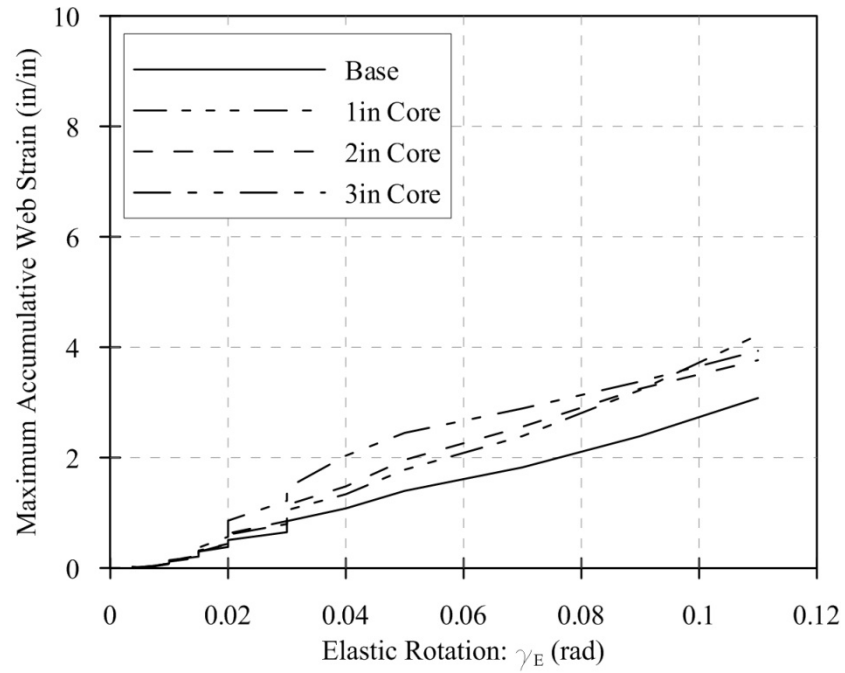


Figure 52: Core Thickness Parameter Web Strain Analysis for 25in Deep Links

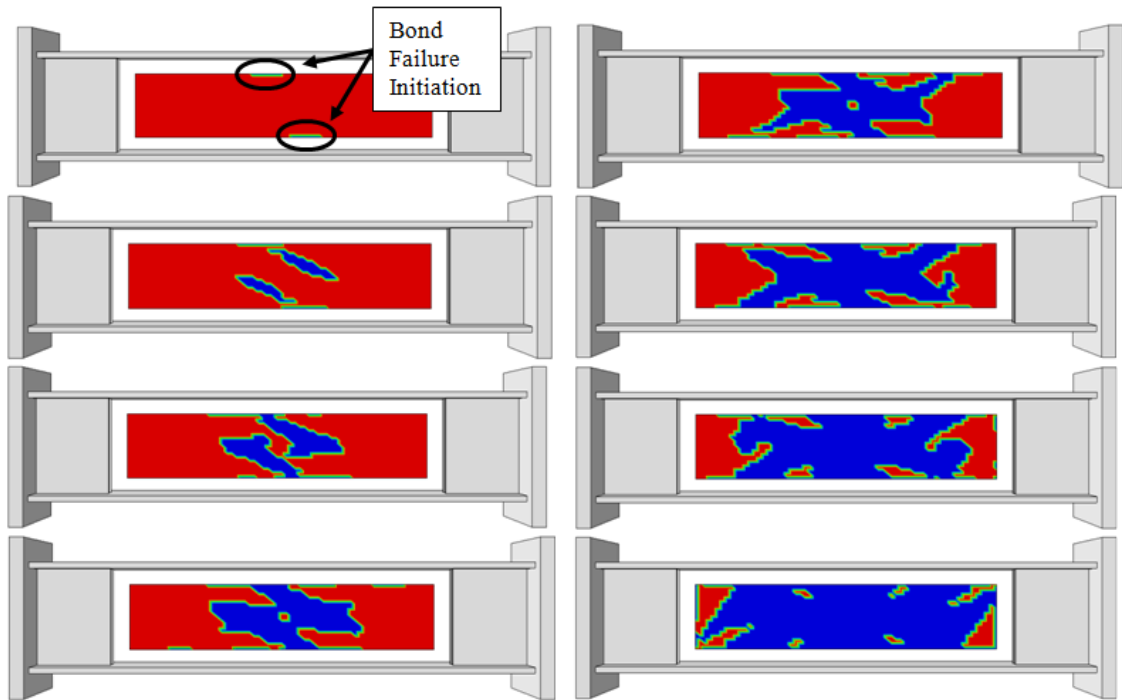


Figure 53: Debonding Propagation in Link 14DN1_1000

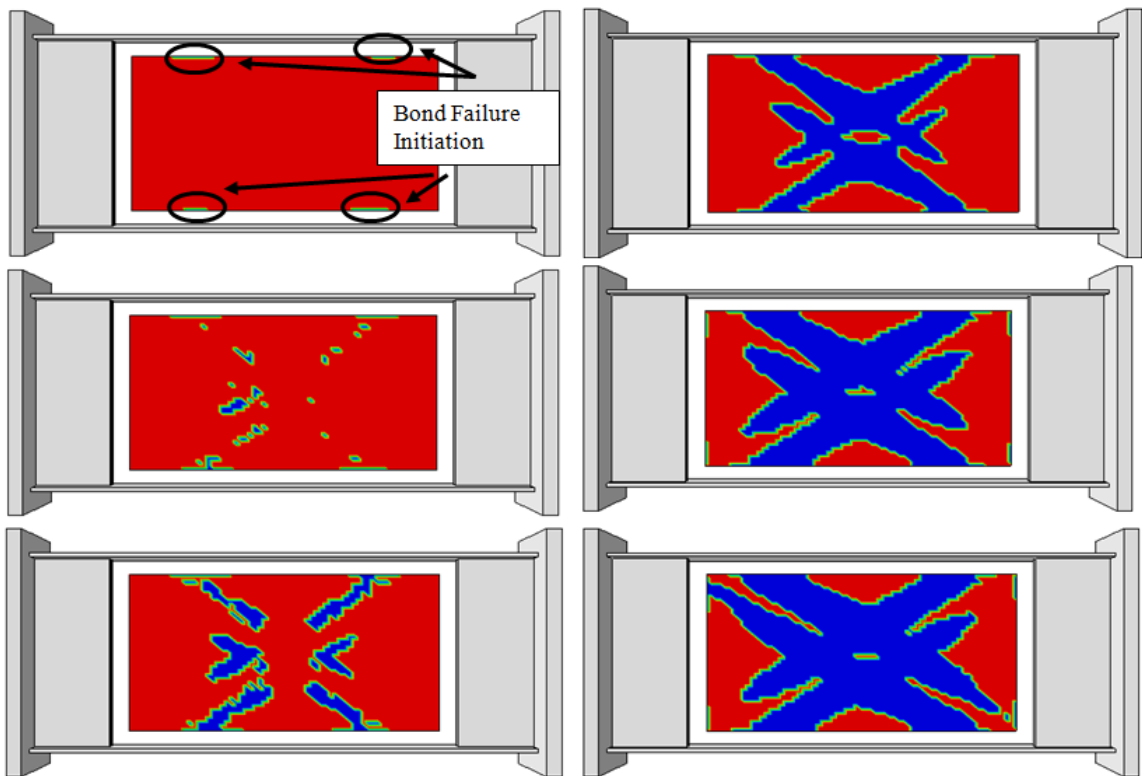


Figure 54: Debonding Propagation in Link 25DN1_1000

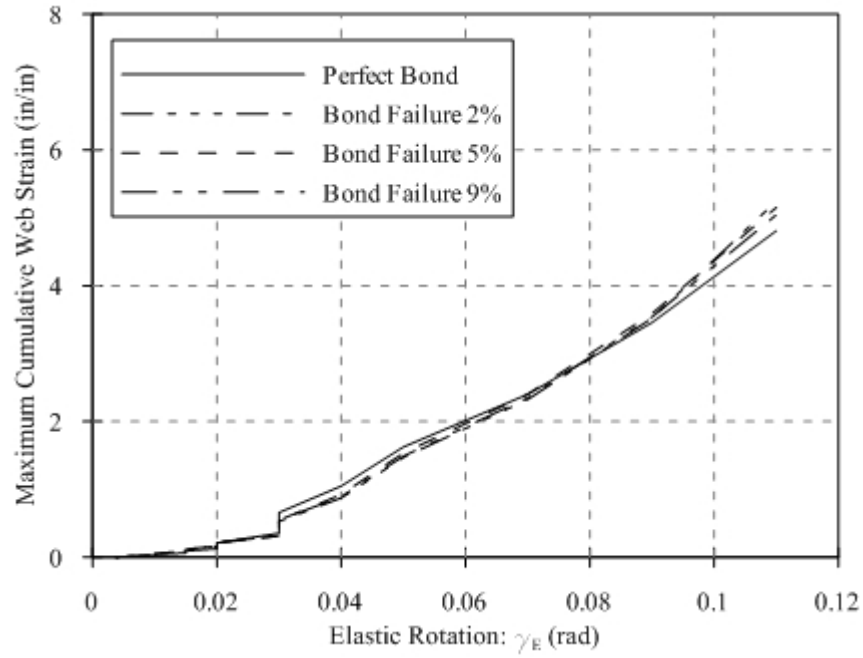


Figure 55: Debonding Parameter Web Strain Analysis for Link 14DN1_1000

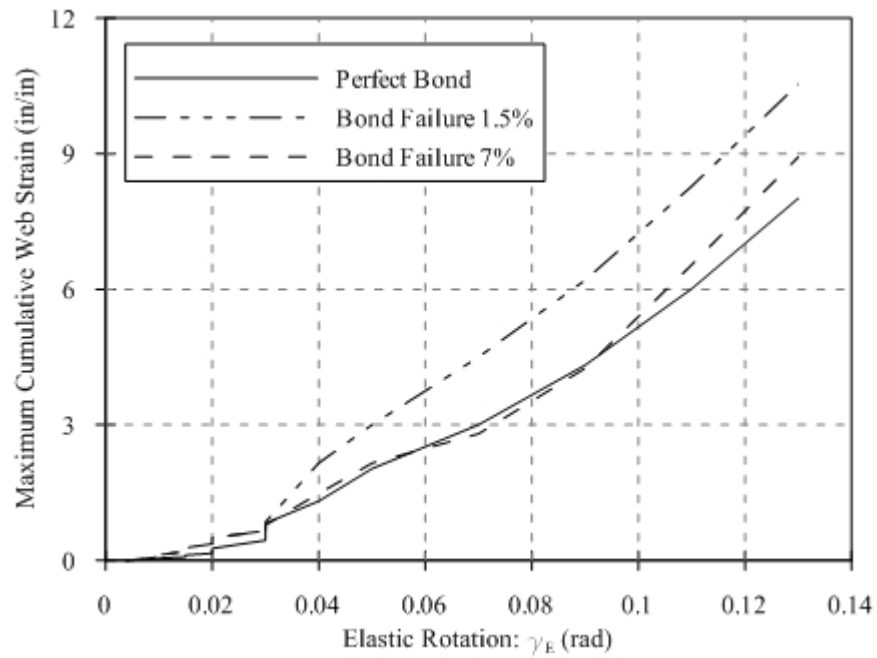


Figure 56: Debonding Parameter Web Strain Analysis for Link 25DN1_1000

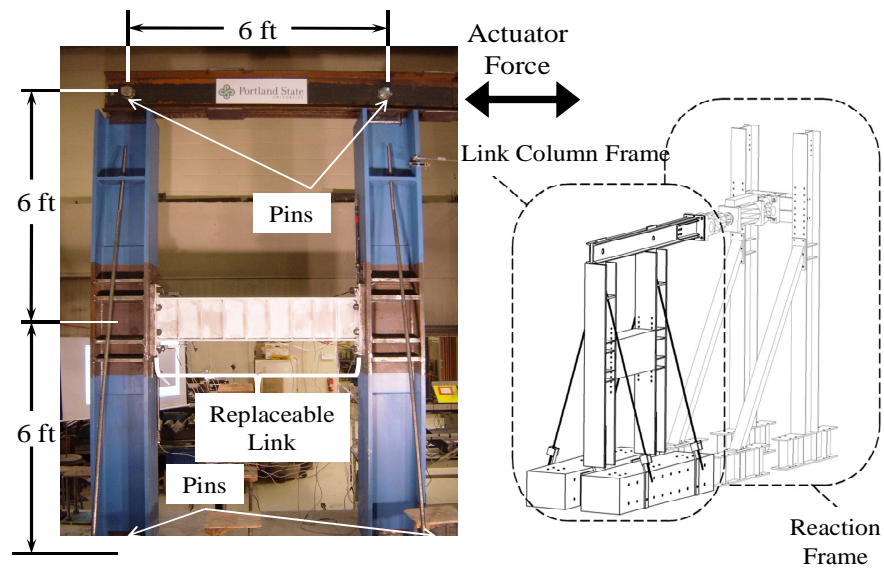


Figure 57: Experimental Apparatus (Lewis, 2010)

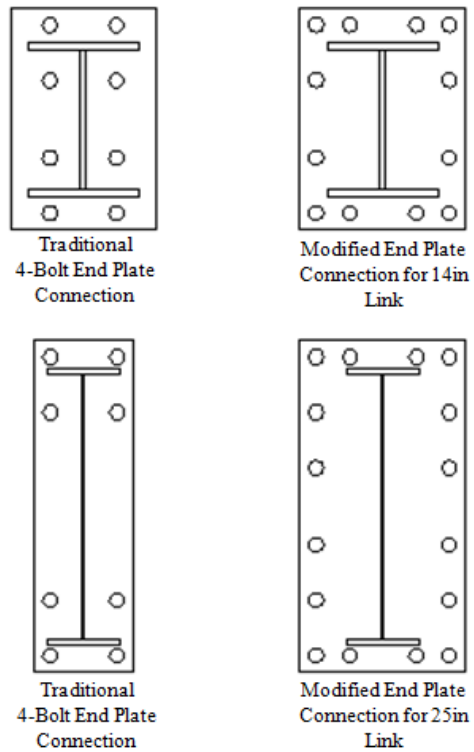


Figure 58: Traditional and Modified Bolted End Plate Connections

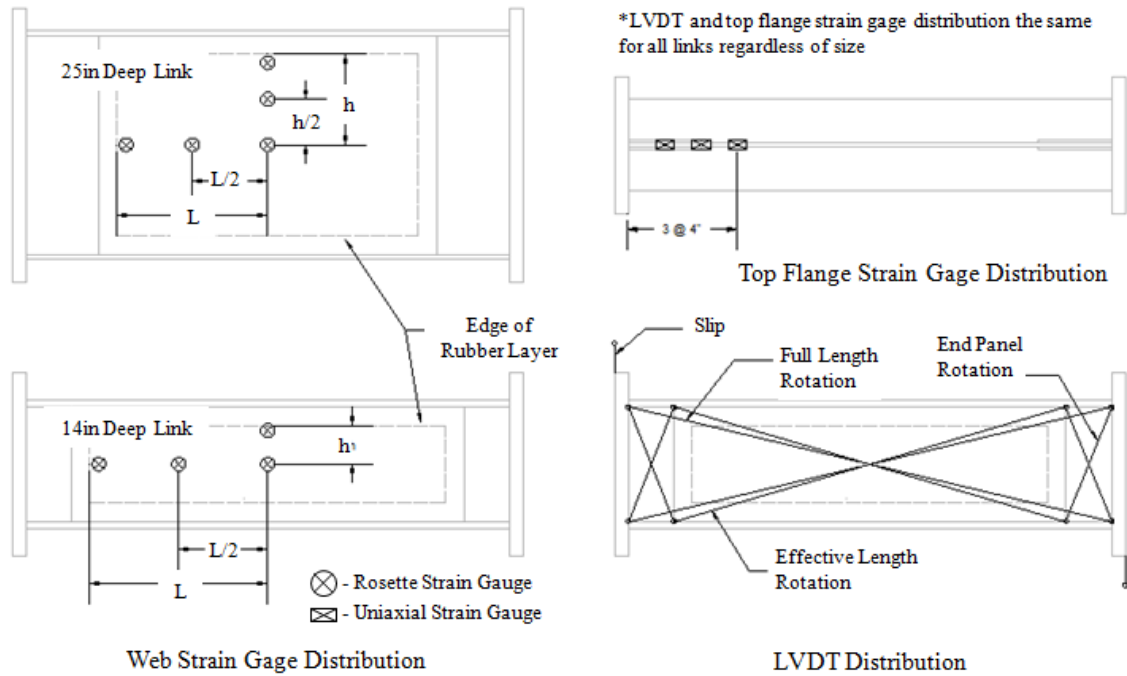


Figure 59: Instrumentation Schematic

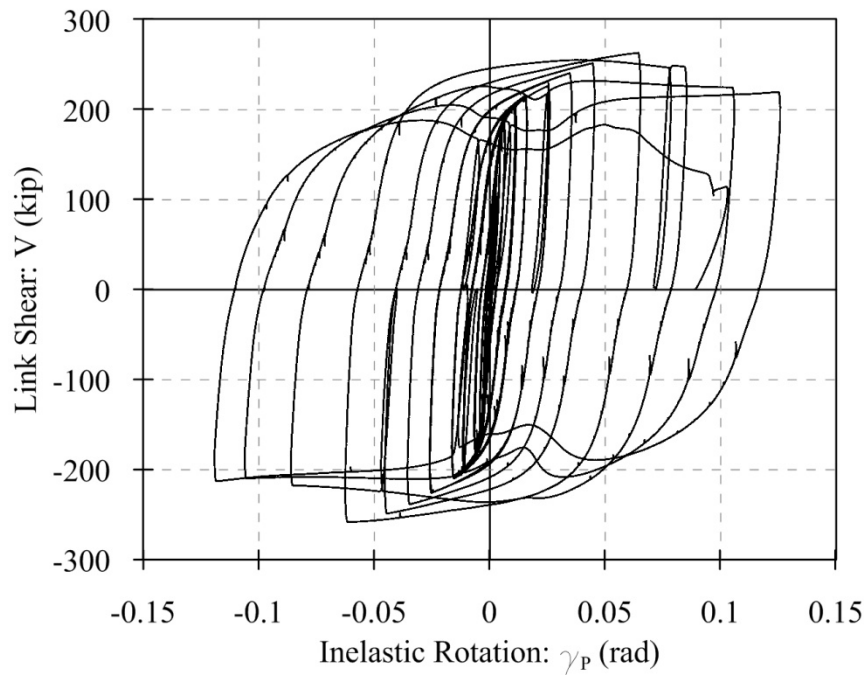


Figure 60: Experimental Hysteresis of Link 14DBase

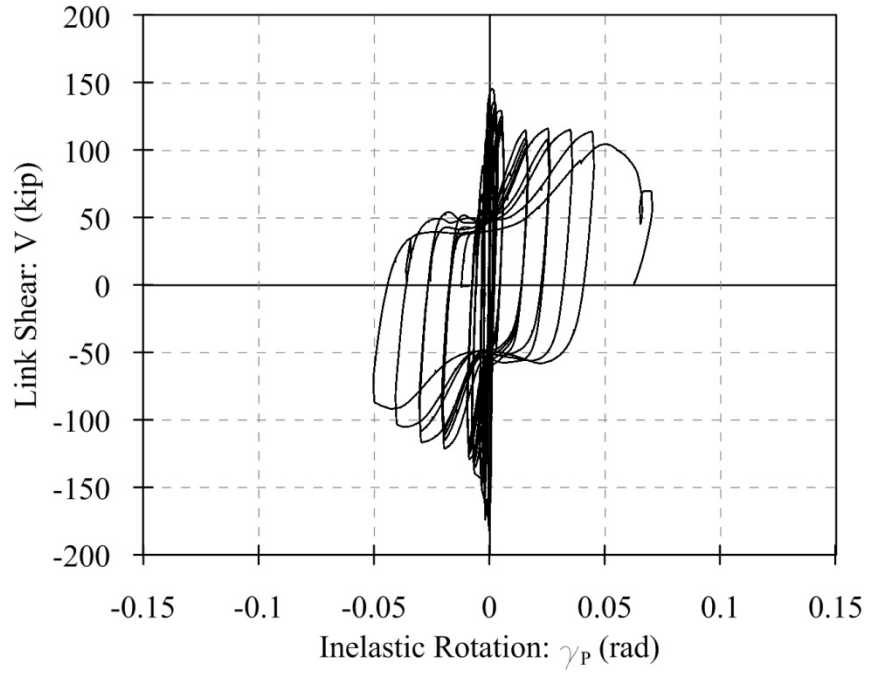


Figure 61: Experimental Hysteresis of Link 25DBase

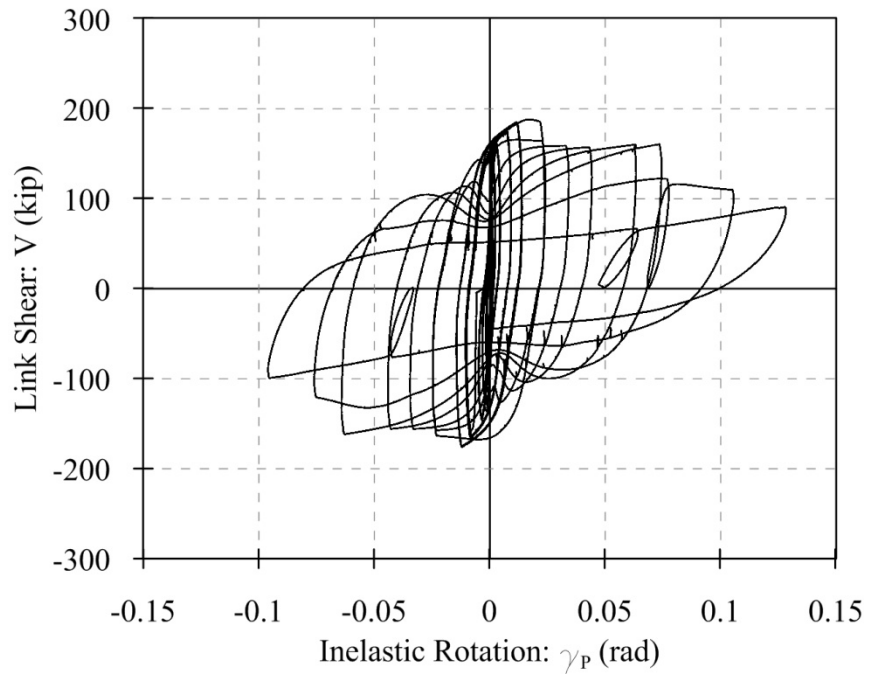


Figure 62: Experimental Hysteresis of Link 14DN3_1000

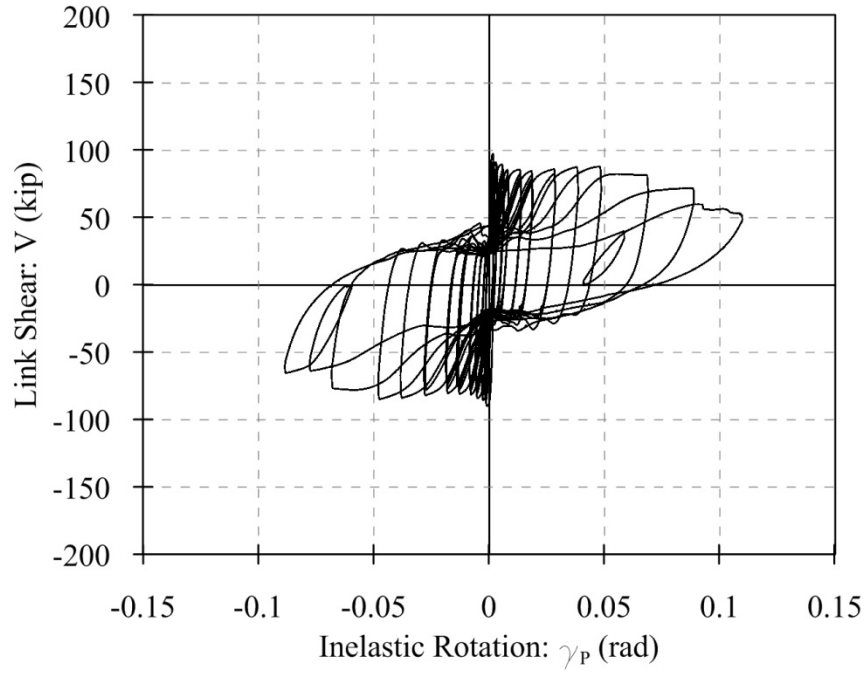


Figure 63: Experimental Hysteresis of Link 25DN1_1000

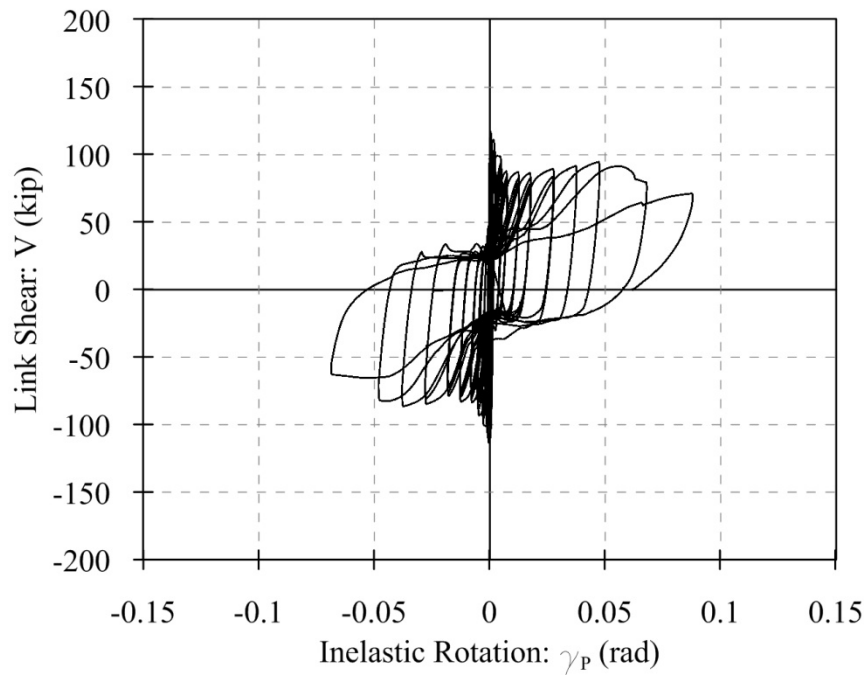


Figure 64: Experimental Hysteresis of Link 25DN3_1000

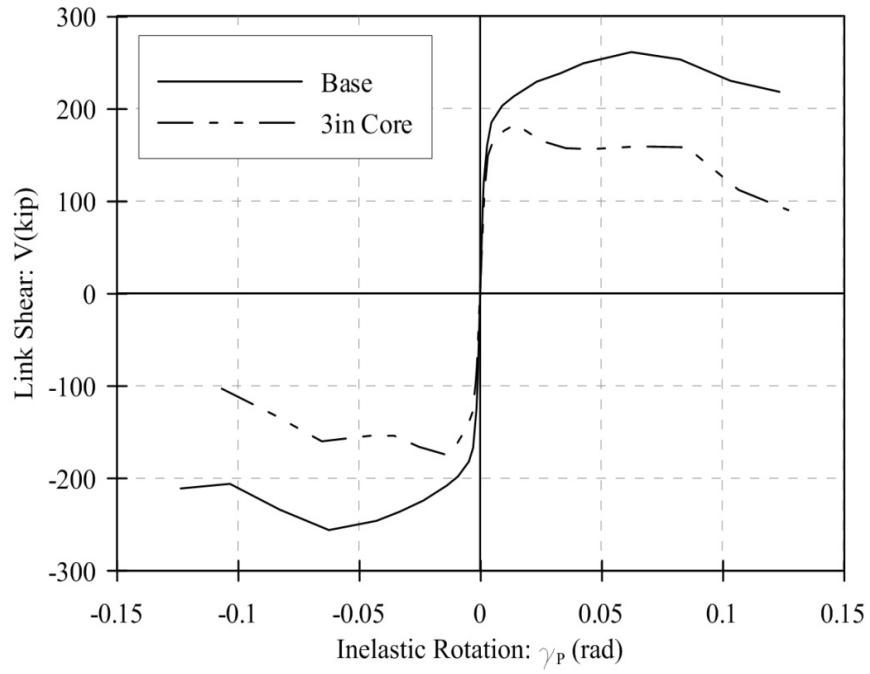


Figure 65: Experimental Back Bone Comparisons for 14in Deep Links

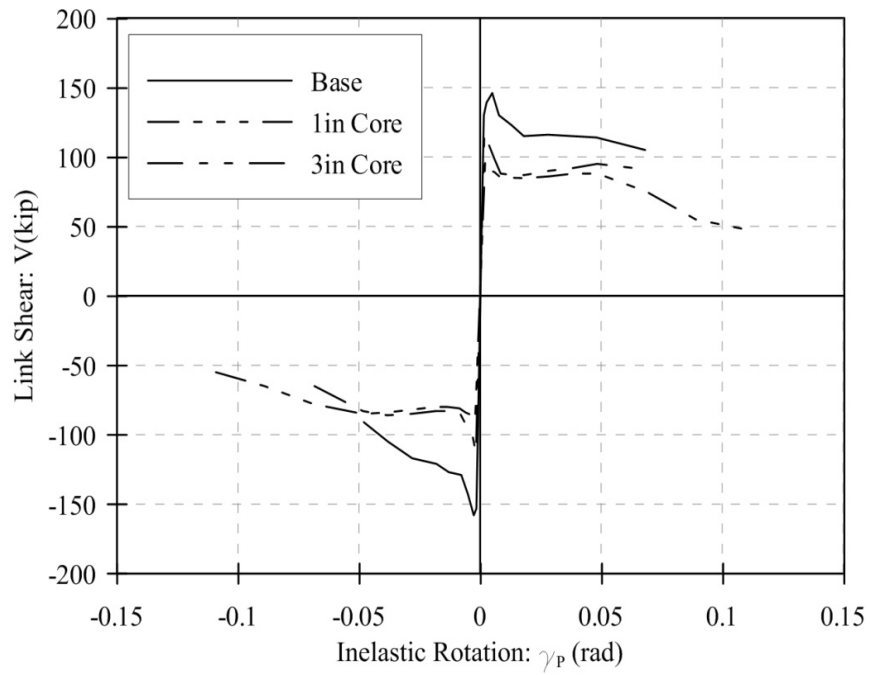


Figure 66: Experimental Back Bone Comparisons for 25in Deep Links

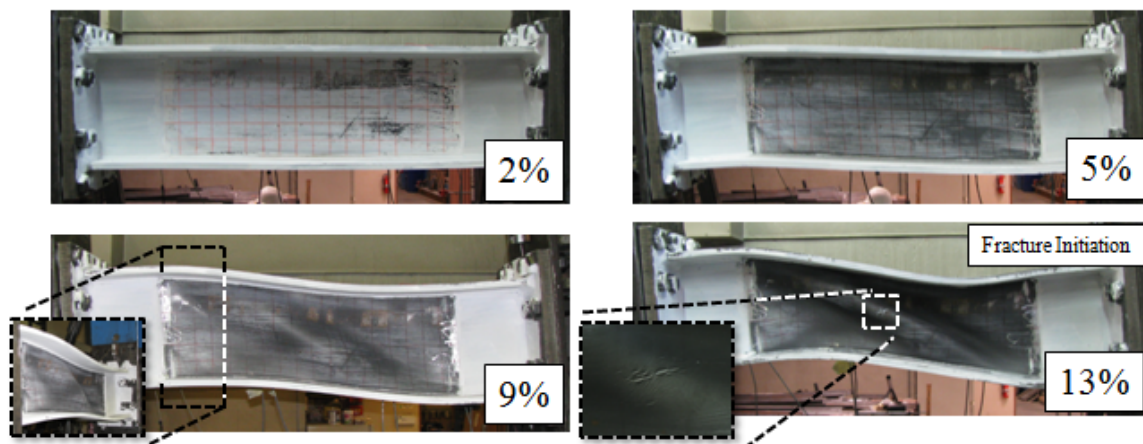


Figure 67: White Wash Strain Distribution in Link 14DBase

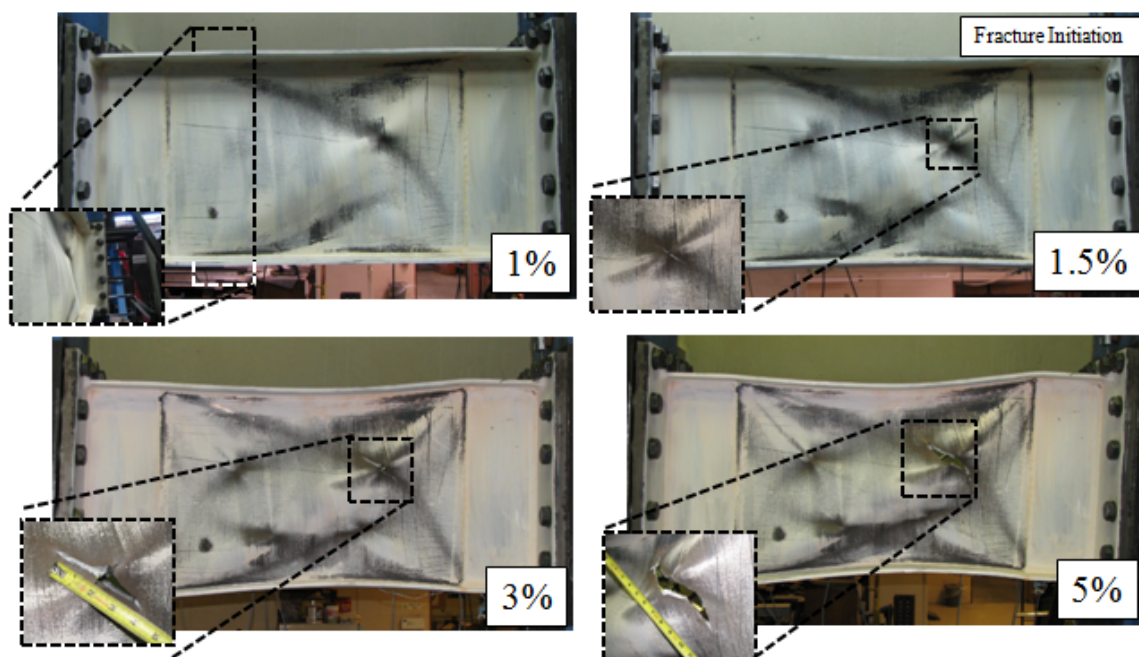


Figure 68: White Wash Strain Distribution in Link 25DBase

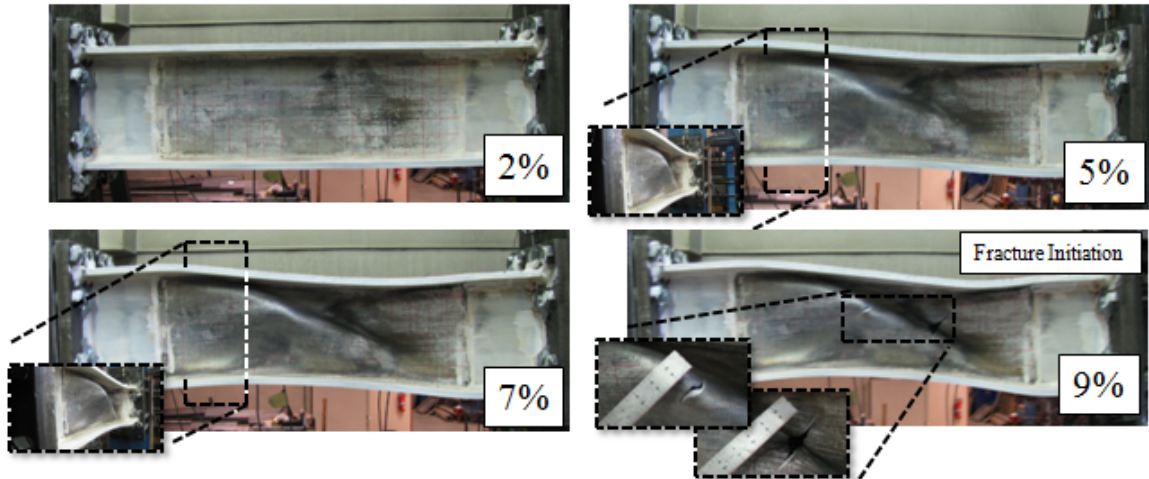


Figure 69: White Wash Strain Distribution in Link 14DN3_1000

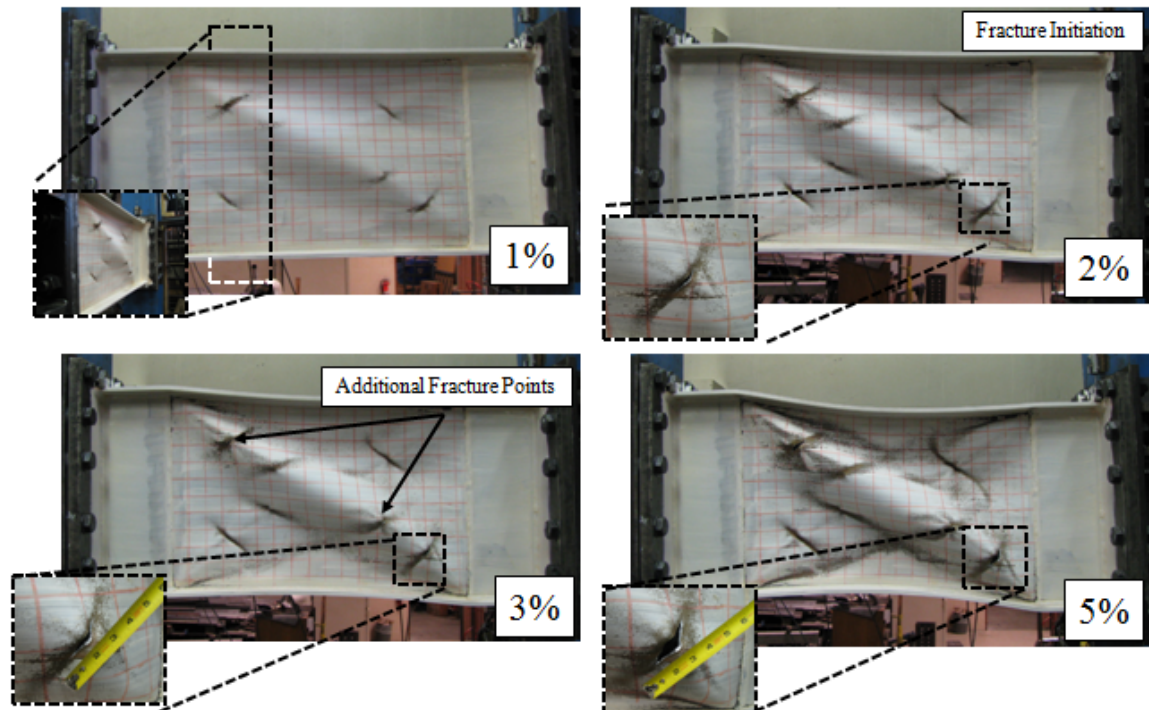


Figure 70: White Wash Strain Distribution in Link 25DN1_1000

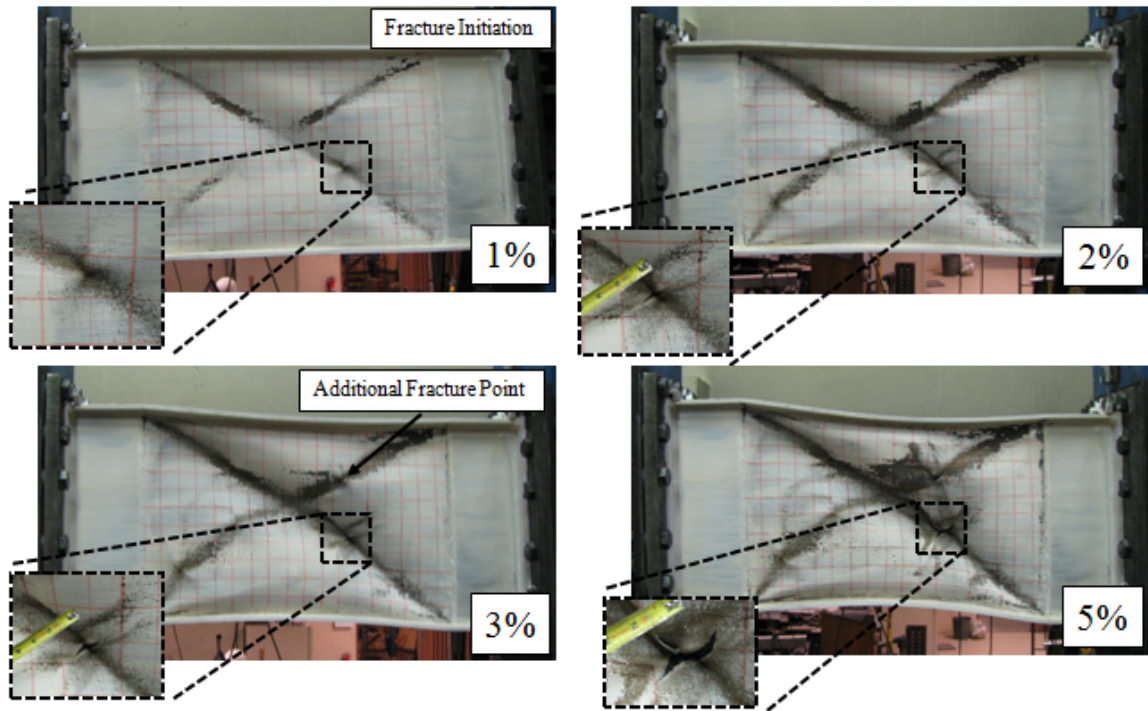
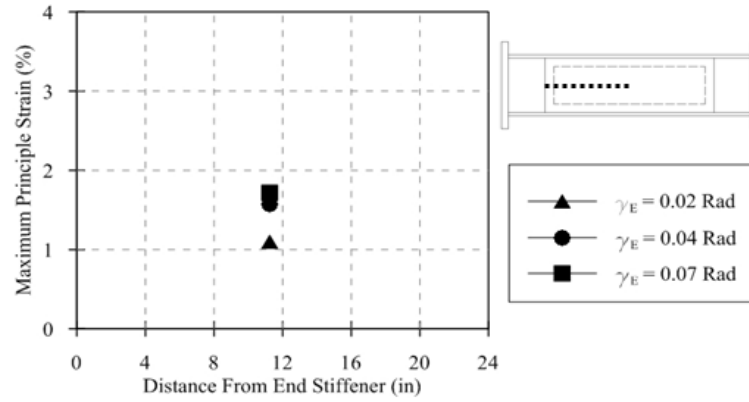
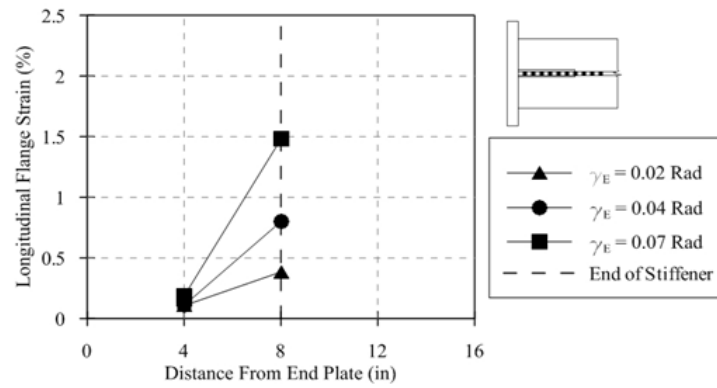


Figure 71: White Wash Strain Distribution in Link 25DN3_1000

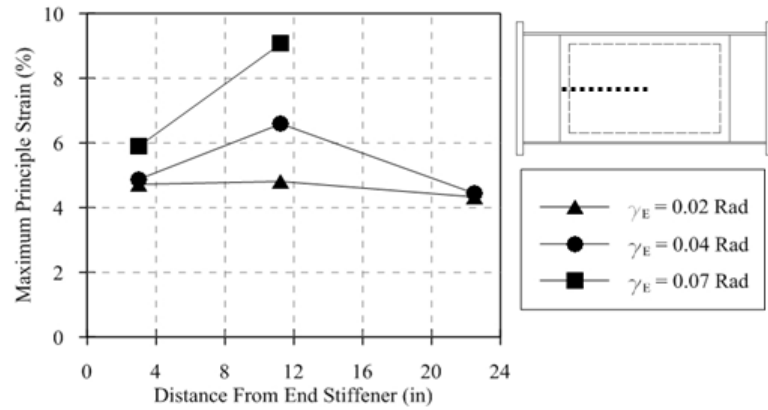


Horizontal Web Strain Distribution

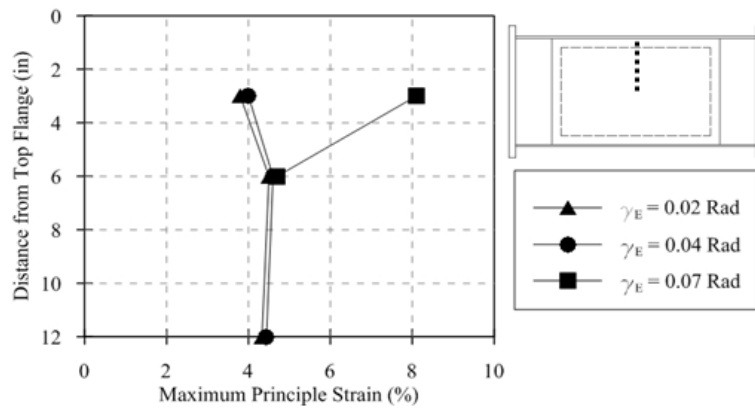


Flange Strain Distribution

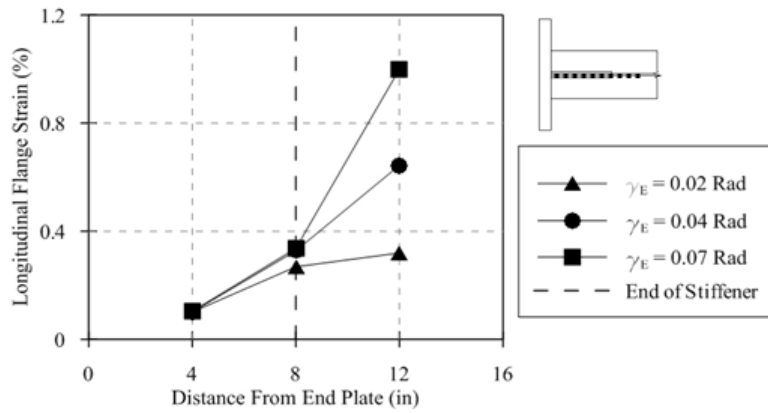
Figure 72: Discrete Experimental Strain Distribution in Link 14DBase



Horizontal Web Strain Distribution

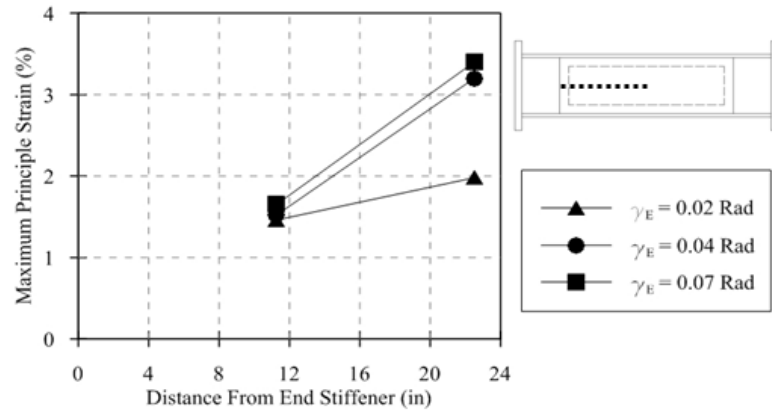


Vertical Web Strain Distribution

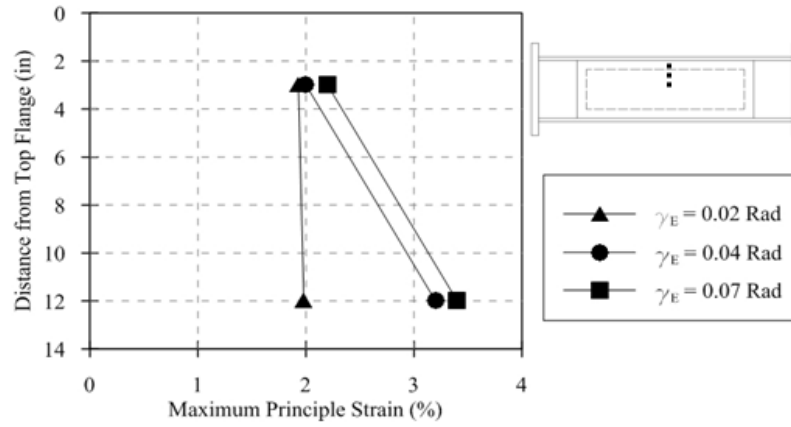


Flange Strain Distribution

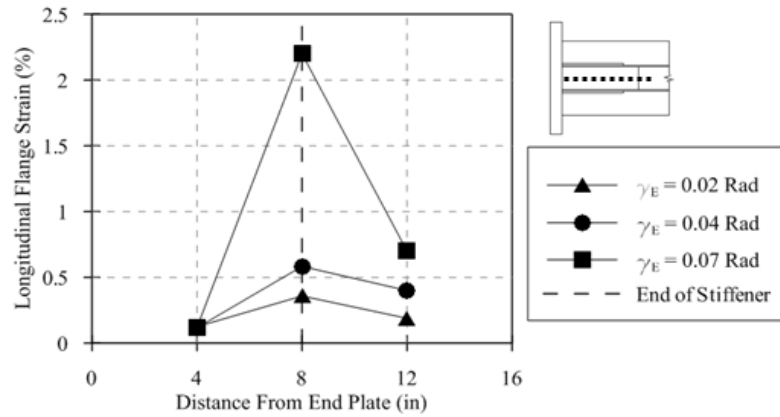
Figure 73: Discrete Experimental Strain Distribution in Link 25DBase



Horizontal Web Strain Distribution

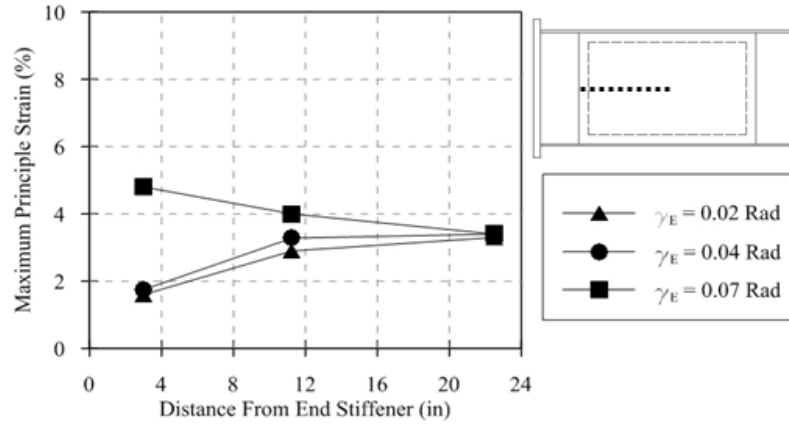


Vertical Web Strain Distribution

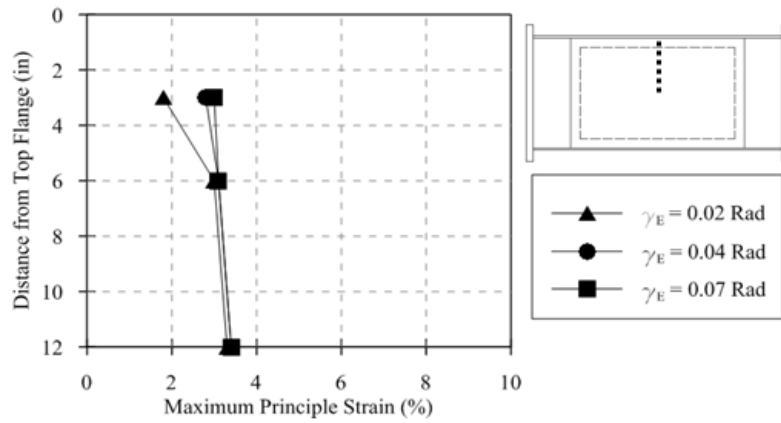


Flange Strain Distribution

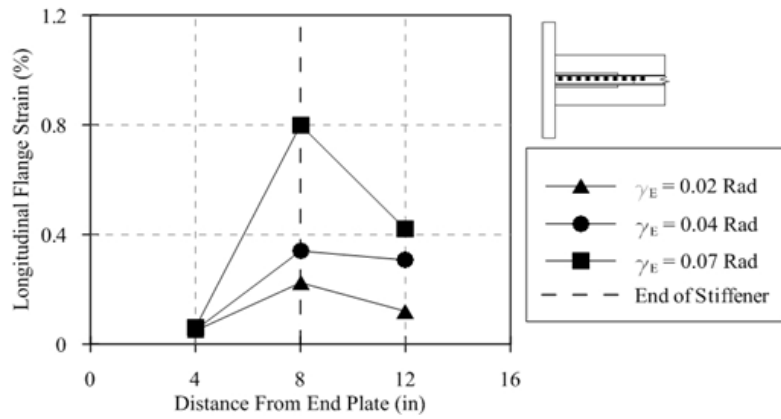
Figure 74: Discrete Experimental Strain Distribution in Link 14DN3_1000



Horizontal Web Strain Distribution

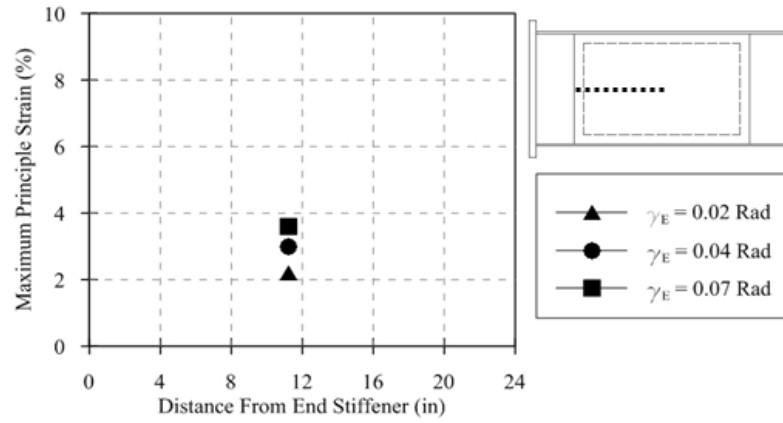


Vertical Web Strain Distribution

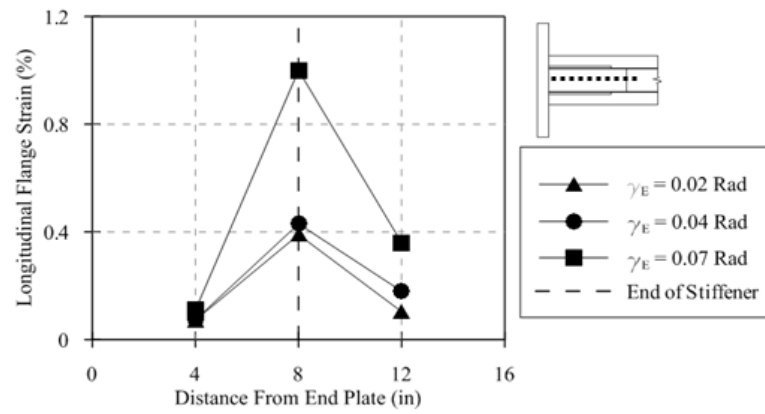


Flange Strain Distribution

Figure 75: Discrete Experimental Strain Distribution in Link 25DN1_1000



Horizontal Web Strain Analysis



Flange Strain Analysis

Figure 76: Discrete Experimental Strain Distribution in Link 25DN3_1000

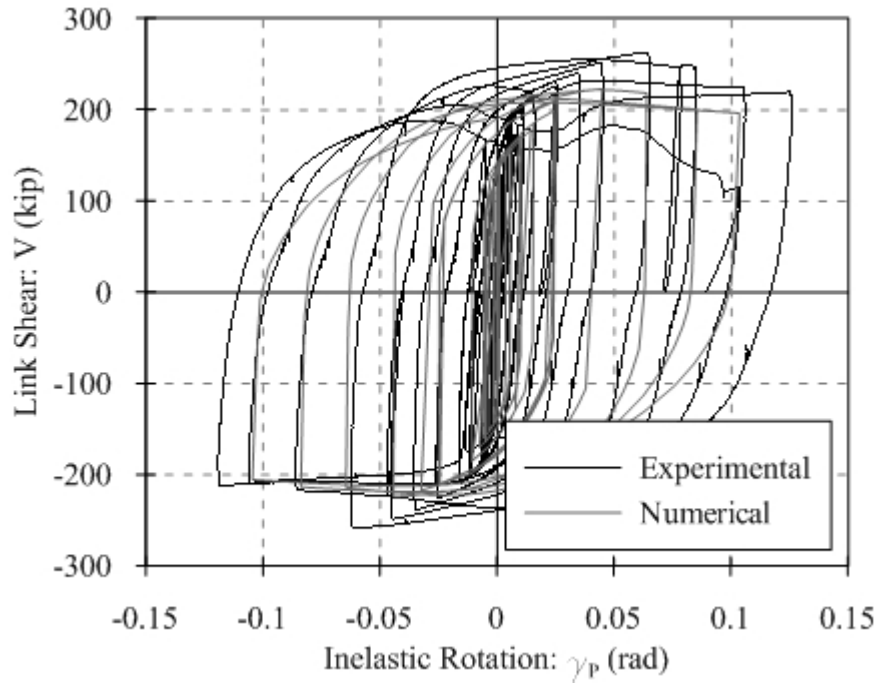


Figure 77: Link 14DBase Numerical and Experimental Hysteretic Comparison

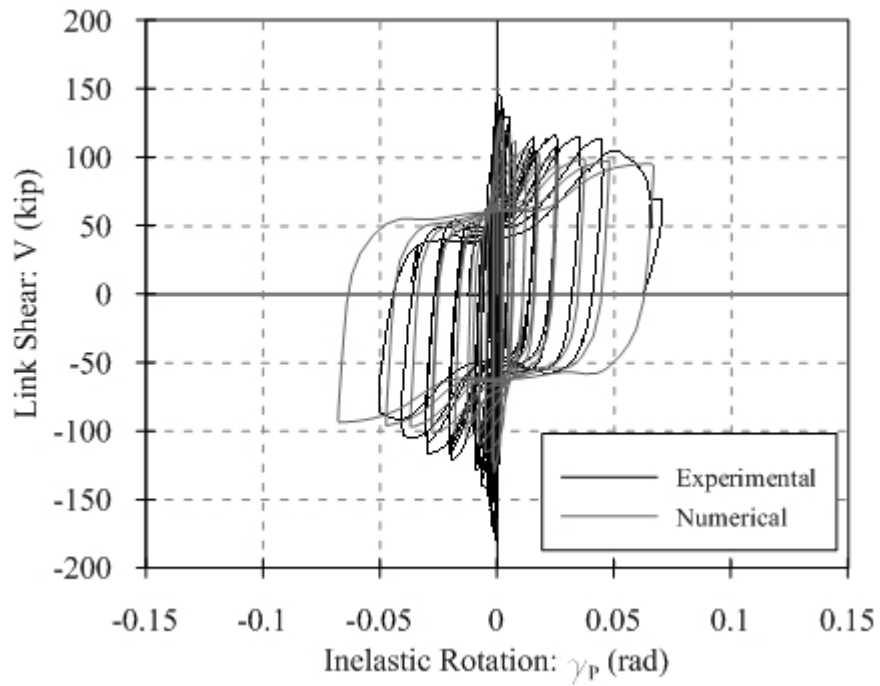


Figure 78: Link 25 DBase Numerical and Experimental Hysteretic Comparison

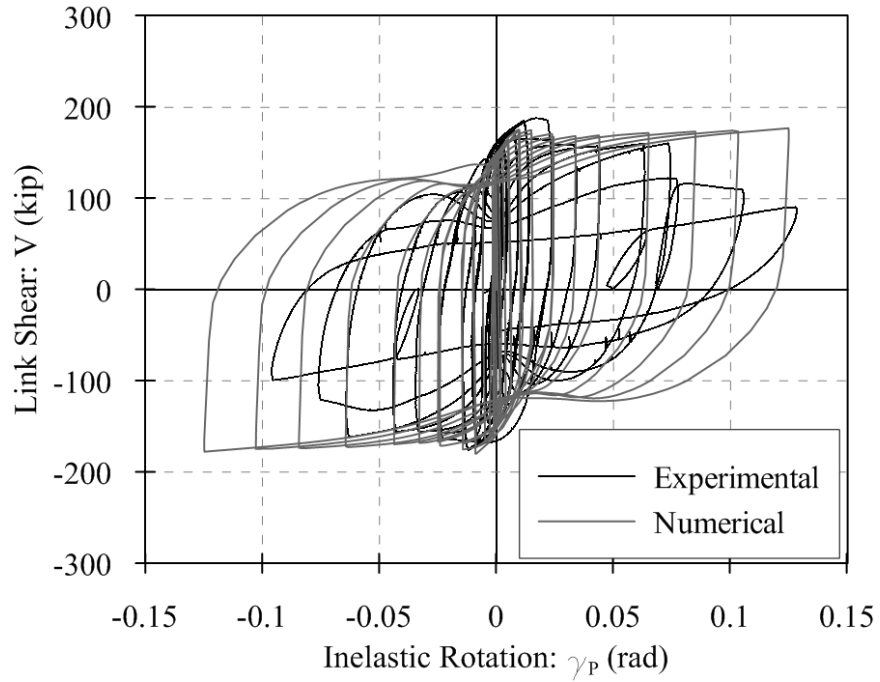


Figure 79: Link 14DN3_1000 Numerical and Experimental Hysteretic Comparison

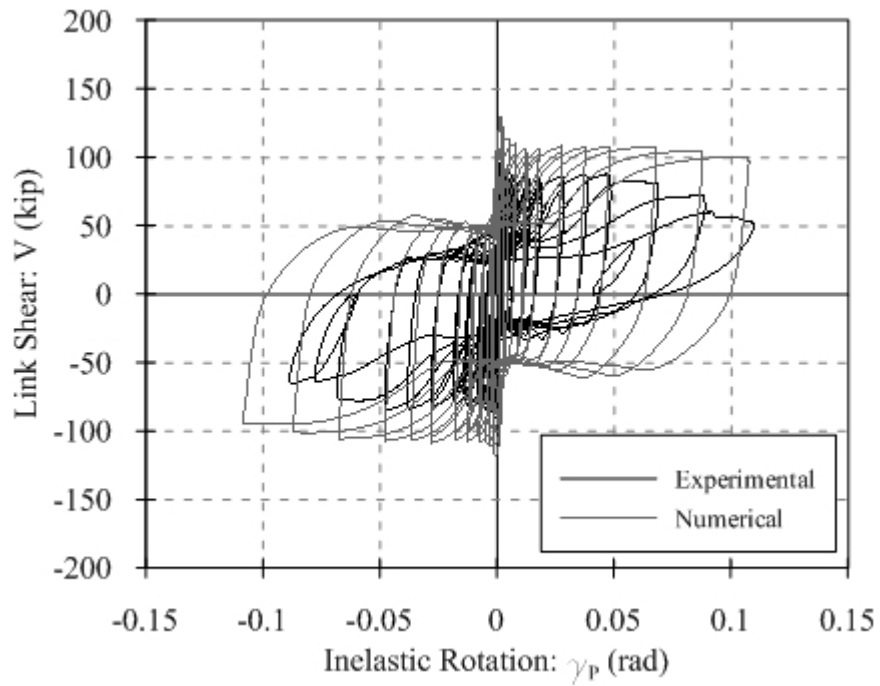


Figure 80: Link 25DN1_1000 Numerical and Experimental Hysteretic Comparison

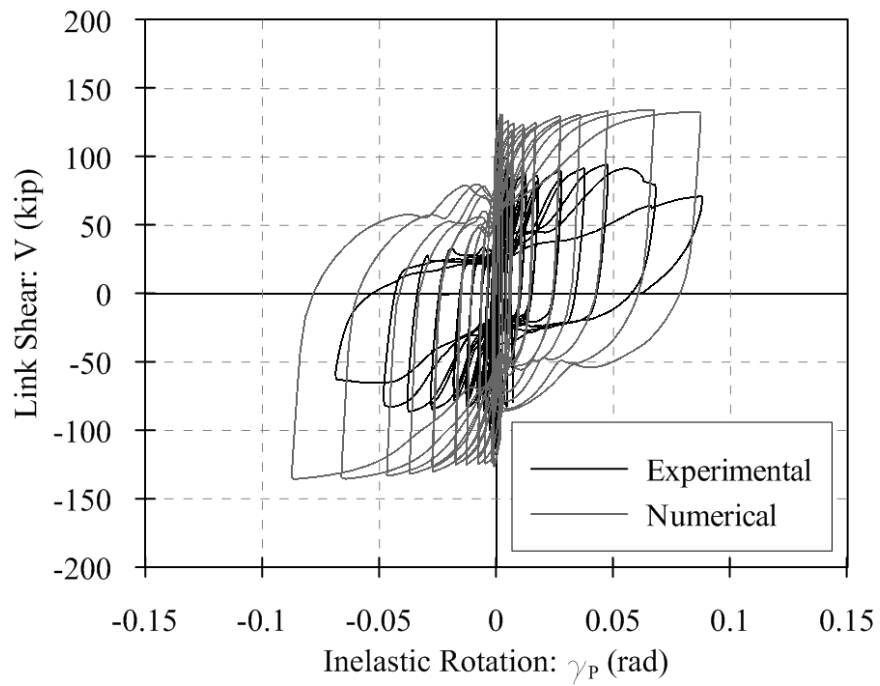


Figure 81: Link 25DN3_1000 Numerical and Experimental Hysteretic Comparison

References

- American Institute of Steel Construction, Inc. (AISC). (2005). *Seismic Provisions for Structural Steel Buildings. Standard ANSI/AISC 341-05*. Chicago, Illinois: American Institute of Steel Construction, Inc.
- American Institute of Steel Construction, Inc. (AISC). (2005). *Steel Construction Manual Thirteenth Edition*. Chicago, Illinois: American Institute of Steel Construction, Inc.
- Astaneh. (2000). Steel Plate Shear Walls. *U.S.-Japan Workshop on Seismic Fracture Issues in Steel Structures*. San Francisco.
- Astaneh-ASL, A. (2000). Steel Plate Shear Walls. *U.S.-Japan Partnership for Advanced Steel Structures*. San Francisco.
- Berman, J. W., & Bruneau, M. (2004). Steel Plate Shear Walls Are Not Plate Girders. *Engineering Journal* , 95-106.
- Bradley, G., Chang, P., & McKenna, G. (2001). Rubber Modeling Using Uniaxial Test Data. *Journal of Applied Polymer Science* , 837-848.
- Briscoe, C. R., Mantell, S. C., & Davidson, J. H. (2010). Shear Buckling in Foam-Filled Web Core Sandwich Panels Using a Pasternak Foundation Model. *Thin Walled Structures* , 460-468.
- Broderick, B., & Thomson, A. (2000). *Cyclic Testing of Flush End-Plate Semi-Rigid Steel Connections*. Rotterdam: Mazzolani and Tremblay.
- Chao, S.-H. K.-T. (2006). Ductile Web Fracture Initiation in Steel Shear Links. *Journal of Structural Engineering* , 1192-1200.

- Czaplicki, N. S. (1996). *Design and Behavior of High Performance Steel I-Girders with Composite Webs*. Bethlehem PA: Lehigh University.
- Driver Robert G., A. H. (2002). *Behavior of Internally Stiffened Webs for Bridge Girders Using High Performance Steel*. Bethlehem PA: Lehigh University.
- Duncan, B., Maxwell, A., & Crocker, L. H. (1999). *Performance of Adhesive Joints Programme Project PAJ1-Failure Criteria and Their Application to Visco-Elastic/Visco-Plastic Materials*. Middlesex: National Physical Laboratory.
- Dusicka, P., & Lewis, G. (2007). Numerical Analyses of Cyclic Shear Deformation Response of Short Beams with Sandwich Webs. *Structural Stability Research Council Annual Stability Conference Proceedings* (pp. 585-598). New Orleans: Structural Stability Research Council University of Missouri-Rolla.
- Dusicka, P., Berman, J. W., & Purasinghe, R. (2009). Steel Frame Lateral System Concept Utilizing Replaceable Links. *NZSEE Conference*.
- Dusicka, P., Itani, A. M., & Buckle, I. G. (2006). Cyclic Response of Plate Steels Under Large Inelastic Strains. *Journal of Construction Research* , 1-9.
- Dusicka, P., Itani, A. M., & Buckle, I. G. (2004). Evaluation of Conventional and Specialty Steels in Shear Link Hysteretic Energy Dissipators. *13th World Conference on Earthquake Engineering*, (p. Paper No. 522). Vancouver, B.C.
- Fagerburg, L., & Zenkert, D. (2005). Imperfection-Induced Wrinkling Material Failure in Sandwich Panels. *Journal of Sandwich Structures and Materials* , 195-219.
- Fenz Daniel, C. M. (2005). *Further Development, Testing and Modeling of the Axon Seismic Isolation System*. Buffalo: State University of New York Buffalo.

- Fortney, P. J., Bahram, S. M., & Rassati, G. A. (2007). Large-Scale Testing of a Replaceable "Fuse" Steel Coupoing Beam. *Journal of Structural Engineering* , 1801-1807.
- Gent, A. (1958). On the relation between indentation hardness and Young's modulus. *International Rubber Institute Transactions*, (pp. 46-57).
- Hertz, D., & Farinella, A. (1998). *Shore Durometer and Engineering Properties*. New York: The New York Rubber Group.
- Kasia, K., & Popov, E. (1986). Cyclic Web Buckling Control for Shear Link Beams. *Journal of Structural Engineering* , 505-523.
- Lashgari, A. M. (2009). Finite Element Analysis of Thin Steel Plate Shear Walls. *World Academy of Science, Engineering and Technology* , 436-440.
- Lee, S. C., & Yoo, C. H. (1998). Strength of Plate Girder Web Panels Under Pure Shear. *Journal of Structural Engineering* , 184-194.
- Lewis, G. R. (2010). Replaceable Shear and Flexure Links for the Linked Column Frame System. *Masters Thesis* . Portland State University.
- Lopatin, A., & Morozov, E. (2008). Symmetrical FACING Wrinkling of Composite Sandwich Panels. *Journal of Sandwich Structures and Materials* , 475-497.
- Marsh, C., Ajam, W., & Ha, H.-K. (1988). Finite Element Analysis of Post Buckled Shear Webs. *Journal of Structural Engineering* , 1571-1587.
- Marsh, C., Ajam, W., & Ha, H.-K. (1988). Finite Element Analysis of Postbuckled Shear Webs. *Journal of Structural Engineering* , 1571-1587.

- McDaniel, C. C., Uang, C.-M., & Seible, F. (2003). cyclic Testing of Built-Up Steel Shear Links for the New Bay Bridge. *Journal of Structural Engineering* , 801-809.
- Meyer-Piening. (2006). Sandwich Plates: Stresses, Deflection, Buckling and Wrinkling Loads - A Case Study. *Journal of Sandwich Structures and Materials* , 381-394.
- Murray, T. M., & Sumner, E. A. (2003). Steel Design Guide 4 Extended End Plate Moment Connections Seismic and Wind Applications. Chicago: AISC.
- Narayanan, R. (1983). *Plated Structures: Stability and Strength*. New York: Elsevier Science Publishing Co.
- NASA. (1971). *Buckling Strength of Structural Plates*. National Aeronautics and Space Administration.
- Nishino, F., & Hasegawa, A. (1977). Consideration on Basler's Shear Strngth Theory. *Stability of Steel Structures* .
- Okazaki, T. E. (2006). Cyclic Loading Behavior of EBF Links constructed of ASTM A992 Steel. *Journal of Construction Steel Research* , 751-765.
- Okazaki, T., Arce, G., Ryu, H.-C., & Engelhardt, M. D. (2005). Experimental Study of Local Buckling, Overstrength, and Fracture of Links in Eccentrically Braced Frames. *Journal of Structural Engineering* , 1526-1535.
- Ramadan, T., & Ghobarah, A. (1995). Behaviour of Bolted Link-Column Joints in Eccentrically Braced Frames. *Canadian Journal of Civil Engineering* , 745-754.
- Richards, P. W.-M. (2005). Effect of Flange Width-Thickness Ratio on Eccentrically Braced Frames Link Cyclic Rotation Capacity. *Journal of Structural Engineering* , 1546-1552.

- Shishkin, J. J., Driver, R. G., & Grondin, G. Y. (2009). Analysis of Steel Plate Shear Walls Using the Modified Strip Model. *Journal of Structural Engineering* , 1357-1366.
- Simulia. (2010). *Abaqus Users Manual V. 6.9*. Providence, RI: Dassault Systems Simulia.
- Stratan, A., & Dubina, D. (2004). *Bolted Links for Eccentrically Braced Steel Frames*.
- Thorburn, L., Kulak, G., & Montgomery, C. (1983). *Analysis of Steel Plate Shear Walls*. Edmonton: University of Alberta.
- Timoshenko, S. (1936). *Theory of Elastic Stability*. New York: McGraw-Hill Book Company.
- Vinson, J. R. (1999). *The Behavior of Sandwich Structures of Isotropic and Composite Materials*. Lancaster, PA: Technomic Publishing Company, Inc.

Appendix

A. Link and End Plate Design

A.1 14in Deep Link Design

14in Deep Sandwich Link Design

Try link design similar to W14x68 or W14x38

Properties of W14x68:

$$\begin{aligned}A_g &:= 20\text{in}^2 \\d &:= 14\text{in} \\t_w &:= 0.415\text{in} \\b_f &:= 10\text{in} \\t_f &:= 0.72\text{in}\end{aligned}$$

Properties of W14x38:

$$\begin{aligned}A_{gm} &:= 11.2\text{in}^2 \\d_m &:= 14.1\text{in} \\t_{wm} &:= 0.31\text{in} \\b_{fm} &:= 6.77\text{in} \\t_{fm} &:= 0.51\text{in}\end{aligned}$$

Design Values:

$$\begin{aligned}\phi_b &:= 0.9 \\ \phi_w &:= 0.75\end{aligned}$$

Weld Properties:

$$F_w := 70\text{ksi}$$

Design Loads:

$$\begin{aligned}P_u &:= 2\text{kip} \\M_u &:= 4200\text{kip}\cdot\text{in} \\V_u &:= 150\text{kip}\end{aligned}$$

Steel Properties:

$$\begin{aligned}E &:= 29000\text{ksi} \\F_y &:= 50\text{ksi} \\F_u &:= 65\text{ksi}\end{aligned}$$

Link Properties:

$$\begin{aligned}P_{ys} &:= 100\text{kip} \\e_s &:= 53\text{in} \\F_{yw} &:= 36\text{ksi} \\F_{uw} &:= 50\text{ksi}\end{aligned}$$

1. Select Trial Depth and Flange Thickness

Try:

$$d_s := 14\text{in}$$

Try:

$$t_{fs} := 0.75\text{in}$$

Determine h:

$$h := d_s - 2 \cdot t_{fs} = 12.5\text{in}$$

2. Determine Web Thickness

From AISC Equations F13-3 and F13-4:

$$t_{\text{req.133}} := \frac{h}{11.7 \sqrt{\frac{E}{F_y}}} = 0.044\text{in}$$

$$t_{\text{req.134}} := \frac{h}{0.42 \frac{E}{F_y}} = 0.051\text{in}$$

3. Select Trial Web Thickness

$$t_{ws} := \frac{4}{8} \text{ in}$$

4. Determine if the Web is Seismically Compact

$$\lambda_{ws} := \frac{h}{t_{ws}} = 25 \qquad C_a := \frac{P_u}{\phi_b \cdot P_{ys}}$$

$$\lambda_{psw} := \text{if} \left[(C_a \leq 0.125), 3.14 \sqrt{\frac{E}{F_y}} \cdot (1 - 1.54 C_a), 1.12 \sqrt{\frac{E}{F_y}} \cdot (2.33 - C_a) \right]$$

$$\lambda_{\text{lower.limit}} := 1.49 \sqrt{\frac{E}{F_y}}$$

$$\text{answer} := \text{if} \left[(\lambda_{ws} \leq \lambda_{psw}), \text{"seismically compact"}, \text{"not seismically compact"} \right]$$

$$\text{answer} = \text{"seismically compact"}$$

$$A_{ws} := t_{ws} \cdot h$$

5. Determine the Required Flange Size

$$A_{fs\text{required}} := \frac{\frac{M_u}{\phi_b}}{h \cdot F_y} - \frac{A_{ws}}{6} = 6.425 \text{ in}^2$$

Assuming the Original Estimate of Flange Thickness is Retained bf becomes:

$$b_{fs\text{theo}} := \frac{A_{fs\text{required}}}{t_{fs}} = 8.567 \text{ in}$$

6. Select Flange Width:

$$b_{fs} := 10 \cdot \text{in}$$

$$A_{fs\text{actual}} := b_{fs} \cdot t_{fs} = 7.5 \cdot \text{in}^2$$

7. Determine if the Compression Flange is Seismically Compact:

$$\lambda_{fs} := \frac{b_{fs}}{2t_{fs}} = 6.667$$

$$\lambda_{psf} := 0.3 \cdot \sqrt{\frac{E}{F_y}} = 7.225$$

$$\text{answer}_1 := \text{if} \left[\left(\lambda_{fs} \leq \lambda_{psf} \right), \text{"seismically compact"}, \text{"not seismically compact"} \right]$$

$$\text{answer}_1 = \text{"seismically compact"}$$

8. Calculate Properties of the Trial Member:

$$A_{gs} := 2 \cdot b_{fs} \cdot t_{fs} + t_{ws} \cdot h = 21.25 \cdot \text{in}^2$$

$$I_x := \frac{1}{12} t_{ws} \cdot h^3 + 2 \cdot b_{fs} \cdot t_{fs} \cdot \left(\left(\frac{h}{2} + \frac{t_{fs}}{2} \right) \right)^2 = 739.74 \cdot \text{in}^4$$

$$S_x := \frac{I_x}{\frac{d}{2}} = 105.677 \cdot \text{in}^3$$

9. Check Flexural Strength:

$$a_{ws} := \frac{h \cdot t_{ws}}{b_{fs} \cdot t_{fs}} = 0.833$$

$$R_{pgt} := 1 - \frac{a_{ws}}{1200 + 300 a_{ws}} \cdot \left(\frac{h}{t_{ws}} - 5.7 \cdot \sqrt{\frac{E}{F_y}} \right) = 1.065$$

$$R_{pg} := \text{if} \left[\left(R_{pgt} \leq 1 \right), R_{pgt}, 1 \right] = 1$$

$$M_p := R_{pg} \cdot F_y \cdot S_x = 5.284 \times 10^3 \cdot \text{kip} \cdot \text{in}$$

$$\frac{2 \cdot M_p}{e_s} = 199.39 \text{ kip}$$

10. Check Shear Strength:

$$V_p := 0.6 F_{yw} \cdot A_{ws} = 135 \text{ kip}$$

$$V_n := \text{if} \left[\left(V_p > \frac{2 \cdot M_p}{e_s} \right), \frac{2 \cdot M_p}{e_s}, V_p \right] = 135 \text{ kip}$$

$$\text{shearcheck} := \text{if} \left(\phi_b \cdot V_n \leq V_u, \text{"will fail in test frame"}, \text{"too strong for test frame"} \right)$$

$$\text{shearcheck} = \text{"will fail in test frame"}$$

11. Design Welds

$$a_{\min} := \text{if} \left[\left(\frac{t_{ws}}{2} < \frac{1}{4} \text{ in} \right), \frac{1}{8} \text{ in}, \frac{3}{16} \text{ in} \right] = 0.187 \text{ in}$$

If Necessary: $a_{\text{trial}} := \frac{4}{16} \text{ in}$

$$\phi R_n := \phi_w \cdot 0.707 a_{\text{trial}} \cdot 0.6 F_w = 5.568 \frac{\text{kip}}{\text{in}}$$

$$\text{CapacityPerInch} := 2 \cdot \phi R_n = 11.135 \frac{\text{kip}}{\text{in}}$$

$$Q := A_{f\text{actual}} \cdot \frac{h}{2} = 46.875 \text{ in}^3$$

$$\frac{V_n \cdot Q}{I_x} = 8.555 \frac{\text{kip}}{\text{in}}$$

Check Base Metal:

$$\text{Yield: } \phi R_{\text{nbaseyield}} := 2 \cdot \left(1 \cdot 0.6 F_{yw} \cdot \frac{t_{ws}}{2} \right) = 10.8 \frac{\text{kip}}{\text{in}}$$

$$\text{Rupture: } \phi R_{\text{nbaserupture}} := 2 \cdot \left(0.75 \cdot 0.6 F_{uw} \cdot \frac{t_{ws}}{2} \right) = 11.25 \frac{\text{kip}}{\text{in}}$$

$$\text{WeldStrength} := \text{if} \left[\left(\phi R_{\text{nbaserupture}} > \text{CapacityPerInch} \right), \text{CapacityPerInch}, \phi R_{\text{nbaserupture}} \right]$$

$$\text{answer}_3 := \text{if} \left[\left(\text{WeldStrength} > \frac{V_n \cdot Q}{I_x} \right), \text{"Weld Strength OK"}, \text{"Weld Fail"} \right]$$

$\text{answer}_3 = \text{"Weld Strength OK"}$ Flange to Web - Use 5/16" Fillet Welds

12. Check Shear Dominated Requirements

$$\text{answer}_4 := \text{if} \left[\left(\frac{1.6 M_p}{V_p} > e_s \right), \text{"Use As Short Link"}, \text{"Redesign"} \right]$$

$$1.6 \frac{M_p}{V_p} = 62.623 \text{ in}$$

$\text{answer}_4 = \text{"Use As Short Link"}$

13. Design End Stiffeners

Width:

$$b_{\text{stiffener}} := 5 \text{ in}$$

Thickness:

$$t_{\text{stiffener}} := \text{if} \left(0.75 t_{ws} < \frac{3}{8} \text{ in}, 0.75 t_{ws}, \frac{3}{8} \text{ in} \right)$$

$$t_{\text{stiffener}} = 0.375 \text{ in}$$

End Stiffener Weld Strength:

$$\text{RequiredCapacity} := b_{\text{stiffener}} \cdot t_{\text{stiffener}} \cdot F_{yw} = 67.5 \text{ kip}$$

$$\text{RequiredCapacityPerInch} := \frac{\text{RequiredCapacity}}{12.5 \text{ in}} = 5.4 \frac{\text{kip}}{\text{in}}$$

$$a_{\text{required}} := \frac{\text{RequiredCapacityPerInch}}{\phi_w \cdot 0.6 F_w \cdot 0.707} = 0.242 \text{ in}$$

Use 1/4" welds around the end stiffeners

A.2 25in Deep Link Design

25in Sandwich Link Design

Properties of W14x68:

$$A_g := 20 \text{ in}^2$$

$$d := 14 \text{ in}$$

$$t_w := 0.415 \text{ in}$$

$$b_f := 10 \text{ in}$$

$$t_f := 0.72 \text{ in}$$

Properties of W14x38:

$$A_{gm} := 11.2 \text{ in}^2$$

$$d_m := 14.1 \text{ in}$$

$$t_{wm} := 0.31 \text{ in}$$

$$b_{fm} := 6.77 \text{ in}$$

$$t_{fm} := 0.51 \text{ in}$$

Design Values:

$$\phi_b := 0.9$$

$$\phi_w := 0.75$$

Weld Properties:

$$F_w := 70 \text{ ksi}$$

Design Loads:

$$P_u := 2 \text{ kip}$$

$$M_u := 4200 \text{ kip}\cdot\text{in}$$

$$V_u := 150 \text{ kip}$$

Steel Properties:

$$E := 29000 \text{ ksi}$$

$$F_y := 62 \text{ ksi}$$

$$F_u := 87 \text{ ksi}$$

Link Properties:

$$P_{ys} := 1000 \text{ kip}$$

$$e_s := 53 \text{ in}$$

$$F_{yw} := 36 \text{ ksi}$$

$$F_{uw} := 62.3 \text{ ksi}$$

1. Select Trial Depth and Flange Thickness

Try:

Try:

$$d_s := 25 \text{ in}$$

$$t_{fs} := 0.5 \text{ in}$$

Determine h:

$$h := d_s - 2 \cdot t_{fs} = 24 \text{ in}$$

2. Determine Web Thickness

From AISC Equations F13-3 and F13-4:

$$t_{\text{req.133}} := \frac{h}{11.7 \sqrt{\frac{E}{F_y}}} = 0.095 \text{ in}$$

$$t_{\text{req.134}} := \frac{h}{0.42 \frac{E}{F_y}} = 0.122 \text{ in}$$

3. Select Trial Web Thickness

$$t_{ws} := \frac{2}{8} \text{ in}$$

4. Determine if the Web is Seismically Compact

$$\lambda_{ws} := \frac{h}{t_{ws}} = 96 \quad C_a := \frac{P_u}{\phi_b \cdot P_{ys}}$$

$$\lambda_{psw} := \text{if} \left[(C_a \leq 0.125), 3.14 \sqrt{\frac{E}{F_y}} \cdot (1 - 1.54 C_a), 1.12 \sqrt{\frac{E}{F_y}} \cdot (2.33 - C_a) \right]$$

$$\lambda_{\text{lower.limit}} := 1.49 \sqrt{\frac{E}{F_y}}$$

$$\text{answer} := \text{if} \left[(\lambda_{ws} \leq \lambda_{psw}), \text{"seismically compact"} , \text{"not seismically compact"} \right]$$

$$\text{answer} = \text{"not seismically compact"}$$

$$A_{ws} := t_{ws} \cdot h = 6 \cdot \text{in}^2$$

5. Determine the Required Flange Size

$$A_{fs\text{required}} := \frac{\frac{M_u}{\phi_b}}{h \cdot F_y} - \frac{A_{ws}}{6} = 2.136 \text{ in}^2$$

Assuming the Original Estimate of Flange Thickness is Retained bf becomes:

$$b_{fs\text{theo}} := \frac{A_{fs\text{required}}}{t_{fs}} = 4.272 \text{ in}$$

6. Select Flange Width:

$$b_{fs} := 6.5 \text{ in}$$

$$A_{fs\text{actual}} := b_{fs} \cdot t_{fs} = 3.25 \text{ in}^2$$

7. Determine if the Compression Flange is Seismically Compact:

$$\lambda_{fs} := \frac{b_{fs}}{2t_{fs}} = 6.5$$

$$\lambda_{psf} := 0.3 \cdot \sqrt{\frac{E}{F_y}} = 6.488$$

$$\text{answer}_1 := \text{if} \left[\left(\lambda_{fs} \leq \lambda_{psf} \right), \text{"seismically compact"}, \text{"not seismically compact"} \right]$$

$$\text{answer}_1 = \text{"not seismically compact"}$$

8. Calculate Properties of the Trial Member:

$$A_{gs} := 2 \cdot b_{fs} \cdot t_{fs} + t_{ws} \cdot h = 12.5 \text{ in}^2$$

$$I_x := \frac{1}{12} t_{ws} \cdot h^3 + 2 \cdot b_{fs} \cdot t_{fs} \cdot \left(\left(\frac{h}{2} + \frac{t_{fs}}{2} \right) \right)^2 = 1.263 \times 10^3 \cdot \text{in}^4$$

$$S_x := \frac{I_x}{\frac{d}{2}} = 180.487 \text{ in}^3$$

9. Check Flexural Strength:

$$a_{ws} := \frac{h \cdot t_{ws}}{b_{fs} \cdot t_{fs}} = 1.846$$

$$R_{pgt} := 1 - \frac{a_{ws}}{1200 + 300 a_{ws}} \cdot \left(\frac{h}{t_{ws}} - 5.7 \cdot \sqrt{\frac{E}{F_y}} \right) = 1.029$$

$$R_{pg} := \text{if} \left[\left(R_{pgt} \leq 1 \right), R_{pgt}, 1 \right] = 1$$

$$M_p := R_{pg} \cdot F_y \cdot S_x = 1.119 \times 10^4 \cdot \text{kip} \cdot \text{in}$$

$$\frac{2 \cdot M_p}{e_s} = 422.27 \text{ kip}$$

10. Check Shear Strength:

$$V_p := 0.6 F_{yw} \cdot A_{ws} = 129.6 \text{ kip}$$

$$V_n := \text{if} \left[\left(V_p > \frac{2 \cdot M_p}{e_s} \right), \frac{2 M_p}{e_s}, V_p \right] = 129.6 \text{ kip}$$

$$\text{shearcheck} := \text{if} \left(\phi_b \cdot V_n \leq V_u, \text{"will fail in test frame"}, \text{"too strong for test frame"} \right)$$

$$\text{shearcheck} = \text{"will fail in test frame"}$$

11. Design Welds

$$a_{\min} := \text{if} \left[\left(\frac{t_{ws}}{2} < \frac{1}{4} \text{ in} \right), \frac{1}{8} \text{ in}, \frac{3}{16} \text{ in} \right] = 0.125 \text{ in}$$

If Necessary: $a_{\text{trial}} := \frac{2}{16} \text{ in}$

$$\phi R_n := \phi_w \cdot 0.707 a_{\text{trial}} \cdot 0.6 F_w = 2.784 \frac{\text{kip}}{\text{in}}$$

$$\text{CapacityPerInch} := 2 \cdot \phi R_n = 5.568 \frac{\text{kip}}{\text{in}}$$

$$Q := A_{\text{fsactual}} \cdot \frac{h}{2} = 39 \text{ in}^3$$

$$\frac{V_n \cdot Q}{I_x} = 4.001 \frac{\text{kip}}{\text{in}}$$

Check Base Metal:

$$\text{Yield: } \phi R_{\text{nbaseyield}} := 2 \cdot \left(1 \cdot 0.6 F_{yw} \cdot \frac{t_{ws}}{2} \right) = 5.4 \frac{\text{kip}}{\text{in}}$$

$$\text{Rupture: } \phi R_{\text{nbase rupture}} := 2 \cdot \left(0.75 \cdot 0.6 F_{uw} \cdot \frac{t_{ws}}{2} \right) = 7.009 \frac{\text{kip}}{\text{in}}$$

$$\text{WeldStrength} := \text{if} \left[\left(\phi R_{\text{nbase rupture}} > \text{CapacityPerInch} \right), \text{CapacityPerInch}, \phi R_{\text{nbase rupture}} \right]$$

$$\text{answer}_3 := \text{if} \left[\left(\text{WeldStrength} > \frac{V_n \cdot Q}{I_x} \right), \text{"Weld Strength OK"}, \text{"Weld Fail"} \right]$$

answer₃ = "Weld Strength OK" Flange to Web - Use 5/16" Fillet Welds

12. Check Shear Dominated Requirements

$$\text{answer}_4 := \text{if} \left[\left(\frac{1.6 M_p}{V_p} > e_s \right), \text{"Use As Short Link"}, \text{"Redesign"} \right]$$

$$1.6 \frac{M_p}{V_p} = 138.15 \text{ in}$$

$$2 \cdot \frac{M_p}{V_p \cdot e_s} = 3.258$$

answer₄ = "Use As Short Link"

13. Design End Stiffeners

Width:

$$b_{\text{stiffener}} := 5 \text{ in}$$

Thickness:

$$t_{\text{stiffener}} := \text{if} \left(0.75 t_{ws} < \frac{3}{8} \text{ in}, 0.75 t_{ws}, \frac{3}{8} \text{ in} \right)$$

$$t_{\text{stiffener}} = 0.187 \text{ in}$$

End Stiffener Weld Strength:

$$\text{RequiredCapacity} := b_{\text{stiffener}} \cdot t_{\text{stiffener}} \cdot F_{yw} = 33.75 \text{ kip}$$

$$\text{RequiredCapacityPerInch} := \frac{\text{RequiredCapacity}}{12.5 \text{ in}} = 2.7 \frac{\text{kip}}{\text{in}}$$

$$a_{\text{required}} := \frac{\text{RequiredCapacityPerInch}}{\phi_w \cdot 0.6 F_w \cdot 0.707} = 0.121 \text{ in}$$

Use 1/4" welds around the end stiffeners

A.3 Link End Plate Connection Design – 14in Deep Link

Link to End Plate Connection - Based on Design Guide 4

Link: W12x22	Built up Section:	LCF Beam: W14x145
$d_b := 12.7 \text{ in}$	$d_{bs} := 14 \text{ in}$	$d_c := 14.8 \text{ in}$
$t_{wb} := .55 \text{ in}$	$F_{yfs} := 50 \text{ ksi}$	$t_{wc} := .68 \text{ in}$
$b_{fb} := 12.2 \text{ in}$	$t_{ws} := 0.5 \text{ in}$	$F_{yws} := 36 \text{ ksi}$
$t_{fb} := .9 \text{ in}$	$b_{fs} := 10 \text{ in}$	$F_{ufs} := 65 \text{ ksi}$
$k_b := 1.50 \text{ in}$	$t_{fs} := 0.75 \text{ in}$	$F_{uws} := 50 \text{ ksi}$
$Z_{xb} := 13 \text{ in}^3$	$I_{xs} := 739.74 \text{ in}^4$	$k_c := 1.69 \text{ in}$
$F_{yb} := 50 \text{ ksi}$	$S_{xs} := 105.677 \text{ in}^3$	$h := 11.42 \text{ in}$
$F_{ub} := 65 \text{ ksi}$	$V_{ps} := 135 \text{ kip}$	$Z_{xc} := 298 \text{ in}^3$
$V_{pb} := 180 \text{ kip}$	$h_s := 12.5 \text{ in}$	$F_{yc} := 50 \text{ ksi}$
		$F_{uc} := 65 \text{ ksi}$

End Plate	Design Values	Bolts
$F_{yp} := 50 \text{ ksi}$	$R_{yb} := 1.1$	$F_t := 113 \text{ ksi}$
$F_{up} := 65 \text{ ksi}$	$R_{ys} := 1.5$	$F_v := 75 \text{ ksi}$
$b_p := 13.2 \text{ in}$	$V_{ub} := 340 \text{ kip}$	
$g_1 := 8 \text{ in}$	$e_b := 53 \text{ in}$	
$t_p := 1.5 \text{ in}$	$\phi := 0.75$	
$L_e := 1.5 \text{ in}$	$\phi_b := 0.9$	
$s_b := 1.5 \text{ in}$	$E := 29000 \text{ ksi}$	
$c_1 := 5 \text{ in}$		

Link Side Design

1. Determine Design Moment

$$M_{pshearover} := V_{ps} \cdot \frac{e_b}{2} = 3.578 \times 10^3 \cdot \text{kip} \cdot \text{in} \quad M_{pshear} := 1.25 R_{yb} \cdot V_{ps} \cdot \frac{e_b}{2} = 4.919 \times 10^3 \cdot \text{kip} \cdot \text{in}$$

2. Select Connection Configuration: Four-Bolt Extended Unstiffened

(note: design modification results by adding bolts to the side of the required bolts, this modification doesn't necessarily produce a doubling in load in the plastic range)

Compare bolt pattern on the LCF to the link to determine bolt places

Greg W12x96:

$$p_{fib} := 1.95 \text{ in} \quad p_{fob} := 2.15 \text{ in} \quad d_{eb} := 1.5 \text{ in}$$

$$h_{0b} := d_b + p_{fob} - \frac{t_{fb}}{2} = 14.4 \text{ in}$$

$$h_{1b} := d_b - t_{fb} - p_{fib} - \frac{t_{fb}}{2} = 9.4 \text{ in}$$

Max Built up Link:

$$p_{fis} := 2.75 \text{ in} \quad p_{fos} := 1.5 \text{ in}$$

$$h_{0s} := d_{bs} + p_{fos} - \frac{t_{ws}}{2} = 15.25 \text{ in}$$

$$h_{1s} := d_{bs} - t_{fs} - p_{fis} - \frac{t_{fs}}{2} = 10.125 \text{ in}$$

3. Determine Required Bolt Diameter

$$d_{breq1row} := \sqrt{2 \cdot \frac{M_{pshear}}{\pi \cdot \phi \cdot F_t \cdot (h_{0s} + h_{1s})}} = 1.207 \text{ in}$$

$$d_{breq2rows} := \sqrt{1 \cdot \frac{M_{pshear}}{\pi \cdot \phi \cdot F_t \cdot (h_{0s} + h_{1s})}} = 0.853 \text{ in}$$

4. Select Trial Bolt Diameter and Calculate No Prying Moment Capacity

$$\text{Try: } d_{bolt} := 1.25 \text{ in}$$

$$M_{np} := 4 \cdot \frac{d_{bolt}^2 \cdot \pi}{4} \cdot F_t \cdot (h_{0s} + h_{1s}) = 1.408 \times 10^4 \cdot \text{kip} \cdot \text{in}$$

5. Determine Required End Plate Thickness

$$s_1 := \frac{1}{2} \cdot \sqrt{b_p \cdot g_1} = 5.138 \text{ in}$$

$$Y_p := \frac{b_p}{2} \cdot \left[h_{1s} \cdot \left(\frac{1}{p_{fis}} + \frac{1}{s_1} \right) + h_{0s} \cdot \frac{1}{p_{fos}} - \frac{1}{2} \right] + \frac{2}{g_1} \cdot h_{1s} \cdot (p_{fis} + s_1) = 121.073 \text{ in}$$

$$t_{preq} := \sqrt{\frac{1.11 \cdot \phi \cdot M_{np}}{\phi_b \cdot F_{yp} \cdot Y_p}} = 1.467 \text{ in}$$

6. Calculate Factored Beam Flange Shear Force and Check Shear Yielding and Rupture

$$F_{fu} := \frac{M_{pshear}}{d_{bs} - t_{fs}} = 371.25 \text{ kip}$$

Yield:

$$\phi R_{ny} := \phi_b \cdot 0.6 F_{yp} \cdot b_p \cdot t_p$$

$$\text{answer} := \text{if} \left(\frac{F_{fu}}{2} > \phi R_{ny}, \text{"NO GOOD"}, \text{"OK"} \right) = \text{"OK"}$$

$$\text{answer} = \text{"OK"}$$

Rupture:

$$A_{np} := \left[b_p - 2 \cdot \left[d_{bolt} + \left(\frac{1 \text{ in}}{8} \right) \right] \right] \cdot t_p = 15.675 \text{ in}^2$$

$$\phi R_{nr} := \phi \cdot 0.6 F_{up} \cdot A_{np}$$

$$\text{answer}_1 := \text{if} \left(\frac{F_{fu}}{2} > \phi R_{nr}, \text{"NO GOOD"}, \text{"OK"} \right)$$

$$\text{answer}_1 = \text{"OK"}$$

7. Check Bolt Shear Rupture Strength of Bolts in Compression Flange

$$\phi R_{nbolt} := \phi \cdot 8 \cdot F_v \cdot \frac{\pi \cdot d_{bolt}^2}{4}$$

$$answer_2 := \text{if}(\phi R_{nbolt} > V_{ub}, "OK", "NO GOOD")$$

$$answer_2 = "OK"$$

8. Check Bolt Bearing/Tear Out Failure of End Plate and Column Flange

$$BearingLimit := 2.4 \cdot d_{bolt} \cdot t_p \cdot F_{up} = 292.5 \text{ kip} \quad (\text{per bolt})$$

$$h_b := d_{bolt} + \frac{1}{16} \text{ in}$$

$$L_{ce} := p_{fos} + t_{fs} + p_{fis} - h_b = 3.688 \text{ in}$$

Outer Bolts Control:

$$R_{nouter} := 1.2 \cdot L_{ce} \cdot t_p \cdot F_{up} = 431.438 \text{ kip}$$

Total Bearing Strength:

$$R_{nbeartot} := \text{if}(BearingLimit > R_{nouter}, R_{nouter} \cdot 8, BearingLimit \cdot 8)$$

$$answer_3 := \text{if}(R_{nbeartot} > V_{ub}, "OK", "NO GOOD")$$

$$answer_3 = "OK"$$

9. Check the Column Flange for Flexural Yielding

$$s_c := 0.5 \cdot \sqrt{b_{fc} \cdot g_1} = 5.568 \text{ in}$$

$$p_{so} := 2.25 \text{ in}$$

$$p_{si} := 2.25 \text{ in}$$

$$Y_c := \frac{b_{fc}}{2} \cdot h_{1s} \cdot \frac{1}{s_c} + \frac{\text{lin}^2}{p_{si}} + h_{0s} \cdot \frac{\text{lin}}{s_c} + \frac{\text{lin}^2}{p_{so}} + \frac{2}{g_1} \cdot h_{1s} \cdot (s_c + p_{si}) + \frac{h_{0s} \cdot (s_c + p_{so})}{\text{in}} = 156.73 \text{ in}$$

$$t_{fcreq} := \sqrt{1.11 \cdot \phi \cdot \frac{M_{np}}{\phi_b \cdot F_{yc} \cdot Y_c}} = 1.289 \text{ in}$$

$$\text{answer}_t := \text{if}(t_{fcreq} \geq t_{fc}, \text{"NO GOOD"}, \text{"OK"})$$

$$\text{answer}_t = \text{"NO GOOD"}$$

10. Check the Local Column Web Yielding

$$C_t := 1$$

$$N_1 := t_{fs} + 2 \cdot \text{lin} = 2.75 \text{ in}$$

$$\phi R_{nwebyield} := \phi \cdot C_t \cdot (6 \cdot k_c + N_1 + 2 \cdot t_p) \cdot F_{yc} \cdot (t_{wc} + \text{lin}) = 1.001 \times 10^3 \cdot \text{kip}$$

$$\text{answer}_4 := \text{if}(\phi R_{nwebyield} > F_{fu}, \text{"OK"}, \text{"NO GOOD"})$$

$$\text{answer}_4 = \text{"OK"}$$

11. Check the Column Web Buckling Strength at Beam Compression Flange

$$h_{ws} := 12.5 \text{ in}$$

$$\phi R_{nwebbuckle} := \frac{\phi \cdot 24 \cdot (t_{wc} + \text{lin})^3 \cdot \sqrt{E \cdot F_{yc}}}{h_{ws}} = 8.222 \times 10^3 \cdot \text{kip}$$

$$\text{answer}_5 := \text{if}(\phi R_{nwebbuckle} \geq F_{fu}, \text{"OK"}, \text{"NO GOOD"})$$

$$\text{answer}_5 = \text{"OK"}$$

12. Check Web Crippling Strength

$$\phi R_{nwebcripple} = \phi 0.8 (t_{wc} + l_{in})^2 \left[1 + 3 \left(\frac{N_1}{d_c} \right) \left[\frac{(t_{wc} + l_{in})}{t_{fc}} \right]^{1.5} \right] \cdot \sqrt{\frac{E F_{yc} t_{fc}}{(t_{wc} + l_{in})}} = 3.395 \times 10^3 \text{ kip}$$

$$\text{answer}_6 := \text{if}(\phi R_{nwebcripple} \geq F_{fu}, \text{"OK"}, \text{"NO GOOD"})$$

$$\text{answer}_6 = \text{"OK"}$$

13. Design Welds

Beam Flange to End Plate

$$F_{fumin} := 0.6 F_{yb} \cdot b_{fs} \cdot t_{fs} = 225 \text{ kip}$$

$$F_{fuactual} := \text{if}[(F_{fu} > F_{fumin}), F_{fu}, F_{fumin}]$$

$$F_{fudesign} := F_{fuactual} \cdot 1.1 \cdot 1.1$$

$$l_{fw} := b_{fs} + (b_{fs} - t_{ws}) = 19.5 \text{ in}$$

$$D_f := \frac{F_{fudesign}}{l_{fw} \cdot 1.5 \cdot 1.392} = 11.033 \frac{\text{kip}}{\text{in}} \quad 16\text{ths of an inch}$$

$$a_{\max} := t_{fs} - \frac{1}{16} \text{ in} = 0.688 \text{ in}$$

Use 11/16" Fillet Weld

Beam Web to End Plate in Tension Region

$$D_{wt} := \frac{0.6 F_{yb} \cdot t_{ws}}{2 \cdot 1.392} = 5.388 \frac{\text{kip}}{\text{in}} \quad 16\text{ths of an inch}$$

$$D_{wc} := \frac{V_{ps}}{2 \cdot 1.392 \left(\frac{d_{bs}}{2} - t_{fs} \right)} = 7.759 \frac{\text{kip}}{\text{in}} \quad 16\text{ths of an inch}$$

$$D_{w\text{required}} := \text{if}[(D_{wt} > D_{wc}), D_{wt}, D_{wc}]$$

$$D_{w\text{required}} = 7.759 \frac{\text{kip}}{\text{in}} \quad 16\text{ths of an inch}$$

$$a_{\text{maxweb}} := \frac{t_{ws}}{2} - \frac{1}{16} \text{in} = 0.187 \text{in}$$

Need 1/2" fillet welds

Allowed 4/16" fillet welds based on web thickness

Split the difference. Use 3/8" fillet weld

A.4 Link End Plate Connection Design – 25in Deep Link

Link to End Plate Connection - Based on Design Guide 4

Link: W12x22

$$d_b := 12.7 \text{in}$$

$$t_{wb} := .55 \text{in}$$

$$b_{fb} := 12.2 \text{in}$$

$$t_{fb} := .9 \text{in}$$

$$k_b := 1.50 \text{in}$$

$$Z_{xb} := 13 \text{in}^3$$

$$F_{yb} := 50 \text{ksi}$$

$$F_{ub} := 65 \text{ksi}$$

$$V_{pb} := 180 \text{kip}$$

Built up Section:

$$d_{bs} := 25 \text{in} \quad F_{yfs} := 50 \text{ksi}$$

$$t_{ws} := 0.25 \text{in} \quad F_{yws} := 36 \text{ksi}$$

$$b_{fs} := 6.5 \text{in} \quad F_{ufs} := 65 \text{ksi}$$

$$t_{fs} := 0.5 \text{in} \quad F_{uws} := 50 \text{ksi}$$

$$I_{xs} := 1.263 \cdot 10^3 \text{in}^4$$

$$S_{xs} := 180.487 \text{in}^3$$

$$V_{ps} := 129.6 \text{kip}$$

$$h_s := 24 \text{in}$$

LCF Beam: W14x145

$$d_c := 14.8 \text{in}$$

$$t_{wc} := .68 \text{in}$$

$$b_{fc} := 15.5 \text{in}$$

$$t_{fc} := 1.09 \text{in}$$

$$k_c := 1.69 \text{in}$$

$$h := 11.42 \text{in}$$

$$Z_{xc} := 298 \text{in}^3$$

$$F_{yc} := 50 \text{ksi}$$

$$F_{uc} := 65 \text{ksi}$$

End Plate

$$F_{yp} := 50 \text{ksi}$$

$$F_{up} := 65 \text{ksi}$$

$$b_p := 13.2 \text{in}$$

$$g_1 := 8 \text{in}$$

$$t_p := 1.5 \text{in}$$

$$L_e := 1.5 \text{in}$$

$$s_b := 1.5 \text{in}$$

$$c_1 := 5 \text{in}$$

Design Values

$$R_{yb} := 1.1$$

$$R_{ys} := 1.5$$

$$V_{ub} := 340 \text{kip}$$

$$e_b := 53 \text{in}$$

$$\phi := 0.75$$

$$\phi_b := 0.9$$

$$E := 29000 \text{ksi}$$

Bolts

$$F_t := 113 \text{ksi}$$

$$F_v := 75 \text{ksi}$$

Link Side Design

1. Determine Design Moment

$$M_{\text{pshearover}} := V_{\text{ps}} \cdot \frac{e_b}{2} = 3.434 \times 10^3 \cdot \text{kip} \cdot \text{in} \quad M_{\text{pshear}} := 1.25 R_{\text{ys}} \cdot V_{\text{ps}} \cdot \frac{e_b}{2} = 6.439 \times 10^3 \cdot \text{kip} \cdot \text{in}$$

2. Select Connection Configuration: Four-Bolt Extended Unstiffened

(note: design modification results by adding bolts to the side of the required bolts, this modification doesn't necessarily produce a doubling in load in the plastic range)

Compare bolt pattern on the LCF to the link to determine bolt places

Greg W12x96:

$$p_{\text{fib}} := 1.95 \text{ in} \quad p_{\text{fob}} := 2.15 \text{ in} \quad d_{\text{eb}} := 1.5 \text{ in}$$

$$h_{0b} := d_b + p_{\text{fob}} - \frac{t_{\text{fb}}}{2} = 14.4 \text{ in}$$

$$h_{1b} := d_b - t_{\text{fb}} - p_{\text{fib}} - \frac{t_{\text{fb}}}{2} = 9.4 \text{ in}$$

Max Built up Link:

$$p_{\text{fis}} := 2.75 \text{ in} \quad p_{\text{fos}} := 1.5 \text{ in}$$

$$h_{0s} := d_{\text{bs}} + p_{\text{fos}} - \frac{t_{\text{ws}}}{2} = 26.375 \text{ in}$$

$$h_{1s} := d_{\text{bs}} - t_{\text{fs}} - p_{\text{fis}} - \frac{t_{\text{fs}}}{2} = 21.5 \text{ in}$$

3. Determine Required Bolt Diameter

$$d_{\text{breq1row}} := \sqrt{2 \cdot \frac{M_{\text{pshear}}}{\pi \cdot \phi \cdot F_t \cdot (h_{0s} + h_{1s})}} = 1.005 \text{ in}$$

$$d_{\text{breq2rows}} := \sqrt{1 \cdot \frac{M_{\text{pshear}}}{\pi \cdot \phi \cdot F_t \cdot (h_{0s} + h_{1s})}} = 0.711 \text{ in}$$

4. Select Trial Bolt Diameter and Calculate No Prying Moment Capacity

$$\text{Try: } d_{\text{bolt}} := 1.25 \text{ in}$$

$$M_{\text{np}} := 4 \cdot \frac{d_{\text{bolt}}^2 \cdot \pi}{4} \cdot F_t \cdot (h_{0s} + h_{1s}) = 2.656 \times 10^4 \cdot \text{kip} \cdot \text{in}$$

5. Determine Required End Plate Thickness

$$s_1 := \frac{1}{2} \cdot \sqrt{b_p \cdot g_1} = 5.138 \text{ in}$$

$$Y_p := \frac{b_p}{2} \cdot \left[h_{1s} \cdot \left(\frac{1}{p_{fis}} + \frac{1}{s_1} \right) + h_{0s} \cdot \frac{1}{p_{fos}} - \frac{1}{2} \right] + \frac{2}{g_1} \cdot h_{1s} \cdot (p_{fis} + s_1) = 234.366 \text{ in}$$

$$t_{preq} := \sqrt{\frac{1.11 \cdot \phi \cdot M_{np}}{\phi_b \cdot F_{yp} \cdot Y_p}} = 1.448 \text{ in}$$

6. Calculate Factored Beam Flange Shear Force and Check Shear Yielding and Rupture

$$F_{fu} := \frac{M_{pshear}}{d_{bs} - t_{fs}} = 262.837 \text{ kip}$$

Yield:

$$\phi R_{ny} := \phi_b \cdot 0.6 F_{yp} \cdot b_p \cdot t_p$$

$$\text{answer} := \text{if} \left(\frac{F_{fu}}{2} > \phi R_{ny}, \text{"NO GOOD"}, \text{"OK"} \right) = \text{"OK"}$$

answer = "OK"

Rupture:

$$A_{np} := \left[b_p - 2 \cdot \left[d_{bolt} + \left(\frac{1 \text{ in}}{8} \right) \right] \right] \cdot t_p = 15.675 \text{ in}^2$$

$$\phi R_{nr} := \phi \cdot 0.6 F_{up} \cdot A_{np}$$

$$\text{answer}_1 := \text{if} \left(\frac{F_{fu}}{2} > \phi R_{nr}, \text{"NO GOOD"}, \text{"OK"} \right)$$

answer₁ = "OK"

7. Check Bolt Shear Rupture Strength of Bolts in Compression Flange

$$\phi R_{nbolt} := \phi \cdot 8 \cdot F_v \cdot \frac{\pi \cdot d_{bolt}^2}{4}$$

$$answer_2 := \text{if}(\phi R_{nbolt} > V_{ub}, \text{"OK"}, \text{"NO GOOD"})$$

$$answer_2 = \text{"OK"}$$

8. Check Bolt Bearing/Tear Out Failure of End Plate and Column Flange

$$\text{BearingLimit} := 2.4 \cdot d_{bolt} \cdot t_p \cdot F_{up} = 292.5 \text{ kip} \quad (\text{per bolt})$$

$$h_b := d_{bolt} + \frac{1}{16} \text{ in}$$

$$L_{ce} := p_{fos} + t_{fs} + p_{fis} - h_b = 3.437 \text{ in}$$

Outer Bolts Control:

$$R_{nouter} := 1.2 \cdot L_{ce} \cdot t_p \cdot F_{up} = 402.187 \text{ kip}$$

Total Bearing Strength:

$$R_{nbeartot} := \text{if}(\text{BearingLimit} > R_{nouter}, R_{nouter} \cdot 8, \text{BearingLimit} \cdot 8)$$

$$answer_3 := \text{if}(R_{nbeartot} > V_{ub}, \text{"OK"}, \text{"NO GOOD"})$$

$$answer_3 = \text{"OK"}$$

9. Check the Column Flange for Flexural Yielding

$$s_c := 0.5 \cdot \sqrt{b_{fc} \cdot g_1} = 5.568 \text{ in}$$

$$p_{so} := 2.25 \text{ in}$$

$$p_{si} := 2.25 \text{ in}$$

$$Y_c := \frac{b_{fc}}{2} \cdot h_{1s} \cdot \frac{1}{s_c} + \frac{\text{lin}^2}{p_{si}} + h_{0s} \cdot \frac{\text{lin}}{s_c} + \frac{\text{lin}^2}{p_{so}} + \frac{2}{g_1} \cdot h_{1s} \cdot (s_c + p_{si}) + \frac{h_{0s} \cdot (s_c + p_{so})}{\text{in}} = 283.767 \text{ in}$$

$$t_{fcreq} := \sqrt{1.11 \cdot \phi \cdot \frac{M_{np}}{\phi_b \cdot F_{yc} \cdot Y_c}} = 1.316 \text{ in}$$

$$\text{answer}_t := \text{if}(t_{fcreq} \geq t_{fc}, \text{"NO GOOD"}, \text{"OK"})$$

$$\text{answer}_t = \text{"NO GOOD"}$$

10. Check the Local Column Web Yielding

$$C_t := 1$$

$$N_1 := t_{fs} + 2 \cdot \text{lin} = 2.5 \text{ in}$$

$$\phi R_{nwebyield} := \phi \cdot C_t \cdot (6 \cdot k_c + N_1 + 2 \cdot t_p) \cdot F_{yc} \cdot (t_{wc} + \text{lin}) = 985.32 \text{ kip}$$

$$\text{answer}_4 := \text{if}(\phi R_{nwebyield} > F_{fu}, \text{"OK"}, \text{"NO GOOD"})$$

$$\text{answer}_4 = \text{"OK"}$$

11. Check the Column Web Buckling Strength at Beam Compression Flange

$$h_{ws} := 12.5 \text{ in}$$

$$\phi R_{nwebbuckle} := \frac{\phi \cdot 24 \cdot (t_{wc} + \text{lin})^3 \cdot \sqrt{E \cdot F_{yc}}}{h_{ws}} = 8.222 \times 10^3 \cdot \text{kip}$$

$$\text{answer}_5 := \text{if}(\phi R_{nwebbuckle} \geq F_{fu}, \text{"OK"}, \text{"NO GOOD"})$$

$$\text{answer}_5 = \text{"OK"}$$

12. Check Web Crippling Strength

$$\phi R_{nwebcripple} := \phi \cdot 0.8 (t_{wc} + l_{in})^2 \cdot \left[1 + 3 \cdot \left(\frac{N_1}{d_c} \right) \cdot \left[\frac{(t_{wc} + l_{in})}{t_{fc}} \right]^{1.5} \right] \cdot \sqrt{\frac{E \cdot F_{yc} \cdot t_{fc}}{(t_{wc} + l_{in})}} = 3.235 \times 10^3 \text{ kip}$$

$$\text{answer}_6 := \text{if}(\phi R_{nwebcripple} \geq F_{fu}, \text{"OK"}, \text{"NO GOOD"})$$

$$\text{answer}_6 = \text{"OK"}$$

13. Design Welds

Beam Flange to End Plate

$$F_{fumin} := 0.6 F_{yb} \cdot b_{fs} \cdot t_{fs} = 97.5 \text{ kip}$$

$$F_{fuactual} := \text{if}[(F_{fu} > F_{fumin}), F_{fu}, F_{fumin}]$$

$$F_{fudesign} := F_{fuactual} \cdot 1.1 \cdot 1.1$$

$$l_{fw} := b_{fs} + (b_{fs} - t_{ws}) = 12.75 \text{ in}$$

$$D_f := \frac{F_{fudesign}}{l_{fw} \cdot 1.5 \cdot 1.392} = 11.946 \frac{\text{kip}}{\text{in}} \quad 16\text{ths of an inch}$$

$$a_{\max} := t_{fs} - \frac{1}{16} \text{ in} = 0.438 \text{ in}$$

Use 5/8" Fillet Weld

Beam Web to End Plate in Tension Region

$$D_{wt} := \frac{0.6 F_{yb} \cdot t_{ws}}{2 \cdot 1.392} = 2.694 \frac{\text{kip}}{\text{in}} \quad 16\text{ths of an inch}$$

$$D_{wc} := \frac{V_{ps}}{2 \cdot 1.392 \left(\frac{d_{bs}}{2} - t_{fs} \right)} = 3.879 \frac{\text{kip}}{\text{in}} \quad 16\text{ths of an inch}$$

$$D_{w\text{required}} := \text{if}[(D_{wt} > D_{wc}), D_{wt}, D_{wc}]$$

$$D_{w\text{required}} = 3.879 \frac{\text{kip}}{\text{in}} \quad 16\text{ths of an inch}$$

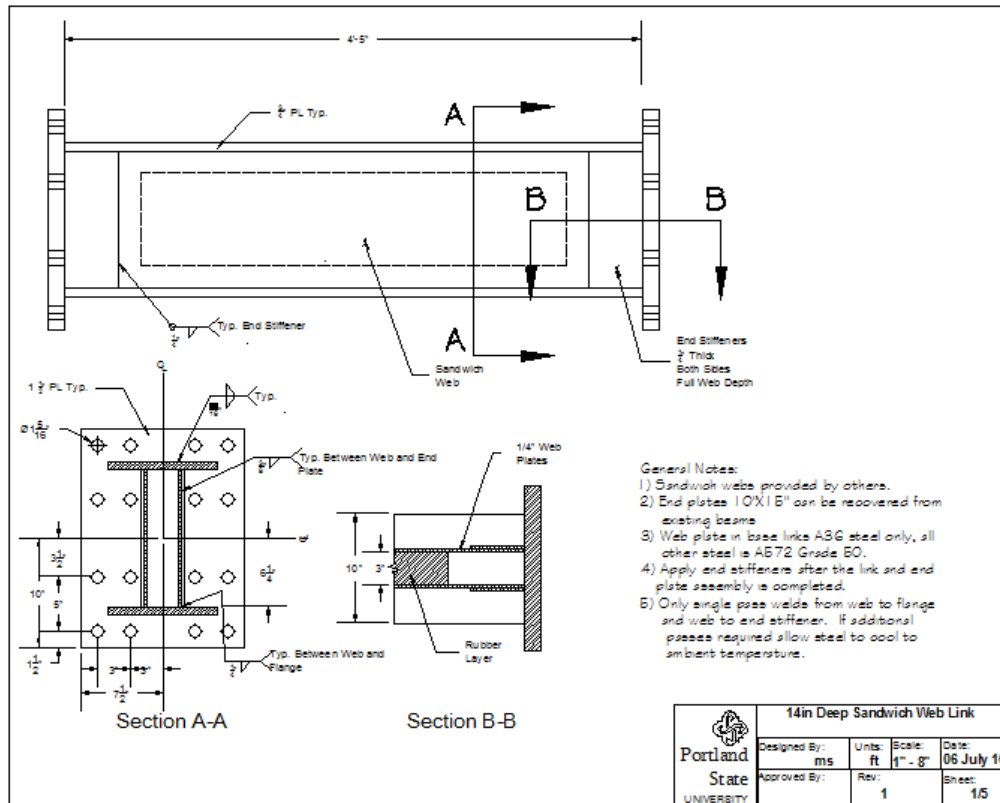
$$a_{\text{maxweb}} := \frac{t_{ws}}{2} - \frac{1}{16} \text{in} = 0.063 \text{in}$$

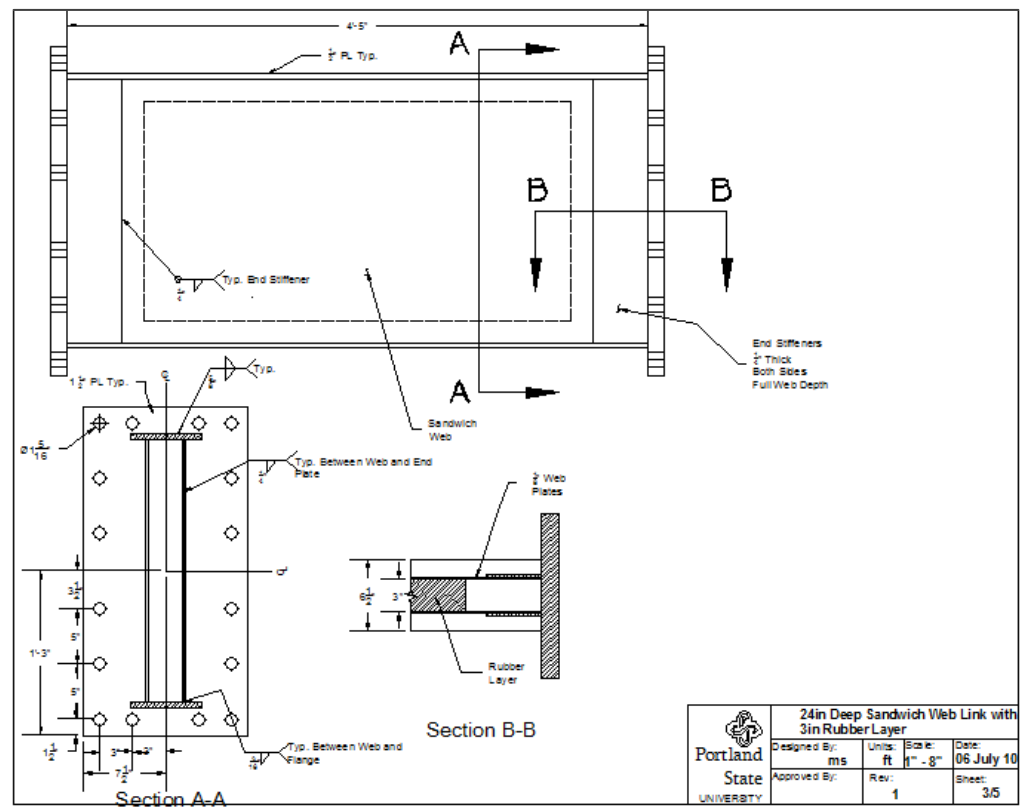
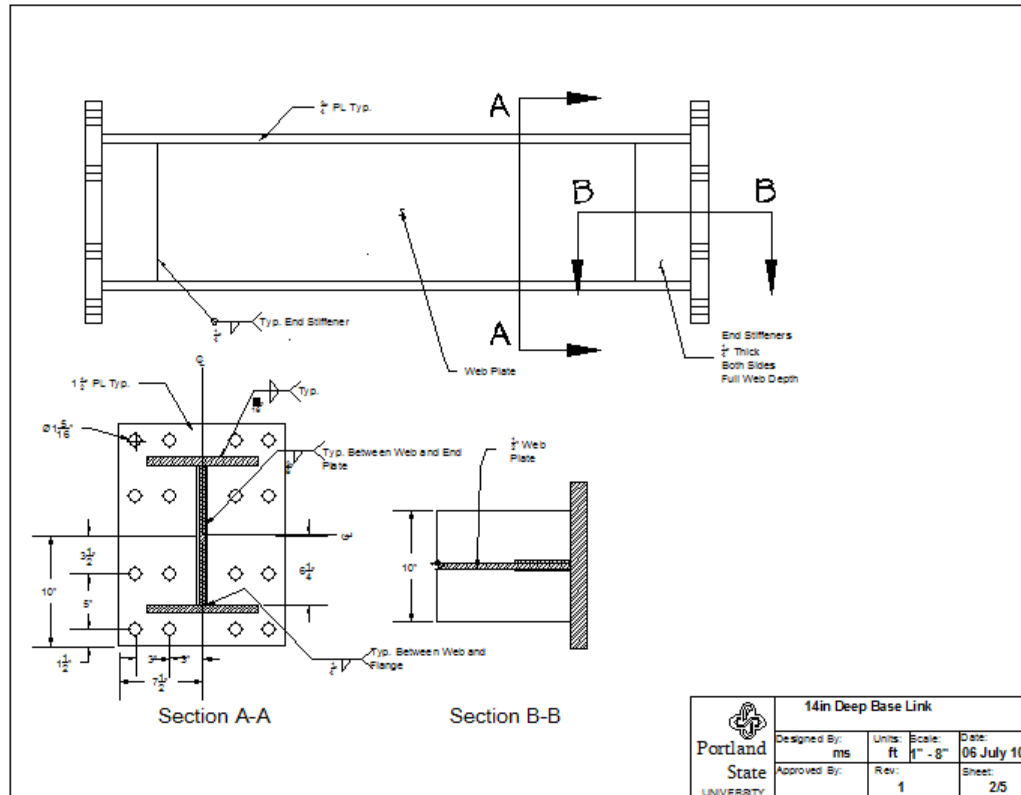
Need 1/4" fillet welds

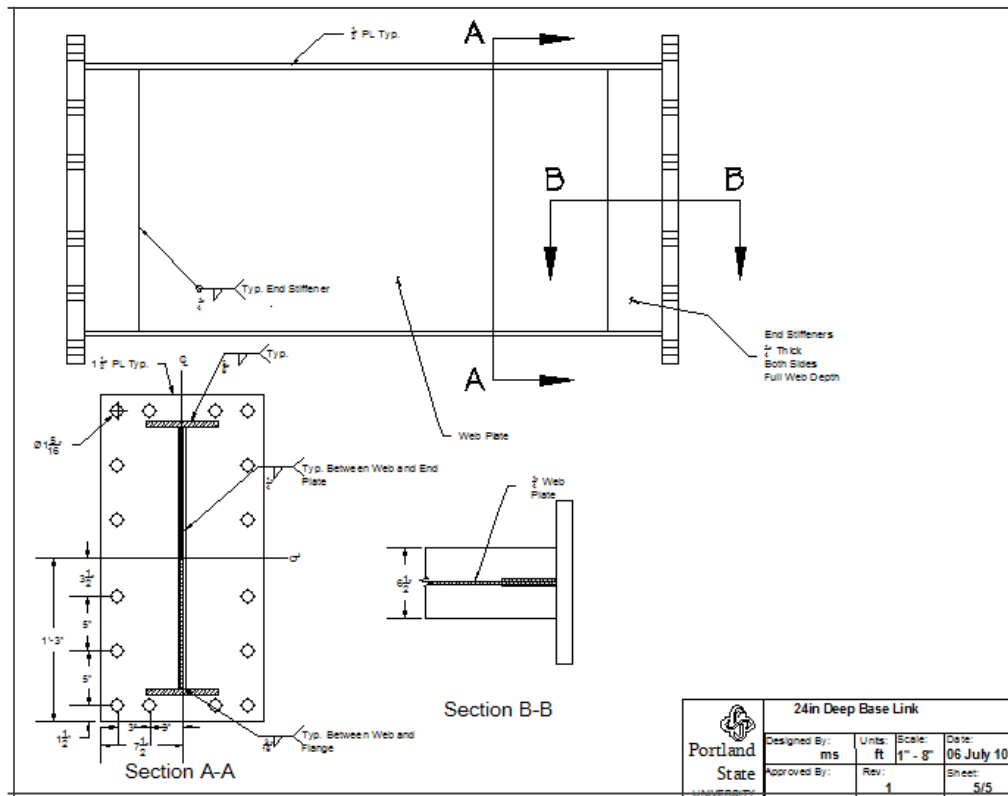
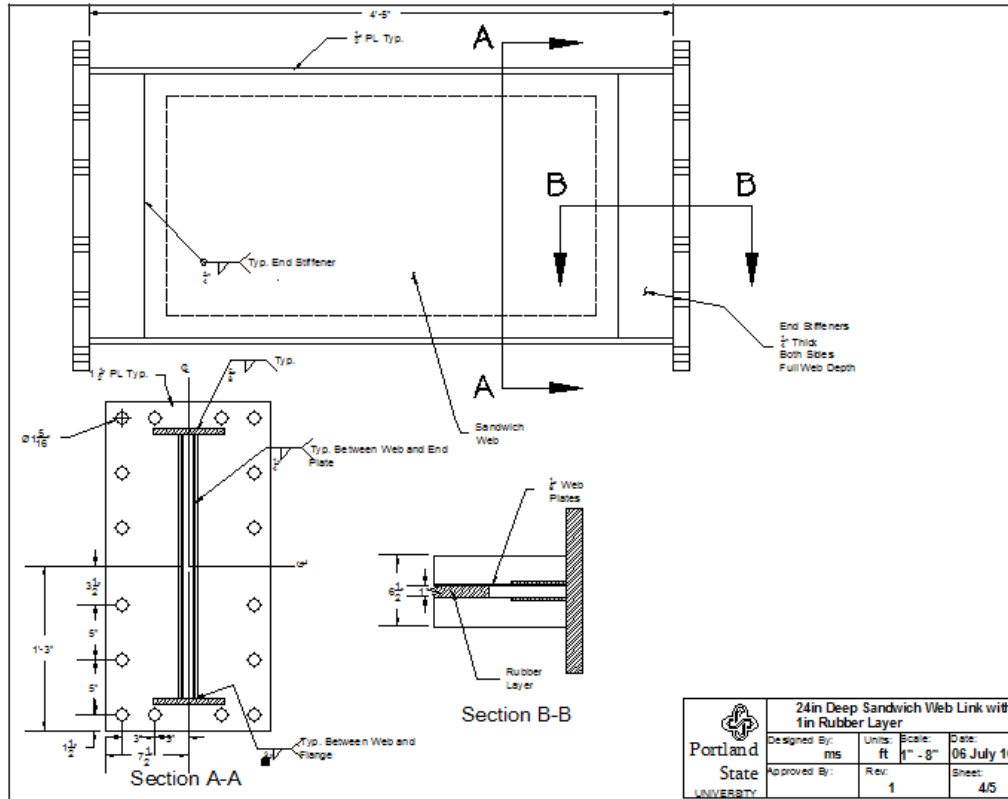
Allowed 2/16" fillet welds based on web thickness

Split the difference. Use 3/16" fillet weld

B. Shop Drawings of Links

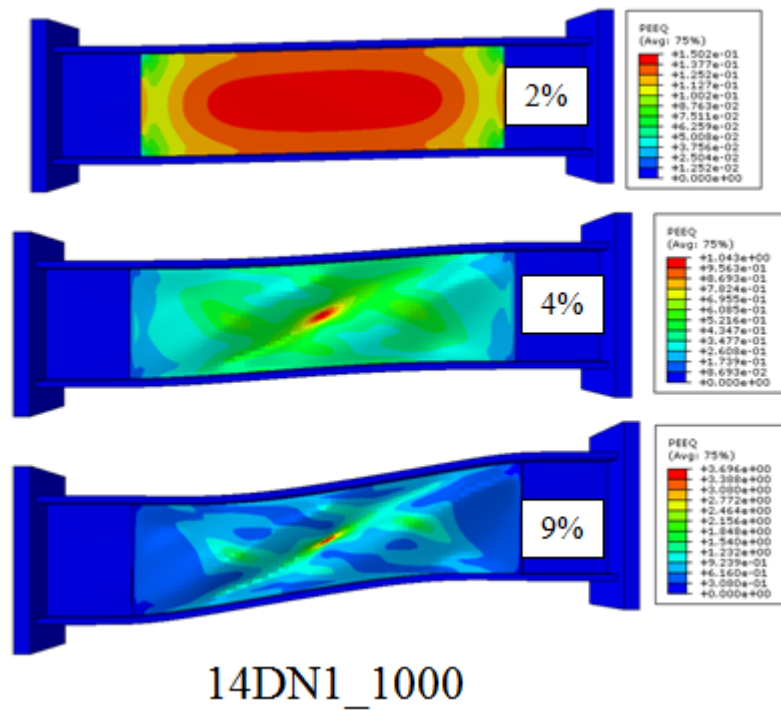
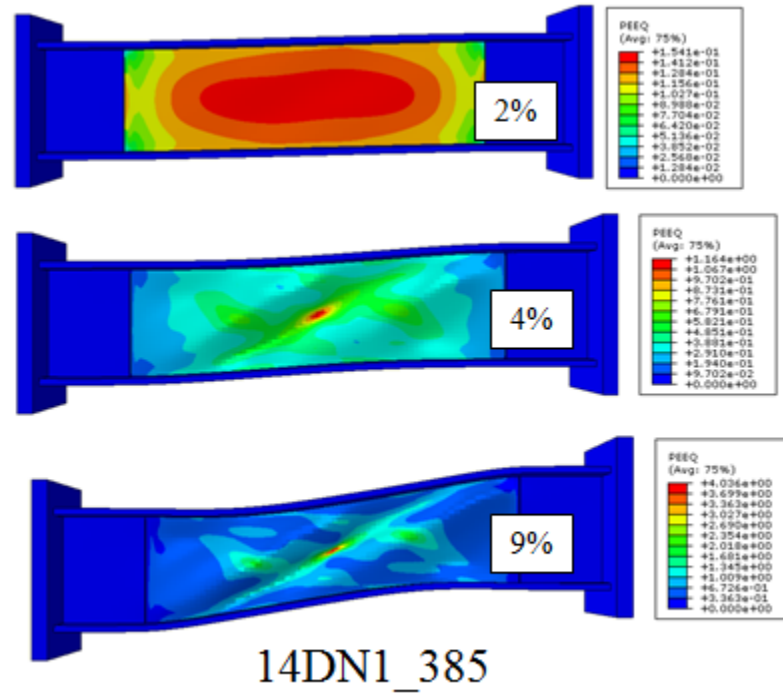


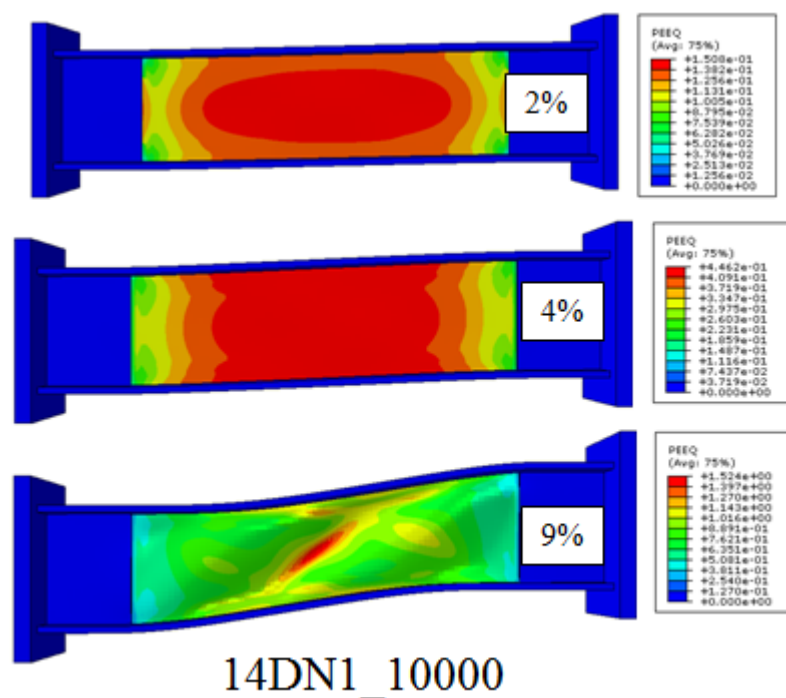
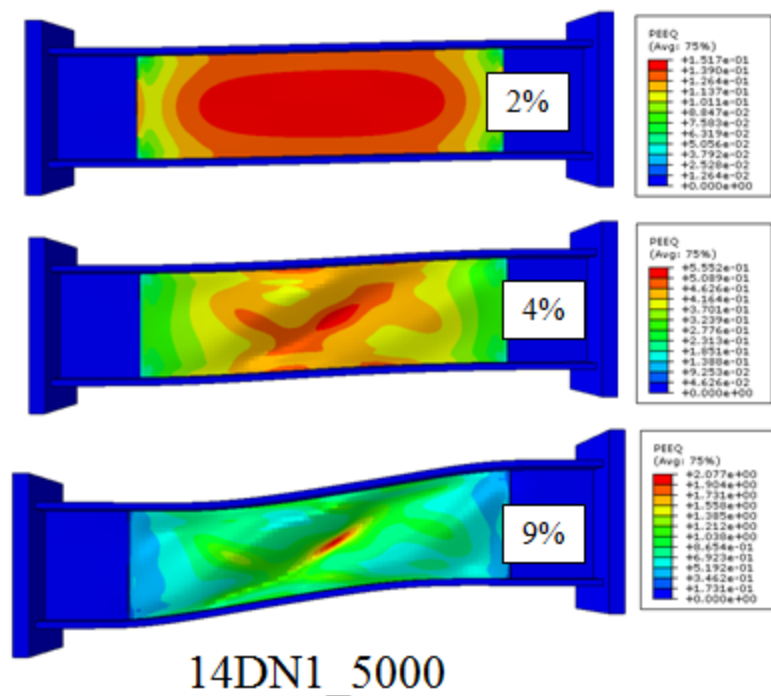


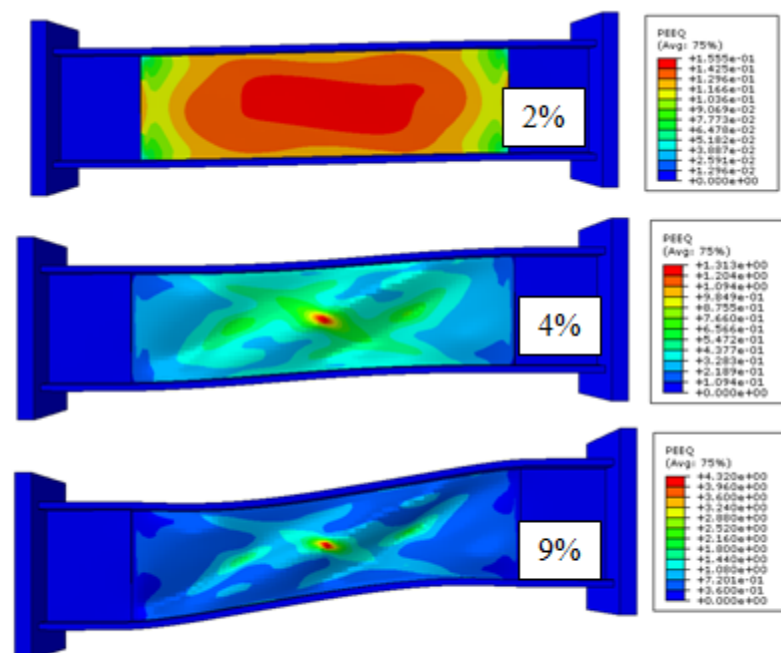


C. Finite Element Analysis Web Strain Distributions

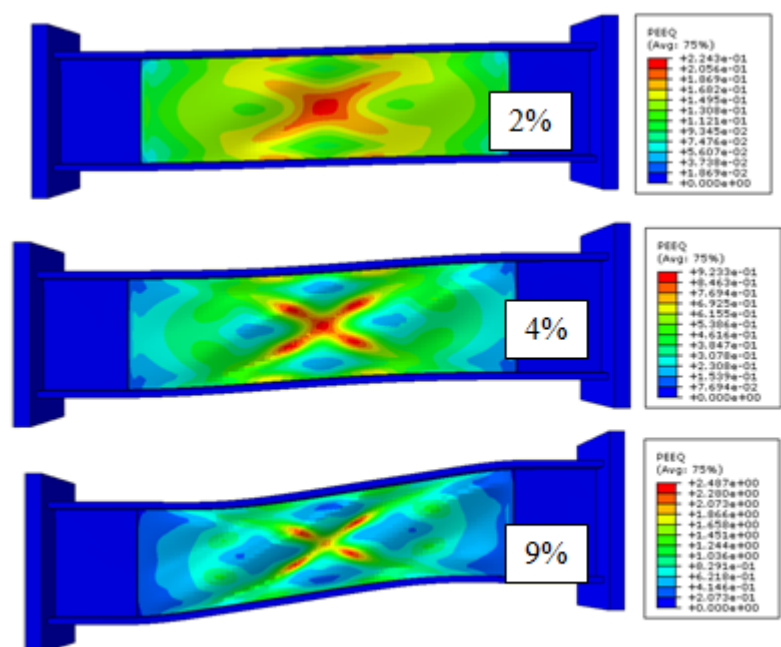
C.1 14in Deep Links





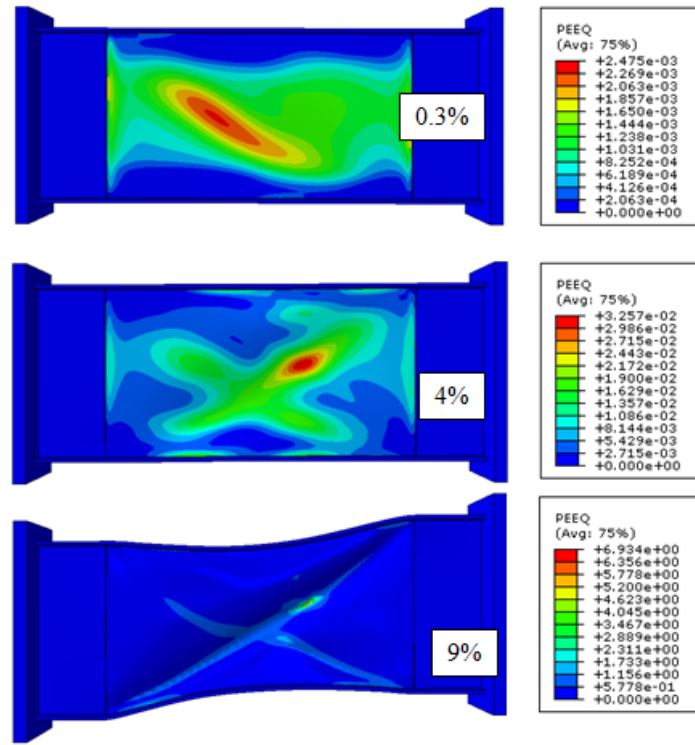


14DN2_1000

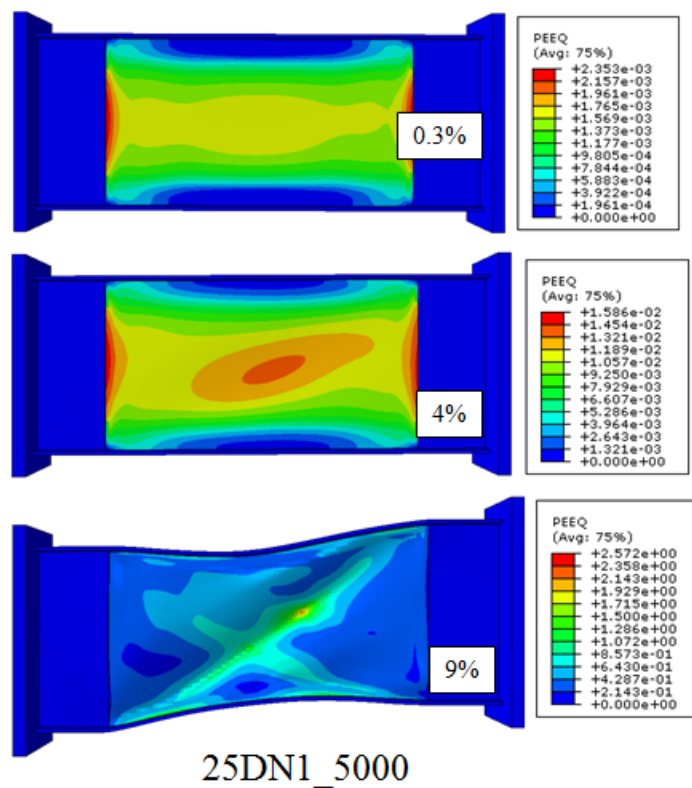
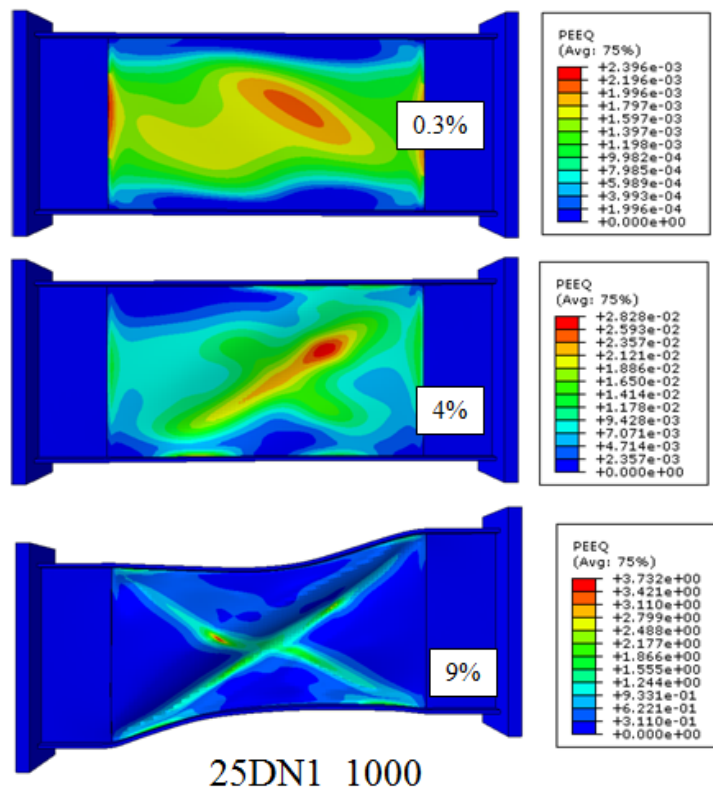


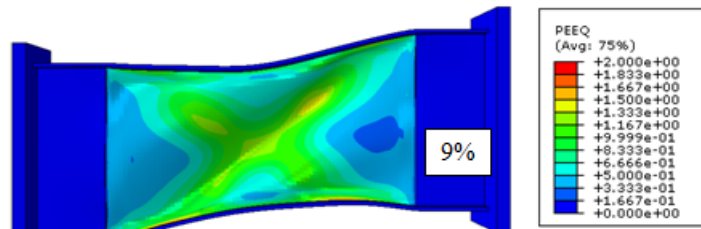
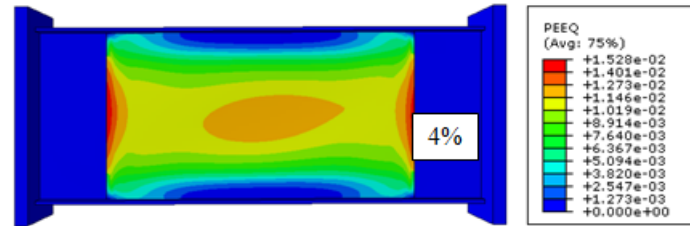
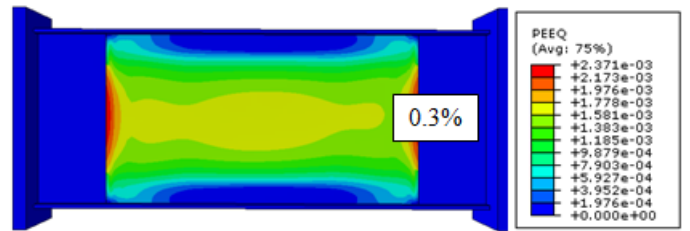
14DN3_1000

C.2 25in Deep Links

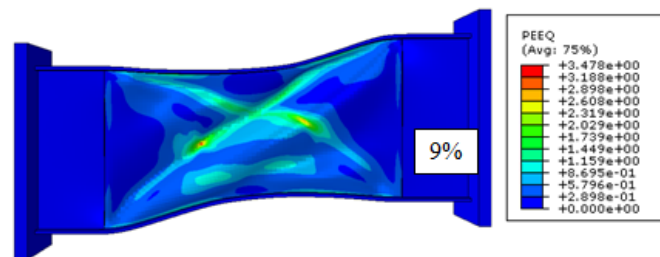
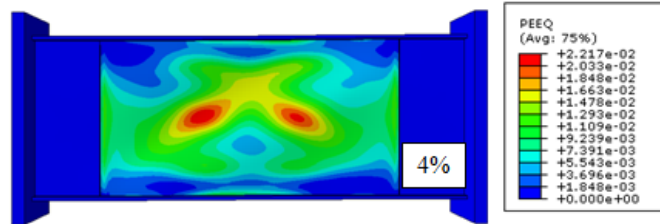
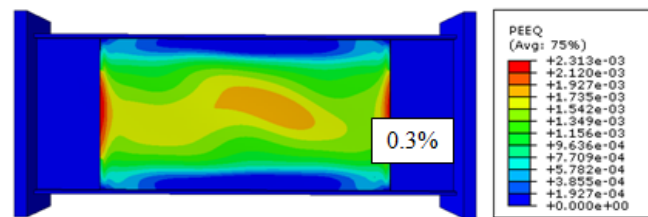


25DN1_385

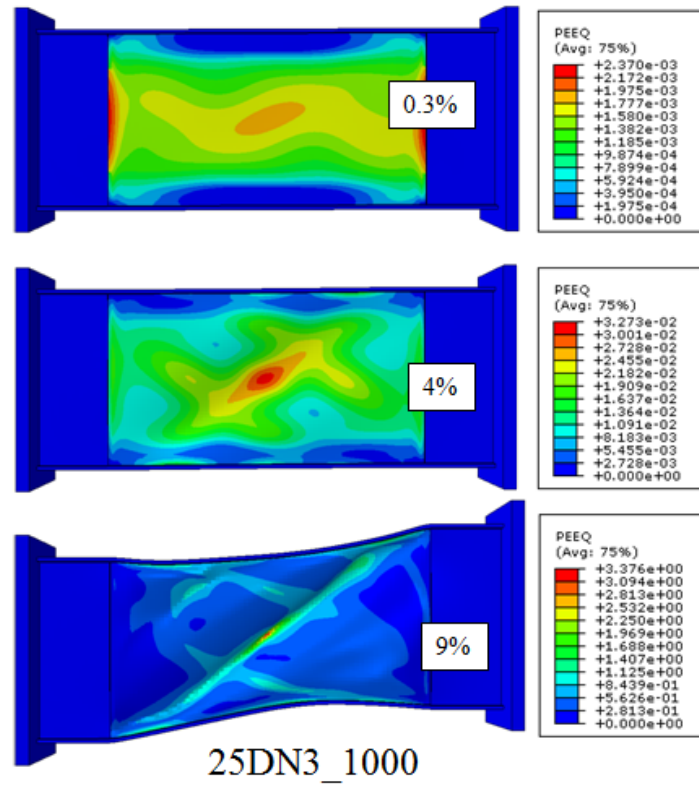




25DN1_10000

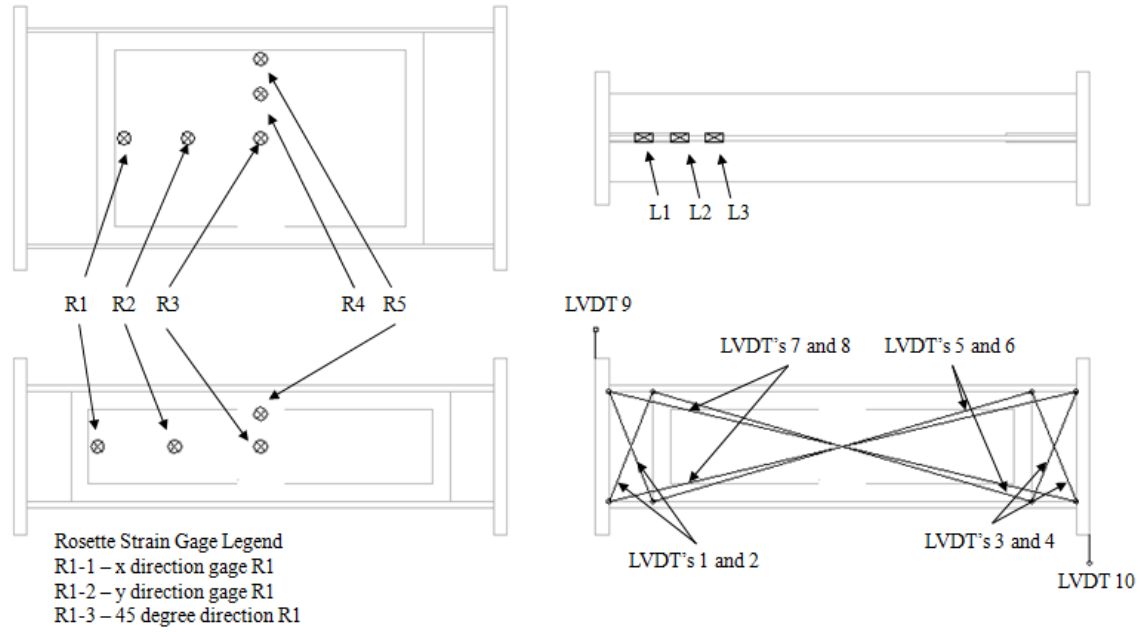


25DN2_1000

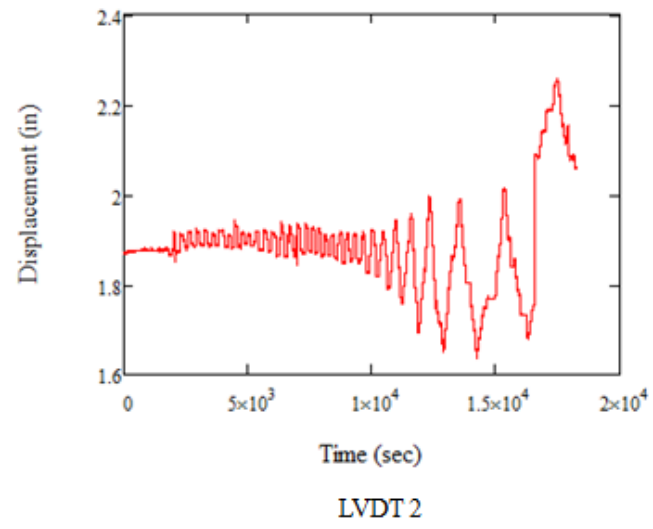
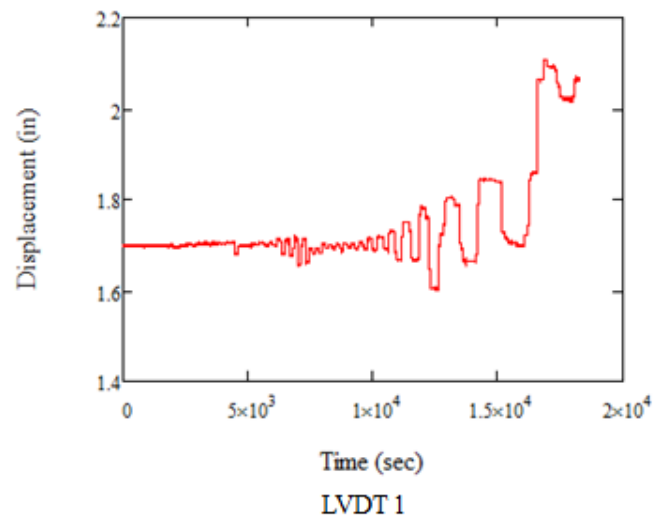


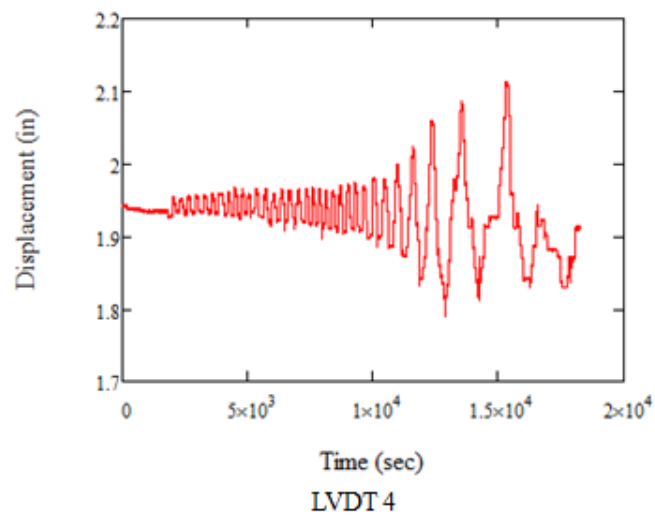
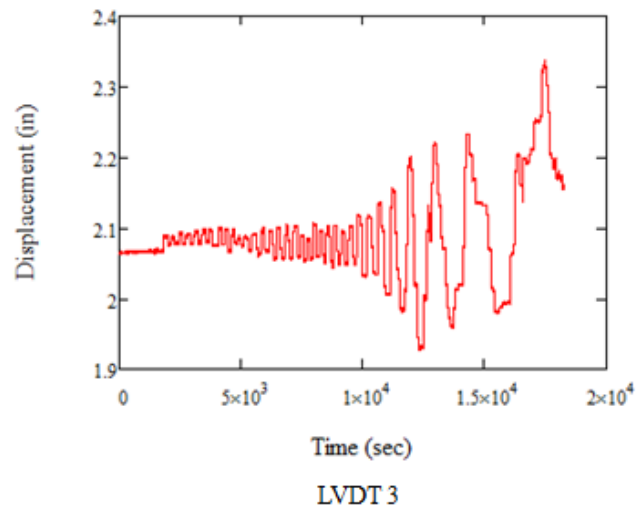
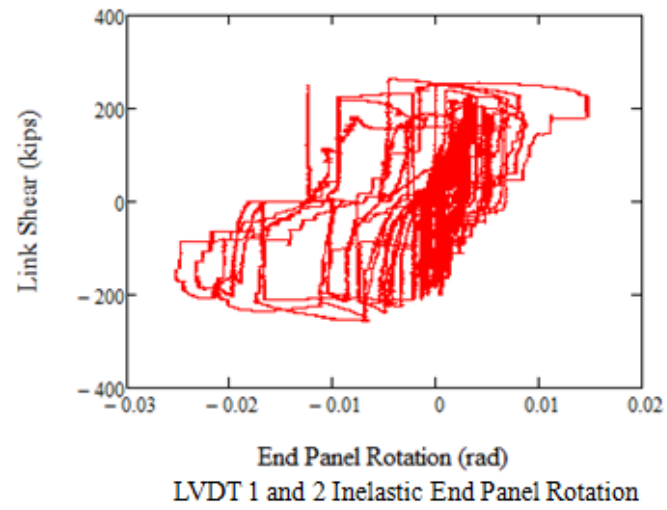
D. Experimental Data Sets

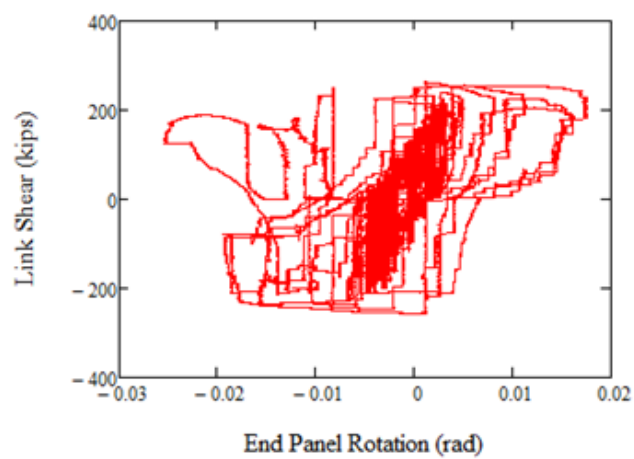
D.1 Data Set Instrumentation Schematic



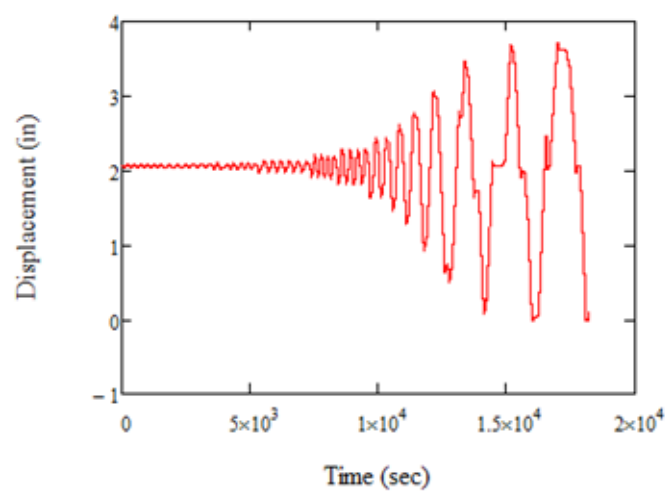
D.2 Link 14DBase



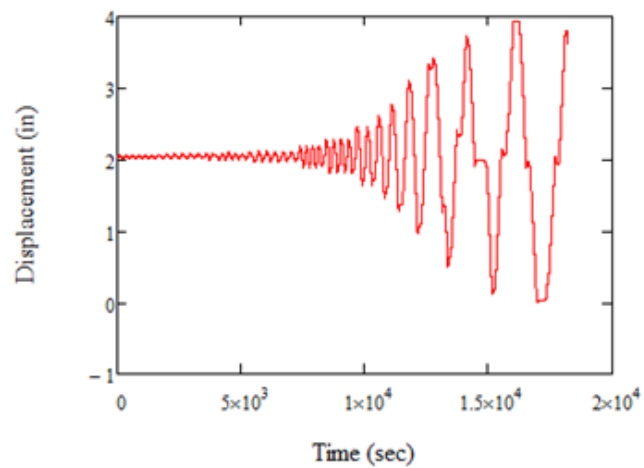




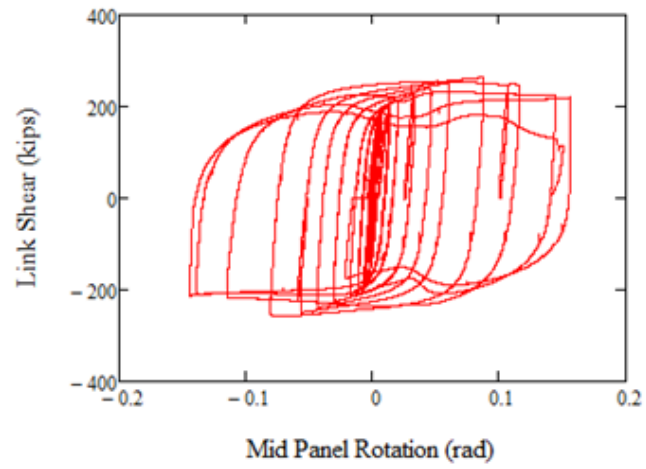
LVDT 3 and 4 Inelastic End Panel Rotation



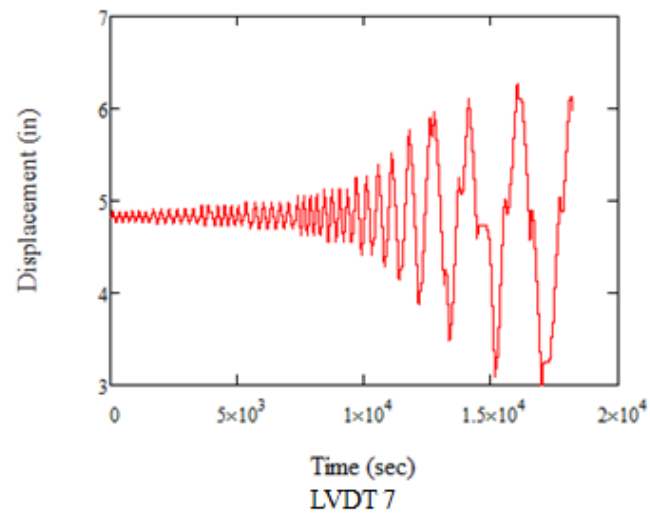
LVDT 5



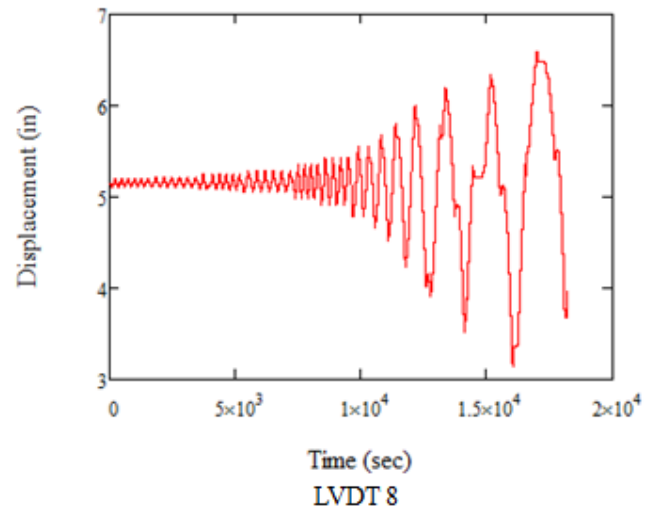
LVDT 6



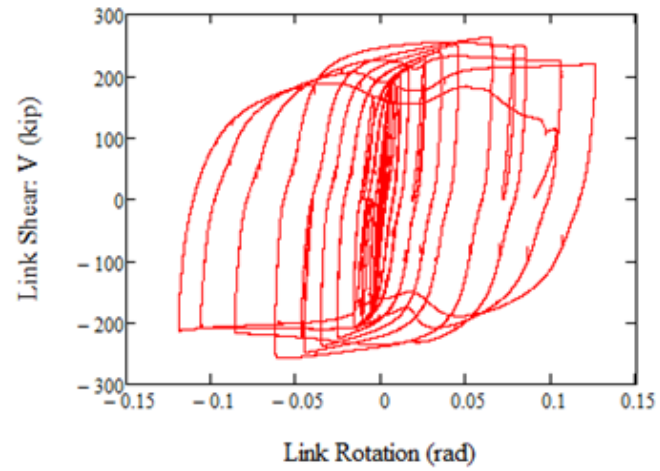
LVDT 5 and 6 Inelastic Mid Panel Rotation



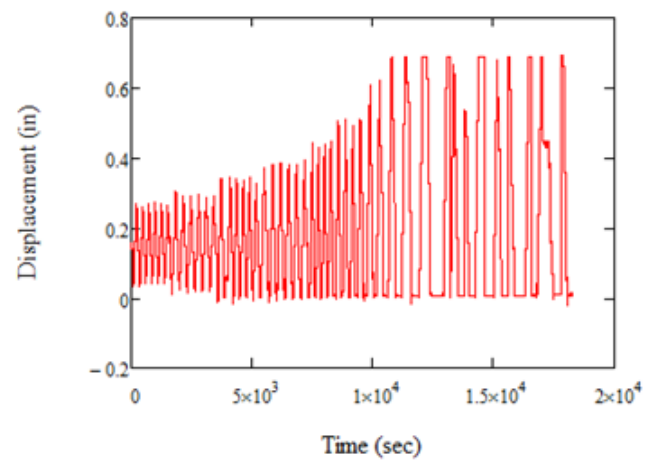
LVDT 7



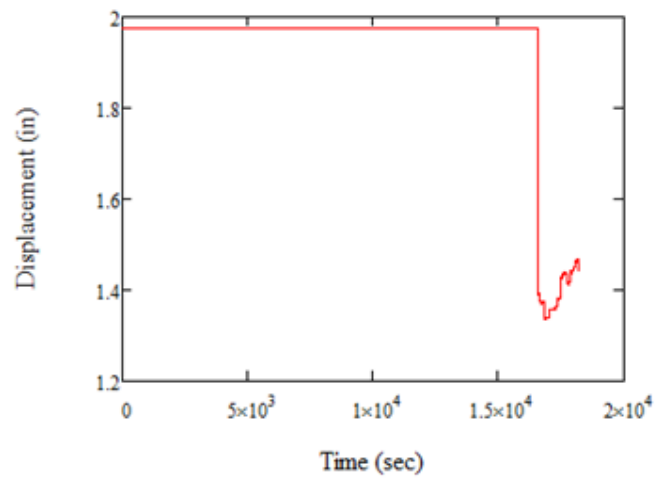
LVDT 8



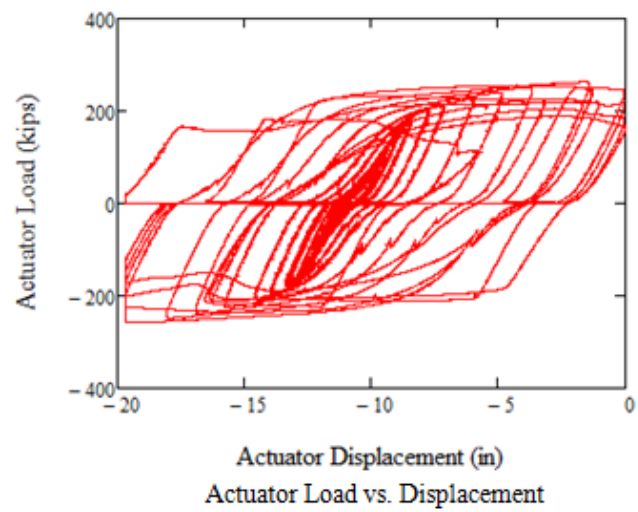
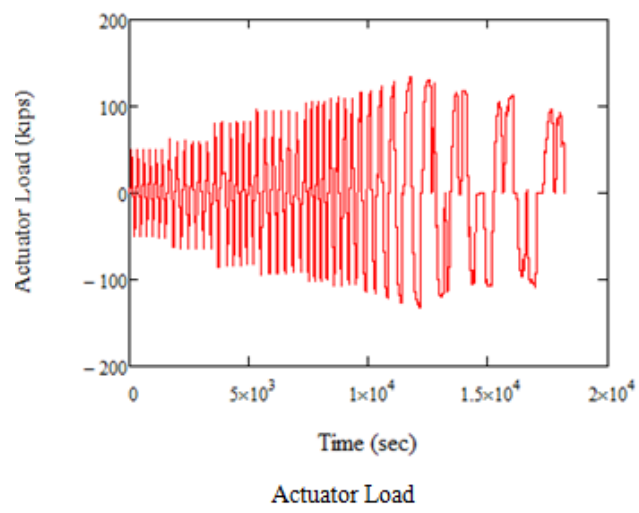
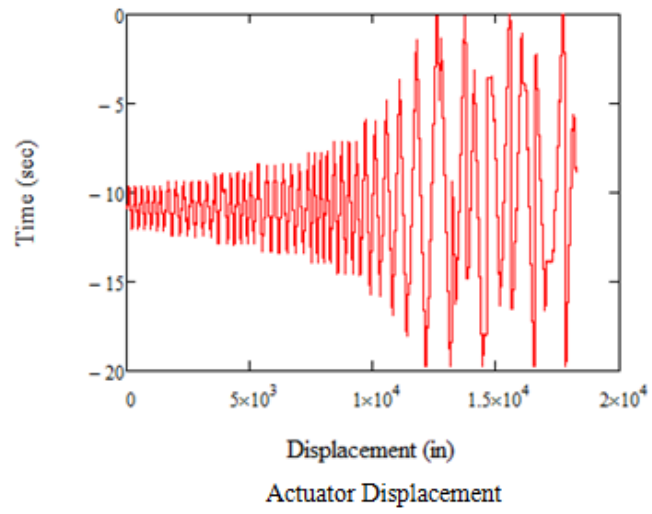
LVDT 7 and 8 Inelastic Rotation

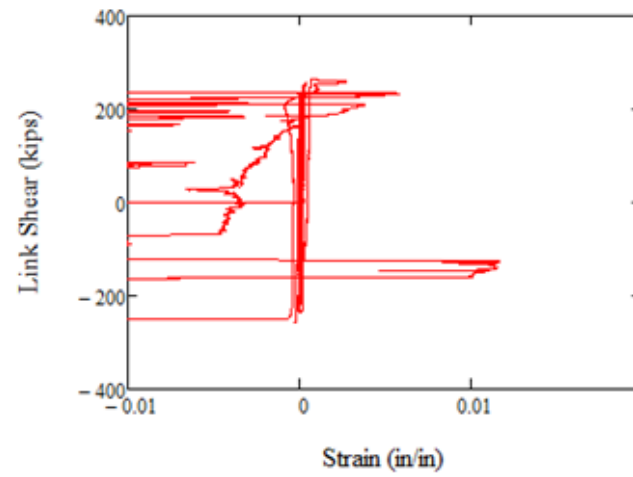


LVDT 9

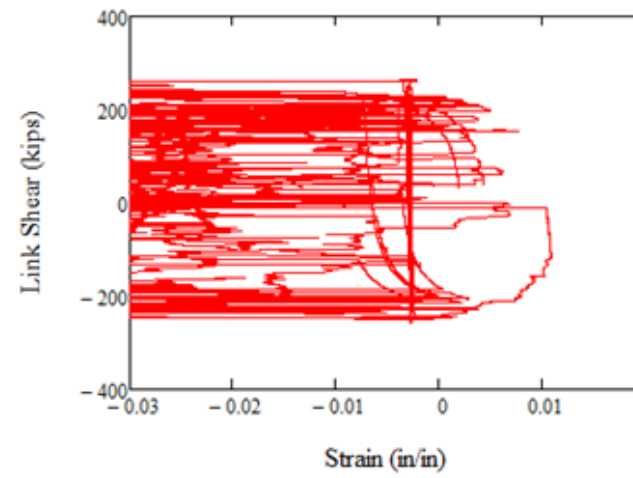


LVDT 10

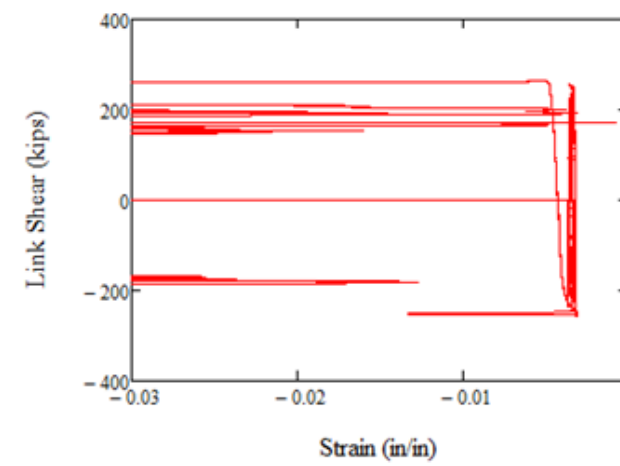




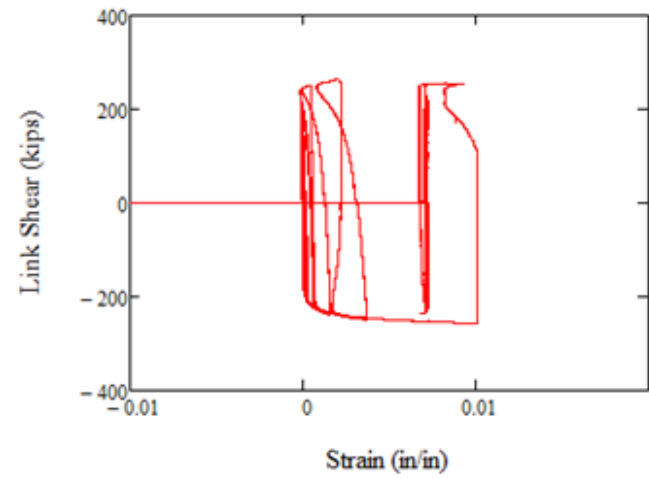
R1-1



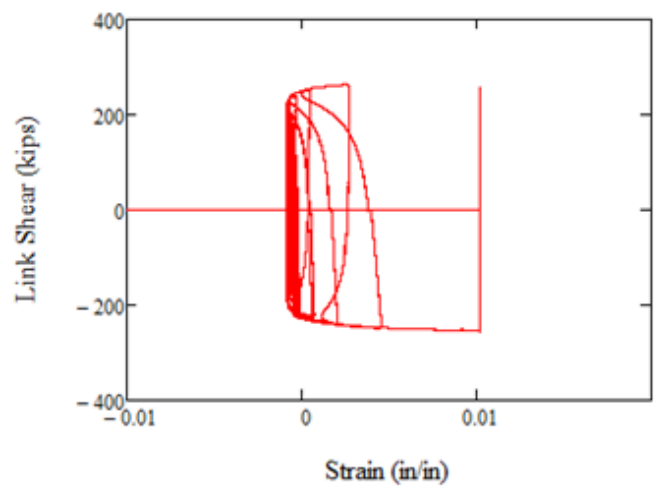
R1-2



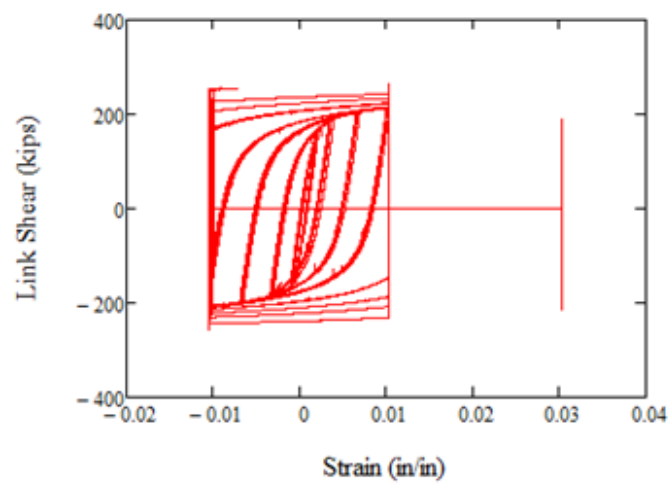
R1-3



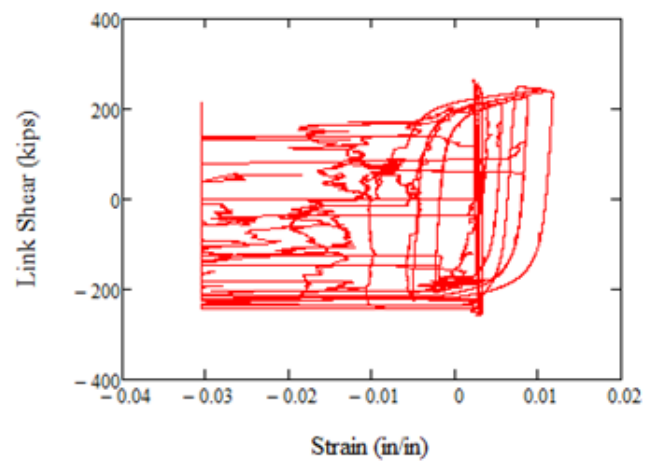
R2-1



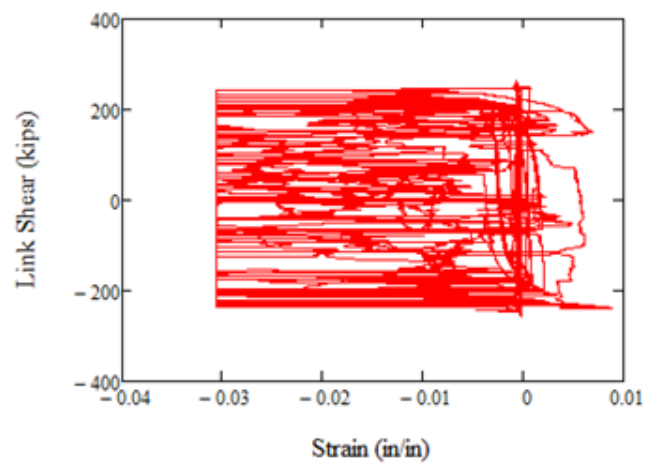
R2-2



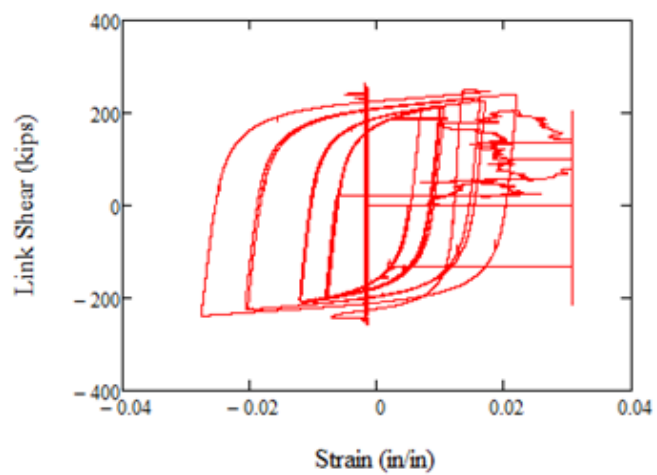
R2-3



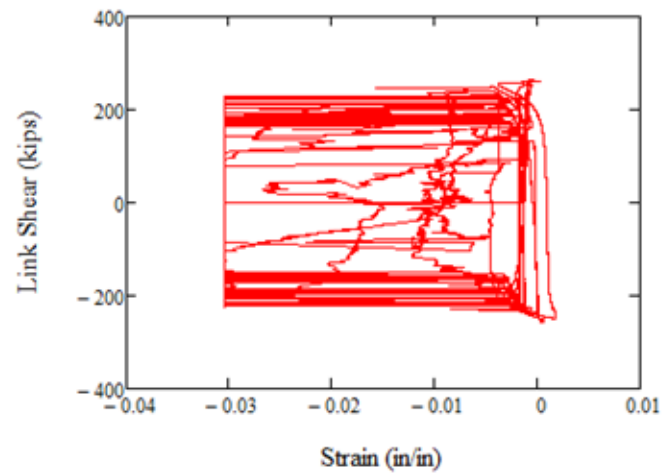
R3-1



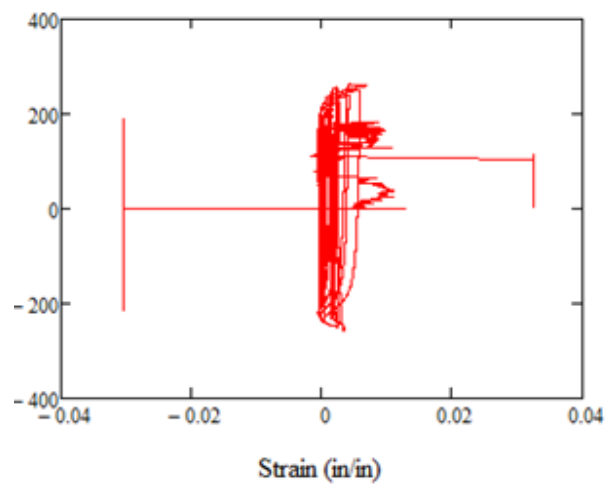
R3-2



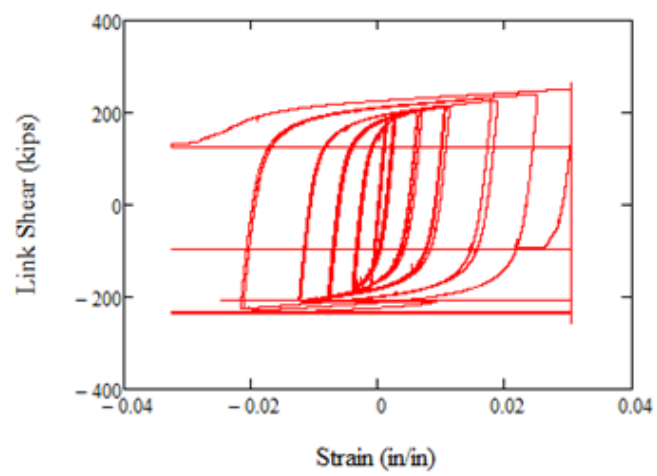
R3-3



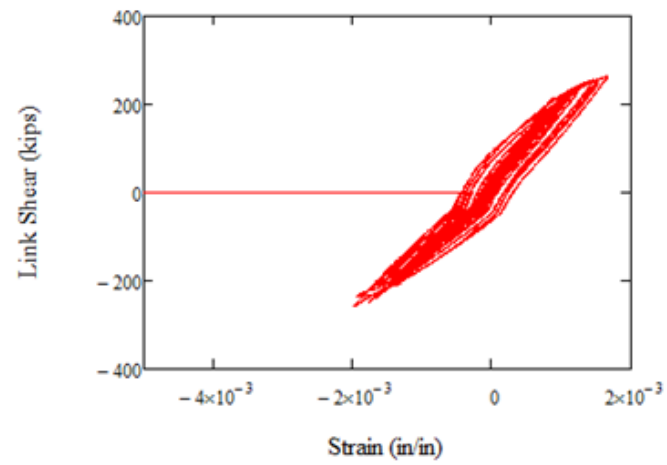
R5-1



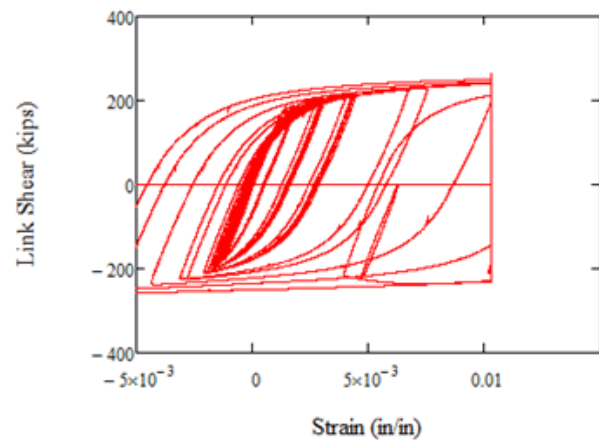
R5-2



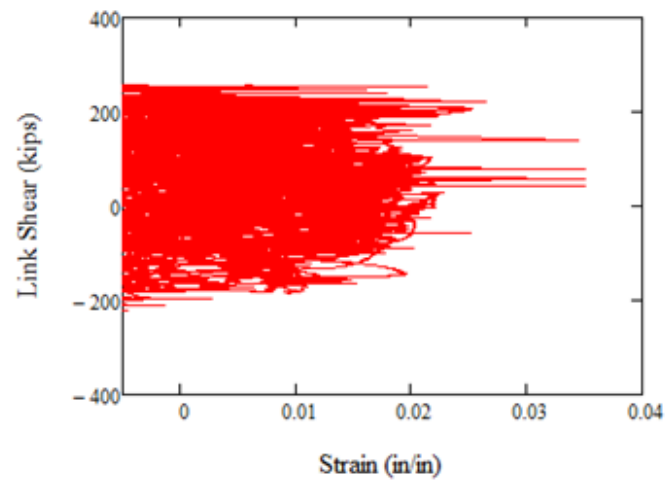
R5-3



L1

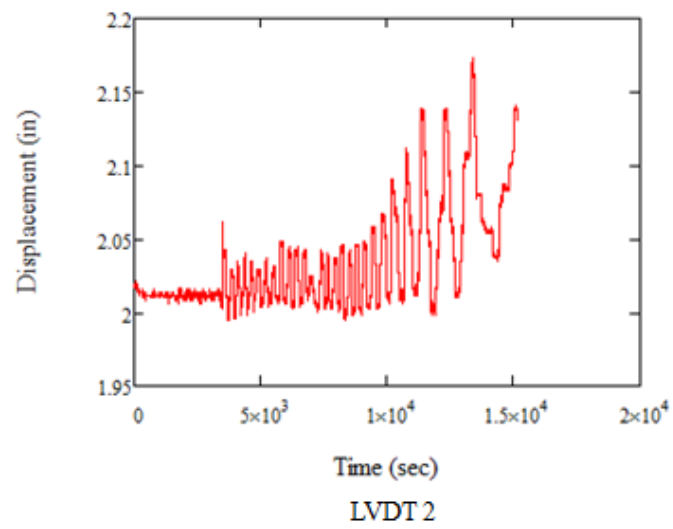
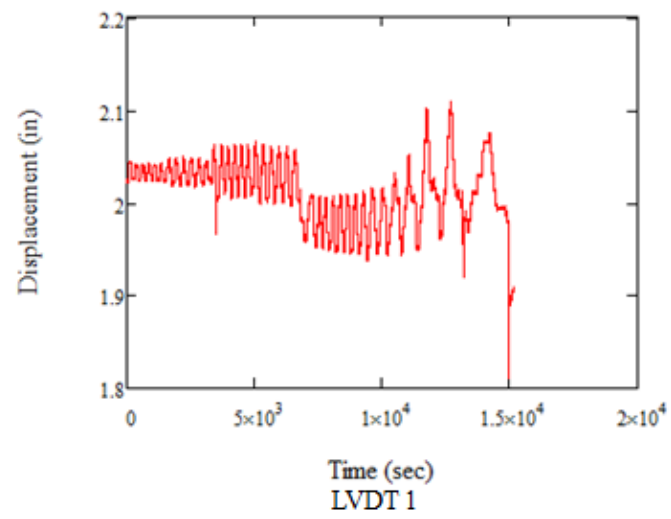


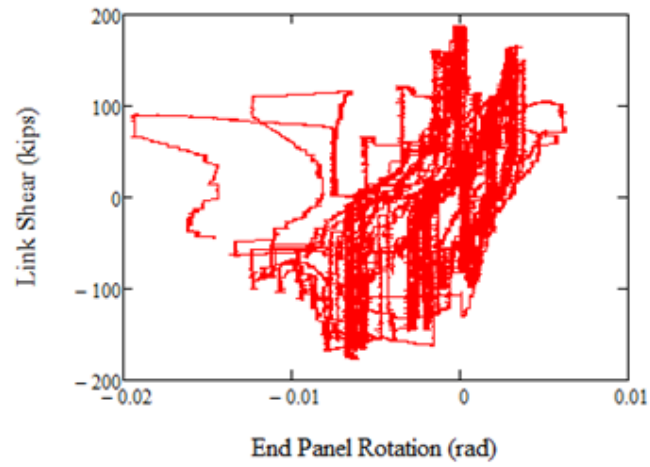
L2



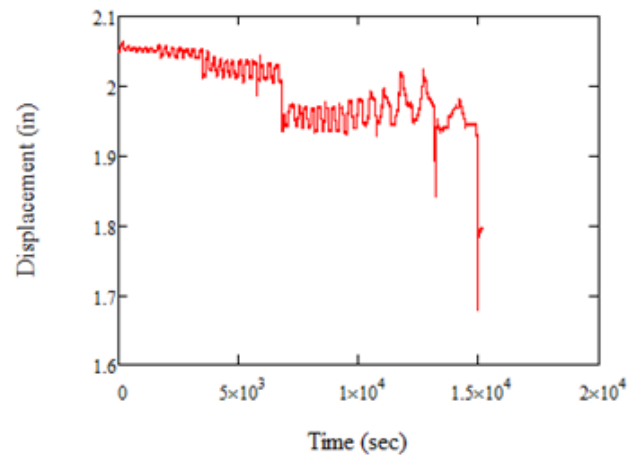
L3

D.3 Link 14DN3_1000

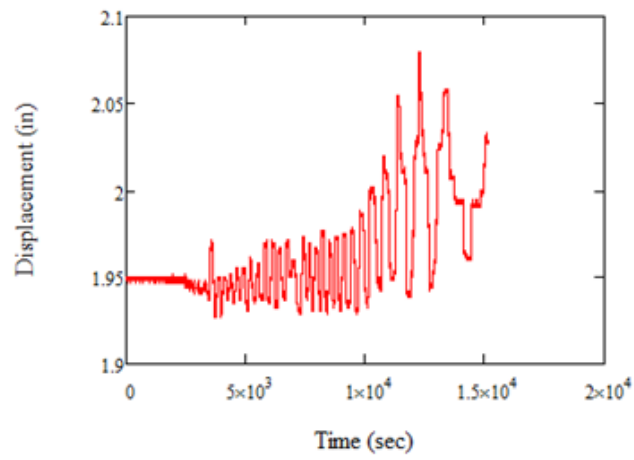




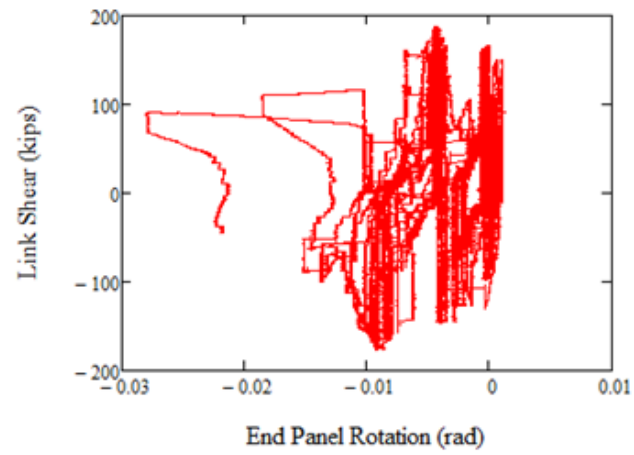
LVDT 1 and 2 Inelastic End Panel Rotation



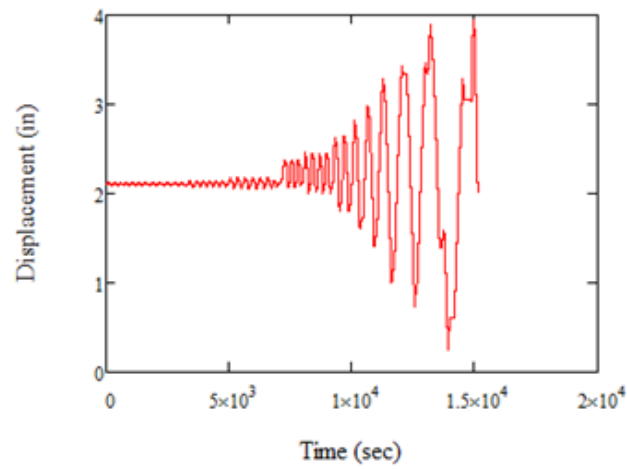
LVDT 3



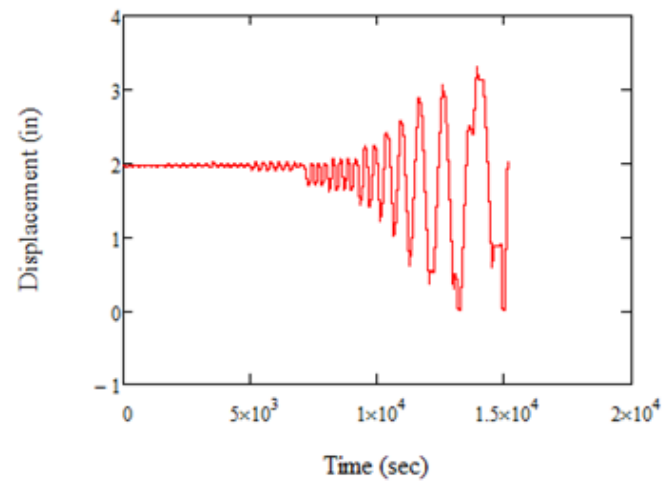
LVDT 4



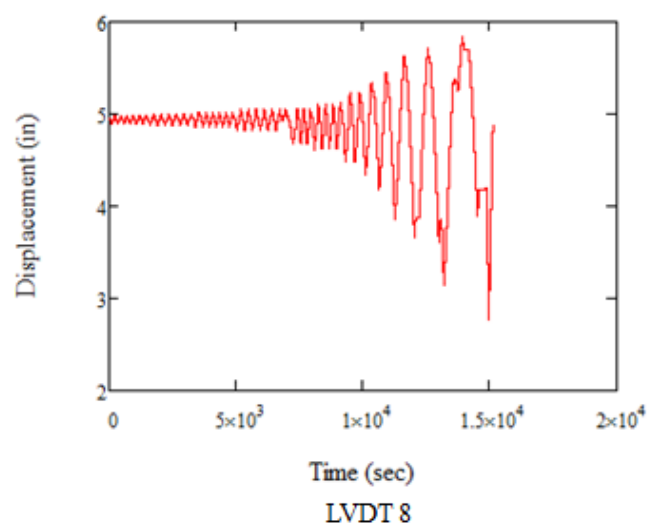
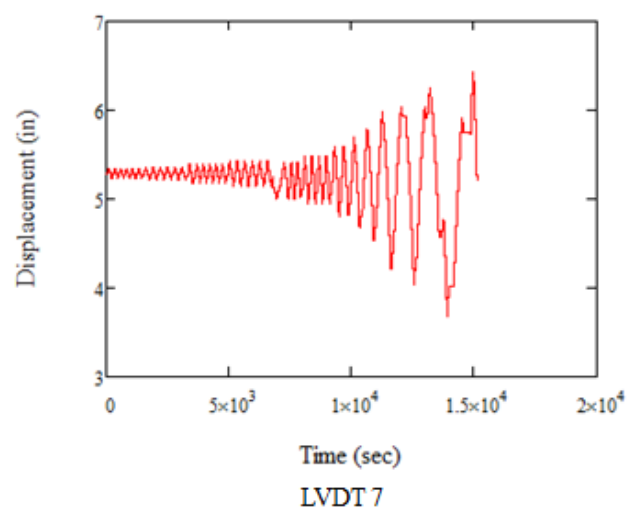
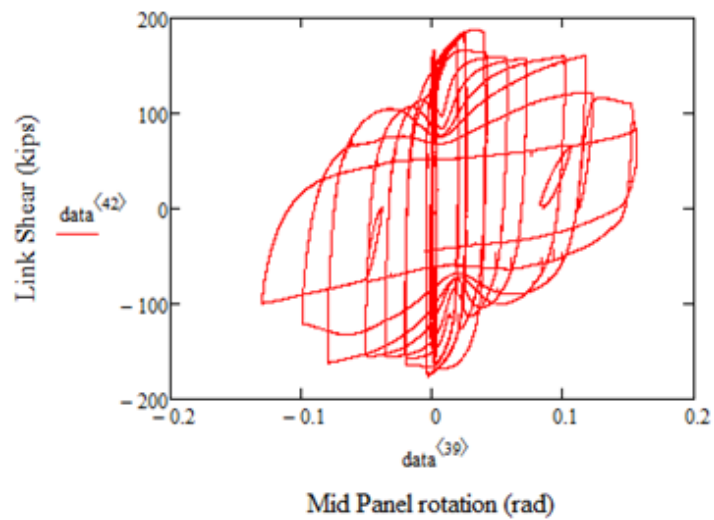
LVDT 3 and 4 Inelastic End Panel Rotation

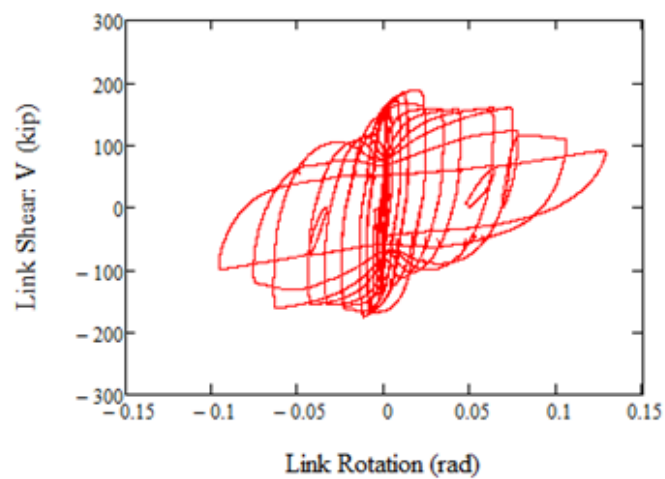


LVDT 5

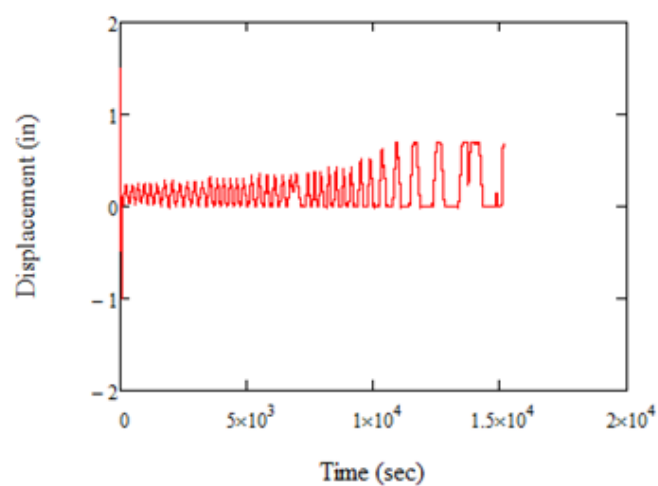


LVDT 6

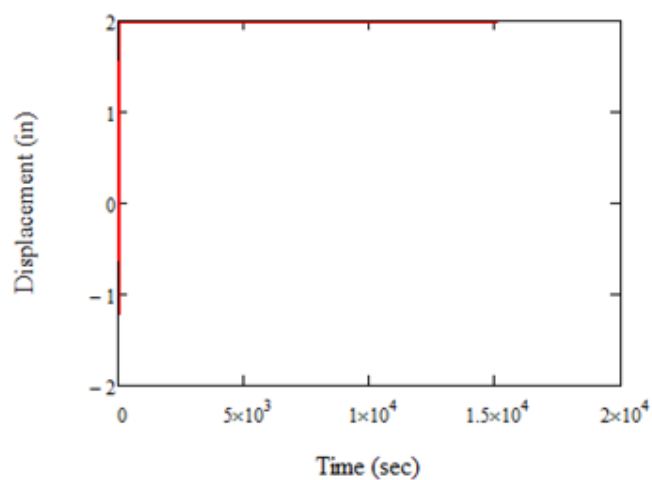




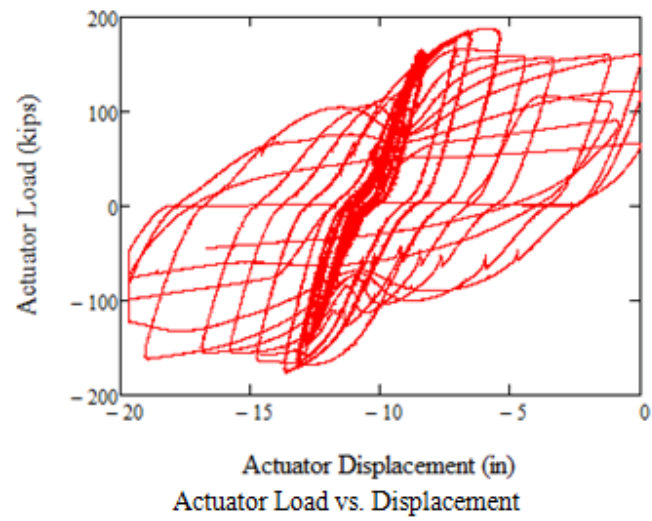
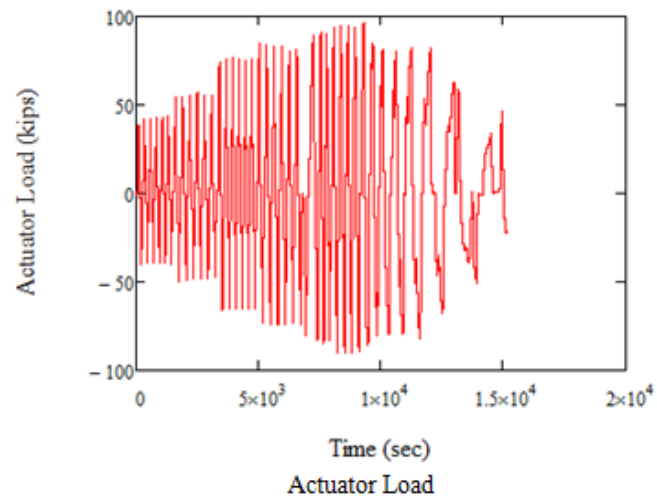
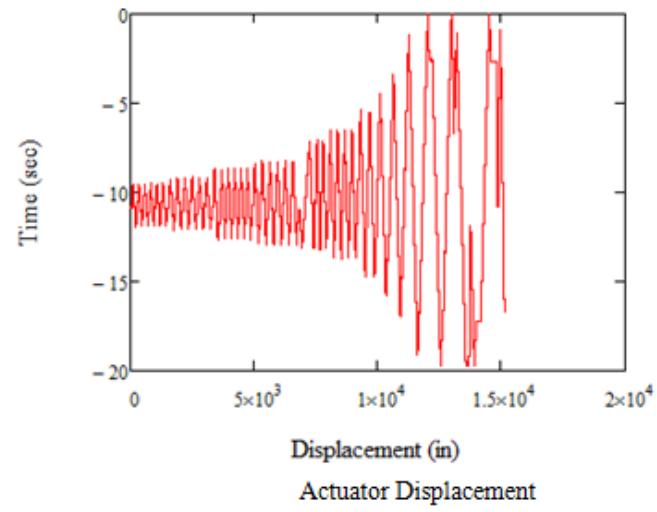
LVDT 7 and 8 Inelastic Rotation

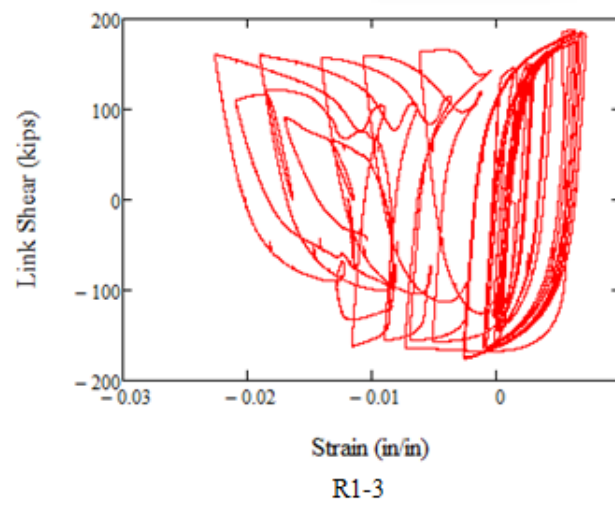
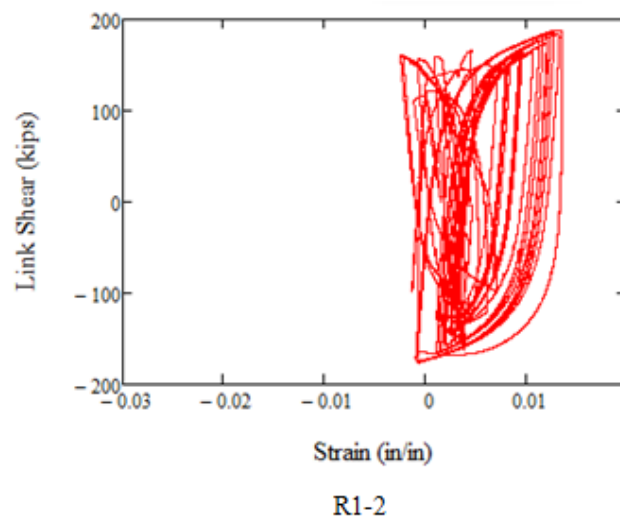
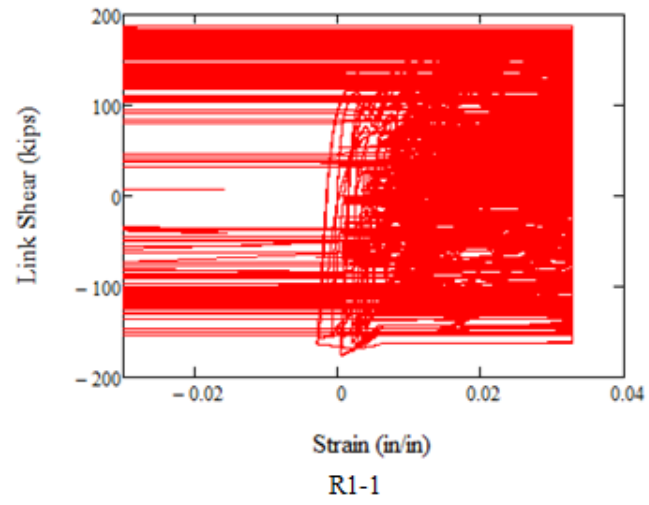


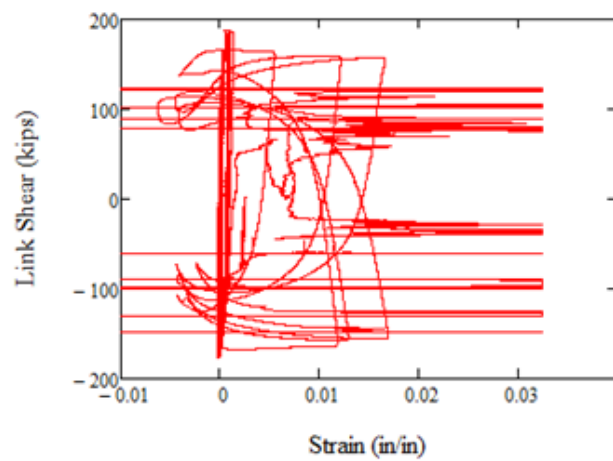
LVDT 9



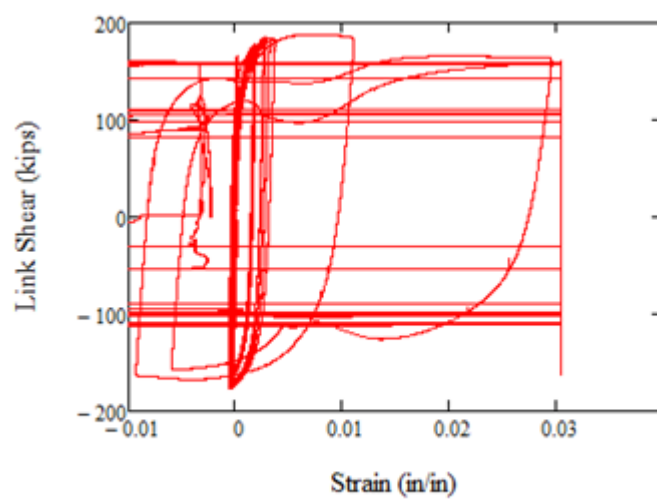
LVDT 10



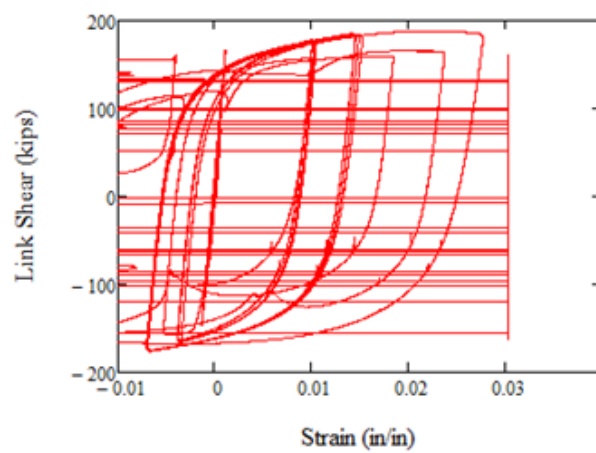




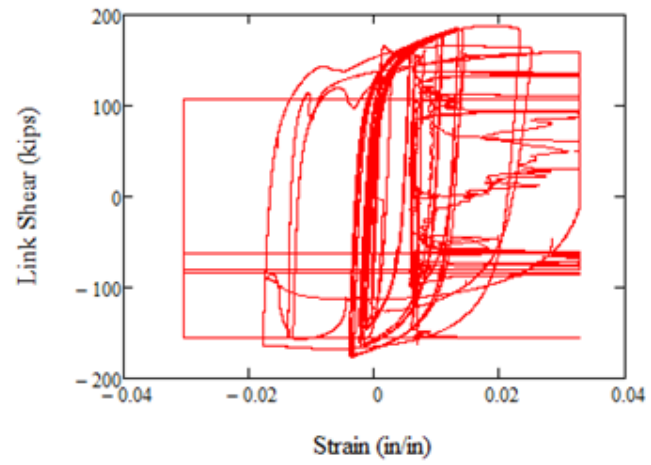
R2-1



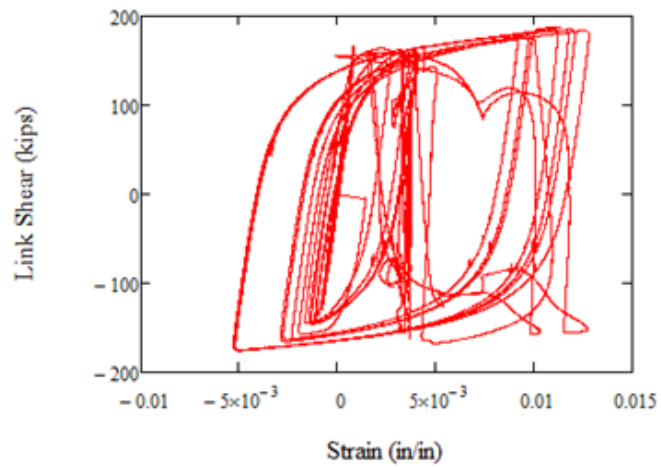
R2-2



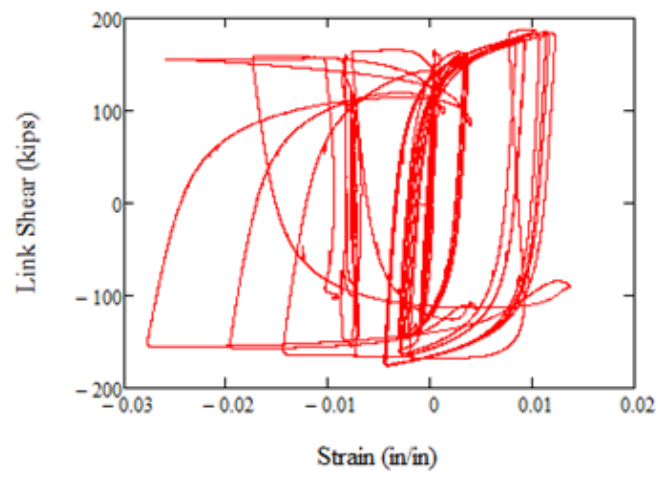
R2-3



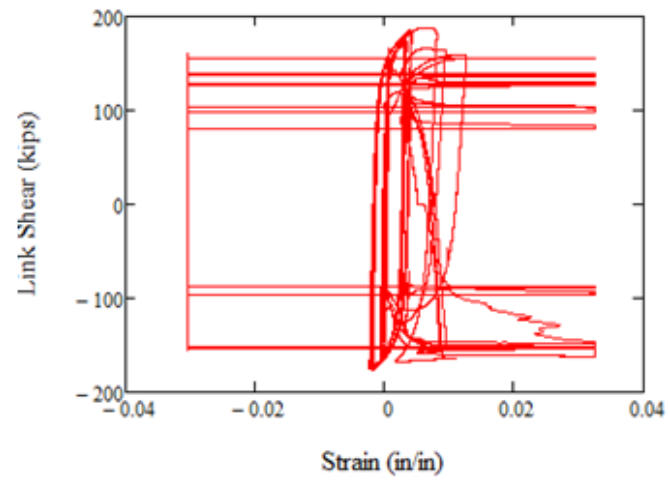
R3-1



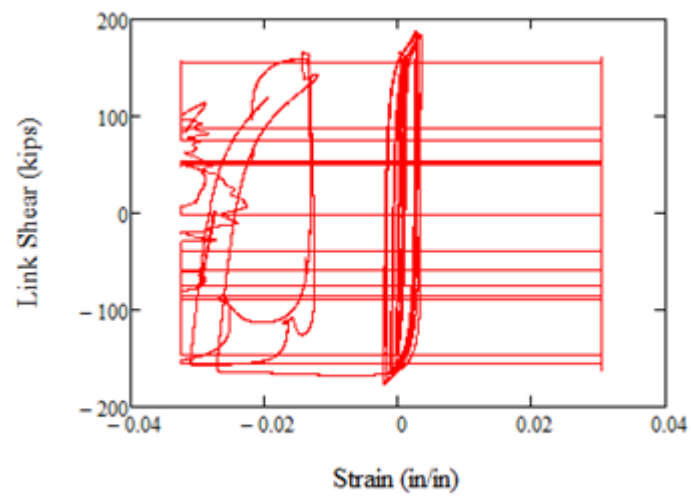
R3-2



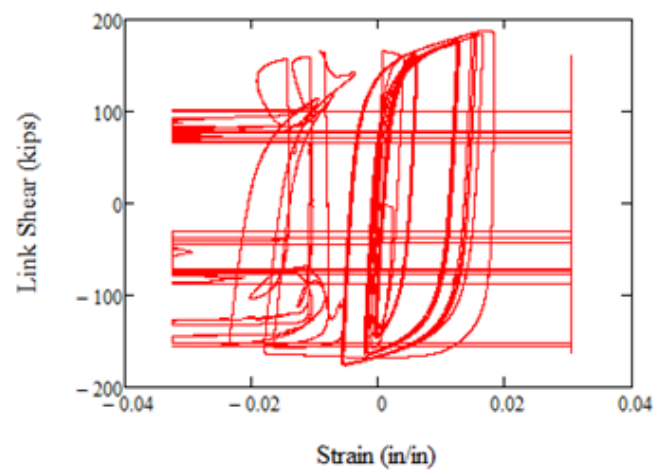
R3-3



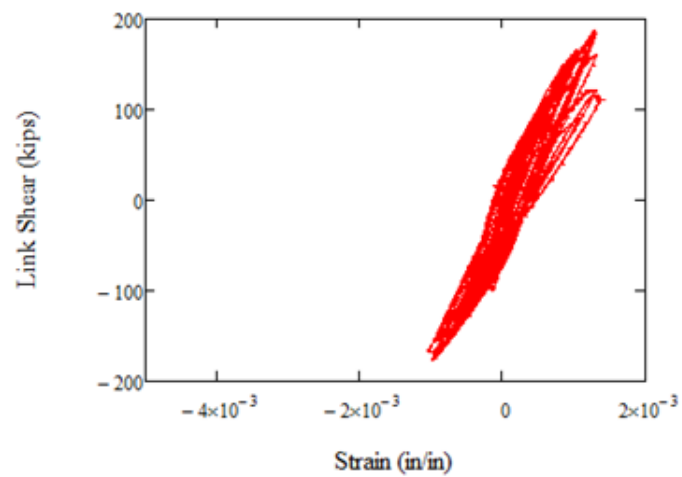
R5-1



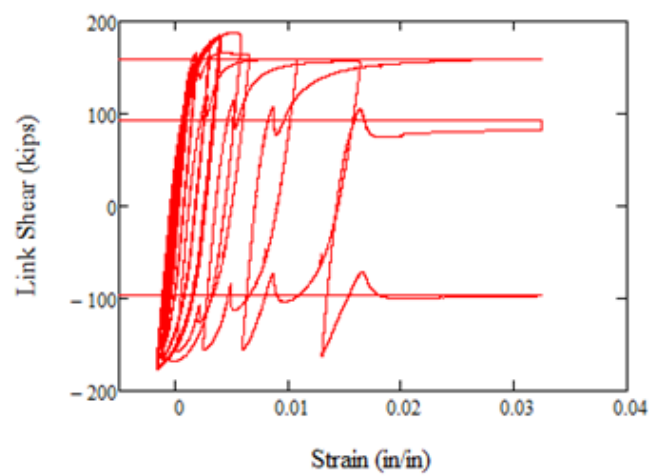
R5-2



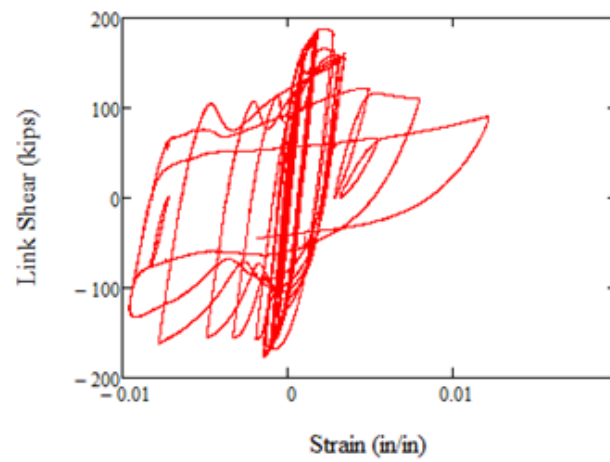
R5-3



L1

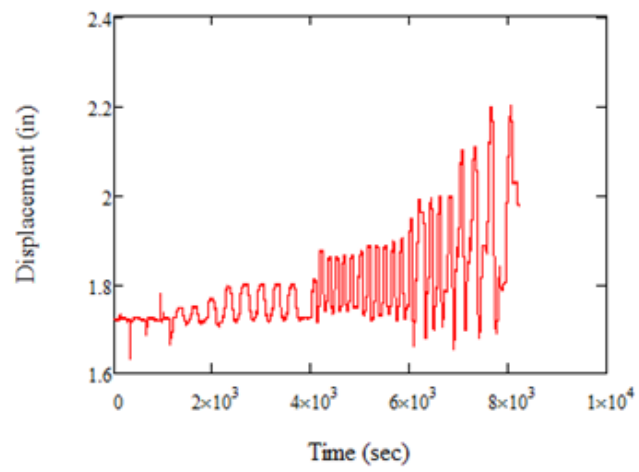


L2

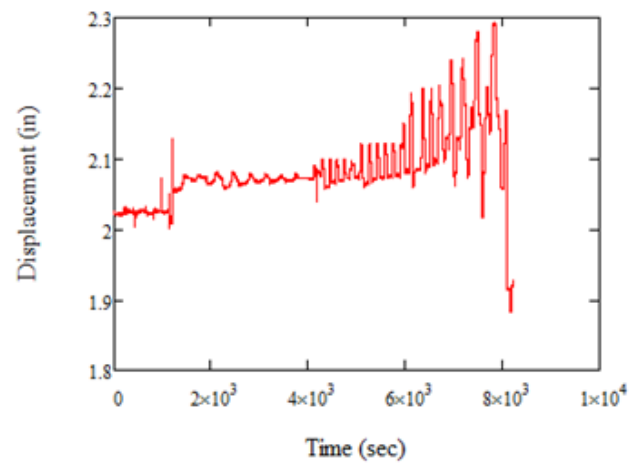


L3

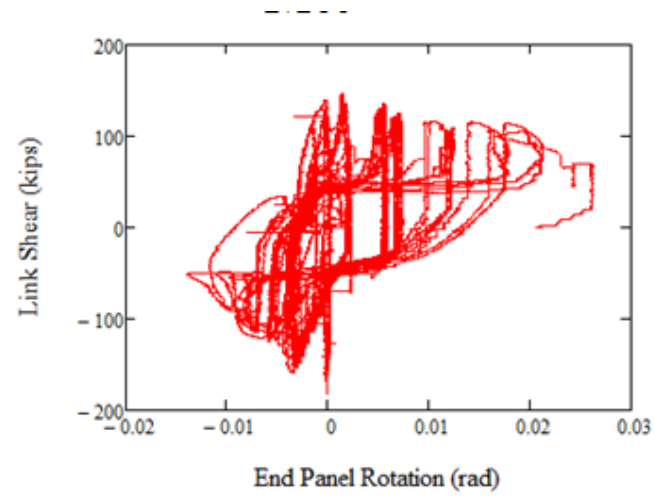
D.4 Link 25DBase



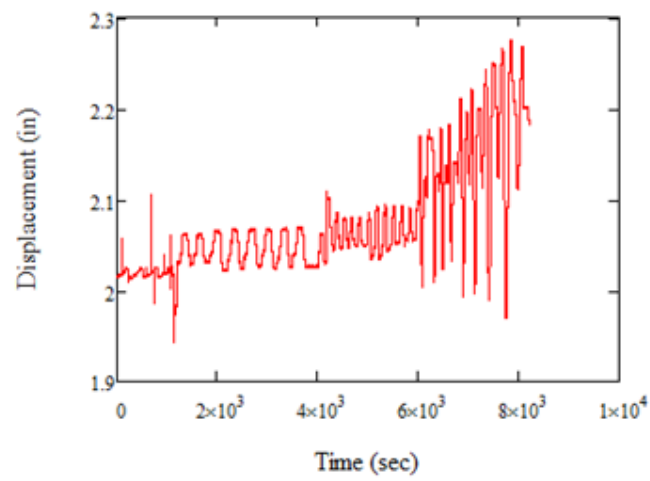
LVDT 1



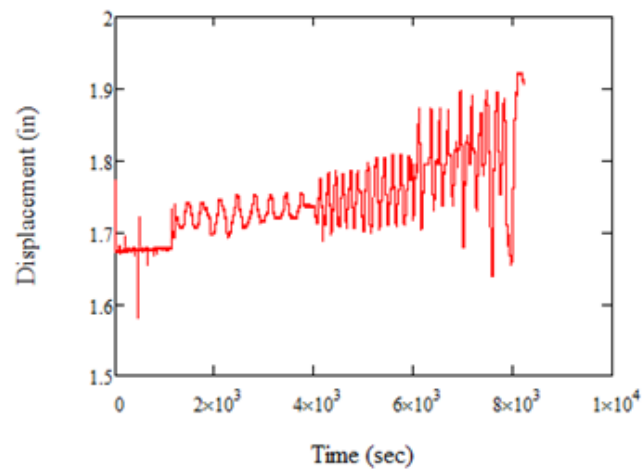
LVDT 2



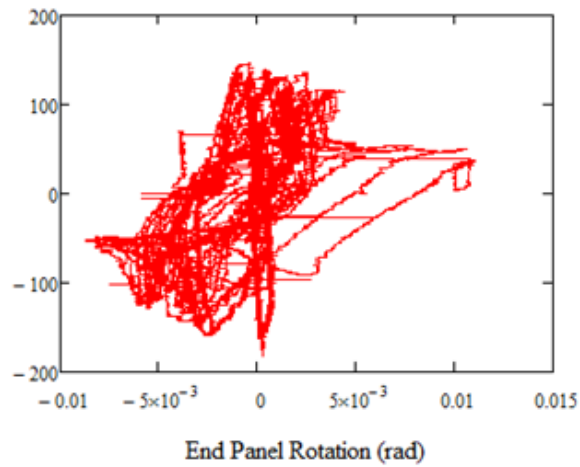
LVDT 1 and 2 Inelastic End Panel Rotation



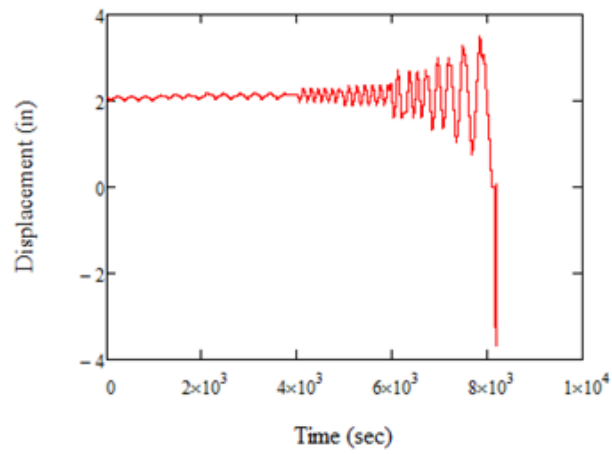
LVDT 3



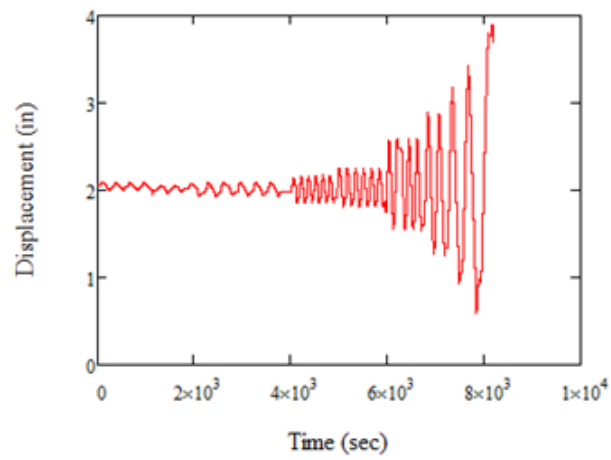
LVDT 4



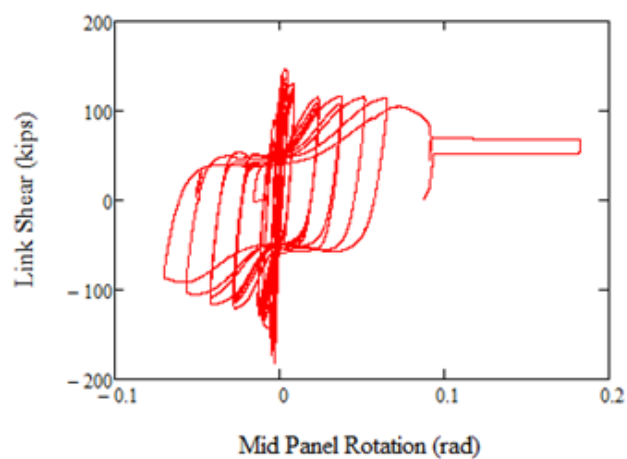
LVDT 3 and 4 Inelastic End Panel Rotation



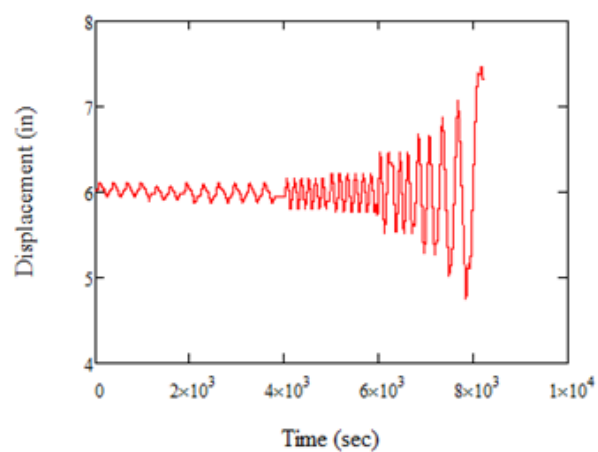
LVDT 5



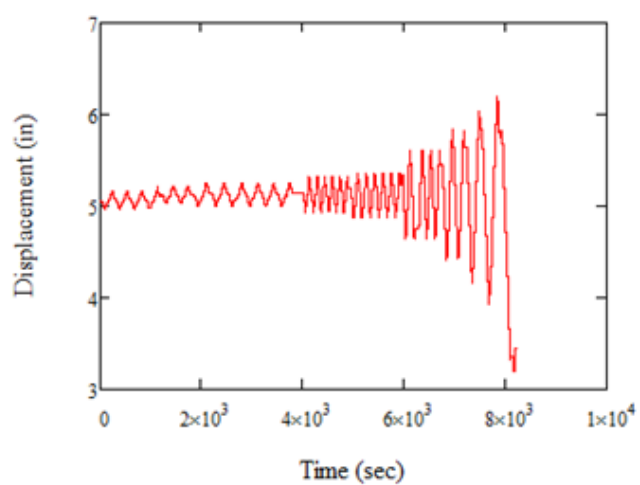
LVDT 6



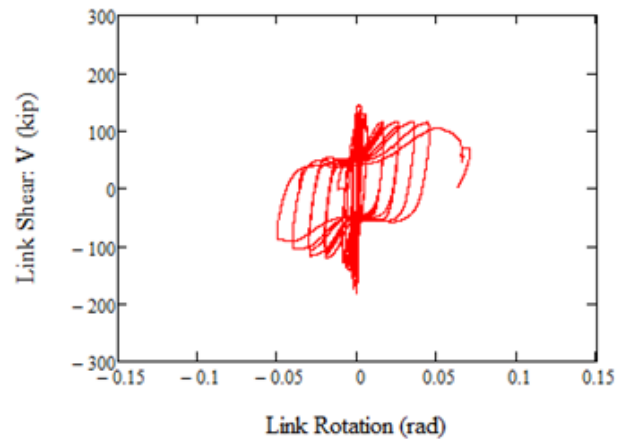
LVDT 5 and 6 Inelastic Mid Panel Rotation



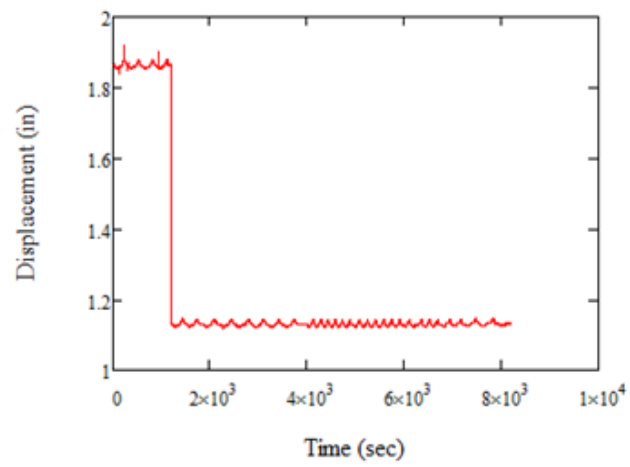
LVDT 7



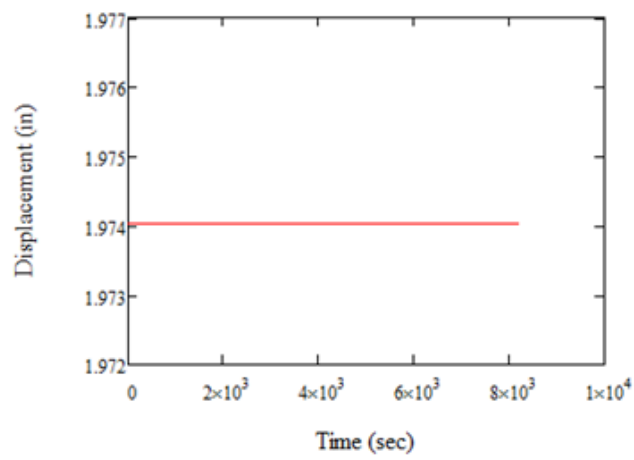
LVDT 8



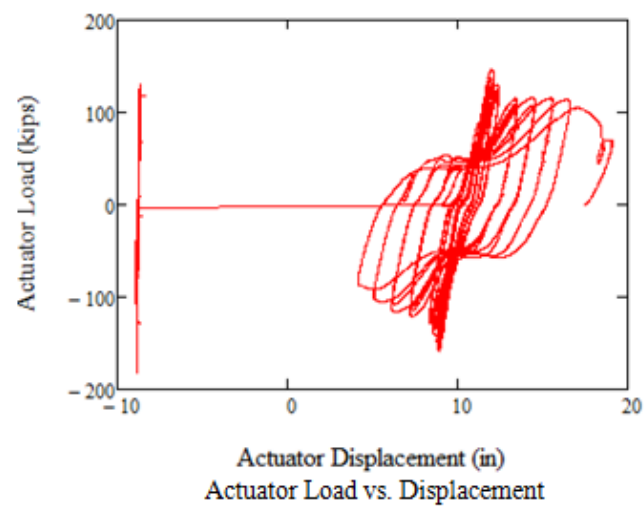
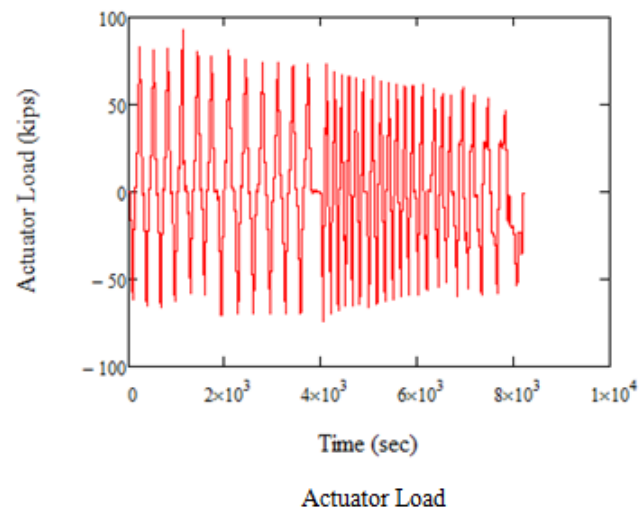
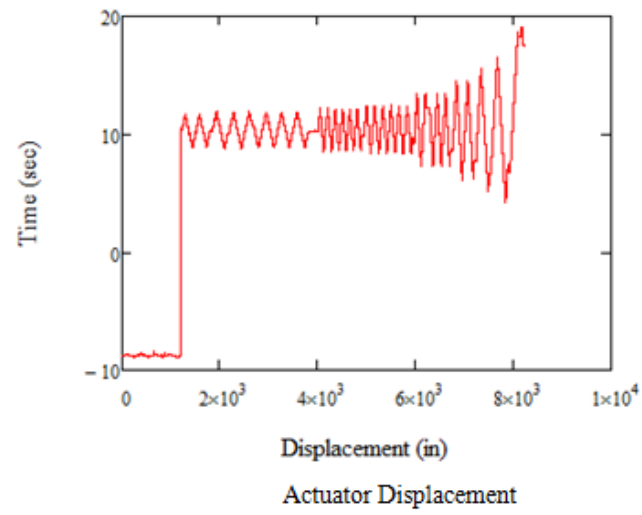
LVDT 7 and 8 Inelastic Rotation

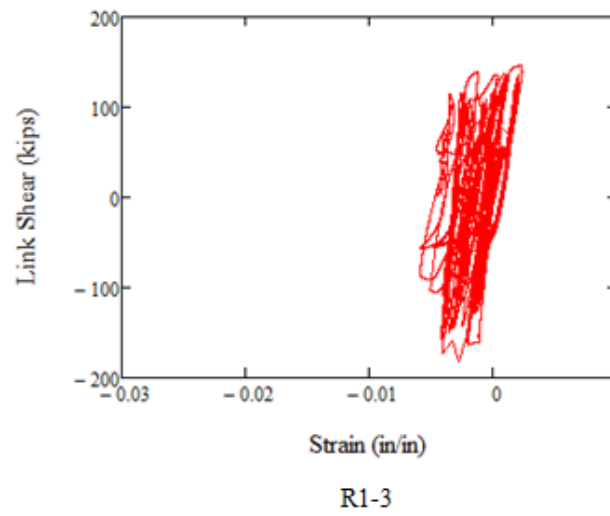
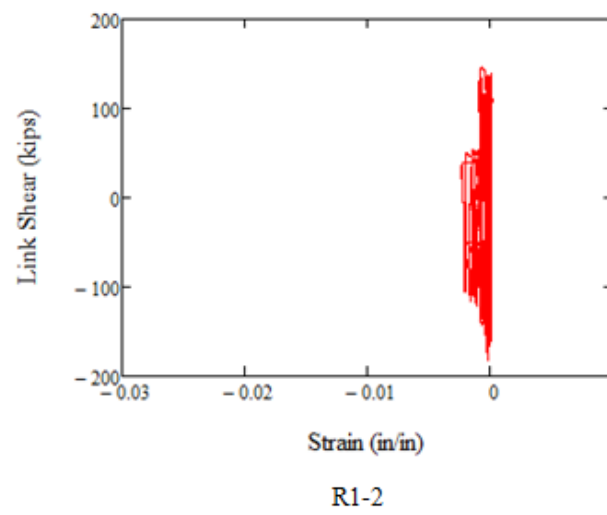
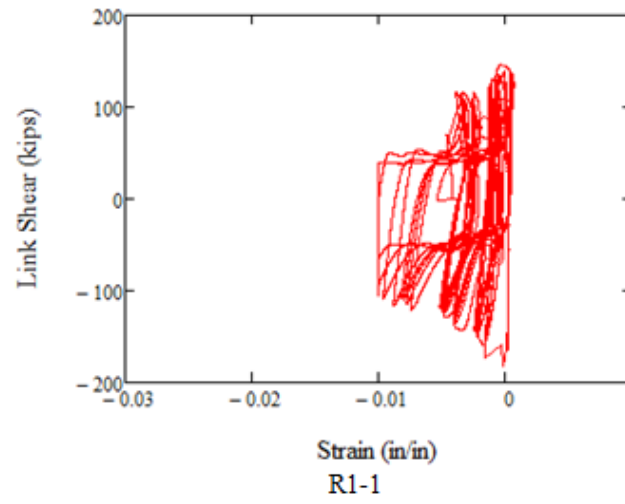


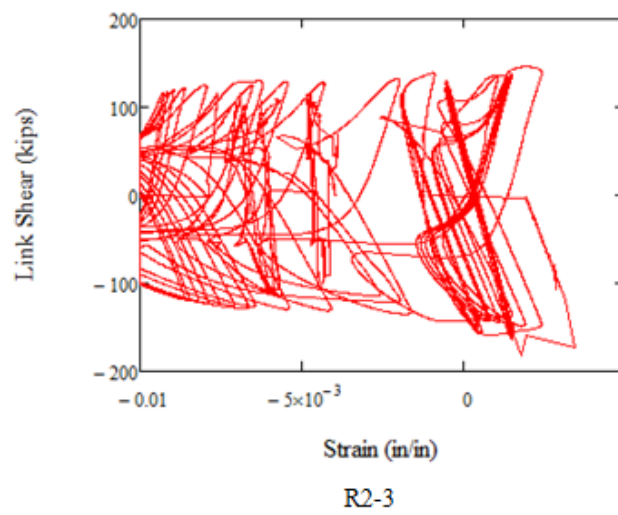
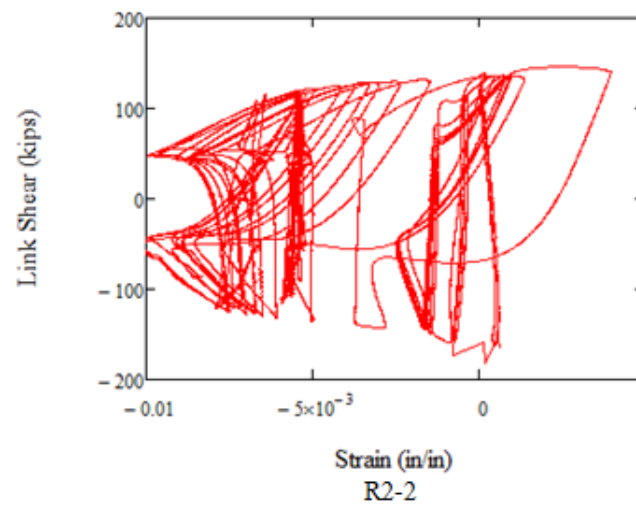
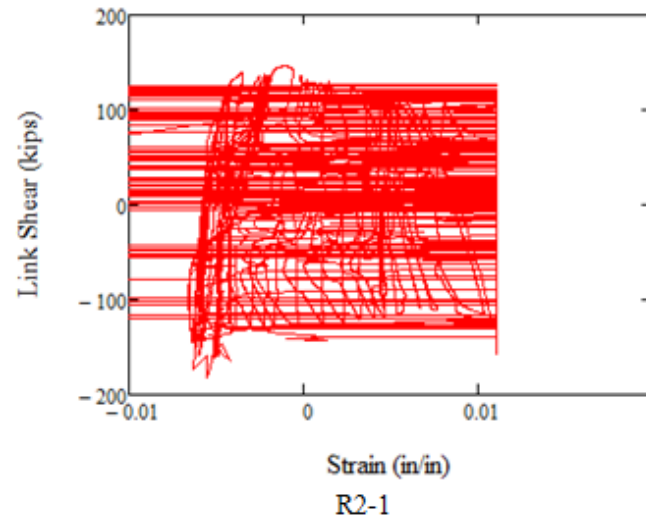
LVDT 9

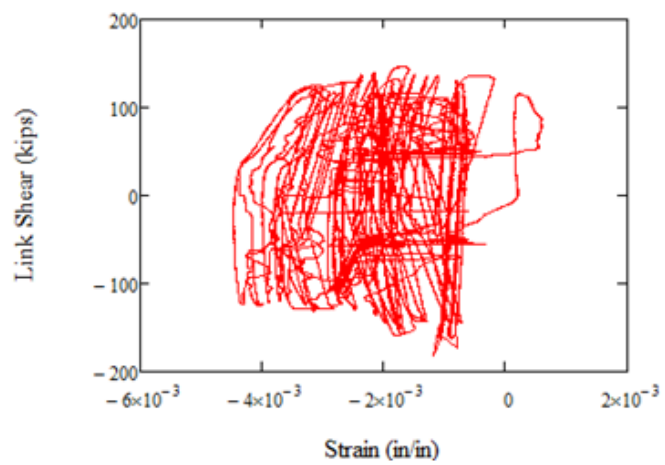


LVDT 10

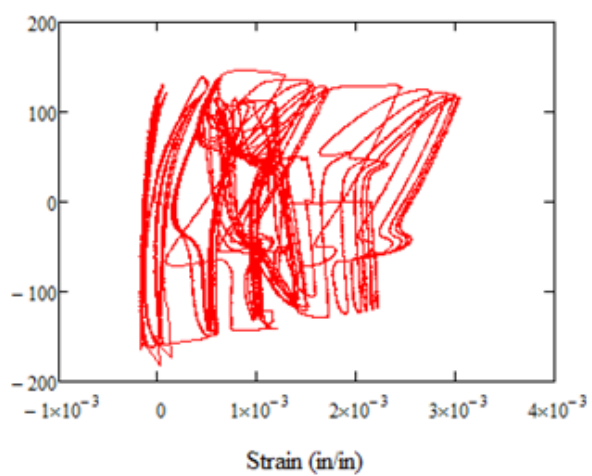




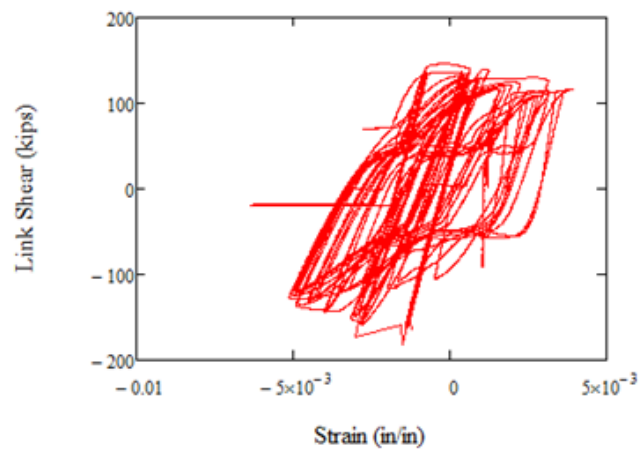




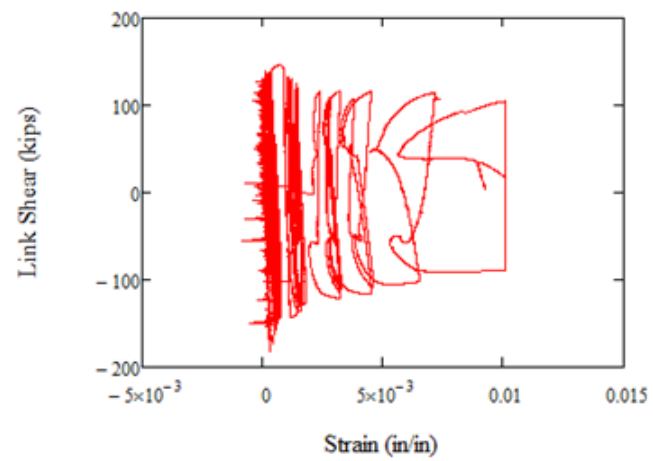
R3-1



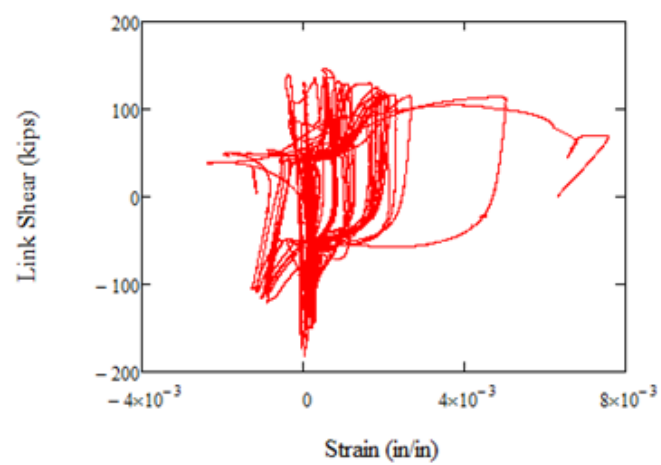
R3-2



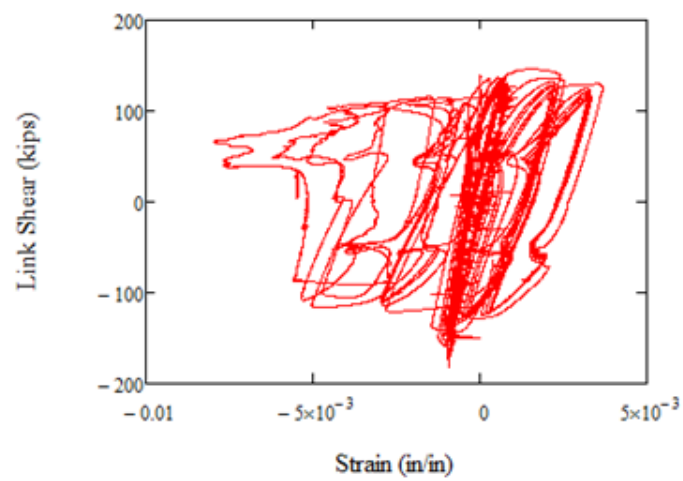
R3-3



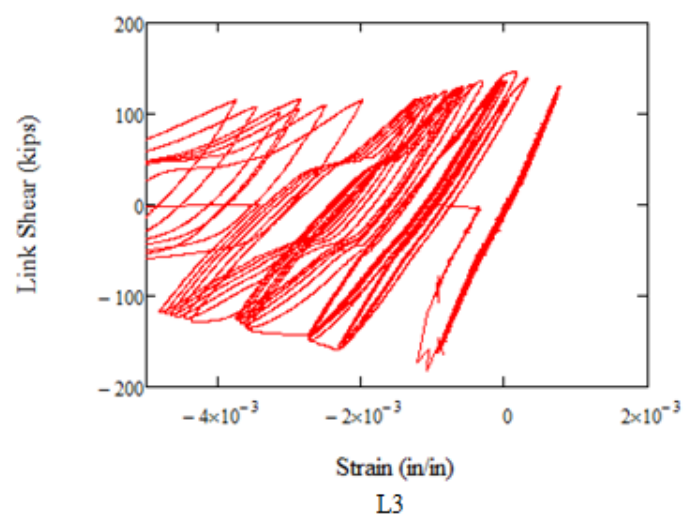
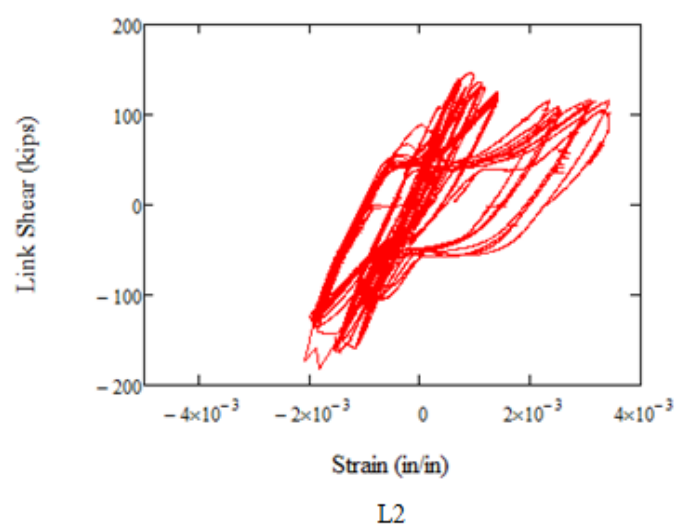
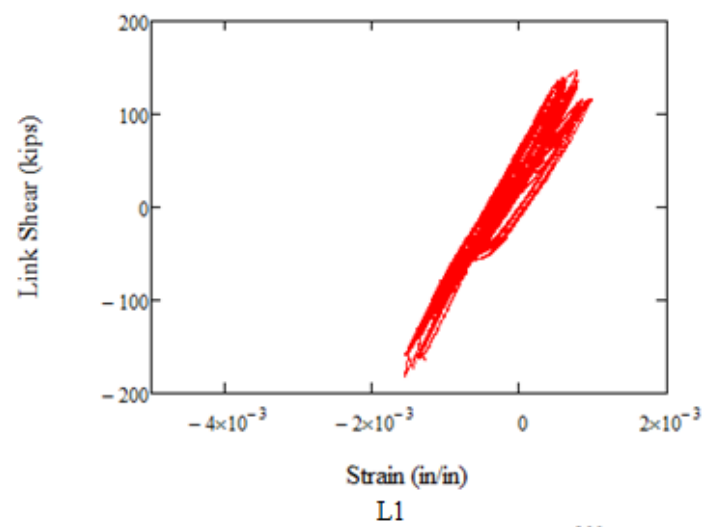
R5-1



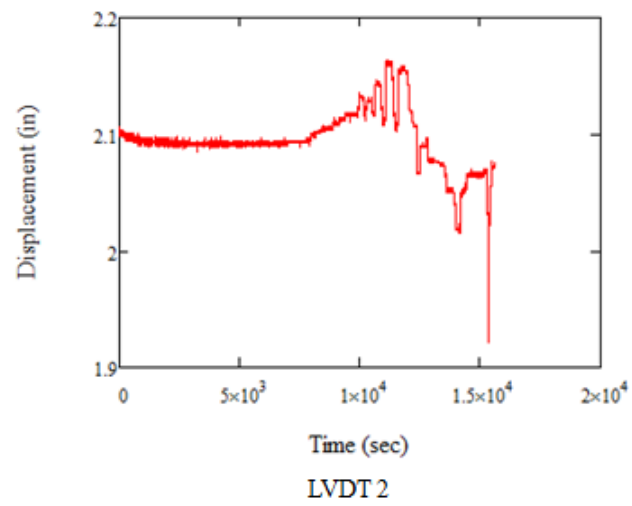
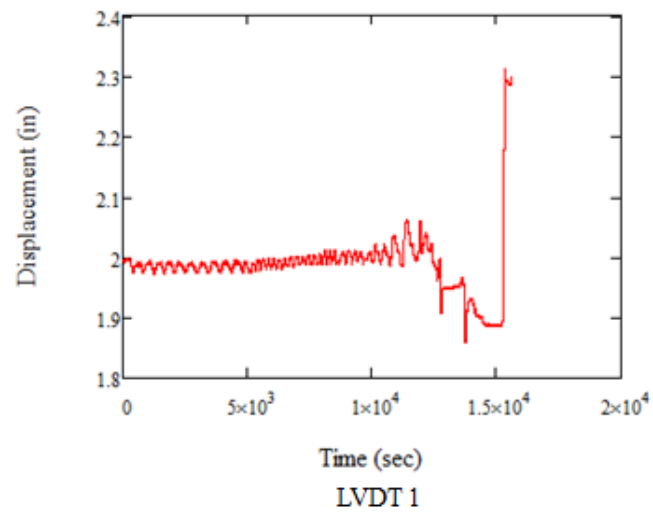
R5-2

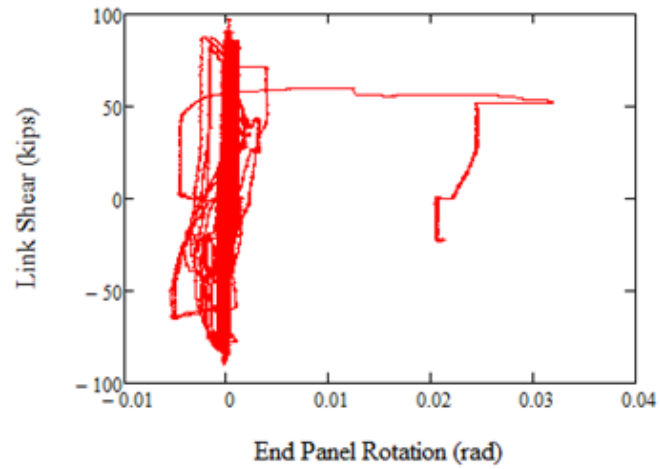


R5-3

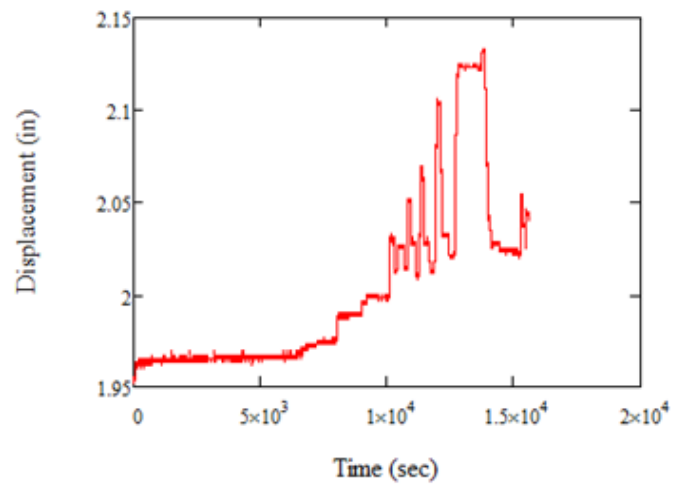


D.5 Link 25DN1_1000

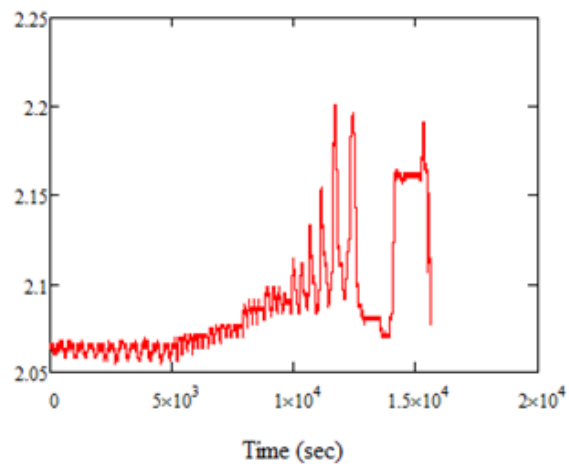




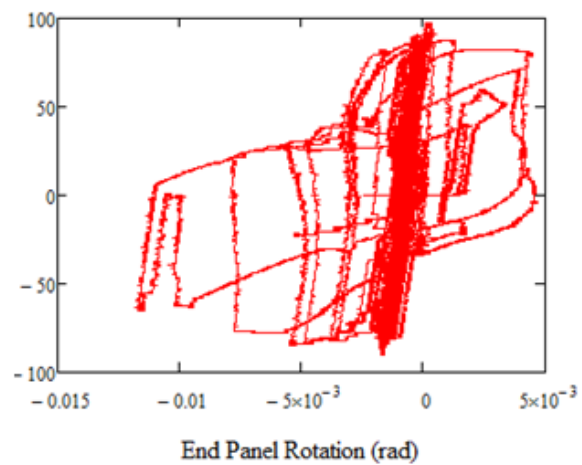
LVDT 1 and 2 Inelastic End Panel Rotation



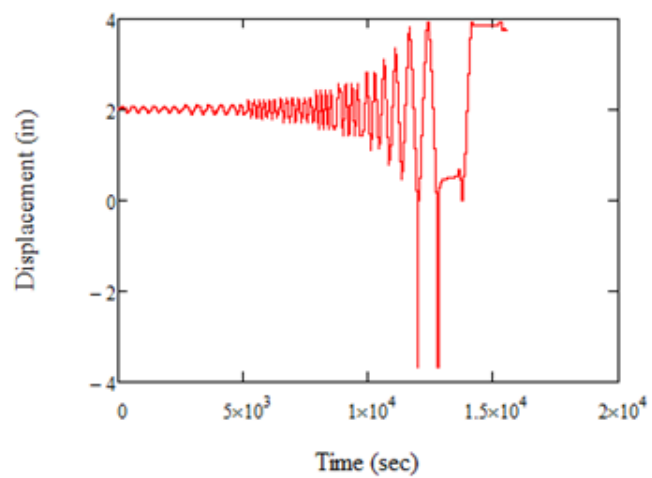
LVDT 3



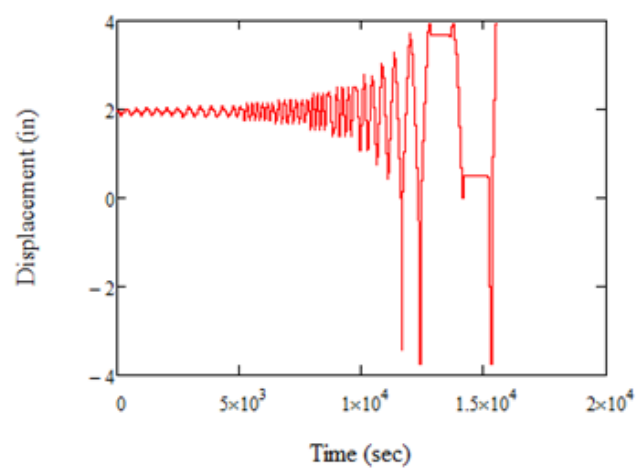
LVDT 4



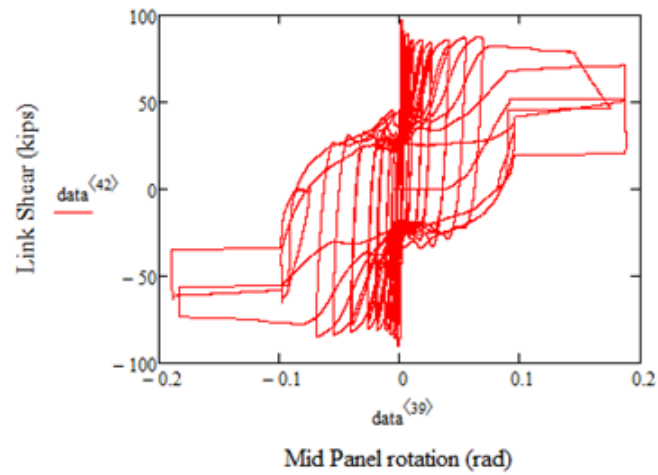
LVDT 3 and 4 Inelastic End Panel Rotation



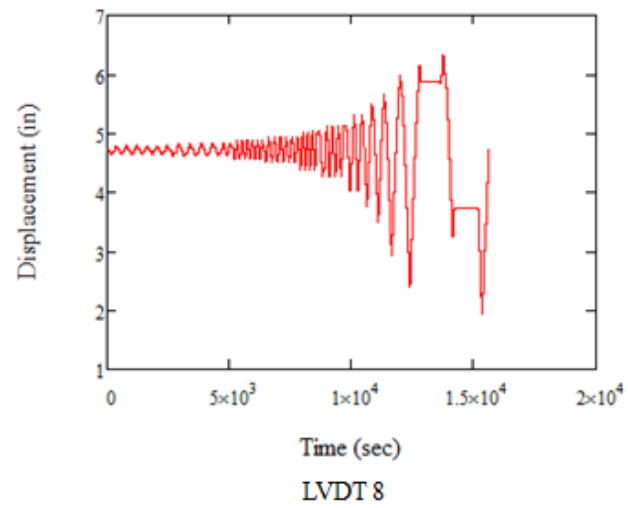
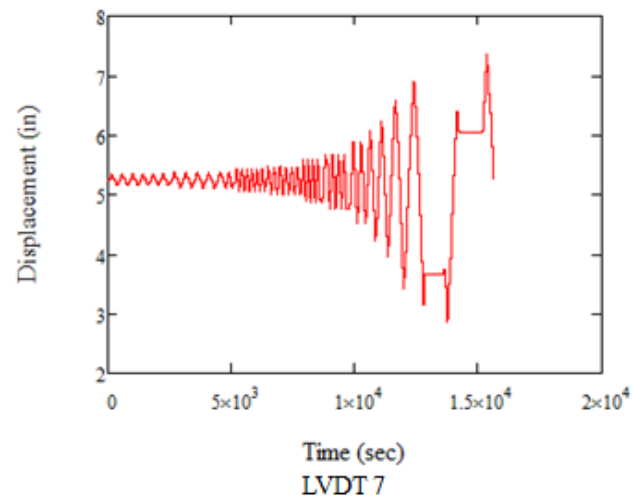
LVDT 5

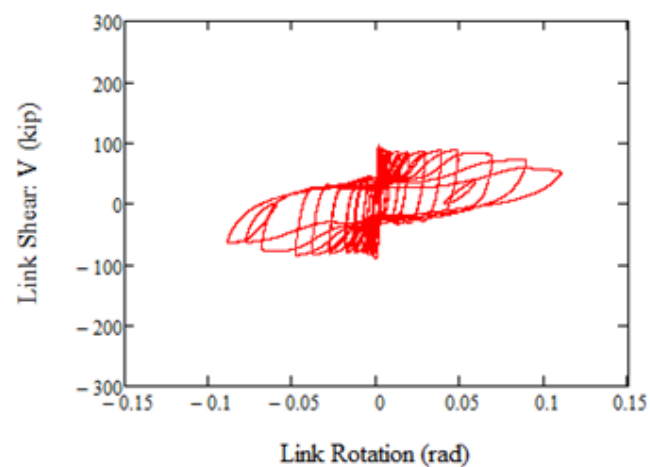


LVDT 6

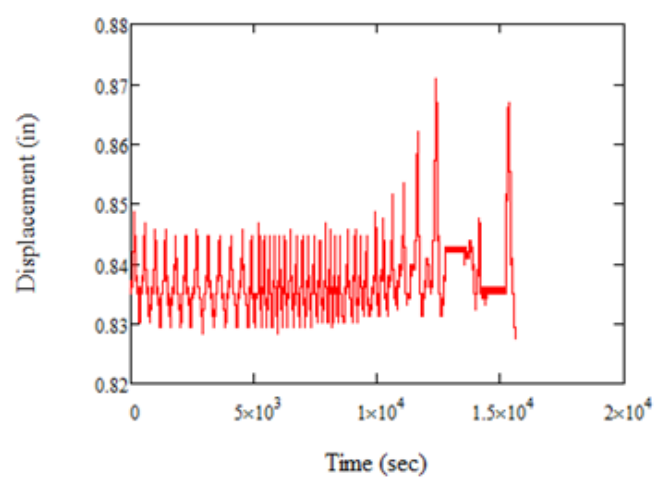


LVDT 5 and 6 Inelastic Mid Panel Rotation

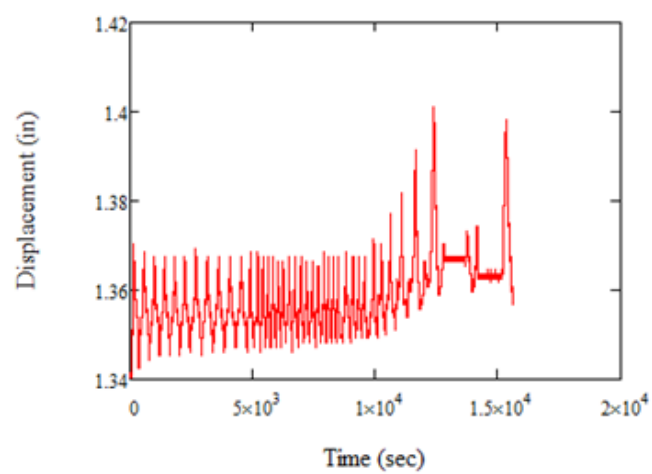




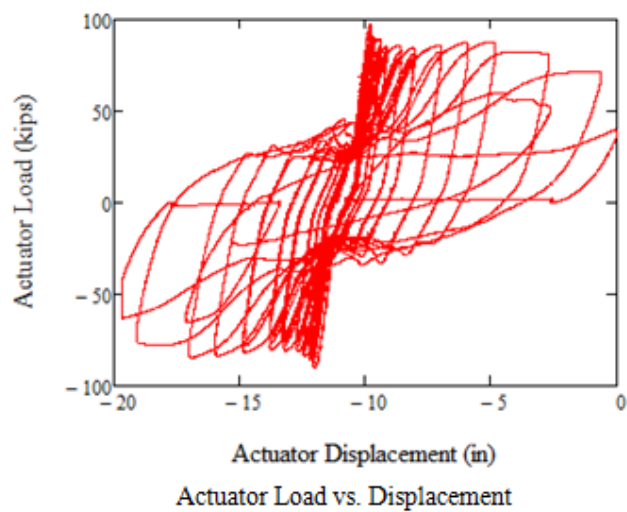
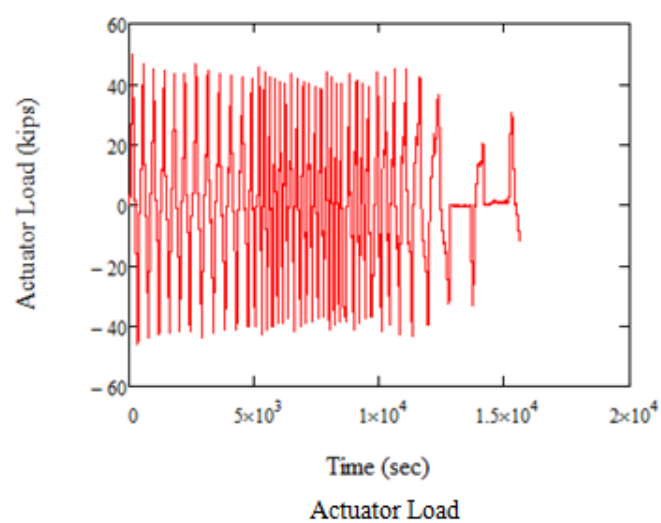
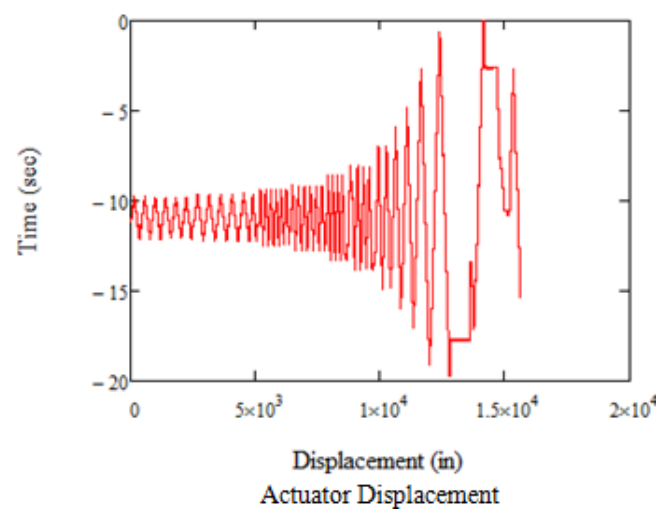
LVDT 7 and 8 Inelastic Rotation

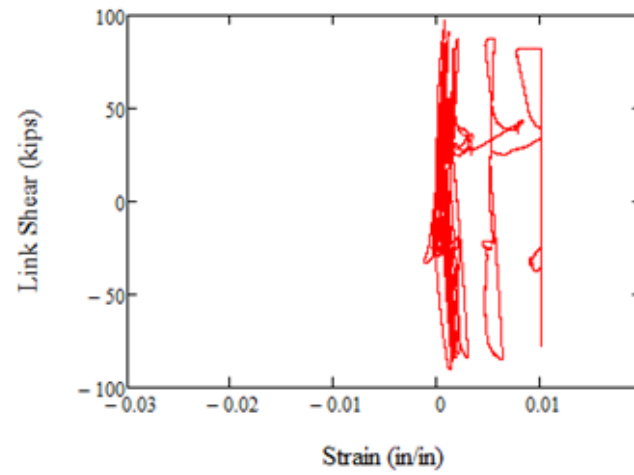


LVDT 9

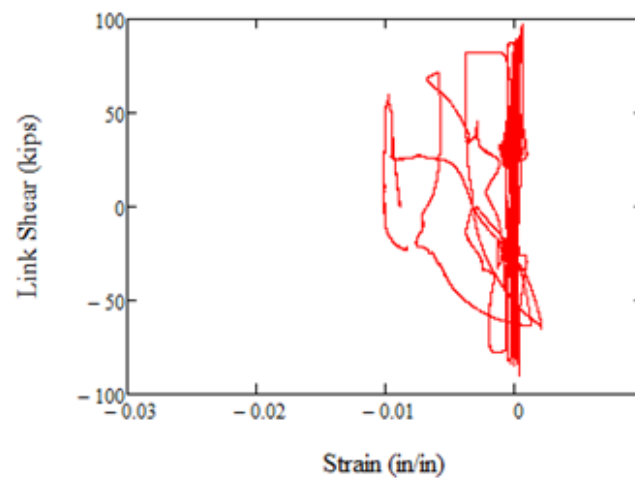


LVDT 10

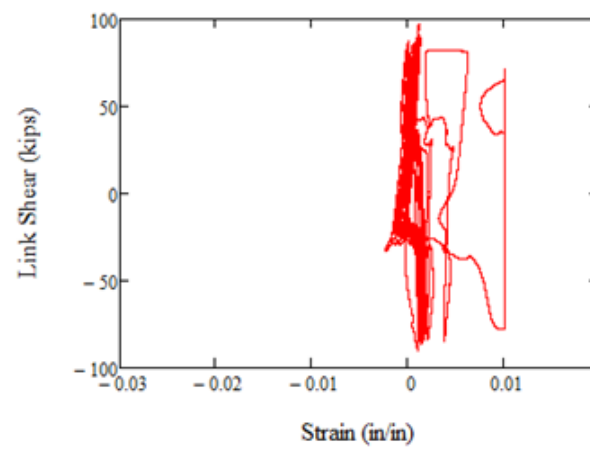




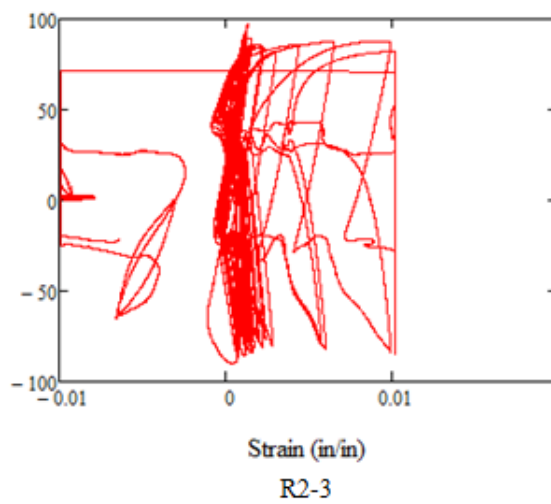
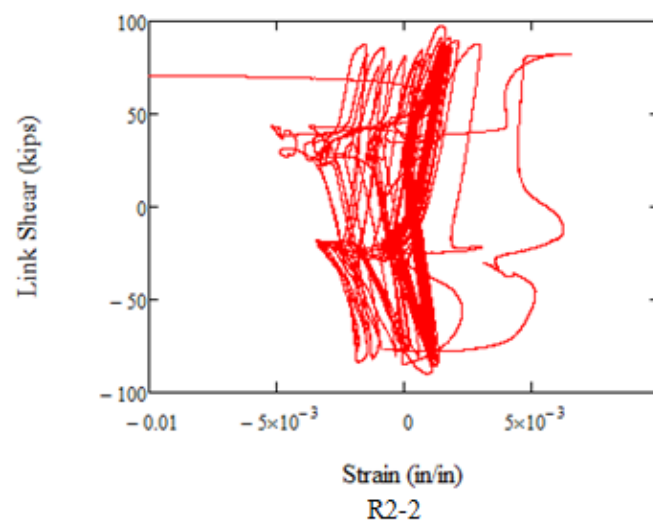
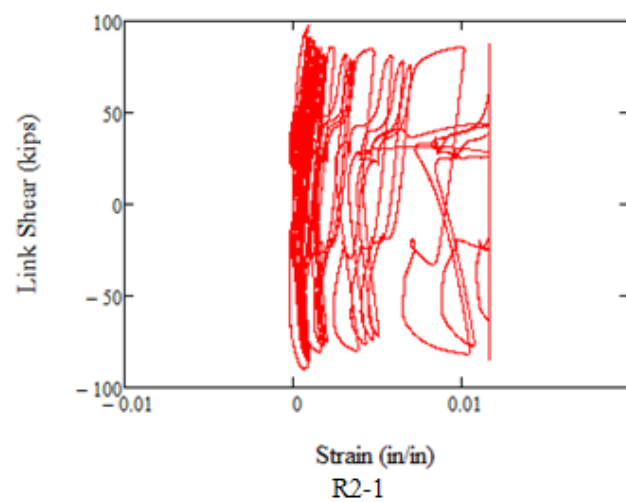
R1-1

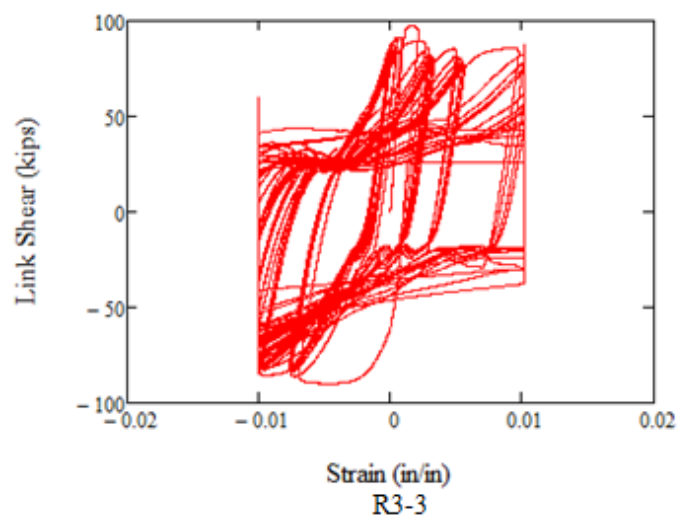
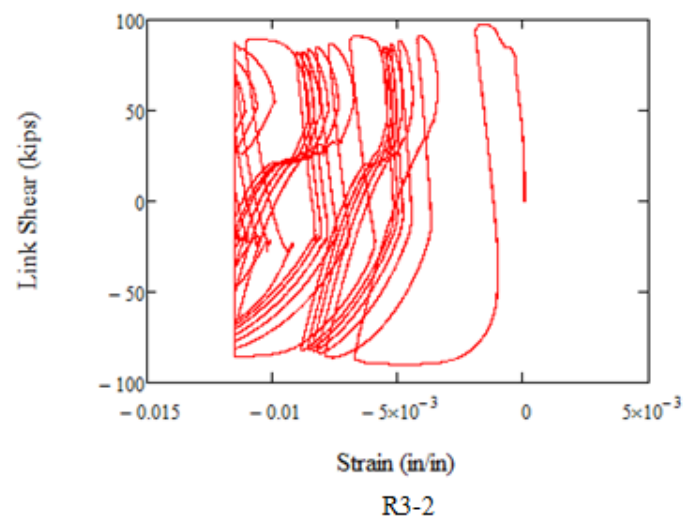
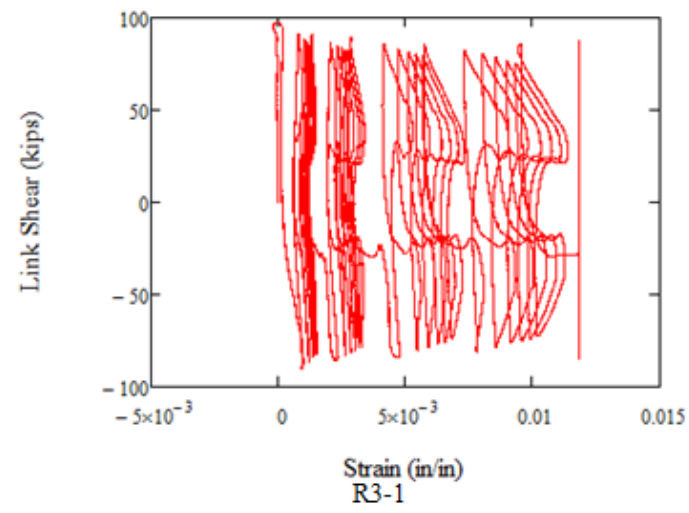


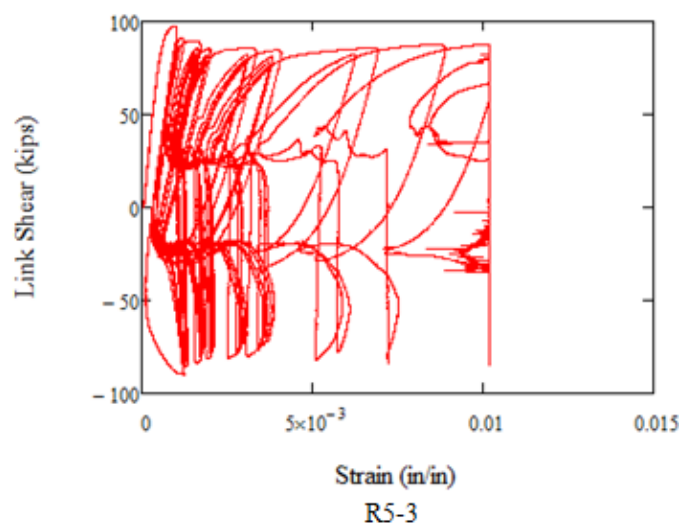
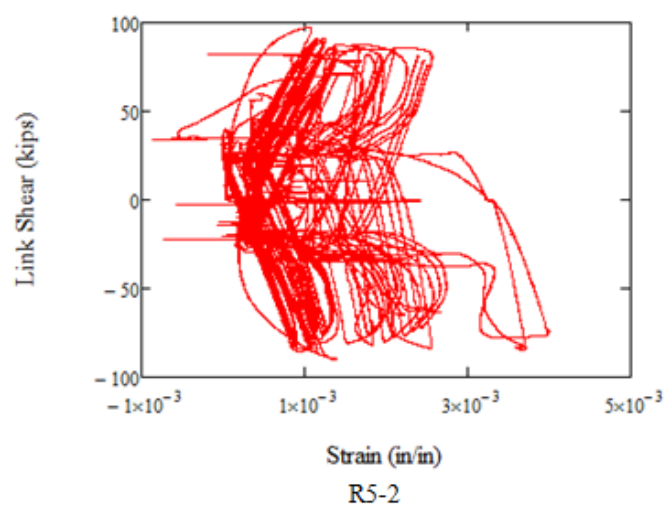
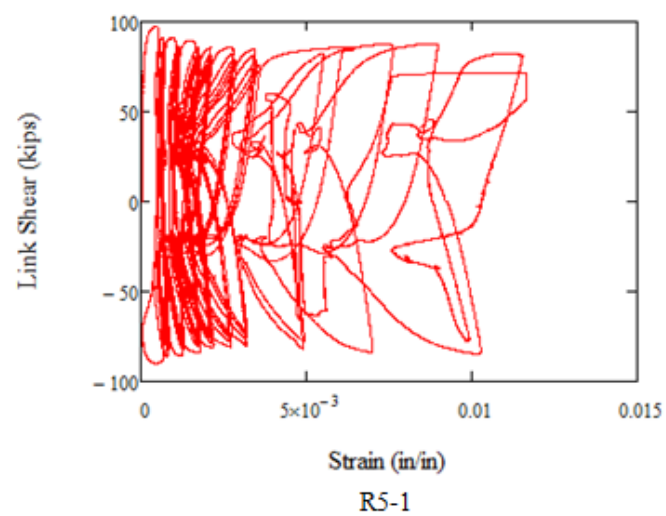
R1-2

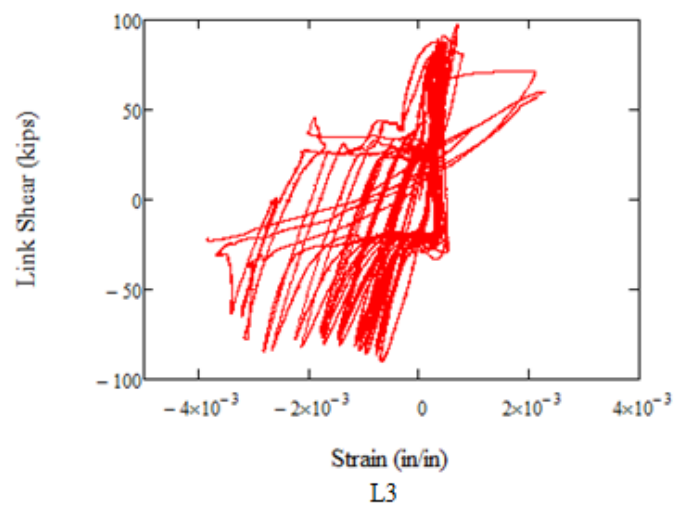
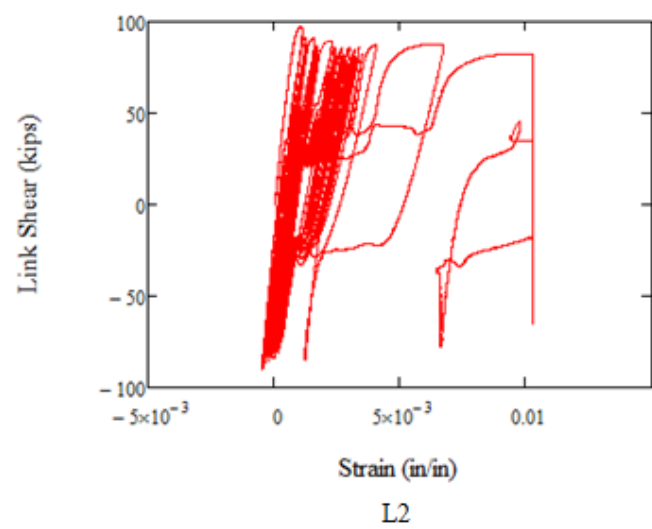
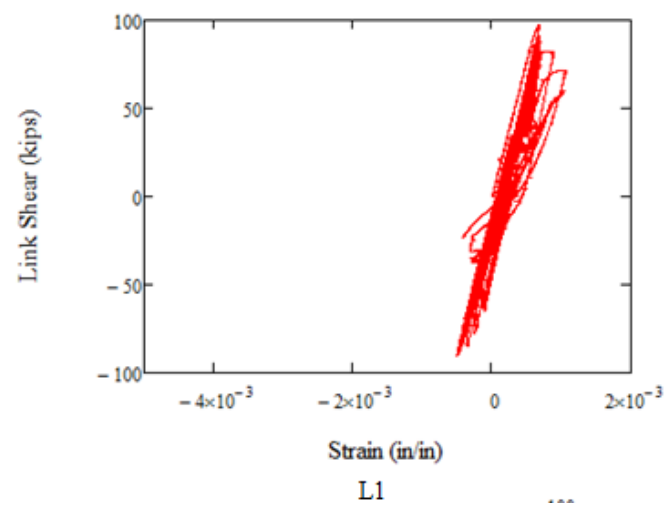


R1-3

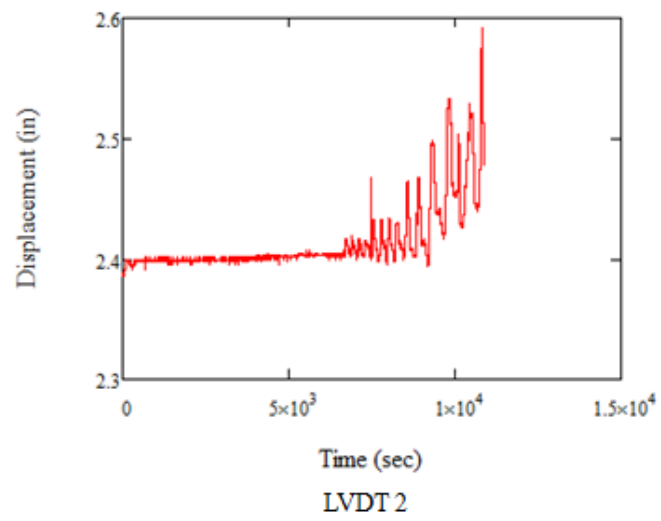
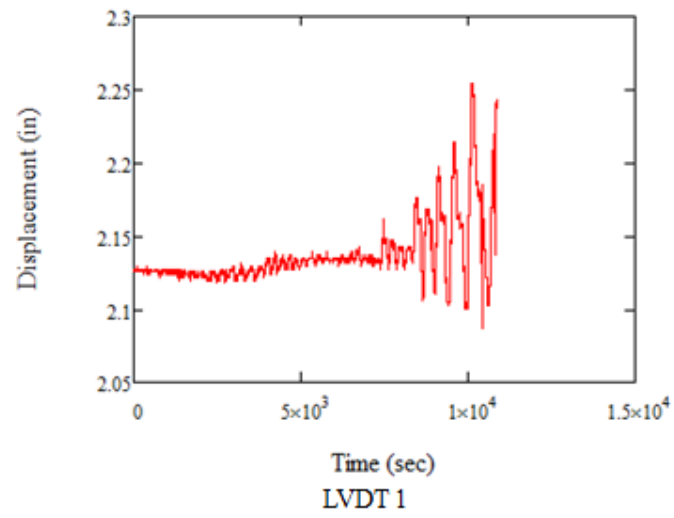


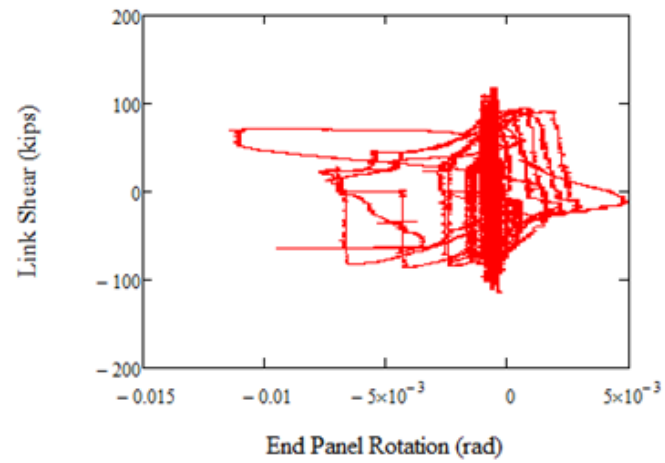




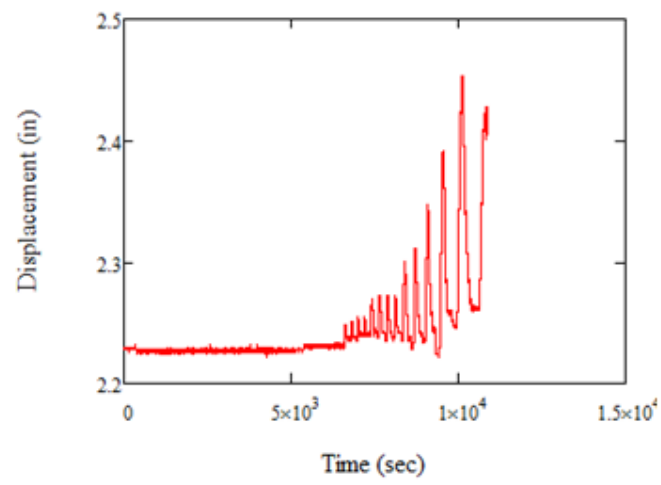


D.6 Link 25DN3_1000

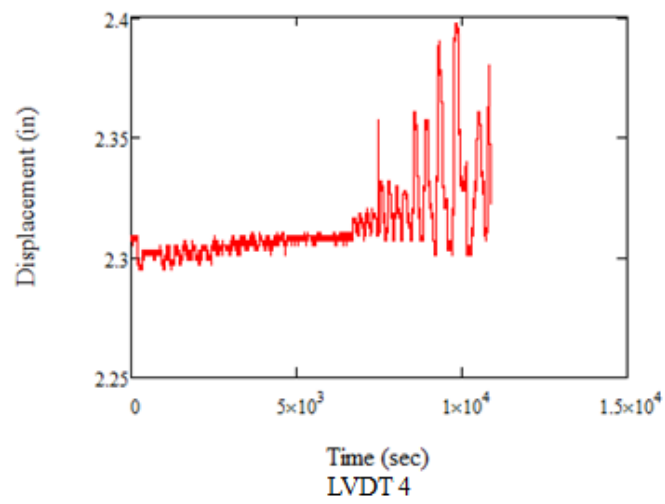




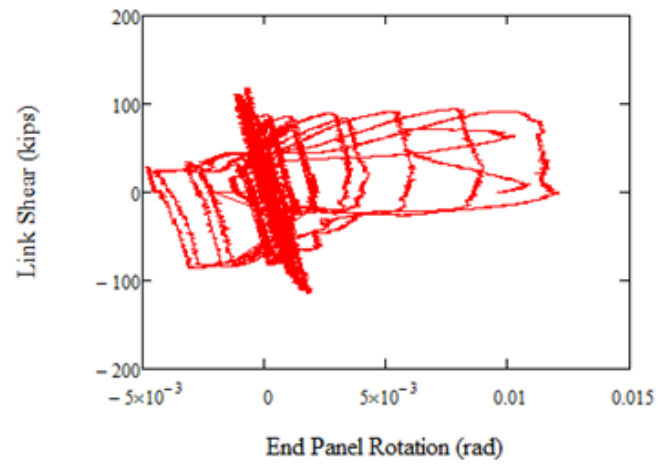
LVDT 1 and 2 Inelastic End Panel Rotation



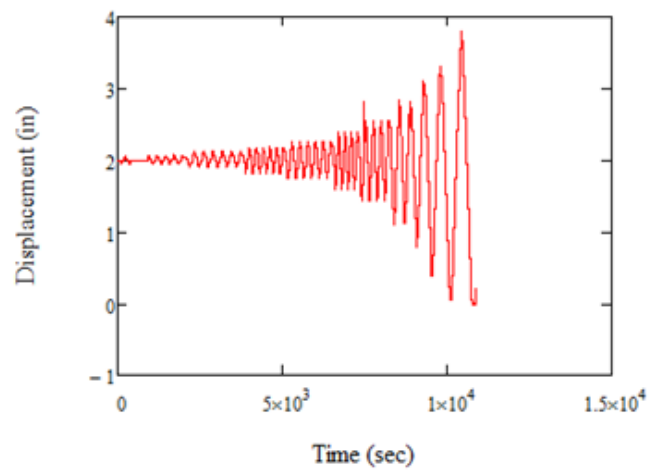
LVDT 3



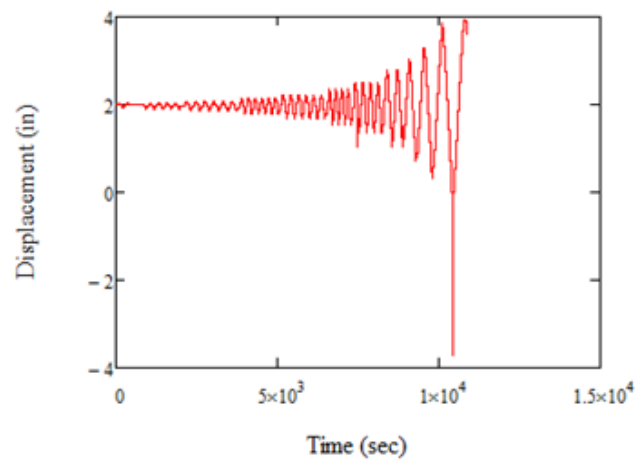
LVDT 4



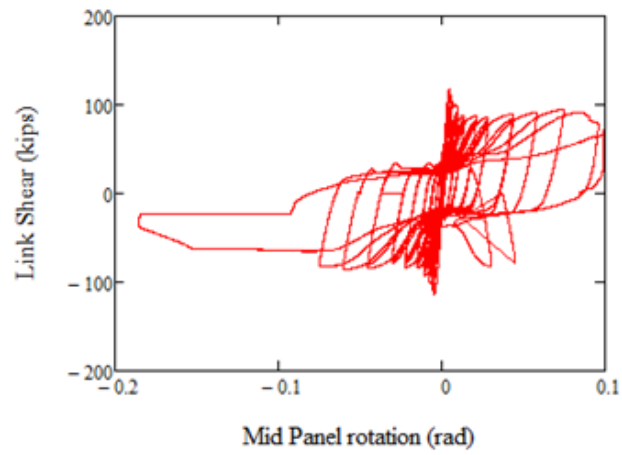
LVDT 3 and 4 Inelastic End Panel Rotation



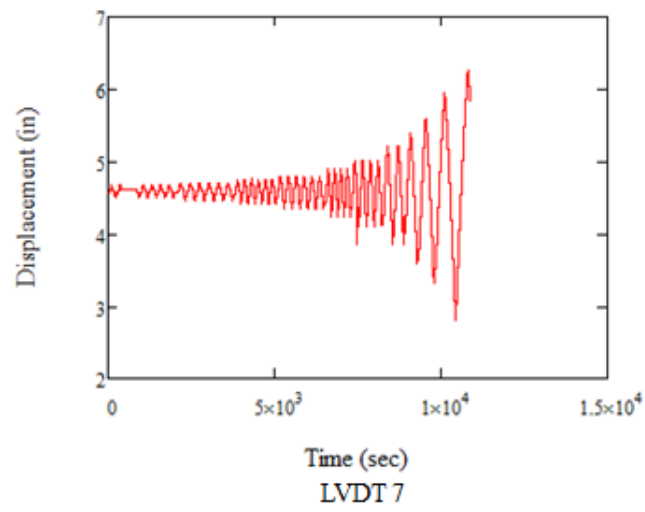
LVDT 5



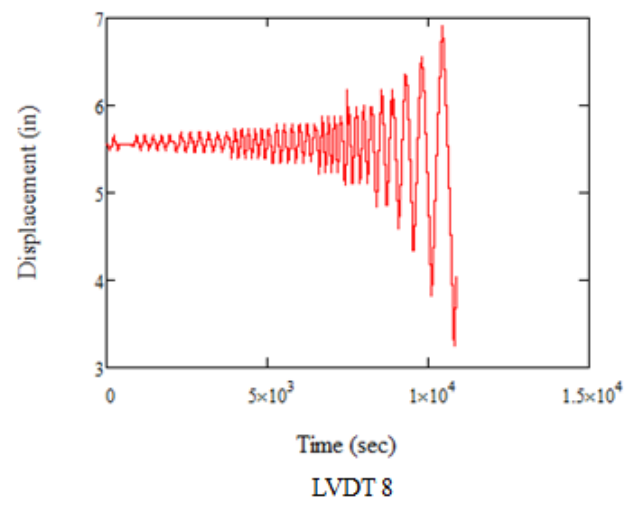
LVDT 6



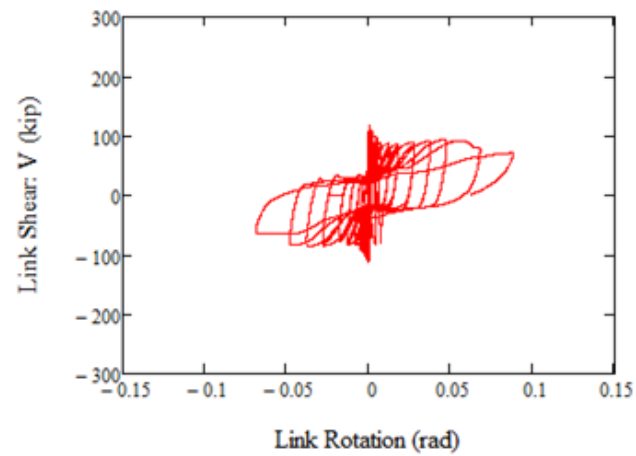
LVDT 5 and 6 Inelastic Mid Panel Rotation



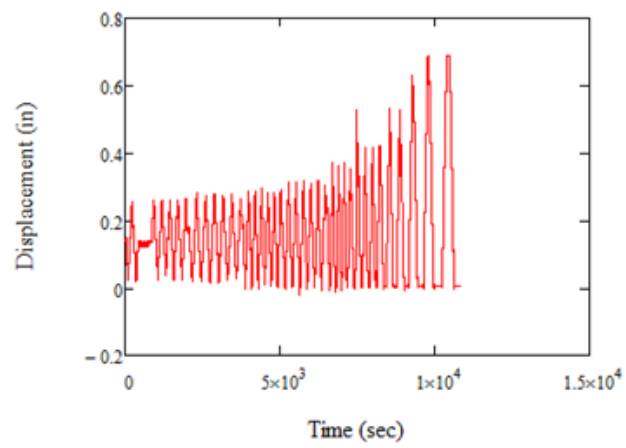
LVDT 7



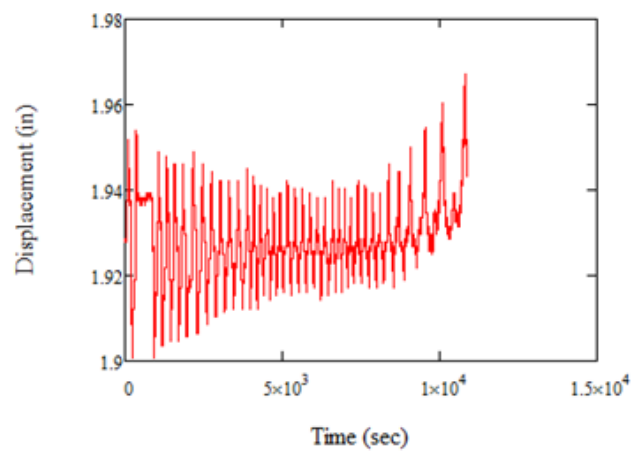
LVDT 8



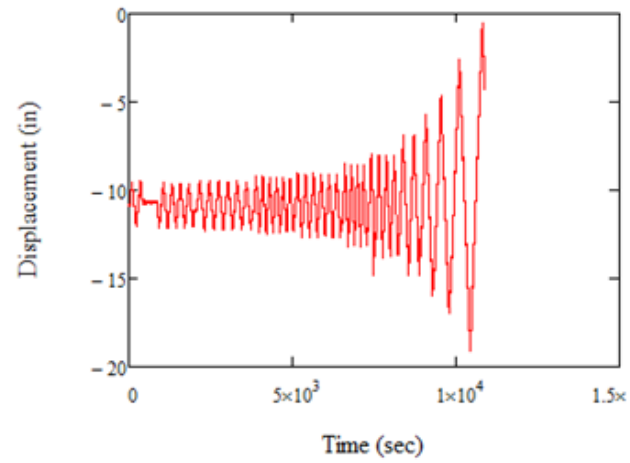
LVDT 7 and 8 Inelastic Rotation



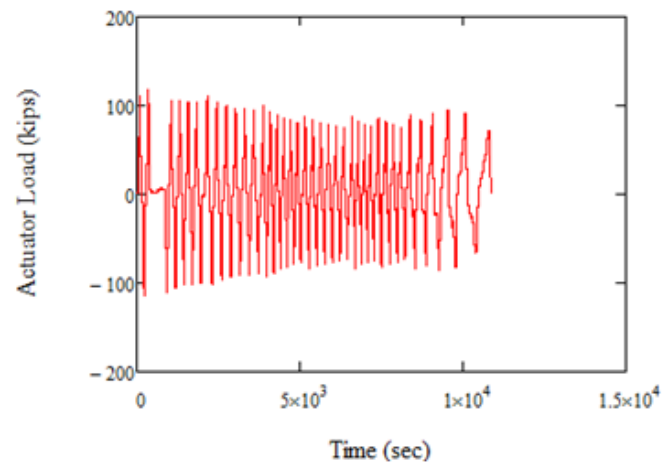
LVDT 9



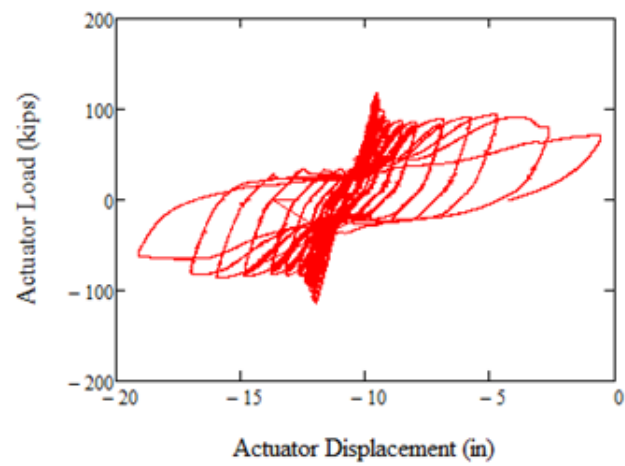
LVDT 10



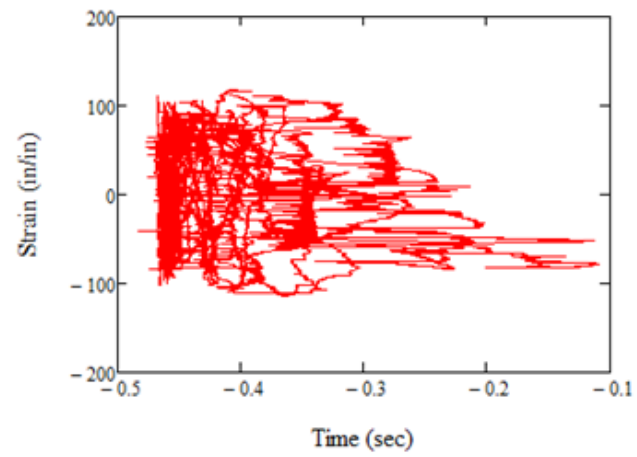
Actuator Displacement



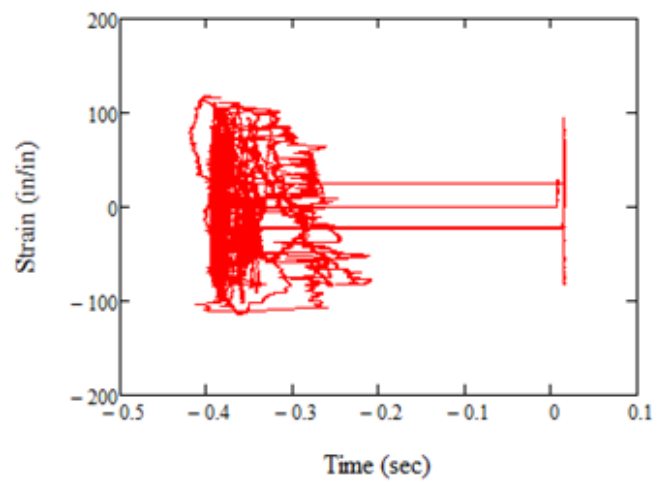
Actuator Load



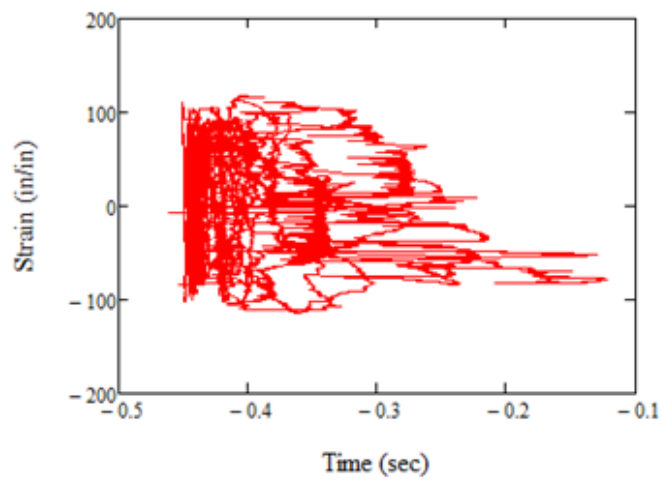
Actuator Load vs. Displacement



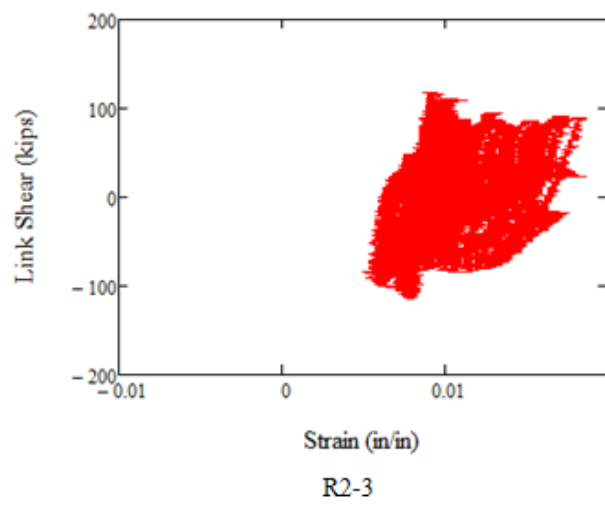
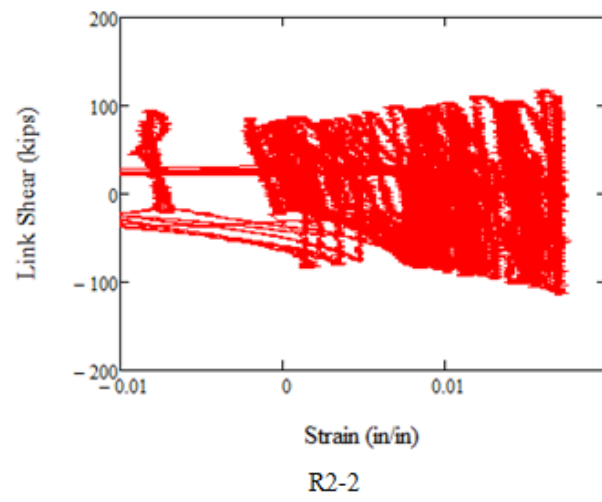
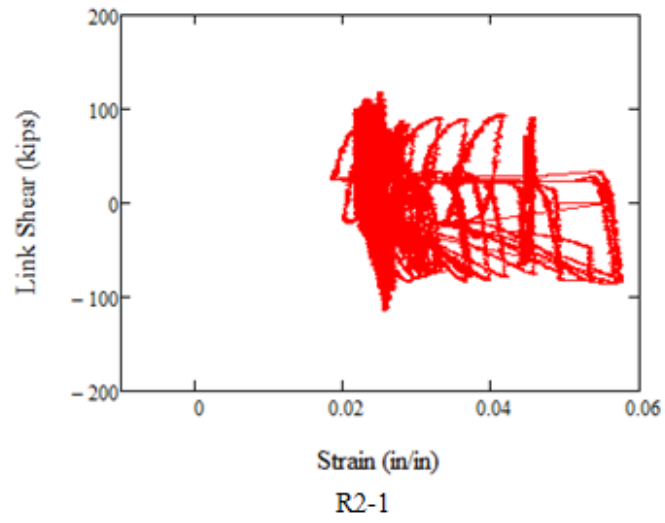
R1-1

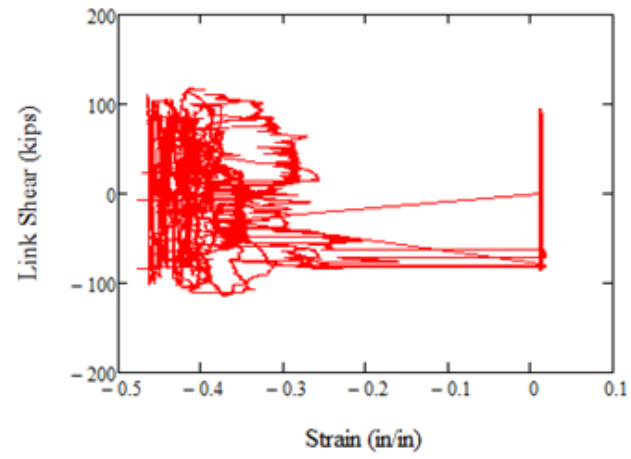


R1-2

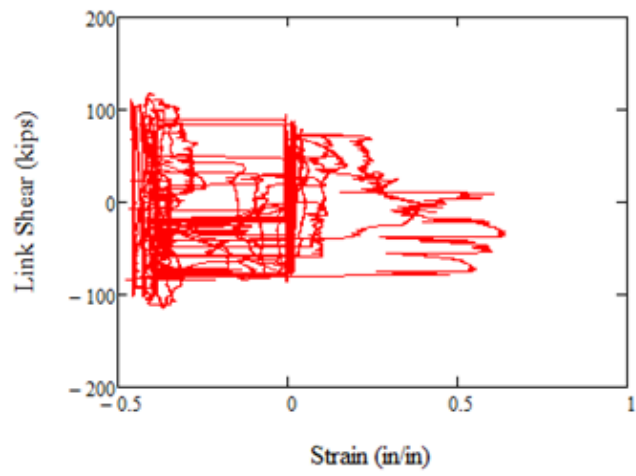


R1-3

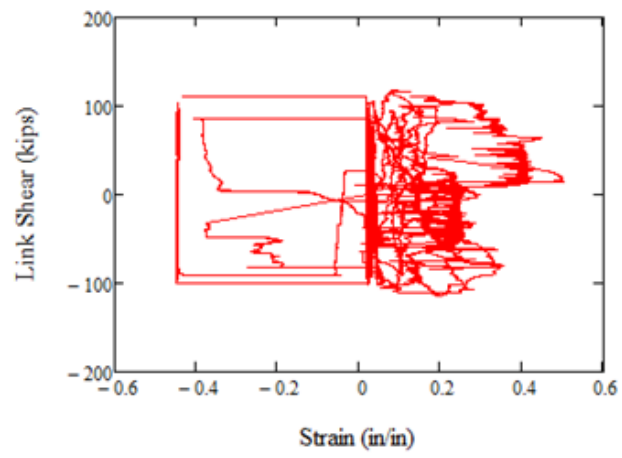




R3-1



R3-2



R3-3

